

**Medical-Image-Based Aorta Modeling with  
Zero-Stress-State Estimation Correlated with  
Anatomical Observation**

by

**Takafumi SASAKI**

**Doctor of Engineering**

Waseda University

February 2019

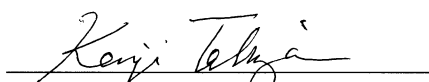
**Medical-Image-Based Aorta Modeling with  
Zero-Stress-State Estimation Correlated with  
Anatomical Observation**

by

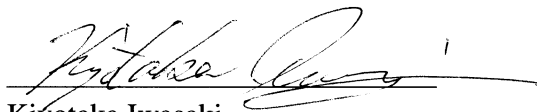
**Takafumi SASAKI**  
**Doctor of Engineering**

Waseda University  
Graduate School of Creative Science and Engineering  
Department of Modern Mechanical Engineering  
Research on Applied Mechanics of Fluid–Structure Interaction

APPROVED, THESIS COMMITTEE:



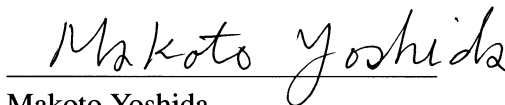
Kenji Takizawa, Chair  
Professor of Modern Mechanical Engineering



Kiyotaka Iwasaki  
Professor of Modern Mechanical Engineering



Jin Kusaka  
Professor of Modern Mechanical Engineering



Makoto Yoshida  
Professor of Modern Mechanical Engineering



Kosei Ishimura  
Professor of Modern Mechanical Engineering

February 2019



## Acknowledgment

I would like to thank Professor Kenji Takizawa first for giving countless help, advice, and guides to me. All my experience at Takizawa Laboratory made me stand at the starting line of an engineer's life, and recognize my strengths and weaknesses. Moreover, I admire the dedication that Professor Takizawa has been challenging for anything, and I will keep challenging as Professor Takizawa showed me. If Professor had not given such precious time, I would not stand here. I would like thank him again here.

I am grateful to Professor Tayfun E. Tezduyar for taking much time helping me. In the stay at Rice University for half of a year, Professor gave me precious experiences. Furthermore, my two papers and conferences I attended would not be done without his rigorous scientific advice. In particular, Professor often helped through asking me some technical questions when I am confused how to explain my research effectively. Like that, Professor gave me innumerable advice. Therefore, I am an honor to work with Professor Tezduyar, and such experiences would be irreplaceable in my life.

Special thanks also go to Professor Kiyotaka Iwasaki, Professor Jin Kusaka, Professor Makoto Yoshida, and Professor Kosei Ishimura whose comments and advice from a mechanical engineering perspective made enormous contributions to this thesis. I learned essential viewpoints as a mechanical engineer.

I would also like to thank Professor Mitsuo Umezu for caring about me since I was in Umezu Laboratory as an undergraduate student. Professor gave much advice about not only mechanical engineering but also a researcher's life.

I appreciate supports from Professor Hiroshi Suito, Professor Takuya Ueda, and Professor Keiichi Itatani. Many opinions which I received presented great opportunities to think about the position I am standing in.

There are many thanks for all of the members in Takizawa Laboratory. I could not have done this thesis without their cooperation. Notably, Dr. Yuto Ootoguro, Taro Kanai, Takashi Kuraishi, Levent Aydinbakar, and Takuya Terahara let me had a wonderful time to research together.

The work was supported in part by the Program for Leading Graduate Schools, "Graduate Program for Embodiment Informatics" of the Ministry of Education, Culture, Sports, Science, and Technology; Grant-in-Aid for JSPS Research Fellow 18J14680.

Finally, I would also like to express my gratitude to my family for their warm encouragements and moral support.

# Contents

List of Illustrations	vii
List of Tables	xv
<b>1 Introduction</b>	<b>1</b>
1.1 Aorta . . . . .	2
1.1.1 Histology and material characteristics . . . . .	2
1.1.2 Residual stress . . . . .	4
1.1.3 Aortic disease . . . . .	7
1.2 Numerical approaches in arterial dynamics . . . . .	9
1.3 Existing research studies on ZSS . . . . .	10
1.3.1 EZP method . . . . .	11
1.3.2 Modeled-prestress method . . . . .	12
1.3.3 Modeled-ZSS method . . . . .	13
1.3.4 Inverse-design method . . . . .	13
1.3.5 Element-based ZSS (EBZSS) . . . . .	14
1.4 Research objective . . . . .	15
1.5 Overview . . . . .	16
<b>2 Formulations for Structural Mechanics</b>	<b>18</b>
2.1 Kinematics . . . . .	18
2.2 Natural coordinate system . . . . .	20
2.3 Principle of virtual work and variational formulation of structural mechanics . . . . .	25
2.4 Conservation of mass . . . . .	26
2.5 Total Lagrangian formulation of structural mechanics . . . . .	27
2.6 Element-based total Lagrangian (EBTL) method . . . . .	28

2.6.1	EBZSS . . . . .	28
2.7	Boundary conditions . . . . .	29
2.8	Strain-energy function . . . . .	29
2.8.1	Compressible material . . . . .	36
2.8.2	Incompressible material . . . . .	50
2.9	Constitutive equations . . . . .	51
<b>3</b>	<b>Isogeometric Discretization</b>	<b>55</b>
3.1	B-splines . . . . .	55
3.1.1	Knot vectors . . . . .	55
3.1.2	Basis functions . . . . .	56
3.1.3	Derivatives of B-spline basis functions . . . . .	56
3.2	NURBS . . . . .	56
3.3	T-splines . . . . .	57
3.4	Bézier extraction . . . . .	58
<b>4</b>	<b>EBZSS with Isogeometric Discretization</b>	<b>60</b>
4.1	EBTL method with isogeometric discretization . . . . .	61
4.2	Modeling the ZSS initial guess: straight-tube ZSS template . . . . .	64
4.3	2D test computations . . . . .	65
4.3.1	Curvature matching in the ZSS . . . . .	67
4.3.2	Computational results . . . . .	68
4.4	3D computation . . . . .	71
4.4.1	Surface and volume mesh generation for the target geometry . . . . .	73
4.4.2	Mesh generation for $(\mathbf{X}_0^e)^0$ . . . . .	73
4.4.3	Iterations to calculate $\mathbf{X}_0^e$ . . . . .	76
4.4.4	Observations on the results . . . . .	76
4.5	Concluding remarks . . . . .	77
<b>5</b>	<b>IPBZSS Estimation</b>	<b>87</b>
5.1	EBTL method with IPBZSS . . . . .	88
5.1.1	IPBZSS . . . . .	88

5.1.2	EBZSS to IPBZSS . . . . .	90
5.1.3	IPBZSS to EBZSS . . . . .	90
5.1.4	An iterative method . . . . .	90
5.2	ZSS Initial guess based on the shell model of the artery . . . . .	92
5.2.1	Inner-surface coordinates in the target state . . . . .	93
5.2.2	Inner-surface coordinates in the ZSS . . . . .	95
5.2.3	Wall coordinates in the target state . . . . .	97
5.2.4	Wall coordinates in the ZSS . . . . .	98
5.2.5	Calculating the components of the ZSS metric tensor at each integration point . . . . .	99
5.2.6	Design of the ZSS . . . . .	100
5.3	Numerical examples . . . . .	101
5.3.1	Y-shaped tube . . . . .	101
5.3.2	Patient-specific aorta geometry . . . . .	109
5.4	Concluding remarks . . . . .	111

## **6 ZSS Estimation with Anatomical Observation 118**

6.1	Coordinate systems for the artery inner surface and wall . . . . .	119
6.1.1	Mesh generation . . . . .	119
6.1.2	Wall coordinates in the target state . . . . .	120
6.1.3	Wall coordinates in the ZSS . . . . .	124
6.2	Analytical expression and the ZSS initial guess design . . . . .	126
6.2.1	Analytical solution based Kirchhoff–Love shell theory . . . . .	126
6.2.2	The ZSS initial guess design . . . . .	131
6.3	Numerical examples . . . . .	132
6.3.1	Analytical solution for constant stretch on the inner surface . . . . .	132
6.3.2	Straight tube . . . . .	132
6.3.3	Y-shaped tube . . . . .	133
6.3.4	Patient-specific aorta . . . . .	142
6.4	Evaluations . . . . .	145
6.4.1	Comparison between the initial guess and the converged ZSS . . . . .	145

6.4.2	Stretch distribution . . . . .	158
6.5	Concluding remarks . . . . .	159
<b>7</b>	<b>Concluding Remarks</b>	<b>161</b>
7.1	EBZSS estimation with isogeometric discretization . . . . .	162
7.2	IPBZSS estimation . . . . .	162
7.3	ZSS estimation with anatomical observation . . . . .	163
<b>A</b>	<b>Constitutive models</b>	<b>165</b>
A.1	Neo-Hookean model . . . . .	165
A.2	The isotropic version of Kappa model . . . . .	168
	<b>Bibliography</b>	<b>172</b>

## Illustrations

1.1	Cardiovascular system [2]. The red colored region is the aorta . . . . .	3
1.2	Major components of an artery. Three layers in the wall: intima, media, and adventitia [5] . . . . .	4
1.3	The cross-sectional shape of the aorta of a cat [12]. Before ( <i>left</i> ) and after the cut ( <i>right</i> ) . . . . .	5
1.4	Definitions of the opening angles ( $\phi$ and $\phi'$ ) of arteries with radial cut . .	5
1.5	Open up response results with human aortas [16]. One cut example ( <i>left</i> ) and summarized curvature changes ( <i>right</i> ) . . . . .	6
1.6	Opening angles [17]. Variations in ages ( <i>left</i> ) and gender ( <i>right</i> ). The $x$ -axis indicates the normalized axial location from the ascending part to the end of the descending part . . . . .	6
1.7	Creep of the opening angle [17]. Normalized angles against the values at 60 min in time. Young ( <i>upper</i> ) and old ( <i>bottom</i> ), male ( <i>left</i> ) and female ( <i>right</i> ) subjects. The symbols show the positions in normalized axial locations of the aortic rings . . . . .	7
1.8	Types of aneurysms. Fusiform-shaped ( <i>left</i> ), and saccular-shaped ( <i>right</i> ) aneurysms . . . . .	8
1.9	Cardiovascular system. Cross-sectional images from CT ( <i>left</i> ) and MRI ( <i>right</i> ) . . . . .	9
1.10	Aorta geometry which is constructed by using MDCT 3D reconstruction	10
1.11	Concept image of the EZP method. The parameters $p$ is the inflation pressure, and $p_{img}$ is the inflation blood pressure at the time that the medical-image-based geometry was obtained in a cardiac cycle . . . . .	12

1.12	ZSS modeling. The method uses cylinder coordinate, $R(r)$ , $\Theta(\theta)$ , and $Z(z)$ . The parameters $L$ is the axial length, $A$ and $B$ are the inner and outer radius, $\alpha$ is the opening angle. ZSS ( <i>left</i> ) and unloaded configuration ( <i>right</i> ) . . . . .	13
1.13	Concept image of EBZSS. The bottom process is defining the ZSS initial guess like the modeled-ZSS method. The above process is converging ZSS so that the deformed shape is matched to the target state . . . . .	15
1.14	Overview . . . . .	17
3.1	T-spline control grid. The center point is an extraordinary point. The cross points with three edges in the surface are T-junctions . . . . .	58
4.1	The position $\times$ is the where $(\mathbf{X}_0^e)^{i+1}$ is calculated in a Bézier element. The representative position $\xi_a$ is assigned to the Bézier control point $a$ . Straight paths are described from $\mathbf{0}$ to $\xi_a$ , and $\times$ is the midpoint . . . . .	63
4.2	Straight tube in the target ( <i>left</i> ) and ZS ( <i>right</i> ) states. The dashed lines denote the arterial-wall midsurface in each state . . . . .	65
4.3	Quadratic B-spline meshes with 4, 8, 16, 32, 64, and 128 elements. The <i>red</i> circles are the control points and the <i>gray</i> part is the actual tube . . . . .	66
4.4	Cubic B-spline meshes with 4, 8, 16, 32, 64, and 128 elements. The <i>red</i> circles are the control points and the <i>gray</i> part is the actual tube . . . . .	67
4.5	Representation of the radius of curvature within an element with quadratic ( <i>left</i> ) and cubic ( <i>right</i> ) B-splines. The curves are for the six meshes, $\xi$ is the circumferential parametric coordinate, and $\bar{\rho}$ is the average radius . . . . .	68
4.6	1/4 arcs of circles. Quadratic ( <i>left</i> ) and cubic ( <i>right</i> ) B-spline representations. Circles are control points, red solid lines are physical arcs . . . . .	68
4.7	Standard deviation of $\rho/\bar{\rho}$ as a function of the arc angle $\Delta\theta$ represented by a B-spline element, where $\bar{\rho}$ is the average radius . . . . .	69



4.8	Curvature matching in the ZSS. Quadratic basis functions with 8 elements. The B-spline mesh in the target state ( <i>top left</i> ) is converted to Bézier representation ( <i>top right</i> ). From that, for the specified $\phi$ and for a given value of $\alpha$ , element configurations are built with the objective of having constant radius of curvature in the ZSS ( <i>bottom right</i> ). Then that is converted back to B-spline representation ( <i>bottom left</i> ) . . . . .	70
4.9	Curvature matching in the ZSS. Cubic basis functions with 8 elements. The B-spline mesh in the target state ( <i>top left</i> ) is converted to Bézier representation ( <i>top right</i> ). From that, for the specified $\phi$ and for a given value of $\alpha$ , element configurations are built with the objective of having constant radius of curvature in the ZSS ( <i>bottom right</i> ). Then that is converted back to B-spline representation ( <i>bottom left</i> ) . . . . .	71
4.10	Curvature matching in the ZSS. Standard deviation of $\rho_0/\bar{\rho}_0$ as a function of the arc angle $\Delta\theta$ represented by a Bézier element, where $\bar{\rho}_0$ is the average radius . . . . .	72
4.11	Average curvature in the deformed state as a function of $\alpha$ for the six meshes with quadratic B-splines, where $\bar{\kappa}$ is the curvature in the target state . . . . .	73
4.12	Average curvature in the deformed state as a function of $\alpha$ for the six meshes with cubic B-splines, where $\bar{\kappa}$ is the curvature in the target state . . . . .	74
4.13	For all the meshes, $\alpha$ value that matches the target curvature . . . . .	75
4.14	Schematic display of the integration points . . . . .	75
4.15	Radial stretches for the meshes with 8 elements and quadratic ( <i>left</i> ) and cubic ( <i>right</i> ) B-splines . . . . .	76
4.16	Circumferential stretches for the meshes with 16 elements and quadratic ( <i>left</i> ) and cubic ( <i>right</i> ) B-splines . . . . .	77
4.17	Relative error in the radial and circumferential stretches at all 8 integration points for the meshes with quadratic ( <i>left</i> ) and cubic ( <i>right</i> ) B-splines. The colors represent different meshes, with the same color convention used in Figure 4.11. The relative error is calculated based on the value obtained from the mesh with 128 elements and cubic B-splines . . . . .	78

4.18	Surface geometry . . . . .	78
4.19	Volume geometry. <i>Red</i> surface indicates the inner surface. The left is inlet, and the right is outlet of blood flow . . . . .	79
4.20	Distribution of the maximum principal curvature . . . . .	79
4.21	Directions of maximum principal curvature . . . . .	80
4.22	Physical and ideal elements. The gray colored shape represents the physical element, and the lines and points represent the corresponding ideal Bézier control element. Target state ( <i>left</i> ) and ZSS ( <i>right</i> ) . . . . .	80
4.23	Control mesh in the target state, with the blue lines representing the mesh we use, which is based on the control-point spacing we chose in the radial direction, and with the black lines representing equal spacing of control points in the radial direction . . . . .	80
4.24	Element representation of $(\mathbf{X}_0^e)^0$ . . . . .	81
4.25	Maximum principal stretch from $(\mathbf{X}_0^e)^0$ and $\mathbf{X}_{\text{REF}}$ The whole domain ( <i>left</i> ) and the clipped view ( <i>right</i> ) . . . . .	81
4.26	Minimum principal stretch from $(\mathbf{X}_0^e)^0$ and $\mathbf{X}_{\text{REF}}$ The whole domain ( <i>left</i> ) and the clipped view ( <i>right</i> ) . . . . .	81
4.27	Radial stretch from $(\mathbf{X}_0^e)^0$ and $\mathbf{X}_{\text{REF}}$ The whole domain ( <i>left</i> ) and the clipped view ( <i>right</i> ) . . . . .	82
4.28	Elements of $(\mathbf{X}_0^e)^0$ ( <i>left</i> ) and $\mathbf{y}^0$ ( <i>right</i> ) . . . . .	82
4.29	Elements of $(\mathbf{X}_0^e)^1$ ( <i>left</i> ) and $\mathbf{y}^1$ ( <i>right</i> ) . . . . .	83
4.30	Elements of $(\mathbf{X}_0^e)^2$ ( <i>left</i> ) and $\mathbf{y}^2$ ( <i>right</i> ) . . . . .	83
4.31	Elements of $(\mathbf{X}_0^e)^{300}$ ( <i>left</i> ) and $\mathbf{y}^{300}$ ( <i>right</i> ) . . . . .	84
4.32	Elements of $(\mathbf{X}_0^e)^{1000}$ ( <i>left</i> ) and $\mathbf{y}^{1000}$ ( <i>right</i> ) . . . . .	84
4.33	Maximum of $\ \mathbf{y}^i\ $ as a function of $i$ (EBZSS iteration counter) . . . . .	85
4.34	Maximum principal stretch from converged $\mathbf{X}_0^e$ and $\mathbf{X}_{\text{REF}}$ . The whole domain ( <i>left</i> ) and the clipped view ( <i>right</i> ) . . . . .	85
4.35	Minimum principal stretch from converged $\mathbf{X}_0^e$ and $\mathbf{X}_{\text{REF}}$ . The whole domain ( <i>left</i> ) and the clipped view ( <i>right</i> ) . . . . .	85
4.36	Radial stretch stretch from converged $\mathbf{X}_0^e$ and $\mathbf{X}_{\text{REF}}$ . The whole domain ( <i>left</i> ) and the clipped view ( <i>right</i> ) . . . . .	86

5.1	Y-shaped tube. Target state. The end diameters are 20, 14 and 10 mm . . .	102
5.2	Y-shaped tube. Mesh made of cubic and quartic T-splines. <i>Red</i> circles represent the control points. The parts with the quartic T-splines, obtained by order elevation, are around the two extraordinary points, each connected to six edges . . . . .	103
5.3	Y-shaped tube. Wall thickness distribution . . . . .	104
5.4	Y-shaped tube. The IPBZSS initial guess, shown using the EBZSS representation . . . . .	104
5.5	Y-shaped tube. An element in the target state ( <i>left</i> ) and the corresponding IPBZSS initial guess, shown using the EBZSS representation ( <i>right</i> ) . . .	105
5.6	Y-shaped tube. Colored by $\ y\ $ computed from the converged IPBZSS . . .	105
5.7	Y-shaped tube. The maximum principal stretch, from the IPBZSS initial guess ( <i>top</i> ) and from the converged IPBZSS ( <i>bottom</i> ). Whole elements ( <i>left</i> ) and the clipped view ( <i>right</i> ) . . . . .	106
5.8	Y-shaped tube. The minimum principal stretch, from the IPBZSS initial guess ( <i>top</i> ) and from the converged IPBZSS ( <i>bottom</i> ). Whole elements ( <i>left</i> ) and the clipped view ( <i>right</i> ) . . . . .	107
5.9	Y-shaped tube. The converged IPBZSS element corresponding to the element in Figure 5.5, shown using the EBZSS representation . . . . .	107
5.10	Y-shaped tube. Colored by $\ y\ $ computed after converting the converged IPBZSS to EBZSS . . . . .	108
5.11	Y-shaped tube. The maximum principal stretch, obtained after converting the converged IPBZSS to EBZSS. Whole geometry ( <i>left</i> ) and clipped view ( <i>right</i> ) . . . . .	108
5.12	Patient-specific aorta geometry. Target state, extracted from medical images ( <i>left</i> ). The inlet diameter is about 25 mm. Mesh made of cubic and quartic T-splines ( <i>right</i> ). <i>Red</i> circles represent the control points. The parts with the quartic T-splines, obtained by order elevation [98], are around the eight extraordinary points . . . . .	109
5.13	Patient-specific aorta geometry. Wall thickness distribution . . . . .	110

5.14	Patient-specific aorta geometry. The IPBZSS initial guess, shown using the EBZSS representation . . . . .	111
5.15	Patient-specific aorta geometry. Colored by $\ \mathbf{y}\ $ computed from the converged IPBZSS . . . . .	112
5.16	Patient-specific aorta geometry. The maximum principal stretch, from the IPBZSS initial guess ( <i>top</i> ) and from the converged IPBZSS ( <i>bottom</i> ) Whole elements ( <i>left</i> ) and the clipped view ( <i>right</i> ) . . . . .	114
5.17	Patient-specific aorta geometry. The minimum principal stretch, from the IPBZSS initial guess ( <i>top</i> ) and from the converged IPBZSS ( <i>bottom</i> ) Whole elements ( <i>left</i> ) and the clipped view ( <i>right</i> ) . . . . .	115
5.18	Patient-specific aorta geometry. Colored by $\ \mathbf{y}\ $ computed after converting the converged IPBZSS to EBZSS . . . . .	116
5.19	Patient-specific aorta geometry. The maximum principal stretch, obtained after converting the converged IPBZSS to EBZSS. Whole geometry ( <i>left</i> ) and clipped view ( <i>right</i> ) . . . . .	117
6.1	The coordinate system with the normal based on the closest point . . . . .	121
6.2	The coordinate system with the normal based on the two axis of the natural coordinates, $\mathbf{g}_1$ and $\mathbf{g}_2$ . . . . .	122
6.3	Opening angle $\phi_1$ over the space formed by $\hat{\mathbf{k}}_1 h_{th}$ and $\hat{\mathbf{k}}_2 h_{th}$ . . . . .	133
6.4	Straight tube. The mesh has $\mathbf{g}_3$ in $\mathbf{n}$ direction . . . . .	134
6.5	Straight tube. The mesh has $\mathbf{g}_3$ skew to $\mathbf{n}$ direction . . . . .	134
6.6	Straight tube. Maximum principal stretch for the mesh in Figure 6.4. From the ZSS initial guess ( <i>left</i> ) and the converged ZSS ( <i>right</i> ) . . . . .	135
6.7	Straight tube. Minimum principal stretch for the mesh in Figure 6.4. From the ZSS initial guess ( <i>left</i> ) and the converged ZSS ( <i>right</i> ) . . . . .	135
6.8	Straight tube. Maximum principal stretch for the mesh in Figure 6.5. From the ZSS initial guess ( <i>left</i> ) and the converged ZSS ( <i>right</i> ) . . . . .	136
6.9	Straight tube. Minimum principal stretch for the mesh in Figure 6.5. From the ZSS initial guess ( <i>left</i> ) and the converged ZSS ( <i>right</i> ) . . . . .	136
6.10	Y-shaped tube. $\hat{\mathbf{k}}_1 h_{th}$ ( <i>left</i> ) and $\hat{\mathbf{k}}_2 h_{th}$ ( <i>right</i> ) . . . . .	137

6.11	Y-shaped tube. Inner-surface mesh made of cubic and quartic T-splines. <i>Red</i> circles represent the control points. The parts with the quartic T-splines, obtained by order elevation [98], are around the two extraordinary points, each connected to six edges . . . . .	137
6.12	Y-shaped tube. The IPBZSS, shown using the EBZSS representation. From the ZSS initial guess ( <i>top</i> ) and the converged ZSS ( <i>bottom</i> ) . . . . .	138
6.13	Y-shaped tube. Maximum principal stretch. From the ZSS initial guess ( <i>top</i> ) and the converged ZSS ( <i>bottom</i> ) . . . . .	139
6.14	Y-shaped tube. Minimum principal stretch. From the ZSS initial guess ( <i>top</i> ) and the converged ZSS ( <i>bottom</i> ) . . . . .	140
6.15	Y-shaped tube. Stretch in $\hat{\mathbf{n}}$ direction. From the ZSS initial guess ( <i>top</i> ) and the converged ZSS ( <i>bottom</i> ) . . . . .	141
6.16	Patient-specific aorta. $\hat{\kappa}_1$ ( $\text{mm}^{-1}$ ) ( <i>left</i> ) and $\hat{\kappa}_2$ ( $\text{mm}^{-1}$ ) ( <i>right</i> ). The maximum and minimum values are $1.822 \text{ mm}^{-1}$ and $-0.2810 \text{ mm}^{-1}$ with $\hat{\kappa}_1$ ( $\text{mm}^{-1}$ ), and the maximum and minimum values are $0.1973 \text{ mm}^{-1}$ and $-1.543 \text{ mm}^{-1}$ with $\hat{\kappa}_2$ ( $\text{mm}^{-1}$ ) . . . . .	142
6.17	Patient-specific aorta. Inner-surface mesh ( <i>left</i> ) and Volume mesh ( <i>right</i> ), made of cubic and quartic T-splines. <i>Red</i> circles represent the control points. The parts with the quartic T-splines, obtained by order elevation [98], are around the two extraordinary points, each connected to six edges . . . . .	143
6.18	Patient-specific aorta. $h_{\text{th}}$ (mm) . . . . .	144
6.19	Patient-specific aorta. The IPBZSS, shown using the EBZSS representation. From the ZSS initial guess ( <i>top</i> ) and the converged ZSS ( <i>bottom</i> ) . . . . .	146
6.20	Patient-specific aorta. Maximum principal stretch. From the ZSS initial guess ( <i>top</i> ) and the converged ZSS ( <i>bottom</i> ) . . . . .	147
6.21	Patient-specific aorta. Minimum principal stretch. From the ZSS initial guess ( <i>top</i> ) and the converged ZSS ( <i>bottom</i> ) . . . . .	148
6.22	Patient-specific aorta. Stretch in $\hat{\mathbf{n}}$ direction. From the ZSS initial guess ( <i>top</i> ) and the converged ZSS ( <i>bottom</i> ) . . . . .	149

6.23	Y-shaped tube. Maximum principal stretch for the mesh in Figure 5.2. From the ZSS initial guess ( <i>top</i> ) and the converged ZSS ( <i>bottom</i> ) . . . . .	150
6.24	Y-shaped tube. Minimum principal stretch for the mesh in Figure 5.2. From the ZSS initial guess ( <i>top</i> ) and the converged ZSS ( <i>bottom</i> ) . . . . .	151
6.25	Patient-specific aorta. Maximum principal stretch for the mesh in Figure 5.12. From the ZSS initial guess ( <i>top</i> ) and the converged ZSS ( <i>bottom</i> ) . . . . .	152
6.26	Patient-specific aorta. Minimum principal stretch for the mesh in Figure 5.12. From the ZSS initial guess ( <i>top</i> ) and the converged ZSS ( <i>bottom</i> ) . . . . .	153
6.27	Y-shaped tube. The $ 1 - (\lambda_1)^0/(\lambda_1)^\infty $ with the method in Chapter 5 ( <i>top</i> ) and this chapter ( <i>bottom</i> ) . . . . .	154
6.28	Y-shaped tube. The $ 1 - (\lambda_2)^0/(\lambda_2)^\infty $ with the method in Chapter 5 ( <i>top</i> ) and this chapter ( <i>bottom</i> ) . . . . .	155
6.29	Patient-specific aorta geometry. The $ 1 - (\lambda_1)^0/(\lambda_1)^\infty $ with the method in Chapter 5 ( <i>top</i> ) and this chapter ( <i>bottom</i> ) . . . . .	156
6.30	Patient-specific aorta geometry. The $ 1 - (\lambda_2)^0/(\lambda_2)^\infty $ with the method in Chapter 5 ( <i>top</i> ) and this chapter ( <i>bottom</i> ) . . . . .	157
6.31	Average $ 1 - (\lambda_1)^0/(\lambda_1)^\infty $ . Y-shaped tube ( <i>red</i> ) and the patient-specific aorta geometry ( <i>blue</i> ) . . . . .	158
6.32	Patient-specific aorta geometry. Gaussian curvature. Positive value regions ( <i>red</i> ) and negative value regions ( <i>blue</i> ) . . . . .	159

## Tables

4.1	Stretch values at the integration points for the mesh with 128 elements and cubic B-splines. The values along the inner and outer lines are identical for the number of digits displayed . . . . .	72
-----	--	----

# Chapter 1

## Introduction

Numerical approaches have recently been developed for revealing onsets, aiding in diagnoses, selecting treatment strategies, and predicting prognosis of arterial diseases. However, there are three challenges with regard to their use in clinical practice. First, given the fact that numerical approaches require some measurable data with regard to the phenomena, patient-specific data are not always accessible. Non-invasive data, such as medical images from imaging modalities like computed tomography (CT) and magnetic resonance imaging (MRI), can only be obtained after a definitive diagnosis has been made. On the other hand, invasive data, such as catheter-related angiographic image, are difficult to obtain because of the inherent risk for patients and insurance coverage issues. In addition, unmeasured data, such as material properties, also exist. In this thesis, the invasive and unmeasured data are referred to “invisible data.” The second challenge is that a modeling method is required for the invisible data. A multiple-unknowns problem has possibly multiple solutions. Giving data other than a target unknown is necessary to prevent that condition, but difficult because of the first challenge. Finally, the last challenge involves the validation-related observation of the modeling method. In particular, a model of unmeasured data can not be validated, therefore, effects of the modeling have to be recognized.

Arterial dynamics, in particular to aortic dynamics, is known as the fluid–structure interaction (FSI) problem, this thesis primarily focuses on the modeling method for invisible data in the structure part of the arterial FSI problem. When the structure dynamics associated with a particular disease is focused on, the shape, material properties, and a zero-stress state (ZSS) or prestress condition of the target artery are required. Patient-



specific arterial shapes can be obtained from medical images, but information on material properties and the ZSS are difficult to obtain. In this thesis, modeling the ZSS is considered rather than the material properties.

In this chapter, aorta information is given as the research focus in Section 1.1. Numerical approaches on the arterial dynamics are introduced in Section 1.2. Previous researches on ZSS are introduced in Section 1.3. The objective of this thesis is set on the basis of the existing challenges in previous researches in Section 1.4. Finally, the thesis overview is shown in Section 1.5.

## **1.1 Aorta**

The aorta which is the primary target of this thesis is the largest artery located next to the heart with a diameter of approximately 20–25 mm. The aorta is known as the artery which has an elastic function carrying blood flow to its branches. The aorta mainly consists of four regions: ascending, arch, descending, and abdominal regions. The aorta branches into large vessels toward a subclavian artery, a common carotid artery, and a brachiocephalic artery. Figure 1.1 shows the shape and the location of the aorta. Burton has reported that the aortic wall is approximately 2-mm thick, it is approximately 8–10 % of the aortic diameter [1]. Cardiovascular system, including the aorta, has unique functions compared with other vessels. Generally, the arterial wall is deformed as blood flows through the artery in response to the heart. This mutually dependent relationship is called the FSI problem, then cardiovascular arterial dynamics should be considered as the FSI problem especially.

### **1.1.1 Histology and material characteristics**

In this section, the arterial wall histology is introduced with referring to a previously published article [3]. Human arteries consist of three layers: *intima*, *media*, and *adventitia*. The intima consists of endothelial cells and underlying thin basal lamina. That contains

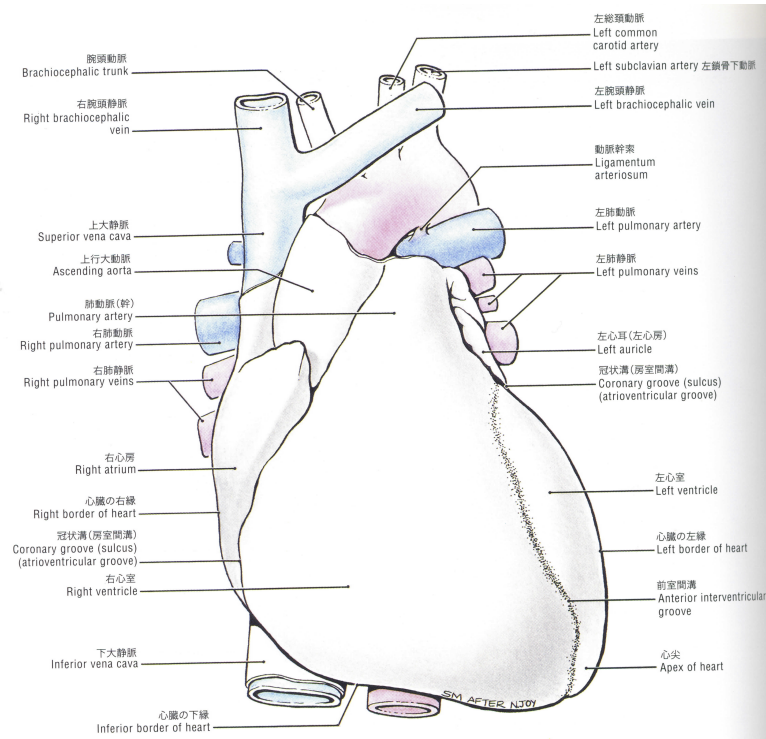


Figure 1.1: Cardiovascular system [2]. The red colored region is the aorta

a subendothelial layer of connective tissues and smooth muscle cells which is oriented axially. The media consists of smooth muscle cells which contain a tissue of elastin and collagen. Smooth muscle is oriented circumferentially, and collagen in the adventitia is oriented axially. Therefore, there is a different response in and out of the plane of the sheet, and it indicates the arterial wall is anisotropic material. Holzapfel et al. has reported an example of arterial structures as an anisotropic material and showed the angles of fibers on each layer [4]. It has also been reported that the arterial wall is not materially homogeneous. Layered material computation may result in jumps in stress across the layers [3]. In the case of simplifying quantification, some previous studies assumed that mechanical characteristics are homogeneous on each layer. Figure 1.2 shows the layered arterial wall with components of the layers.

Hoppmann et al. were first to describe the theory of finite elasticity to quantify the aortic mechanical behavior [6]. Given that the response was similar to those of homogeneous tubes which is assumed as isotropic and incompressible materials, they posited that

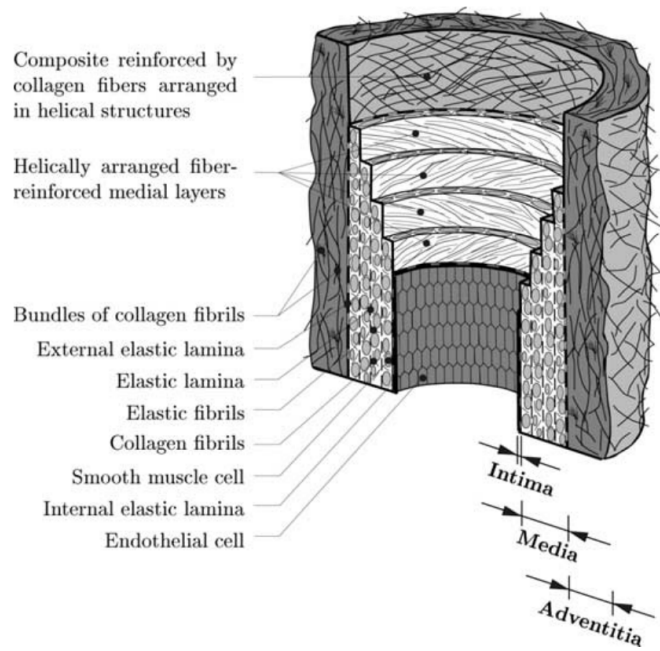


Figure 1.2: Major components of an artery. Three layers in the wall: intima, media, and adventitia [5]

the aortic response could be represented with a strain-energy function, which is referred to as a “hyperelastic material.” The difference between hyperelastic materials and other elastic-plastic material is the existence of energy dissipation [7]. Moreover, hyperelastic materials do not require internal variables for calculation of the energy dissipation. In many years, the aorta had been assumed as an isotropic material [8, 9]. Recently, few anisotropic strain-energy functions have been proposed [5], but still, the isotropic assumption is one of the choices to simplify the aortic response.

### 1.1.2 Residual stress

Arterial shapes obtained from medical images are already loaded by blood pressure and prestressed, which means that the ZSS can not be obtained. The ZSS is useful in different analysis. For instance, in short time-scale problems, using a current (loaded) and reference (unloaded) configurations are sufficient. In contrast, in long time-scale problems such as growth or remodeling, ZSS is needed to be identified.

Fung and Vaishnav et al. reported residual stress and strain in arteries in 1983 [10, 11]. Shortly after, Fung reported that stress-released arterial rings “open up” in response to a radial cut [12]. Figure 1.3 shows the open-up response of the aorta in response to a cut. Note that, the opening angle definition varies in each paper. Humphrey’s two main

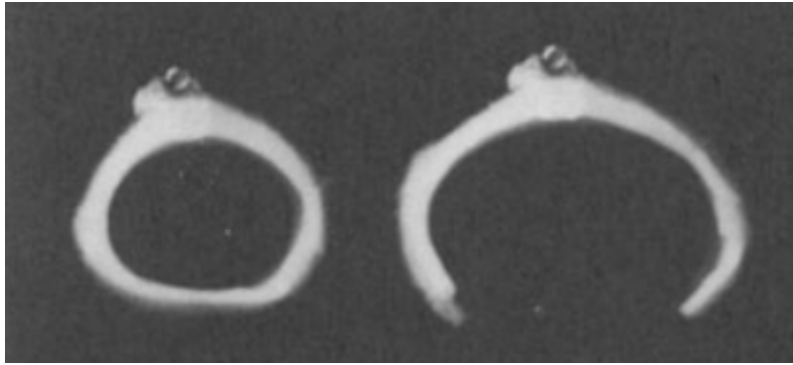


Figure 1.3: The cross-sectional shape of the aorta of a cat [12]. Before (*left*) and after the cut (*right*)

definitions are shown in Figure 4.2. The opening angles  $\phi = 180^\circ$ , and  $\phi' = 2\phi$  indicating that the shape of a cut strip is flat (zero curvature). It should be carefully checked to the definition used in each paper. After the above mentioned publications, many researchers

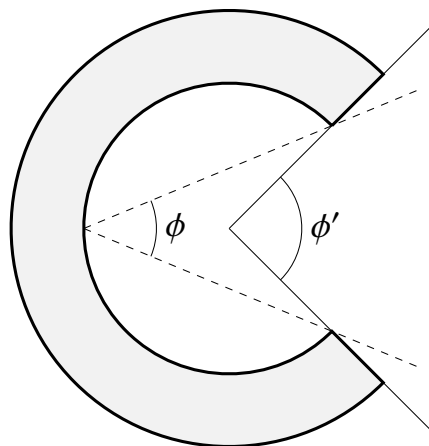


Figure 1.4: Definitions of the opening angles ( $\phi$  and  $\phi'$ ) of arteries with radial cut

have been demonstrated the response by modeling the residual stress and experiments on animals [13, 14, 15, 5, 3]. Holzapfel et al. have investigated the response in the human

aortas of middle-aged individuals ( $48.0 \pm 12.5$  years, mean  $\pm$  SD). They use the definition of  $\phi'$  shown in Figure 4.2, and the average value was approximately  $450^\circ$ . Figure 1.5 shows the result of their experiments. Moreover, Sokolis et al. have demonstrated the

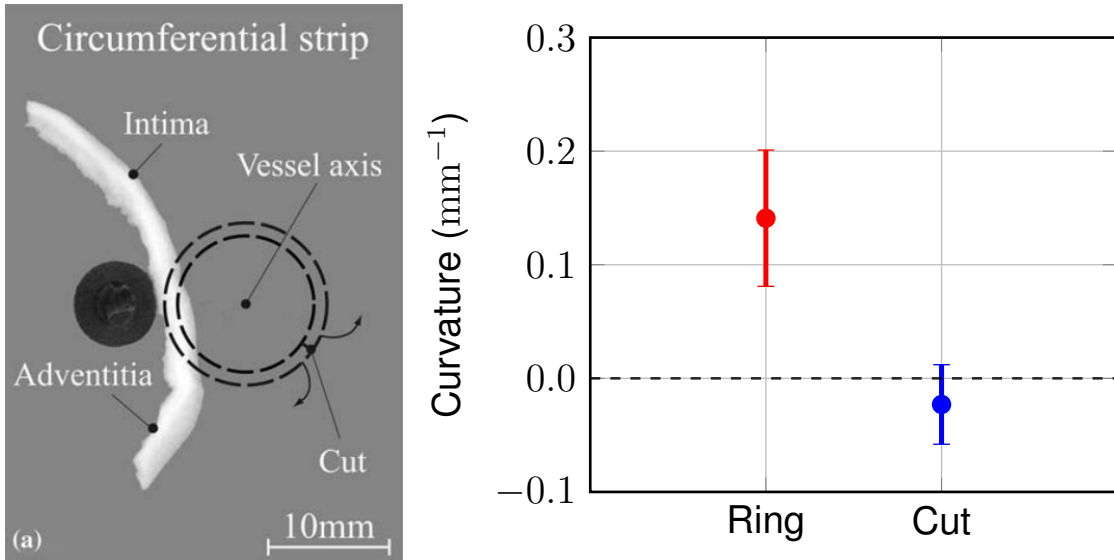


Figure 1.5: Open up response results with human aortas [16]. One cut example (*left*) and summarized curvature changes (*right*)

variations of the opening angles by age and gender [17]. They use the definition of  $\phi$  shown in Figure 4.2, and the values are shown in Figure 1.6. They also show creep of the

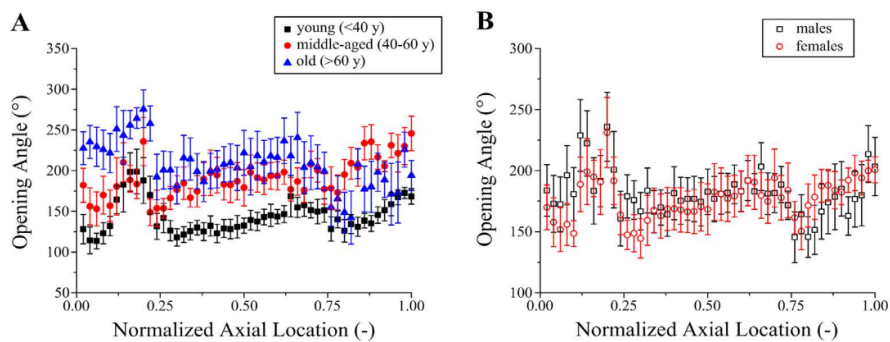


Figure 1.6: Opening angles [17]. Variations in ages (*left*) and gender (*right*). The x-axis indicates the normalized axial location from the ascending part to the end of the descending part

opening angle after a radial cut (see Figure 1.7).

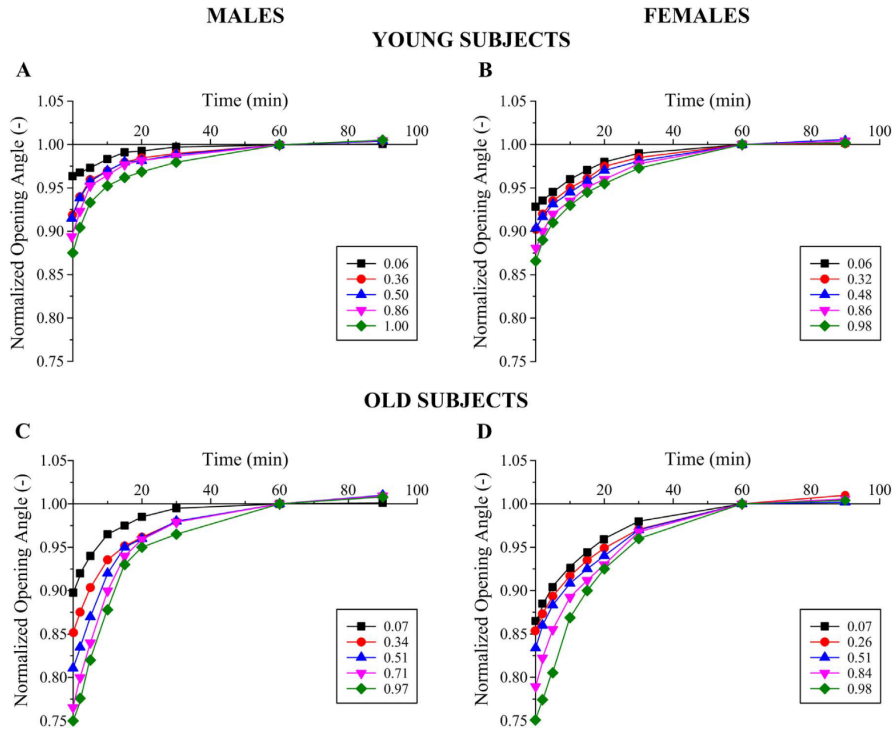


Figure 1.7: Creep of the opening angle [17]. Normalized angles against the values at 60 min in time. Young (*upper*) and old (*bottom*), male (*left*) and female (*right*) subjects. The symbols show the positions in normalized axial locations of the aortic rings

A strong correlation has been reported between the cardiovascular disease and the wall shear stress (WSS) with regard to the blood flow [18, 19, 20, 21, 22, 23]. Either measuring or computing can obtain such values. From these results, the residual stress should be considered also for fluid mechanics computations [24, 25]. They reported that the results of fluid velocity and vorticity are easy to be change by ZSS.

### 1.1.3 Aortic disease

In 2008, there are over 20,000 surgeries for aortic diseases in Japan [26], which is approximately 10 times more compared to that in 1986. The percentage of the number of surgeries for aortic diseases in the cardiovascular surgical area has been increased yearly, representing the seriousness of aortic diseases. Aortic disease is mainly regarded as an aortic aneurysm, and is classified with their shapes into three types according to their

shapes: fusiform-shaped, saccular-shaped, and dissociative aneurysms [27]. The dissociative aneurysms are also called aortic dissection. Figure 1.8 shows the fusiform-shaped and saccular-shaped aneurysms.

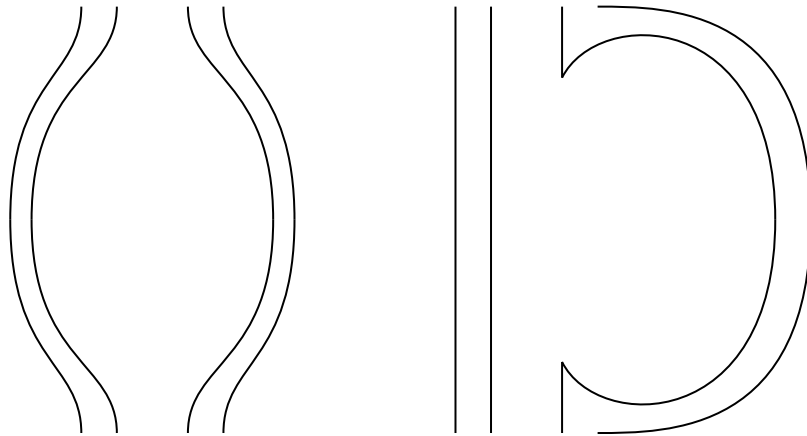


Figure 1.8: Types of aneurysms. Fusiform-shaped (*left*), and saccular-shaped (*right*) aneurysms

Causes of aortic aneurysms are known as atherosclerosis, dissection, inflammation, infection, and external injury. However, although the majority of the patients with aortic aneurysms have the atherosclerotic and dissociative type, the mechanisms of these types of aneurysm remain unknown. Current studies have described that high blood pressure, genetics, or mechanical responses may be related to the causes.

The size of aortic aneurysms are determined initially in the treatment of such conditions, according to the guideline of cardiovascular surgery [28]. Given that image processing capture the shape of the vessels and organs, it is the main diagnostic approach for such diseases. The imaging modalities include X-ray, CT, ultrasound scan, angiography, and MRI. Herein, CT and MRI are discussed, especially.

A contrast agent makes the vessels visible in CT images, which is commonly called CT angiography (CTA). It allows the determination of the size of the aortic aneurysms and the presence of artery calcification, dissection, and thrombi on the wall [2]. In addition, the multidetector CT (MDCT) has been developed recently. MDCT allows 3D reconstruc-

tion of the region detected and measures “geometric height” and “effective height” of the aortic valves [2]. Moreover, MDCT 3D reconstruction is useful to obtain a computational domain of arterial fluid dynamics.

MRI can detect a signal of protons moving in water molecules [29] with contrasts in their velocity. Given that blood move in an in-flow direction, MRI scans the regions with blood flows. MRI also allows 3D reconstruction. Figure 1.9 shows examples of medical images of the cardiovascular system, which were obtained through CT and MRI. Figure 1.10 shows the aorta geometry using MDCT 3D reconstruction.

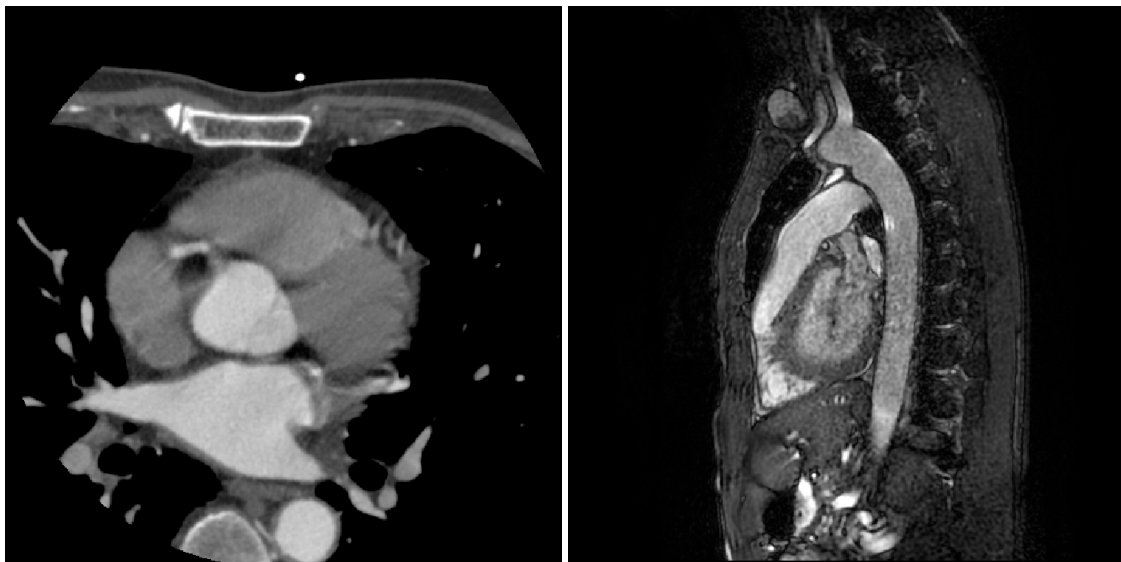


Figure 1.9: Cardiovascular system. Cross-sectional images from CT (*left*) and MRI (*right*)

## 1.2 Numerical approaches in arterial dynamics

As described in Section 1.1, the aorta is in the FSI problem. Computational methods with patient-specific arterial geometries have been introduced [30, 31, 32, 33]. As focusing on the space–time (ST) method, the method has been applied to the cardiovascular fluid mechanics and FSI computations [34, 35, 36, 37, 38, 39, 40, 41, 42, 43, 44, 45, 46, 47, 48, 49, 50, 51, 52, 53, 54, 55]. WSS on the wall and flow field have been computed and



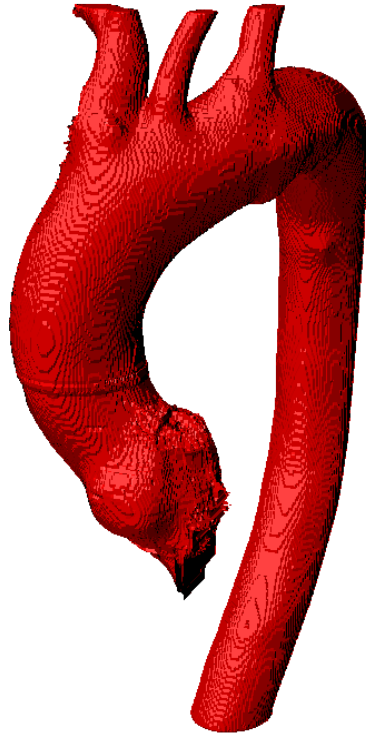


Figure 1.10: Aorta geometry which is constructed by using MDCT 3D reconstruction

observed to reveal the phenomena in arteries, for examples of the arterial computations for the abdominal aorta [56], carotid artery [56], and cerebral aneurysms [57, 58, 59, 60, 61, 62, 63], heart valve flow computation [64, 65, 66, 67, 68, 69], aorta flow analysis [70, 71, 69, 72], and coronary arterial dynamics [73]. These researches have allowed computing arterial dynamics in high accuracy. A challenge particular to patient-specific arterial FSI computations is in the structure part of the FSI computation. That is on how to use the image-based arterial geometry and its residual stress.

### **1.3 Existing research studies on ZSS**

As the earliest part of this chapter, there are required invisible data: material properties and a ZSS. There are two choices to find the invisible data: finding one with given another

data. Finding material properties with a given ZSS assumes that stress conditions are uniform in the surface space, and material properties are varied in the space. On the other hand, finding a ZSS has the opposite assumptions. With considering anatomical histology described in Section 1.1.1, an arterial wall consists of known components such as elastin and collagen cells, then a variation of material properties is in the radial direction because of the components. However, regarding the surface directions (including circumferential and longitudinal directions), material properties might have uniform distribution also because of the layered characteristics. About the ZSS, the distribution is never known in the space. This is the reason why this thesis focuses on the ZSS modeling. Of courses, material properties also have to be considered that should satisfy patient-specific changes, after the ZSS modeling.

Many researchers have proposed methods to estimate the prestress or ZSS. The approaches can be classified into four categories: estimated zero-pressure (EZP) method, modeled-prestress method, modeled-ZSS method, and inverse-design method. After presenting these approaches in the subsequent sections, a current research about ZSS will be also presented.

### **1.3.1 EZP method**

The EZP method for arterial geometries was introduced [74]. It was supposed that the medical-image-based arterial geometries were used as the geometries with zero blood pressure, and the geometries which are acted by time-averaged pressure are required for more realistic results [74, 57]. Therefore, an estimated geometry corresponding to zero blood pressure is estimated with compressing the artery with a given blood pressure beforehand. Particular methods developed with including the newer EZP versions [59, 62, 63, 75, 46]. Figure 1.11 shows the concept image of EZP. However, this approach is as same as the assumption that the opening angle is zero, therefore, the result might be under the unphysical condition.

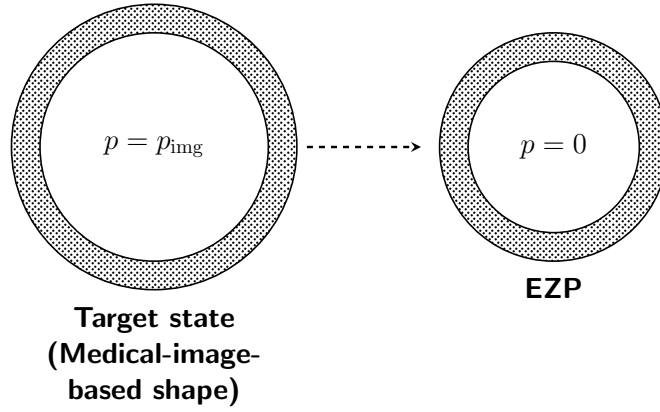


Figure 1.11: Concept image of the EZP method. The parameters  $p$  is the inflation pressure, and  $p_{\text{img}}$  is the inflation blood pressure at the time that the medical-image-based geometry was obtained in a cardiac cycle

### 1.3.2 Modeled-prestress method

A modeled-prestress technique was introduced [42], which was modified [44] and presented also in [75, 46]. The original method assumes that normal stress in the thickness direction must be zero [76]. In a linear strain response case, elastic moduli can be modified with the above-mentioned condition directly. In the method's case, the relationship is nonlinear; thus the authors searched the elastic moduli to satisfy the zero stress condition through the thickness by using Newton iterations. The approach was for shell models, which is refined [44] with defining a prestress tensor in the total Lagrangian formulation:

$$\int_{\Omega_0} \mathbf{w} \cdot \rho_0 \mathbf{a} d\Omega + \int_{\Omega_0} \delta \mathbf{E} : (\mathbf{S} + \mathbf{S}_0) d\Omega - \int_{\Omega_0} \mathbf{w} \cdot \rho_0 \mathbf{f} d\Omega - \int_{(\Gamma_0)_h} \mathbf{w} \cdot \hat{\mathbf{h}} d\Gamma = 0, \quad (1.1)$$

where the symbols and parameters are mentioned in Section 2.5, especially  $\mathbf{S}_0$  in the second term is the prestress tensor. By searching the prestress tensor, the residual strain becomes zero. Therefore, the elastic moduli at all of the regions are assumed as be similar. The assumption may cause difficulties in large deformation problems.

### 1.3.3 Modeled-ZSS method

Holzapfel et al. defined the mathematical model of arterial wall tissue based on the anatomical observation, which is the three-dimensional residual deformation data with human aortas [5, 4, 77]. The model could predict residual stresses in human aortic walls with arbitrary loading conditions. Figure 1.12 shows an example of the modeling method. This approach does not guarantee the deformed shape to be the target shape visualized in

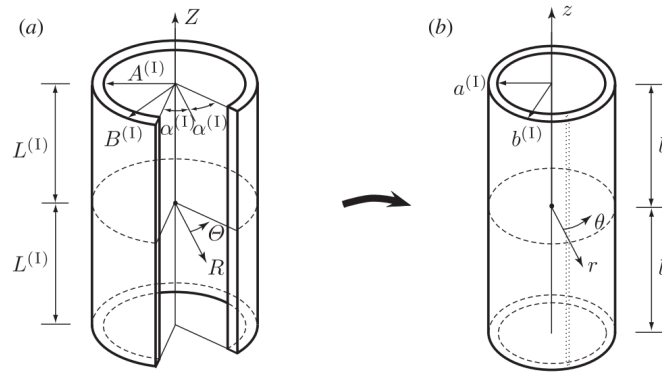


Figure 1.12: ZSS modeling. The method uses cylinder coordinate,  $R(r)$ ,  $\Theta(\theta)$ , and  $Z(z)$ . The parameters  $L$  is the axial length,  $A$  and  $B$  are the inner and outer radius,  $\alpha$  is the opening angle. ZSS (*left*) and unloaded configuration (*right*)

medical images.

### 1.3.4 Inverse-design method

Given that there are two invisible data: material properties, and ZSS, the inverse-design method finds the material properties or the ZSS with matches the deformed shape to the medical-image-based geometry. Regarding the material properties, the method adjusts them around the deformed shape and exclude the average pressure so that the arterial deformation is reasonable at the condition around the average pressure. The approach assumes that the strain around the average pressure is small. Some biomechanical applications have been proposed with this method [78, 79, 80]. However, many researches have used and modified the method for finding the ZSS. In engineering applications, the

method is applied for a turbine blade to obtain the unloaded state [81]. This research assumed the blade is a hyperelastic anisotropic material and is in pressure and centrifugal force conditions. A research finds an undeformed shape when the deformed shape is in minimal-surface condition with inverse analysis [82]. In biomechanics applications, the classical backward incremental method was introduced [83, 84], and an updated version of the method was introduced [85, 86, 87]. The method is adding pressure gradually to obtain a converged unloaded state. This method guarantees the deformed shape to be the target shape. Note that, there are multiple solutions. Regarding creating unloaded shape, this is not a problem especially in form-finding problems [81, 82]. However, given that the biomechanics applications need actual ZSS for their objectives, the multiple solutions cause a problem.

### **1.3.5 Element-based ZSS (EBZSS)**

Our research team has recently introduced a method for estimation of the EBZSS with finite element discretization of the arterial wall [88]. The method combines the concept of the modeled-ZSS (see Section 1.3.3) and the inverse-design (see Section 1.3.4) methods. The method models longitudinal-cut (LC) state based on experimental observation with an opening angle of human aortas, at first. Then, the model is mapped to the geometry extracted from medical images. An iterative method is also introduced that is matching the deformed shape to the medical-image-based geometry. The method is applied to both a single and a three-layered straight tubes. There is an application of a coronary artery [73]. The concept image of EBZSS is shown in Figure 1.13

There are still two difficulties with this method: the complexity of the shape, and the multiple solutions. The method can represent ZSS by each element, but the process requires a group of elements to represent the curvature changing from the reference to the cut shape. It means that it is difficult to obtain a well-converged result with the complexity of the shape such as convex-concave and branched regions. Despite the fact that the

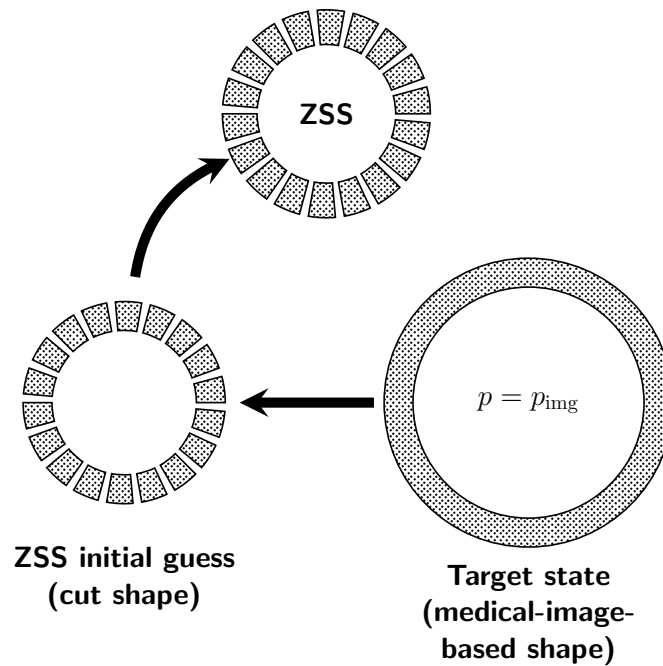


Figure 1.13: Concept image of EBZSS. The bottom process is defining the ZSS initial guess like the modeled-ZSS method. The above process is converging ZSS so that the deformed shape is matched to the target state

EBZSS sets the anatomical ZSS initial guess to address the multiple solution problems in the inverse process, the ZSS is converged at a point that is far from the initial guess, indicating that the converged ZSS is not applied for the anatomical observation of the ZSS, such as the opening angles.

## 1.4 Research objective

The objective of this thesis is to introduce the medical-image-based aorta modeling with ZSS estimation with anatomical observation. For the objective, the following challenges obtained from the existing researches are focused.

**Challenge 1:** Convergence incompleteness according to the geometry complexity

**Challenge 2:** The converged ZSS without anatomical observation

The following three approaches are set for the challenges:

**Approach A:** Apply higher-order shape functions to the EBZSS

**Approach B:** Impose integration-point-based strain

**Approach C:** Design a ZSS initial guess with analytical solutions of the force equilibrium

Approach A, is set for Challenge 1, is an extension of the EBZSS estimation method by using isogeometric discretization (see Chapter 3). Approach B, is also set for Challenge 1, could be a breakthrough that can define the ZSS without its control mesh. This is called integration-point-based ZSS (IPBZSS) estimation. Although T-spline (see Section 3.3) is a useful representation for geometrical complexities, the control mesh structure could be complicated. The control mesh complexity could causes convergence incompleteness on the EBZSS process. Therefore, The IPBZSS could enable adopt T-spline representation to the ZSS modeling. Approach C, is set for Challenge 2, makes the ZSS initial guess similar to the converged ZSS. The analytical solutions of the force equilibrium in the surface normal direction are based on the Kirchhoff–Love shell theory and the plane-stress condition. That enables the converged ZSS is also based on anatomical observation.

## 1.5 Overview

Figure 1.14 shows the overview of this thesis. In Chapter 2, the formulations and boundary conditions for structural mechanics will be presented, which are based on total Lagrangian representation. In Chapter 3, the shape functions for the isogeometric discretization will be presented. By using the formulations and discretization, the extended EBZSS estimation method for Approach 1 will be presented in Chapter 4. In contrast, the IPBZSS estimation method for Approach 2 will be presented in Chapter 5. From the result observation, the ZSS initial guess modeling for Approach 3 will be presented in Chapter 6. Finally, the concluding remarks will be presented in Chapter 7.

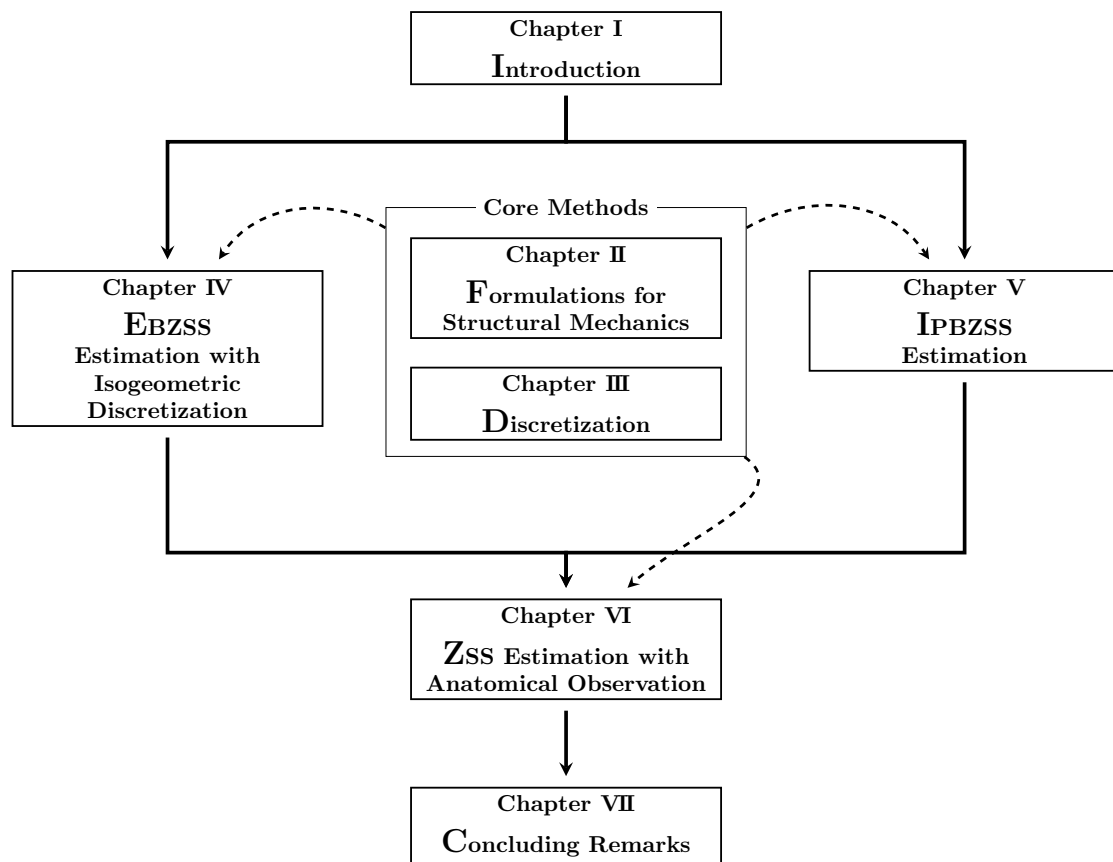


Figure 1.14: Overview



## Chapter 2

### Formulations for Structural Mechanics

In this chapter, the formulations and boundary conditions for structural mechanics, and a constitutive model is presented with referring to [46, 89]. Moreover, the natural coordinate system is also presented. Note that, the inner product is written with the “ $\cdot$ ” symbol, and the tensor product is written without any symbols.

#### 2.1 Kinematics

In this thesis, three domains are defined first. Let  $\Omega_t \subset \mathbb{R}^{n_{sd}}$ ,  $\forall t \in (0, T)$ , and  $\Gamma_t$  represent the structure domain and its boundary in the current configuration, where  $n_{sd}$  is the number of spatial dimensions. Let  $\Omega_0 \subset \mathbb{R}^{n_{sd}}$ , and  $\Gamma_0$  represent the structure domain and its boundary in the ZSS. Let  $\Omega_{REF} \subset \mathbb{R}^{n_{sd}}$ , and  $\Gamma_{REF}$  represent the structure domain and its boundary in the reference configuration. Let  $\mathbf{x}$ ,  $\mathbf{X}_0$ , and  $\mathbf{X}_{REF}$  represent the position of the current, the ZSS, and the reference configuration, respectively. Here,  $\mathbf{y}$  represent the displacement with respect to the reference configuration, and  $\mathbf{y}$  is regarded as the time-varying function with  $\mathbf{X}_{REF}$  and the current position can be set

$$\mathbf{x}(\mathbf{X}_{REF}, t) = \mathbf{X}_{REF} + \mathbf{y}(\mathbf{X}_{REF}, t), \quad (2.1)$$

it means that  $\mathbf{X}_{REF}$  could be mapped in  $\Omega_t$ .

The velocity  $\mathbf{u}$  and the acceleration  $\mathbf{a}$  of the structure are obtained by using the total time derivative of  $\mathbf{y}$ ,

$$\mathbf{u} = \frac{d\mathbf{y}}{dt}, \quad (2.2)$$

and

$$\mathbf{a} = \frac{d^2\mathbf{y}}{dt^2}. \quad (2.3)$$

The deformation gradient tensor  $\mathbf{F}$  is defined as

$$\mathbf{F} \equiv \frac{\partial \mathbf{x}}{\partial \mathbf{X}_0}. \quad (2.4)$$

The right Cauchy–Green deformation tensor  $\mathbf{C}$  is given by

$$\mathbf{C} = \mathbf{F}^T \cdot \mathbf{F}, \quad (2.5)$$

and the Green–Lagrange strain tensor  $\mathbf{E}$  is given by

$$\mathbf{E} = \frac{1}{2}(\mathbf{C} - \mathbf{I}), \quad (2.6)$$

where  $\mathbf{I}$  is a unit tensor. The invariants of  $\mathbf{C}$  are defined as

$$I_1(\mathbf{C}) = \text{tr}\mathbf{C}, \quad (2.7)$$

$$I_2(\mathbf{C}) = \frac{1}{2}((\text{tr}\mathbf{C})^2 - \text{tr}(\mathbf{C}^2)), \quad (2.8)$$

$$I_3(\mathbf{C}) = \det\mathbf{C}. \quad (2.9)$$

In contrast, the left Cauchy–Green deformation tensor  $\mathbf{b}$  is given by

$$\mathbf{b} = \mathbf{F} \cdot \mathbf{F}^T, \quad (2.10)$$

and the Euler–Almansi strain tensor  $\mathbf{e}$  is given by

$$\mathbf{e} = \frac{1}{2}(\mathbf{I} - \mathbf{b}^{-1}). \quad (2.11)$$

The stretch and rotation tensors compose  $\mathbf{F}$  as

$$\mathbf{F} = \mathbf{R} \cdot \mathbf{U} = \mathbf{V} \cdot \mathbf{R}, \quad (2.12)$$

where  $\mathbf{R}$  is the rotation tensor,  $\mathbf{U}$  and  $\mathbf{V}$  are the right and left stretch tensors. This operation is called “polar decomposition.” Then, there are the following relationships:

$$\mathbf{R}^T \cdot \mathbf{R} = \mathbf{I}, \quad (2.13)$$

$$\mathbf{U} = \mathbf{U}^T, \quad (2.14)$$

$$\mathbf{V} = \mathbf{V}^T, \quad (2.15)$$

so that

$$\mathbf{U}^2 = \mathbf{U} \cdot \mathbf{U} = \mathbf{C}, \quad (2.16)$$

$$\mathbf{V}^2 = \mathbf{V} \cdot \mathbf{V} = \mathbf{b}. \quad (2.17)$$

The jacobian  $J$  is defined as

$$J = \det \mathbf{F}. \quad (2.18)$$

## 2.2 Natural coordinate system

In this section, another coordinate system, called “natural coordinate system” is introduced by referring to [89]. It is a powerful way to describe the functions above because the coordinates are along with the curved geometry that is discretized with the isogeomet-

ric method. With the position  $\mathbf{x}$ , the covariant basis vectors are defined as

$$\mathbf{g}_I \equiv \frac{\partial \mathbf{x}}{\partial \xi^I} \quad (2.19)$$

$$= \mathbf{x}_{,I}, \quad (2.20)$$

where  $\xi^I$  is the parametric coordinate, and  $I = 1, \dots, n_{\text{pd}}$ , with  $n_{\text{pd}}$  being the number of parametric dimensions. The components of the metric tensor are defined as

$$g_{IJ} = \mathbf{g}_I \cdot \mathbf{g}_J, \quad (2.21)$$

and these are known as the first fundamental form. Similarly, the contravariant components of the metric tensor can be defined as

$$g^{IJ} = \mathbf{g}^I \cdot \mathbf{g}^J, \quad (2.22)$$

where  $\mathbf{g}^I$  are the contravariant basis vectors, and  $g^{IJ}$  can be obtained with the covariant components:

$$[g^{IJ}] = [g_{IJ}]^{-1}, \quad (2.23)$$

where  $[\bullet]$  indicates the matrix notation of the components. The contravariant basis vectors can be written as

$$\mathbf{g}^I = g^{IJ} \mathbf{g}_J. \quad (2.24)$$

By using similar ways, the vectors and the components are provided in the reference configuration. With the position  $\mathbf{X}_{\text{REF}}$ , the covariant and contravariant basis vectors, and

the components of the metric tensors in the reference configuration are given by

$$(\mathbf{G}_{\text{REF}})_I \equiv \frac{\partial \mathbf{X}_{\text{REF}}}{\partial \xi^I}, \quad (2.25)$$

$$(G_{\text{REF}})_{IJ} = (\mathbf{G}_{\text{REF}})_I \cdot (\mathbf{G}_{\text{REF}})_J, \quad (2.26)$$

$$(G_{\text{REF}})^{IJ} = (\mathbf{G}_{\text{REF}})^I \cdot (\mathbf{G}_{\text{REF}})^J, \quad (2.27)$$

$$[(G_{\text{REF}})^{IJ}] = [(G_{\text{REF}})_{IJ}]^{-1}, \quad (2.28)$$

$$(\mathbf{G}_{\text{REF}})^I = (G_{\text{REF}})^{IJ} (\mathbf{G}_{\text{REF}})_J. \quad (2.29)$$

With the position  $\mathbf{X}_0$  in the ZSS, the covariant and contravariant basis vectors, and the components of the metric tensors in the ZSS are given by

$$\mathbf{G}_I \equiv \frac{\partial \mathbf{X}_0}{\partial \xi^I}, \quad (2.30)$$

$$G_{IJ} = \mathbf{G}_I \cdot \mathbf{G}_J, \quad (2.31)$$

$$G^{IJ} = \mathbf{G}^I \cdot \mathbf{G}^J, \quad (2.32)$$

$$[G^{IJ}] = [G_{IJ}]^{-1}, \quad (2.33)$$

$$\mathbf{G}^I = G^{IJ} \mathbf{G}_J. \quad (2.34)$$

By using the coordinate system, the descriptions in Section 2.1 can be rewritten. Eq. (2.4) is rewritten as

$$\mathbf{F} = \mathbf{g}_I \mathbf{G}^I. \quad (2.35)$$

Moreover, Eq. (2.5) is rewritten with Eq. (2.35) as

$$\mathbf{C} = \mathbf{G}^I \mathbf{g}_I \cdot \mathbf{g}_J \mathbf{G}^J \quad (2.36)$$

$$= g_{IJ} \mathbf{G}^I \mathbf{G}^J \quad (2.37)$$

$$= C_{IJ} \mathbf{G}^I \mathbf{G}^J, \quad (2.38)$$

where  $C_{IJ} = g_{IJ}$ . The contravariant components of  $\mathbf{C}$  are defined from the following relationships:

$$C^{IJ} \mathbf{G}_I \mathbf{G}_J = C_{IJ} \mathbf{G}^I \mathbf{G}^J \quad (2.39)$$

$$= C_{KL} G^{IK} G^{JL} \mathbf{G}_I \mathbf{G}_J, \quad (2.40)$$

then,

$$C^{IJ} = C_{KL} G^{IK} G^{JL} \quad (2.41)$$

$$= g_{KL} G^{IK} G^{JL}. \quad (2.42)$$

With covariant basis vectors,  $\mathbf{C}$  can also be described as

$$\mathbf{C} = g_{KL} G^{IK} G^{JL} \mathbf{G}_I \mathbf{G}_J. \quad (2.43)$$

The inverse of  $\mathbf{C}$  is given by

$$\mathbf{C}^{-1} = \bar{C}^{IJ} \mathbf{G}_I \mathbf{G}_J \quad (2.44)$$

$$= g^{IJ} \mathbf{G}_I \mathbf{G}_J, \quad (2.45)$$

where  $\bar{C}^{IJ}$  is the contravariant components of  $\mathbf{C}^{-1}$ . The definition Eq. (2.45) is from the following relationship:

$$\mathbf{C} \cdot \mathbf{C}^{-1} = g_{IK} g^{LJ} \mathbf{G}^I \mathbf{G}^K \cdot \mathbf{G}_L \mathbf{G}_J \quad (2.46)$$

$$= g_{IK} g^{LJ} \delta_L^K \mathbf{G}^I \mathbf{G}_J \quad (2.47)$$

$$= \delta_L^K (\mathbf{g}_K \cdot \mathbf{g}^L) \mathbf{g}_I \cdot \mathbf{g}^J \mathbf{G}^I \mathbf{G}_J \quad (2.48)$$

$$= \mathbf{g}_I \cdot \mathbf{g}^J \mathbf{G}^I \mathbf{G}_J \quad (2.49)$$

$$= \delta_I^J \mathbf{G}^I \mathbf{G}_J \quad (2.50)$$

$$= \mathbf{I}, \quad (2.51)$$

where the Kronecker delta  $\delta_J^I$  has the useful properties

$$\delta_J^I \mathbf{g}_I = \mathbf{g}_J, \quad (2.52)$$

$$\delta_I^J \mathbf{g}^I = \mathbf{g}^J, \quad (2.53)$$

in which the index  $I$  on  $\mathbf{g}$  is replaced by  $J$ . Eqs. (2.7)–(2.9), are rewritten as

$$I_1(\mathbf{C}) = C_{IJ} G^{IJ} \quad (2.54)$$

$$= g_{IJ} G^{IJ}, \quad (2.55)$$

$$I_2(\mathbf{C}) = \frac{1}{2} \left( (C_{IJ} G^{IJ})^2 - C_{IJ} C^{IJ} \right) \quad (2.56)$$

$$= \frac{1}{2} \left( (g_{IJ} G^{IJ})^2 - g_{IJ} g_{KL} G^{IK} G^{JL} \right), \quad (2.57)$$

$$I_3(\mathbf{C}) = \det[C_{IJ}] \det[G^{IJ}] \quad (2.58)$$

$$= \det[g_{IJ}] \det[G^{IJ}] \quad (2.59)$$

$$= g_o G^o, \quad (2.60)$$

where

$$\text{tr}(\mathbf{C}^2) = \text{tr} \left( C_{IJ} C_{KL} \mathbf{G}^I \mathbf{G}^J \cdot \mathbf{G}^K \mathbf{G}^L \right) \quad (2.61)$$

$$= \text{tr} \left( C_{IJ} C_{KL} G^{JK} \mathbf{G}^I \mathbf{G}^L \right) \quad (2.62)$$

$$= C_{IJ} C_{KL} G^{IL} G^{JK}, \quad (2.63)$$

and determinant values are defined as

$$\det[\bullet_{IJ}] = \bullet_o, \quad (2.64)$$

$$\det[\bullet^{JJ}] = \bullet^o. \quad (2.65)$$

Regarding the stretch by using the given metric tensor  $G_{IJ}$ , the left hand side expression is useful. With the natural coordinates,  $\mathbf{b}$  is rewritten from as

$$\mathbf{b} = \mathbf{g}_I \mathbf{G}^I \cdot \mathbf{G}^J \mathbf{g}_J \quad (2.66)$$

$$= G^{IJ} \mathbf{g}_I \mathbf{g}_J, \quad (2.67)$$

then the inverse of  $\mathbf{b}$  is described as same as Eq. (2.45),

$$\mathbf{b}^{-1} = \bar{b}_{IJ} \mathbf{g}^I \mathbf{g}^J \quad (2.68)$$

$$= G_{IJ} \mathbf{g}^I \mathbf{g}^J. \quad (2.69)$$

### 2.3 Principle of virtual work and variational formulation of structural mechanics

The principle of virtual work is one of the simplest variational principles. The total work  $W$  consists of the internal work  $W_{\text{int}}$  and the external work  $W_{\text{ext}}$ , and then the virtual work is given by

$$\delta W = \delta W_{\text{int}} + \delta W_{\text{ext}} = 0, \quad (2.70)$$

where  $\delta$  denotes their variation with respect to the virtual displacement  $\mathbf{w}$ . The virtual work is defined with the given displacement  $\mathbf{y}$  and taking the directional derivative of  $W$



by

$$\delta W = \left. \frac{d}{d\epsilon} W(\mathbf{y} + \epsilon \mathbf{w}) \right|_{\epsilon=0}. \quad (2.71)$$

The virtual external work  $\delta W_{\text{ext}}$  which includes the inertial and body force, and the surface traction is given by

$$\delta W_{\text{ext}} = \int_{\Omega_t} \mathbf{w} \cdot \rho (\mathbf{f} - \mathbf{a}) d\Omega + \int_{(\Gamma_t)_h} \mathbf{w} \cdot \mathbf{h} d\Gamma, \quad (2.72)$$

where  $\rho$  is the density of the structure in the current configuration,  $\mathbf{f}$  is the body force per unit mass, and  $\mathbf{h}$  is the outer directional traction vector at the boundary  $(\Gamma_t)_h$  of  $\Gamma_t$ . The virtual internal work  $\delta W_{\text{int}}$  is computed as

$$\delta W_{\text{int}} = - \int_{\Omega_0} \delta \mathbf{E} : \mathbf{S} d\Omega, \quad (2.73)$$

where  $\mathbf{S}$  is the second Piola–Kirchhoff stress tensor in the ZSS, and it is work-conjugate to  $\mathbf{E}$ . Put Eqs. (2.72) and (2.73) into Eq. (2.70), and recognize  $\mathbf{w}$  is arbitrary, then the variational formulation of the structural mechanics problem is given by

$$\int_{\Omega_t} \mathbf{w} \cdot \rho \mathbf{a} d\Omega + \int_{\Omega_0} \delta \mathbf{E} : \mathbf{S} d\Omega - \int_{\Omega_t} \mathbf{w} \cdot \rho \mathbf{f} d\Omega - \int_{(\Gamma_t)_h} \mathbf{w} \cdot \mathbf{h} d\Gamma = 0. \quad (2.74)$$

## 2.4 Conservation of mass

The density  $\rho$  in Eq. (2.74) is not known. Firstly, the structural mass  $m$  is defined as

$$m = \int_{\Omega_t} \rho d\Omega. \quad (2.75)$$

The structural mass is assumed that it is conserved at all time, which is written as

$$\frac{dm}{dt} = 0. \quad (2.76)$$

Put Eq. (2.75) into Eq. (2.76), and map into the ZSS,

$$\frac{dm}{dt} = \frac{d}{dt} \int_{\Omega_t} \rho d\Omega \quad (2.77)$$

$$= \int_{\Omega_0} \frac{d(\rho J)}{dt} d\Omega \quad (2.78)$$

$$= 0. \quad (2.79)$$

Because  $\Omega_0$  is arbitrary, the second line of the Eq. (2.78) can be localized to any material point in the structure as

$$\frac{d(\rho J)}{dt} = 0. \quad (2.80)$$

Here, because  $\rho J$  is a function of the material point, it can be written as  $\rho J = \rho J(\mathbf{X})$ . At  $t = 0$  the structure is undeformed, it means  $J = 1$ . By defining  $\rho_0$  is the density in the ZSS, the following point-wise statement of the conservation of mass is obtained:

$$\rho_0 = \rho J. \quad (2.81)$$

## 2.5 Total Lagrangian formulation of structural mechanics

To define the structural mechanics formulation in the ZSS (so-called total Lagrangian formulation [90]), the conversion is started from Eq. (2.74). The inertial and body force

term is converted to the ZSS as

$$\int_{\Omega_t} \mathbf{w} \cdot \rho (\mathbf{a} - \mathbf{f}) d\Omega = \int_{\Omega_0} \mathbf{w} \cdot \rho_0 (\mathbf{a} - \mathbf{f}) d\Omega. \quad (2.82)$$

By combining Eqs. (2.74) and (2.82), the following variational formulation of the structural mechanics problem is obtained:

$$\int_{\Omega_0} \mathbf{w} \cdot \rho_0 \mathbf{a} d\Omega + \int_{\Omega_0} \delta \mathbf{E} : \mathbf{S} d\Omega - \int_{\Omega_0} \mathbf{w} \cdot \rho_0 \mathbf{f} d\Omega - \int_{(\Gamma_0)_h} \mathbf{w} \cdot \hat{\mathbf{h}} d\Gamma = 0, \quad (2.83)$$

where  $\hat{\mathbf{h}}$  is the traction vector acting on  $(\Gamma_0)_h$  of the boundary  $\Gamma_0$  in the ZSS

## 2.6 Element-based total Lagrangian (EBTL) method

The EBTL method is first introduced in [88]. The variational formation given by Eq. (2.74) is converted to obtain the weak form of the structural mechanics equations with the ZSS. By using Eqs. (2.74) and (2.82), the structural mechanics equations based on the total Lagrangian formulation can be written as

$$\int_{\Omega_0} \mathbf{w} \cdot \rho_0 \mathbf{a} d\Omega + \int_{\Omega_0} \delta \mathbf{E} : \mathbf{S} d\Omega - \int_{\Omega_0} \mathbf{w} \cdot \rho_0 \mathbf{f} d\Omega = \int_{(\Gamma_0)_h} \mathbf{w} \cdot \mathbf{h} d\Gamma. \quad (2.84)$$

### 2.6.1 EBZSS

In the EBTL method,  $\Omega_0$  is defined with a set of position  $\mathbf{X}_0^e$  for each element  $e$  [88]. The reference state,  $\mathbf{X}_{\text{REF}}$ , all elements are connected by its mesh lines from nodes, and the displacement  $\mathbf{y}$  is measured on the connected state. For each element,  $\mathbf{F}$  is evaluated as

$$\mathbf{F}^e \equiv \frac{\partial \mathbf{x}}{\partial \mathbf{X}_0^e}, \quad (2.85)$$

$$= \frac{\partial (\mathbf{X}_{\text{REF}} + \mathbf{y})}{\partial \mathbf{X}_0^e}. \quad (2.86)$$

Eq. 2.86 is especially used in the second terms in Eq. (2.84), and the term does not require the orientation. Therefore, the rest of terms is similar to the total Lagrangian formulation which is described in Eq. (2.83).

## 2.7 Boundary conditions

There are two cases of structure mechanics boundary conditions often employed: follower pressure load and elastic-foundation boundary conditions [46]. In this thesis, the follower pressure load boundary condition is described and applied.

This condition is applied to the structural deformation is driven by external pressure loading on  $(\Gamma_t)_h$ . The traction vector  $\mathbf{h}$  is given by

$$\mathbf{h} = -p\mathbf{n}, \quad (2.87)$$

where  $p$  is the magnitude value of the applied pressure, and  $\mathbf{n}$  is the outward normal vector on  $(\Gamma_t)_h$ . Then the surface traction term of Eq. (2.74) can be converted as

$$\int_{(\Gamma_t)_h} \mathbf{w} \cdot \mathbf{h} d\Gamma = - \int_{(\Gamma_t)_h} \mathbf{w} \cdot p\mathbf{n} d\Gamma. \quad (2.88)$$

## 2.8 Strain-energy function

In this thesis, hyperelastic materials are used for arteries. The theory of hyperelasticity assumes the existence of a stored elastic-energy density per unit volume in the ZSS, and a Helmholtz free-energy function  $\varphi$  is described as the strain-energy function. The strain-energy function  $\varphi = \varphi(\mathbf{F})$  is a scalar-valued function of  $\mathbf{F}$ . The function  $\varphi$  is required to be zero where  $\mathbf{F} = \mathbf{I}$ , which is the normalization condition. Since  $\mathbf{C}$  and  $\mathbf{E}$  are given by  $\mathbf{F}$  from Eqs. (2.5) and (2.6),  $\varphi$  can be expressed as a function of  $\mathbf{C}$  and  $\mathbf{E}$ :

$$\varphi = \varphi(\mathbf{C}) = \varphi(\mathbf{E}). \quad (2.89)$$

The second Piola–Kirchhoff stress tensor  $\mathbf{S}$  is defined with  $\varphi$  as

$$\mathbf{S} \equiv \frac{\partial \varphi}{\partial \mathbf{E}}, \quad (2.90)$$

From Eqs. (2.90) and (2.6),

$$\mathbf{S} = 2 \frac{\partial \varphi}{\partial \mathbf{C}}. \quad (2.91)$$

Similarly, the elasticity tensor  $\mathbb{C}$  is defined from Eq. (2.91),

$$\mathbb{C} = 4 \frac{\partial^2 \varphi}{\partial \mathbf{C}^2} \quad (2.92)$$

$$= 2 \frac{\partial \mathbf{S}}{\partial \mathbf{C}}. \quad (2.93)$$

With Eqs. (2.91) and (2.93), the contravariant components of  $\mathbf{S}$ , and the contravariant components of  $\mathbb{C}$  are

$$S^{IJ} = 2 \frac{\partial \varphi}{\partial C_{IJ}}, \quad (2.94)$$

$$\mathbb{C}^{IJKL} = 2 \frac{\partial S^{IJ}}{\partial C_{KL}} \quad (2.95)$$

$$= 4 \frac{\partial^2 \varphi}{\partial C_{IJ} \partial C_{KL}}. \quad (2.96)$$

As showing in Eqs. (2.90) and (2.91),  $\mathbf{S}$  is defined with differentiation with respect to  $\mathbf{E}$  or  $\mathbf{C}$ . Therefore,  $\mathbf{S}$  is also defined as a function of the three invariants of  $\mathbf{C}$  above with the chain rule [89]:

$$\mathbf{S} = 2 \frac{\partial \varphi(\mathbf{C})}{\partial \mathbf{C}} \quad (2.97)$$

$$= 2 \sum_{i=1}^3 \frac{\partial \varphi(I_1, I_2, I_3)}{\partial I_i} \frac{\partial I_i}{\partial \mathbf{C}}, \quad (2.98)$$

where  $\frac{\partial \varphi}{\partial I_i}$  depends on constitutive equations. Given that most of the hyperelastic constitutive equations are written with the invariants of  $\mathbf{C}$ , this description is useful. The partial derivative of the invariants with respect to  $\mathbf{C}$  are written as

$$\frac{\partial I_1}{\partial \mathbf{C}} = \frac{\partial \text{tr} \mathbf{C}}{\partial \mathbf{C}} \quad (2.99)$$

$$= \frac{\partial (\mathbf{I} : \mathbf{C})}{\partial \mathbf{C}} \quad (2.100)$$

$$= \mathbf{I} \quad (2.101)$$

$$= G^{IJ} \mathbf{G}_I \mathbf{G}_J, \quad (2.102)$$

$$\frac{\partial I_2}{\partial \mathbf{C}} = \frac{1}{2} \left( \frac{\partial (\text{tr} \mathbf{C})^2}{\partial \mathbf{C}} - \frac{\partial \text{tr}(\mathbf{C}^2)}{\partial \mathbf{C}} \right) \quad (2.103)$$

$$= I_1 \mathbf{I} - \mathbf{C} \quad (2.104)$$

$$= (I_1 G^{IJ} - C^{IJ}) \mathbf{G}_I \mathbf{G}_J, \quad (2.105)$$

and

$$\frac{\partial I_3}{\partial \mathbf{C}} = \frac{\partial \det \mathbf{C}}{\partial \mathbf{C}} \quad (2.106)$$

$$= I_3 \mathbf{C}^{-1} \quad (2.107)$$

$$= I_3 \bar{C}^{IJ} \mathbf{G}_I \mathbf{G}_J. \quad (2.108)$$

Thus explicit expressions of  $\mathbf{S}$  are obtained from Eq. (2.98):

$$\mathbf{S} = 2 \left( \frac{\partial \varphi}{\partial I_1} \frac{\partial I_1}{\partial \mathbf{C}} + \frac{\partial \varphi}{\partial I_2} \frac{\partial I_2}{\partial \mathbf{C}} + \frac{\partial \varphi}{\partial I_3} \frac{\partial I_3}{\partial \mathbf{C}} \right) \quad (2.109)$$

$$= 2 \left( \left( \frac{\partial \varphi}{\partial I_1} + I_1 \frac{\partial \varphi}{\partial I_2} \right) \mathbf{I} - \frac{\partial \varphi}{\partial I_2} \mathbf{C} + I_3 \frac{\partial \varphi}{\partial I_3} \mathbf{C}^{-1} \right) \quad (2.110)$$

$$= S_1 \mathbf{I} + S_2 \mathbf{C} + S_3 \mathbf{C}^{-1}, \quad (2.111)$$

with the coefficients  $S_1, S_2, S_3$  defined by

$$S_1 = 2 \left( \frac{\partial \varphi}{\partial I_1} + I_1 \frac{\partial \varphi}{\partial I_2} \right), \quad S_2 = -2 \frac{\partial \varphi}{\partial I_2}, \quad S_3 = 2 I_3 \frac{\partial \varphi}{\partial I_3}. \quad (2.112)$$

The coefficients  $S_1, S_2, S_3$  depend on constitutive equations. The contravariant components of  $\mathbf{S}$  are given by

$$S^{IJ} = S_1 G^{IJ} + S_2 C^{IJ} + S_3 \bar{C}^{IJ}. \quad (2.113)$$

From Eq. (2.111),  $\mathbf{C}$  can also be described with the chain rule as same as Eq. (2.98):

$$\mathbf{C} = 2 \sum_{i=1}^3 \frac{\partial \mathbf{S}(S_1, S_2, S_3) \partial I_i}{\partial I_i} \frac{\partial I_i}{\partial \mathbf{C}} \quad (2.114)$$

$$= 2 \left( \left( \sum_{i=1}^3 \frac{\partial S_1 \partial I_i}{\partial I_i \partial \mathbf{C}} \right) \mathbf{I} + S_1 \frac{\partial \mathbf{I}}{\partial \mathbf{C}} + \left( \sum_{i=1}^3 \frac{\partial S_2 \partial I_i}{\partial I_i \partial \mathbf{C}} \right) \mathbf{C} + S_2 \frac{\partial \mathbf{C}}{\partial \mathbf{C}} + \left( \sum_{i=1}^3 \frac{\partial S_3 \partial I_i}{\partial I_i \partial \mathbf{C}} \right) \mathbf{C}^{-1} + S_3 \frac{\partial \mathbf{C}^{-1}}{\partial \mathbf{C}} \right) \quad (2.115)$$

$$= 2 \left( \left( \sum_{i=1}^3 \frac{\partial S_1 \partial I_i}{\partial I_i \partial \mathbf{C}} \right) \mathbf{I} + \left( \sum_{i=1}^3 \frac{\partial S_2 \partial I_i}{\partial I_i \partial \mathbf{C}} \right) \mathbf{C} + S_2 \mathbf{S} + \left( \sum_{i=1}^3 \frac{\partial S_3 \partial I_i}{\partial I_i \partial \mathbf{C}} \right) \mathbf{C}^{-1} - S_3 \mathbf{C}^{-1} \odot \mathbf{C}^{-1} \right). \quad (2.116)$$

where the fourth term of Eq. (2.115),  $\frac{\partial \mathbf{C}}{\partial \mathbf{C}}$  can be obtained with the following relationships:

$$\frac{\partial C_{IJ}}{\partial C_{KL}} = \frac{1}{2}(\delta_{IK}\delta_{JL} + \delta_{IL}\delta_{JK}), \quad (2.117)$$

then

$$\frac{\partial \mathbf{C}}{\partial \mathbf{C}} = \frac{1}{2}(\mathbf{I} + \bar{\mathbf{I}}) \quad (2.118)$$

$$= \mathbf{S}, \quad (2.119)$$

and the sixth term of Eq. (2.115),  $\frac{\partial \mathbf{C}^{-1}}{\partial \mathbf{C}}$  can be obtained with the following relationships:

$$\frac{\partial \bar{C}^{IM}}{\partial C_{KL}} C_{MJ} \bar{C}^{JN} = -\bar{C}^{IM} \frac{\partial C_{MJ}}{\partial C_{KL}} \bar{C}^{JN} \quad (2.120)$$

$$\frac{\partial \bar{C}^{IM}}{\partial C_{KL}} \delta_{MN} = -\frac{1}{2}(\bar{C}^{IM} \delta_{MK} \delta_{JL} \bar{C}^{JN} + \bar{C}^{IM} \delta_{ML} \delta_{JK} \bar{C}^{JN}) \quad (2.121)$$

$$\frac{\partial \bar{C}^{IN}}{\partial C_{KL}} = -\frac{1}{2}(\bar{C}^{IK} \bar{C}^{LN} + \bar{C}^{IL} \bar{C}^{KN}) \quad (2.122)$$

$$\frac{\partial \bar{C}^{IJ}}{\partial C_{KL}} = -\frac{1}{2}(g^{JK} g^{JL} + g^{IL} g^{JK}) \quad (2.123)$$

$$= -g^{IJ} \odot g^{KL}, \quad (2.124)$$

where the symbol  $\odot$  represents the symmetric tensor product. Then, the term can be rewritten as

$$\frac{\partial \mathbf{C}^{-1}}{\partial \mathbf{C}} = -\mathbf{C}^{-1} \odot \mathbf{C}^{-1} \quad (2.125)$$

$$= -\bar{C}^{IJ} \odot \bar{C}^{KL} \mathbf{G}_I \mathbf{G}_J \mathbf{G}_K \mathbf{G}_L \quad (2.126)$$

$$= -g^{IJ} \odot g^{KL} \mathbf{G}_I \mathbf{G}_J \mathbf{G}_K \mathbf{G}_L. \quad (2.127)$$



The summarizing terms of Eq. (2.116) can be described as:

$$\begin{aligned} \left( \sum_{i=1}^3 \frac{\partial S_1 \partial I_i}{\partial I_i \partial \mathbf{C}} \right) \mathbf{I} &= 2 \left( \left( \frac{\partial^2 \varphi}{\partial I_1 \partial I_1} + \frac{\partial \varphi}{\partial I_2} + I_1 \frac{\partial^2 \varphi}{\partial I_1 \partial I_2} \right) \mathbf{I} \mathbf{I} \right. \\ &\quad \left. + \left( \frac{\partial^2 \varphi}{\partial I_1 \partial I_2} + I_1 \frac{\partial^2 \varphi}{\partial I_2 \partial I_2} \right) (I_1 \mathbf{I} - \mathbf{C}) \mathbf{I} + \left( I_3 \frac{\partial^2 \varphi}{\partial I_1 \partial I_3} + I_1 I_3 \frac{\partial^2 \varphi}{\partial I_2 \partial I_3} \right) \mathbf{C}^{-1} \mathbf{I} \right) \end{aligned} \quad (2.128)$$

$$\begin{aligned} &= 2 \left( \left( \frac{\partial^2 \varphi}{\partial I_1 \partial I_1} + \frac{\partial \varphi}{\partial I_2} + 2I_1 \frac{\partial^2 \varphi}{\partial I_1 \partial I_2} + I_1^2 \frac{\partial^2 \varphi}{\partial I_2 \partial I_2} \right) \mathbf{I} \mathbf{I} \right. \\ &\quad \left. - \left( \frac{\partial^2 \varphi}{\partial I_1 \partial I_2} + I_1 \frac{\partial^2 \varphi}{\partial I_2 \partial I_2} \right) \mathbf{C} \mathbf{I} + \left( I_3 \frac{\partial^2 \varphi}{\partial I_1 \partial I_3} + I_1 I_3 \frac{\partial^2 \varphi}{\partial I_2 \partial I_3} \right) \mathbf{C}^{-1} \mathbf{I} \right), \end{aligned} \quad (2.129)$$

$$\left( \sum_{i=1}^8 \frac{\partial S_2 \partial I_i}{\partial I_i \partial \mathbf{C}} \right) \mathbf{C} = 2 \left( -\frac{\partial^2 \varphi}{\partial I_1 \partial I_2} \mathbf{I} \mathbf{C} - \frac{\partial^2 \varphi}{\partial I_2 \partial I_2} (I_1 \mathbf{I} - \mathbf{C}) \mathbf{C} - I_3 \frac{\partial^2 \varphi}{\partial I_2 \partial I_3} \mathbf{C}^{-1} \mathbf{C} \right) \quad (2.130)$$

$$= 2 \left( -\left( \frac{\partial^2 \varphi}{\partial I_1 \partial I_2} + I_1 \frac{\partial^2 \varphi}{\partial I_2 \partial I_2} \right) \mathbf{I} \mathbf{C} + \frac{\partial^2 \varphi}{\partial I_2 \partial I_2} \mathbf{C} \mathbf{C} - I_3 \frac{\partial^2 \varphi}{\partial I_2 \partial I_3} \mathbf{C}^{-1} \mathbf{C} \right), \quad (2.131)$$

and

$$\begin{aligned} \left( \sum_{i=1}^3 \frac{\partial S_3 \partial I_i}{\partial I_i \partial \mathbf{C}} \right) \mathbf{C}^{-1} &= 2 \left( I_3 \frac{\partial^2 \varphi}{\partial I_1 \partial I_3} \mathbf{I} \mathbf{C}^{-1} + I_3 \frac{\partial^2 \varphi}{\partial I_2 \partial I_3} (I_1 \mathbf{I} - \mathbf{C}) \mathbf{C}^{-1} \right. \\ &\quad \left. + \left( I_3 \frac{\partial \varphi}{\partial I_3} + I_3^2 \frac{\partial^2 \varphi}{\partial I_3 \partial I_3} \right) \mathbf{C}^{-1} \mathbf{C}^{-1} \right) \quad (2.132) \\ &= 2 \left( \left( I_3 \frac{\partial^2 \varphi}{\partial I_1 \partial I_3} + I_1 I_3 \frac{\partial^2 \varphi}{\partial I_2 \partial I_3} \right) \mathbf{I} \mathbf{C}^{-1} - I_3 \frac{\partial^2 \varphi}{\partial I_2 \partial I_3} \mathbf{C} \mathbf{C}^{-1} \right) \end{aligned}$$

$$+ \left( I_3 \frac{\partial \varphi}{\partial I_3} + I_3^2 \frac{\partial^2 \varphi}{\partial I_3 \partial I_3} \right) \mathbf{C}^{-1} \mathbf{C}^{-1}. \quad (2.133)$$

Then the explicit expressions of Eq. (2.116) are described as

$$\begin{aligned} \mathbf{C} = & 4 \left( \left( \frac{\partial^2 \varphi}{\partial I_1 \partial I_1} + \frac{\partial \varphi}{\partial I_2} + 2I_1 \frac{\partial^2 \varphi}{\partial I_1 \partial I_2} + I_1^2 \frac{\partial^2 \varphi}{\partial I_2 \partial I_2} \right) \mathbf{I} \mathbf{I} - \left( \frac{\partial^2 \varphi}{\partial I_1 \partial I_2} + I_1 \frac{\partial^2 \varphi}{\partial I_2 \partial I_2} \right) (\mathbf{I} \mathbf{C} + \mathbf{C} \mathbf{I}) \right. \\ & + \left( I_3 \frac{\partial^2 \varphi}{\partial I_1 \partial I_3} + I_1 I_3 \frac{\partial^2 \varphi}{\partial I_2 \partial I_3} \right) (\mathbf{I} \mathbf{C}^{-1} + \mathbf{C}^{-1} \mathbf{I}) + \frac{\partial^2 \varphi}{\partial I_2 \partial I_2} \mathbf{C} \mathbf{C} \\ & - I_3 \frac{\partial^2 \varphi}{\partial I_2 \partial I_3} (\mathbf{C} \mathbf{C}^{-1} + \mathbf{C}^{-1} \mathbf{C}) \\ & \left. + \left( I_3 \frac{\partial \varphi}{\partial I_3} + I_3^2 \frac{\partial^2 \varphi}{\partial I_3 \partial I_3} \right) \mathbf{C}^{-1} \mathbf{C}^{-1} - \frac{\partial \varphi}{\partial I_2} \mathbf{S} - I_3 \frac{\partial \varphi}{\partial I_3} \mathbf{C}^{-1} \odot \mathbf{C}^{-1} \right) \end{aligned} \quad (2.134)$$

$$\begin{aligned} = & \mathbb{C}_1 \mathbf{I} \mathbf{I} + \mathbb{C}_2 (\mathbf{I} \mathbf{C} + \mathbf{C} \mathbf{I}) + \mathbb{C}_3 (\mathbf{I} \mathbf{C}^{-1} + \mathbf{C}^{-1} \mathbf{I}) + \mathbb{C}_4 \mathbf{C} \mathbf{C} \\ & + \mathbb{C}_5 (\mathbf{C} \mathbf{C}^{-1} + \mathbf{C}^{-1} \mathbf{C}) + \mathbb{C}_6 \mathbf{C}^{-1} \mathbf{C}^{-1} + \mathbb{C}_7 \mathbf{C}^{-1} \odot \mathbf{C}^{-1} + \mathbb{C}_8 \mathbf{S}, \end{aligned} \quad (2.135)$$

with the coefficients  $\mathbb{C}_1, \dots, \mathbb{C}_8$  defined by

$$\left. \begin{aligned} \mathbb{C}_1 &= 4 \left( \frac{\partial^2 \varphi}{\partial I_1 \partial I_1} + 2I_1 \frac{\partial^2 \varphi}{\partial I_1 \partial I_2} + \frac{\partial \varphi}{\partial I_2} + I_1^2 \frac{\partial^2 \varphi}{\partial I_2 \partial I_2} \right), \\ \mathbb{C}_2 &= -4 \left( \frac{\partial^2 \varphi}{\partial I_1 \partial I_2} + I_1 \frac{\partial^2 \varphi}{\partial I_2 \partial I_2} \right), \quad \mathbb{C}_3 = 4 \left( I_3 \frac{\partial^2 \varphi}{\partial I_1 \partial I_3} + I_1 I_3 \frac{\partial^2 \varphi}{\partial I_2 \partial I_3} \right), \\ \mathbb{C}_4 &= 4 \frac{\partial^2 \varphi}{\partial I_2 \partial I_2}, \quad \mathbb{C}_5 = -4 I_3 \frac{\partial^2 \varphi}{\partial I_2 \partial I_3}, \\ \mathbb{C}_6 &= 4 \left( I_3 \frac{\partial \varphi}{\partial I_3} + I_3^2 \frac{\partial^2 \varphi}{\partial I_3 \partial I_3} \right), \quad \mathbb{C}_7 = -4 I_3 \frac{\partial \varphi}{\partial I_3}, \quad \mathbb{C}_8 = -4 \frac{\partial \varphi}{\partial I_2}. \end{aligned} \right\} \quad (2.136)$$

The coefficients  $\mathbb{C}_1, \dots, \mathbb{C}_8$  depend on constitutive equations. The contravariant components of  $\mathbb{C}$  are described as:

$$\begin{aligned} \mathbb{C}^{IJKL} = & \mathbb{C}_1 G^{IJ} G^{KL} + \mathbb{C}_2 (G^{IJ} C^{KL} + C^{IJ} G^{KL}) + \mathbb{C}_3 (G^{IJ} g^{KL} + g^{IJ} G^{KL}) + \mathbb{C}_4 C^{IJ} C^{KL} \\ & + \mathbb{C}_5 (C^{IJ} g^{KL} + g^{IJ} C^{KL}) + \mathbb{C}_6 g^{IJ} g^{KL} + \mathbb{C}_7 g^{IJ} \odot g^{KL} + \mathbb{C}_8 G^{IJ} \odot G^{KL}. \end{aligned} \quad (2.137)$$

### 2.8.1 Compressible material

The multiplicative decomposition of  $\mathbf{F}$  into spherical (volume charging) and unimodular (volume serving) parts are considered as

$$\mathbf{F} = (J^{1/3} \mathbf{I}) \cdot \bar{\mathbf{F}}. \quad (2.138)$$

This is originally proposed in [91], and the shape is often used with elastoplasticity referring to [92]. With Eq. (2.138),  $\mathbf{C}$  and  $\mathbf{E}$  are written by

$$\mathbf{C} = J^{2/3} \bar{\mathbf{C}}, \quad (2.139)$$

$$\mathbf{E} = J^{2/3} \bar{\mathbf{E}} + \frac{1}{2} (J^{2/3} - 1) \mathbf{I}, \quad (2.140)$$

then

$$\bar{\mathbf{C}} = \bar{\mathbf{F}}^T \cdot \bar{\mathbf{F}}, \quad (2.141)$$

$$\bar{\mathbf{E}} = \frac{1}{2} (\bar{\mathbf{C}} - \mathbf{I}), \quad (2.142)$$

where the terms  $J^{1/3} \mathbf{I}$  and  $J^{2/3} \mathbf{I}$  take on the volume charging part. On the other hand,  $\bar{\mathbf{F}}$ ,  $\bar{\mathbf{E}}$ , and  $\bar{\mathbf{C}}$  take on on the volume serving part. The invariants of the modified Cauchy–Green

deformation tensor  $\bar{\mathbf{C}}$  are

$$\bar{I}_1(\bar{\mathbf{C}}) = \text{tr}\bar{\mathbf{C}} \quad (2.143)$$

$$= J^{-2/3} I_1, \quad (2.144)$$

$$\bar{I}_2(\bar{\mathbf{C}}) = \frac{1}{2} \left( (\text{tr}\bar{\mathbf{C}})^2 - \text{tr}(\bar{\mathbf{C}}^2) \right) \quad (2.145)$$

$$= J^{-4/3} I_2, \quad (2.146)$$

$$\bar{I}_3(\bar{\mathbf{C}}) = \det\bar{\mathbf{C}} \quad (2.147)$$

$$= 1. \quad (2.148)$$

Here a decoupled representation of  $\varphi$  is defined as

$$\varphi(\mathbf{C}) = \varphi_{\text{iso}}(\bar{\mathbf{C}}) + \varphi_{\text{vol}}(J), \quad (2.149)$$

where  $\varphi_{\text{iso}}(\bar{\mathbf{C}})$  and  $\varphi_{\text{vol}}(J)$  are scalar-valued functions of  $\bar{\mathbf{C}}$  and  $J$ . They indicate the isochoric elastic response and the volumetric elastic response of the material, respectively.

The volumetric part  $\varphi_{\text{vol}}$  is assumed as

$$\varphi_{\text{vol}}(J) = \frac{1}{2\kappa} (\ln J)^2, \quad (2.150)$$

or

$$\varphi_{\text{vol}}(J) = \frac{1}{2\kappa} \left( \frac{1}{2} (J^2 - 1) - \ln J \right), \quad (2.151)$$

where  $\kappa$  is the constant bulk modulus in the ZSS. These two types of the volumetric part are introduced in [89]. Here  $\varphi_{\text{iso}}$  depends on each material form. Similarly,  $\mathbf{S}$  and  $\mathbf{C}$  are

described as below:

$$\mathbf{S} = \mathbf{S}_{\text{iso}} + \mathbf{S}_{\text{vol}}, \quad (2.152)$$

$$\mathbf{C} = \mathbf{C}_{\text{iso}} + \mathbf{C}_{\text{vol}}, \quad (2.153)$$

where  $\mathbf{S}_{\text{iso}}$  and  $\mathbf{S}_{\text{vol}}$  are the isochoric and volumetric parts of  $\mathbf{S}$ , and  $\mathbf{C}_{\text{iso}}$  and  $\mathbf{C}_{\text{vol}}$  are the isochoric and volumetric parts of  $\mathbf{C}$ . In case of Eq. (2.150) with Eq. (2.91),  $\mathbf{S}_{\text{vol}}$  is described as

$$\mathbf{S}_{\text{vol}} = \kappa \frac{\partial \left( (\ln J)^2 \right)}{\partial \mathbf{C}} \quad (2.154)$$

$$= \kappa (2 \ln J) \left( \frac{1}{J} \right) \left( \frac{1}{2} J \mathbf{C}^{-1} \right) \quad (2.155)$$

$$= \kappa \ln J \mathbf{C}^{-1} \quad (2.156)$$

$$= \kappa \ln J \bar{C}^{IJ} \mathbf{G}_I \mathbf{G}_J \quad (2.157)$$

$$= \kappa \ln J g^{IJ} \mathbf{G}_I \mathbf{G}_J, \quad (2.158)$$

and  $\mathbf{C}_{\text{vol}}$  is described as

$$\mathbf{C}_{\text{vol}} = 2\kappa \frac{\partial \left( \ln J \mathbf{C}^{-1} \right)}{\partial \mathbf{C}} \quad (2.159)$$

$$= 2\kappa \left( \frac{\partial (\ln J)}{\partial \mathbf{C}} \mathbf{C}^{-1} + \ln J \frac{\partial (\mathbf{C}^{-1})}{\partial \mathbf{C}} \right) \quad (2.160)$$

$$= 2\kappa \left( \frac{1}{J} \left( \frac{1}{2} J \mathbf{C}^{-1} \right) \mathbf{C}^{-1} - \ln J \mathbf{C}^{-1} \odot \mathbf{C}^{-1} \right) \quad (2.161)$$

$$= \kappa \left( \mathbf{C}^{-1} \mathbf{C}^{-1} - 2 \ln J \mathbf{C}^{-1} \odot \mathbf{C}^{-1} \right) \quad (2.162)$$

$$= \kappa \left( \bar{C}^{IJ} \bar{C}^{KL} - 2 \ln J \bar{C}^{IJ} \odot \bar{C}^{KL} \right) \mathbf{G}_I \mathbf{G}_J \mathbf{G}_K \mathbf{G}_L \quad (2.163)$$

$$= \kappa \left( g^{IJ} g^{KL} - 2 \ln J g^{IJ} \odot g^{KL} \right) \mathbf{G}_I \mathbf{G}_J \mathbf{G}_K \mathbf{G}_L. \quad (2.164)$$

In case of Eq. (2.151) with Eq. (2.91),  $\mathbf{S}_{\text{vol}}$  is described as

$$\mathbf{S}_{\text{vol}} = \kappa \left( \frac{1}{2} \frac{\partial(J^2)}{\partial \mathbf{C}} - \frac{\partial(\ln J)}{\partial \mathbf{C}} \right) \quad (2.165)$$

$$= \kappa \left( \frac{1}{2}(2J) \left( \frac{1}{2} J \mathbf{C}^{-1} \right) - \left( \frac{1}{J} \right) \left( \frac{1}{2} J \mathbf{C}^{-1} \right) \right) \quad (2.166)$$

$$= \frac{\kappa}{2} (J^2 - 1) \mathbf{C}^{-1} \quad (2.167)$$

$$= \frac{1}{2} \kappa (J^2 - 1) \bar{C}^{IJ} \mathbf{G}_I \mathbf{G}_J \quad (2.168)$$

$$= \frac{1}{2} \kappa (J^2 - 1) g^{IJ} \mathbf{G}_I \mathbf{G}_J, \quad (2.169)$$

and  $\mathbf{C}_{\text{vol}}$  is described as

$$\mathbf{C}_{\text{vol}} = \kappa \frac{\partial((J^2 - 1) \mathbf{C}^{-1})}{\partial \mathbf{C}} \quad (2.170)$$

$$= \kappa \left( \frac{\partial(J^2)}{\partial \mathbf{C}} \mathbf{C}^{-1} + (J^2 - 1) \frac{\partial \mathbf{C}^{-1}}{\partial \mathbf{C}} \right) \quad (2.171)$$

$$= \kappa \left( (2J) \left( \frac{1}{2} J \mathbf{C}^{-1} \right) \mathbf{C}^{-1} - (J^2 - 1) \mathbf{C}^{-1} \odot \mathbf{C}^{-1} \right) \quad (2.172)$$

$$= \kappa (J^2 \mathbf{C}^{-1} \mathbf{C}^{-1} - (J^2 - 1) \mathbf{C}^{-1} \odot \mathbf{C}^{-1}) \quad (2.173)$$

$$= \kappa (J^2 \bar{C}^{IJ} \bar{C}^{KL} - (J^2 - 1) \bar{C}^{IJ} \odot \bar{C}^{KL}) \mathbf{G}_I \mathbf{G}_J \mathbf{G}_K \mathbf{G}_L \quad (2.174)$$

$$= \kappa (J^2 g^{IJ} g^{KL} - (J^2 - 1) g^{IJ} \odot g^{KL}) \mathbf{G}_I \mathbf{G}_J \mathbf{G}_K \mathbf{G}_L. \quad (2.175)$$

In contrast,  $\mathbf{S}_{\text{iso}}$  is defined as

$$\mathbf{S}_{\text{iso}} = 2 \frac{\partial \varphi_{\text{iso}}(\bar{I}_1, \bar{I}_2)}{\partial \mathbf{C}} \quad (2.176)$$

$$= 2 \frac{\partial \varphi_{\text{iso}}(\bar{I}_1, \bar{I}_2)}{\partial \bar{\mathbf{C}}} : \frac{\partial \bar{\mathbf{C}}}{\partial \mathbf{C}} \quad (2.177)$$

$$= \bar{\mathbf{S}} : \frac{\partial \bar{\mathbf{C}}}{\partial \mathbf{C}}, \quad (2.178)$$

where the second Piola–Kirchhoff tensor  $\bar{\mathbf{S}}$  with  $\bar{\mathbf{C}}$  is

$$\bar{\mathbf{S}} = 2 \frac{\partial \varphi_{\text{iso}}(\bar{I}_1, \bar{I}_2)}{\partial \bar{\mathbf{C}}} \quad (2.179)$$

$$= \bar{S}_1 \mathbf{I} + \bar{S}_2 \bar{\mathbf{C}} \quad (2.180)$$

$$= \bar{S}_1 \mathbf{I} + J^{-2/3} \bar{S}_2 \mathbf{C} \quad (2.181)$$

$$= (\bar{S}_1 G^{IJ} + J^{-2/3} \bar{S}_2 C^{IJ}) \mathbf{G}_i \mathbf{G}_j, \quad (2.182)$$

with the coefficients  $\bar{S}_1$  and  $\bar{S}_2$  given by

$$\bar{S}_1 = 2 \left( \frac{\partial \varphi_{\text{iso}}(\bar{I}_1, \bar{I}_2)}{\partial \bar{I}_1} + \bar{I}_1 \frac{\partial \varphi_{\text{iso}}(\bar{I}_1, \bar{I}_2)}{\partial \bar{I}_2} \right), \quad \bar{S}_2 = -2 \frac{\partial \varphi_{\text{iso}}(\bar{I}_1, \bar{I}_2)}{\partial \bar{I}_2}, \quad (2.183)$$

and the partial derivative of  $\bar{\mathbf{C}}$  with respect to  $\mathbf{C}$  is as below:

$$\frac{\partial \bar{\mathbf{C}}}{\partial \mathbf{C}} = \frac{\partial J^{-2/3} \mathbf{C}}{\partial \mathbf{C}} \quad (2.184)$$

$$= \mathbf{C} \frac{\partial J^{-2/3}}{\partial \mathbf{C}} + J^{-2/3} \frac{\partial \mathbf{C}}{\partial \mathbf{C}} \quad (2.185)$$

$$= \mathbf{C} \left( -\frac{1}{3} J^{-2/3} \mathbf{C}^{-1} \right) + J^{-2/3} \mathbf{I} \quad (2.186)$$

$$= J^{-2/3} \left( \mathbf{I} - \frac{1}{3} \mathbf{C} \mathbf{C}^{-1} \right) \quad (2.187)$$

$$= J^{-2/3} \mathbf{P}^T, \quad (2.188)$$

where the fourth order tensor  $\mathbf{P}$  is a projection tensor defined as:

$$\mathbf{P} = \mathbf{I} - \frac{1}{3}\mathbf{C}^{-1} \mathbf{C}. \quad (2.189)$$

Here the contravariant components of  $\bar{\mathbf{S}}$  are

$$\bar{S}^{IJ} = \bar{S}_1 G^{IJ} + J^{-2/3} \bar{S}_2 C^{IJ}. \quad (2.190)$$

With Eqs. (2.181) and (2.188), explicit descriptions of Eq. (2.178) are described as

$$\mathbf{S}_{\text{iso}} = J^{-2/3} \mathbf{P} : \bar{\mathbf{S}} \quad (2.191)$$

$$= J^{-2/3} \left( \bar{\mathbf{S}} - \frac{1}{3} \mathbf{C}^{-1} \mathbf{C} : \bar{\mathbf{S}} \right) \quad (2.192)$$

$$= J^{-2/3} \left( \bar{S}_1 G^{IJ} + J^{-2/3} \bar{S}_2 C^{IJ} - \frac{1}{3} (\bar{S}_1 \mathbf{C} : \mathbf{I} + J^{-2/3} \bar{S}_2 \mathbf{C} : \mathbf{C}) \bar{C}^{IJ} \right) \mathbf{G}_I \mathbf{G}_J \quad (2.193)$$

$$= \left( J^{-2/3} \bar{S}_1 \left( G^{IJ} - \frac{1}{3} I_1 \bar{C}^{IJ} \right) + J^{-4/3} \bar{S}_2 \left( C^{IJ} - \frac{1}{3} II_1 \bar{C}^{IJ} \right) \right) \mathbf{G}_I \mathbf{G}_J. \quad (2.194)$$

with the dot product of  $\mathbf{C}$  and  $\bar{\mathbf{S}}$  is calculated with Eq. (2.181) as

$$\mathbf{C} : \bar{\mathbf{S}} = \bar{S}_1 \mathbf{C} : \mathbf{I} + J^{-2/3} \bar{S}_2 \mathbf{C} : \mathbf{C} \quad (2.195)$$

$$= \bar{S}_1 I_1 + J^{-2/3} \bar{S}_2 II_1, \quad (2.196)$$

with the double dot product of two  $\mathbf{C}$  tensors is defined as:

$$II_1 = \mathbf{C} : \mathbf{C} \quad (2.197)$$

$$= C_{IJ} C^{IJ} \quad (2.198)$$

$$= g_{IJ} g_{KL} G^{IK} G^{JL} \quad (2.199)$$



Then, the contravariant components of  $\mathbf{S}_{\text{iso}}$  are

$$S_{\text{iso}}^{IJ} = J^{-2/3} \bar{S}_1 \left( G^{IJ} - \frac{1}{3} I_1 \bar{C}^{IJ} \right) + J^{-4/3} \bar{S}_2 \left( C^{IJ} - \frac{1}{3} II_1 \bar{C}^{IJ} \right) \quad (2.200)$$

$$= J^{-2/3} \bar{S}_1 \left( G^{IJ} - \frac{1}{3} I_1 g^{IJ} \right) + J^{-4/3} \bar{S}_2 \left( g_{KL} G^{IK} G^{JL} - \frac{1}{3} II_1 g^{IJ} \right) \quad (2.201)$$

$$= \bar{\bar{S}}_1 \left( G^{IJ} - \frac{1}{3} I_1 \bar{C}^{IJ} \right) + \bar{\bar{S}}_2 \left( C^{IJ} - \frac{1}{3} II_1 \bar{C}^{IJ} \right), \quad (2.202)$$

where

$$\bar{\bar{S}}_1 = J^{-2/3} \bar{S}_1, \quad \bar{\bar{S}}_2 = J^{-4/3} \bar{S}_2. \quad (2.203)$$

The elastic moduli are described with the partial derivative of  $\mathbf{S}_{\text{iso}}$  with respect to  $\mathbf{C}$ :

$$\mathbf{C}_{\text{iso}} = 2 \frac{\partial \mathbf{S}_{\text{iso}}}{\partial \mathbf{C}} \quad (2.204)$$

$$= 2 \frac{\partial (J^{-2/3} \mathbf{P} : \bar{\mathbf{S}})}{\partial \mathbf{C}} \quad (2.205)$$

$$= 2 (\mathbf{P} : \bar{\mathbf{S}}) \frac{\partial J^{-2/3}}{\partial \mathbf{C}} + 2 J^{-2/3} \frac{\partial (\mathbf{P} : \bar{\mathbf{S}})}{\partial \mathbf{C}}. \quad (2.206)$$

Here the first term of Eq. (2.206) is described as

$$2 (\mathbf{P} : \bar{\mathbf{S}}) \frac{\partial J^{-2/3}}{\partial \mathbf{C}} = -\frac{2}{3} (J^{-2/3} \mathbf{P} : \bar{\mathbf{S}}) \mathbf{C}^{-1} \quad (2.207)$$

$$= -\frac{2}{3} \mathbf{S}_{\text{iso}} \mathbf{C}^{-1}. \quad (2.208)$$

On the other hand, the second term can be expressed as:

$$2J^{-2/3} \frac{\partial (\mathbf{P} : \bar{\mathbf{S}})}{\partial \mathbf{C}} = 2J^{-2/3} \frac{\partial}{\partial \mathbf{C}} \left( \bar{\mathbf{S}} - \frac{1}{3} \mathbf{C}^{-1} \mathbf{C} : \bar{\mathbf{S}} \right) \quad (2.209)$$

$$= 2J^{-2/3} \left( \frac{\partial \bar{\mathbf{S}}}{\partial \bar{\mathbf{C}}} - \frac{1}{3} \frac{\partial (\mathbf{C}^{-1} \mathbf{C} : \bar{\mathbf{S}})}{\partial \bar{\mathbf{C}}} \right) : \frac{\partial \bar{\mathbf{C}}}{\partial \mathbf{C}} \quad (2.210)$$

$$= J^{-4/3} \left( \bar{\mathbf{C}} - \frac{2}{3} \left( \mathbf{C}^{-1} \frac{\partial (\mathbf{C} : \bar{\mathbf{S}})}{\partial \bar{\mathbf{C}}} + \frac{\partial \mathbf{C}^{-1}}{\partial \bar{\mathbf{C}}} (\mathbf{C} : \bar{\mathbf{S}}) \right) \right) : \mathbf{P}^T \quad (2.211)$$

$$= J^{-4/3} \left( \bar{\mathbf{C}} - \frac{1}{3} (\bar{\mathbf{C}}_1 + \bar{\mathbf{C}}_2) \right) : \mathbf{P}^T, \quad (2.212)$$

where the modified elastic moduli  $\bar{\mathbf{C}}$  is given by

$$\bar{\mathbf{C}} = 2 \frac{\partial \bar{\mathbf{S}}}{\partial \bar{\mathbf{C}}} \quad (2.213)$$

$$= \bar{\mathbf{C}}_1 \mathbf{I} \mathbf{I} + \bar{\mathbf{C}}_2 (\mathbf{I} \mathbf{C} + \mathbf{C} \mathbf{I}) + \bar{\mathbf{C}}_3 \mathbf{C} \mathbf{C} + \bar{\mathbf{C}}_4 \mathbf{S} \quad (2.214)$$

$$= (\bar{\mathbf{C}}_1 G^{IJ} G^{KL} + \bar{\mathbf{C}}_2 (G^{IJ} C^{KL} + C^{IJ} G^{KL}) + \bar{\mathbf{C}}_3 C^{IJ} C^{KL} + \bar{\mathbf{C}}_4 G^{IJ} \odot G^{KL}) \mathbf{G}_I \mathbf{G}_J \mathbf{G}_K \mathbf{G}_L, \quad (2.215)$$

with the coefficients  $\bar{\mathbf{C}}_1, \dots, \bar{\mathbf{C}}_4$  defined by

$$\left. \begin{aligned} \bar{\mathbf{C}}_1 &= 4 \left( \frac{\partial^2 \varphi}{\partial \bar{I}_1 \partial \bar{I}_1} + 2\bar{I}_1 \frac{\partial^2 \varphi}{\partial \bar{I}_1 \partial \bar{I}_2} + \frac{\partial \varphi}{\partial \bar{I}_2} + \bar{I}_1^2 \frac{\partial^2 \varphi}{\partial \bar{I}_2 \partial \bar{I}_2} \right), \\ \bar{\mathbf{C}}_2 &= -4 \left( \frac{\partial^2 \varphi}{\partial \bar{I}_1 \partial \bar{I}_2} + \bar{I}_1 \frac{\partial^2 \varphi}{\partial \bar{I}_2 \partial \bar{I}_2} \right), \quad \bar{\mathbf{C}}_3 = 4 \frac{\partial^2 \varphi}{\partial \bar{I}_2 \partial \bar{I}_2}, \quad \bar{\mathbf{C}}_4 = -4 \frac{\partial \varphi}{\partial \bar{I}_2}. \end{aligned} \right\} \quad (2.216)$$

Moreover, two fourth order tensors,  $\bar{\mathbf{C}}_1$  and  $\bar{\mathbf{C}}_2$  in Eq. (2.212), are defined as follows:

$$\bar{\mathbf{C}}_1 = 2\mathbf{C}^{-1} \frac{\partial(\mathbf{C} : \bar{\mathbf{S}})}{\partial \bar{\mathbf{C}}}, \quad (2.217)$$

$$\bar{\mathbf{C}}_2 = 2 \frac{\partial \mathbf{C}^{-1}}{\partial \bar{\mathbf{C}}} (\mathbf{C} : \bar{\mathbf{S}}). \quad (2.218)$$

These terms can be described more explicitly with the chain rule:

$$\bar{\mathbf{C}}_1 = 2\mathbf{C}^{-1} \left( \mathbf{C} : \frac{\partial \bar{\mathbf{S}}}{\partial \bar{\mathbf{C}}} + \frac{\partial \mathbf{C}}{\partial \bar{\mathbf{C}}} : \bar{\mathbf{S}} \right) \quad (2.219)$$

$$= \mathbf{C}^{-1} (\mathbf{C} : \bar{\mathbf{C}} + 2J^{2/3} \mathbf{I} : \bar{\mathbf{S}}) \quad (2.220)$$

$$= \mathbf{C}^{-1} \mathbf{C} : \bar{\mathbf{C}} + 2J^{2/3} \mathbf{C}^{-1} \bar{\mathbf{S}}, \quad (2.221)$$

$$\bar{\mathbf{C}}_2 = 2 \frac{\partial \mathbf{C}^{-1}}{\partial \mathbf{C}} : \frac{\partial \mathbf{C}}{\partial \bar{\mathbf{C}}} (\mathbf{C} : \bar{\mathbf{S}}) \quad (2.222)$$

$$= -2J^{2/3} (\mathbf{C} : \bar{\mathbf{S}}) \mathbf{C}^{-1} \odot \mathbf{C}^{-1}, \quad (2.223)$$

where the partial derivative of  $\mathbf{C}$  with respect to  $\bar{\mathbf{C}}$  is  $J^{-2/3} \mathbf{I}$ . Set Eqs. (2.221) and (2.223) into Eq. (2.212),

$$\begin{aligned} & 2J^{-2/3} \frac{\partial(\mathbf{P} : \bar{\mathbf{S}})}{\partial \bar{\mathbf{C}}} \\ &= J^{-4/3} \left( \bar{\mathbf{C}} - \frac{1}{3} (\mathbf{C}^{-1} \mathbf{C} : \bar{\mathbf{C}} + 2J^{2/3} \mathbf{C}^{-1} \bar{\mathbf{S}} - 2J^{2/3} (\mathbf{C} : \bar{\mathbf{S}}) \mathbf{C}^{-1} \odot \mathbf{C}^{-1}) \right) : \mathbf{P}^T \quad (2.224) \end{aligned}$$

$$= J^{-2/3} \left( J^{-2/3} \left( \mathbf{I} - \frac{1}{3} \mathbf{C}^{-1} \mathbf{C} \right) : \bar{\mathbf{C}} - \frac{2}{3} \mathbf{C}^{-1} \bar{\mathbf{S}} + \frac{2}{3} (\mathbf{C} : \bar{\mathbf{S}}) \mathbf{C}^{-1} \odot \mathbf{C}^{-1} \right) : \mathbf{P}^T \quad (2.225)$$

$$= J^{-4/3} \mathbf{P} : \bar{\mathbf{C}} : \mathbf{P}^T - \frac{2}{3} \mathbf{C}^{-1} J^{-2/3} \mathbf{P} : \bar{\mathbf{S}} + \frac{2}{3} J^{-2/3} (\mathbf{C} : \bar{\mathbf{S}}) \mathbf{C}^{-1} \odot \mathbf{C}^{-1} : \mathbf{P}^T \quad (2.226)$$

$$= J^{-4/3} \mathbf{P} : \bar{\mathbf{C}} : \mathbf{P}^T - \frac{2}{3} \mathbf{C}^{-1} \mathbf{S}_{\text{iso}} + \frac{2}{3} J^{-2/3} (\mathbf{C} : \bar{\mathbf{S}}) \left( \mathbf{C}^{-1} \odot \mathbf{C}^{-1} - \frac{1}{3} \mathbf{C}^{-1} \mathbf{C}^{-1} \right). \quad (2.227)$$

By using Eqs. (2.227) and (2.208), Eq. (2.206) can be described explicitly as:

$$\begin{aligned} \mathbf{C}_{\text{iso}} = & J^{-4/3} \mathbf{P} : \bar{\mathbf{C}} : \mathbf{P}^T + \frac{2}{3} J^{-2/3} (\mathbf{C} : \bar{\mathbf{S}}) \left( \mathbf{C}^{-1} \odot \mathbf{C}^{-1} - \frac{1}{3} \mathbf{C}^{-1} \mathbf{C}^{-1} \right) \\ & - \frac{2}{3} (\mathbf{C}^{-1} \mathbf{S}_{\text{iso}} + \mathbf{S}_{\text{iso}} \mathbf{C}^{-1}). \end{aligned} \quad (2.228)$$

To express contravariant components of  $\mathbf{C}_{\text{iso}}$ , the first term of Eq. (2.228) with Eqs. (2.189) and (2.215) is

$$\begin{aligned} & J^{-4/3} \mathbf{P} : \bar{\mathbf{C}} : \mathbf{P}^T \\ & = J^{-4/3} \left( \mathbf{I} - \frac{1}{3} \mathbf{C}^{-1} \mathbf{C} \right) : \left( \bar{\mathbf{C}}_1 \mathbf{I} \mathbf{I} + \bar{\mathbf{C}}_2 (\mathbf{I} \mathbf{C} + \mathbf{C} \mathbf{I}) + \bar{\mathbf{C}}_3 \mathbf{C} \mathbf{C} + \bar{\mathbf{C}}_4 \mathbf{S} \right) : \left( \mathbf{I} - \frac{1}{3} \mathbf{C} \mathbf{C}^{-1} \right) \end{aligned} \quad (2.229)$$

$$\begin{aligned} & = J^{-4/3} \left( \bar{\mathbf{C}}_1 \left( \mathbf{I} \mathbf{I} - \frac{1}{3} I_1 \mathbf{C}^{-1} \mathbf{I} \right) + \bar{\mathbf{C}}_2 \left( \mathbf{I} \mathbf{C} - \frac{1}{3} I_1 \mathbf{C}^{-1} \mathbf{C} + \mathbf{C} \mathbf{I} - \frac{1}{3} II_1 \mathbf{C}^{-1} \mathbf{I} \right) \right. \\ & \quad \left. + \bar{\mathbf{C}}_3 \left( \mathbf{C} \mathbf{C} - \frac{1}{3} III_1 \mathbf{C}^{-1} \mathbf{C} \right) + \bar{\mathbf{C}}_4 \left( \mathbf{I} \odot \mathbf{I} - \frac{1}{3} \mathbf{C}^{-1} \mathbf{C} \right) \right) : \left( \mathbf{I} - \frac{1}{3} \mathbf{C} \mathbf{C}^{-1} \right) \end{aligned} \quad (2.230)$$

$$\begin{aligned} & = J^{-4/3} \left( \bar{\mathbf{C}}_1 \left( \mathbf{I} \mathbf{I} - \frac{1}{3} I_1 \mathbf{C}^{-1} \mathbf{I} - \frac{1}{3} I_1 \mathbf{I} \mathbf{C}^{-1} + \frac{1}{9} I_1^2 \mathbf{C}^{-1} \mathbf{C}^{-1} \right) \right. \\ & \quad \left. + \bar{\mathbf{C}}_2 \left( \mathbf{I} \mathbf{C} - \frac{1}{3} I_1 \mathbf{C}^{-1} \mathbf{C} + \mathbf{C} \mathbf{I} - \frac{1}{3} II_1 \mathbf{C}^{-1} \mathbf{I} \right. \right. \\ & \quad \left. \left. - \frac{1}{3} III_1 \mathbf{I} \mathbf{C}^{-1} + \frac{1}{9} I_1 III_1 \mathbf{C}^{-1} \mathbf{C}^{-1} - \frac{1}{3} I_1 \mathbf{C} \mathbf{C}^{-1} + \frac{1}{9} I_1 II_1 \mathbf{C}^{-1} \mathbf{C}^{-1} \right) \right) \end{aligned}$$

$$\begin{aligned}
& + \bar{\mathbb{C}}_3 \left( \mathbf{C}\mathbf{C} - \frac{1}{3}H_1\mathbf{C}^{-1}\mathbf{C} - \frac{1}{3}H_1\mathbf{C}\mathbf{C}^{-1} + \frac{1}{9}H_1^2\mathbf{C}^{-1}\mathbf{C}^{-1} \right) \\
& + \bar{\mathbb{C}}_4 \left( \mathbf{S} - \frac{1}{3}\mathbf{C}^{-1}\mathbf{C} - \frac{1}{3}\mathbf{C}\mathbf{C}^{-1} + \frac{1}{9}H_1\mathbf{C}^{-1}\mathbf{C}^{-1} \right) \Bigg) \tag{2.231}
\end{aligned}$$

$$\begin{aligned}
= & J^{-4/3} \left( \bar{\mathbb{C}}_1 \left( \mathbf{I}\mathbf{I} - \frac{1}{3}I_1(\mathbf{I}\mathbf{C}^{-1} + \mathbf{C}^{-1}\mathbf{I}) + \frac{1}{9}I_1^2\mathbf{C}^{-1}\mathbf{C}^{-1} \right) \right. \\
& + \bar{\mathbb{C}}_2 \left( \mathbf{I}\mathbf{C} + \mathbf{C}\mathbf{I} - \frac{1}{3}H_1(\mathbf{I}\mathbf{C}^{-1} + \mathbf{C}^{-1}\mathbf{I}) \right. \\
& \quad \left. \left. - \frac{1}{3}I_1(\mathbf{C}\mathbf{C}^{-1} + \mathbf{C}^{-1}\mathbf{C}) + \frac{2}{9}I_1H_1\mathbf{C}^{-1}\mathbf{C}^{-1} \right) \right. \\
& + \bar{\mathbb{C}}_3 \left( \mathbf{C}\mathbf{C} - \frac{1}{3}H_1(\mathbf{C}\mathbf{C}^{-1} + \mathbf{C}^{-1}\mathbf{C}) + \frac{1}{9}H_1^2\mathbf{C}^{-1}\mathbf{C}^{-1} \right) \\
& \left. + \bar{\mathbb{C}}_4 \left( \mathbf{S} - \frac{1}{3}(\mathbf{C}\mathbf{C}^{-1} + \mathbf{C}^{-1}\mathbf{C}) + \frac{1}{9}H_1\mathbf{C}^{-1}\mathbf{C}^{-1} \right) \right) \tag{2.232}
\end{aligned}$$

$$\begin{aligned}
= & J^{-4/3}\bar{\mathbb{C}}_1\mathbf{I}\mathbf{I} + J^{-4/3}\bar{\mathbb{C}}_2(\mathbf{I}\mathbf{C} + \mathbf{C}\mathbf{I}) - \frac{J^{-4/3}}{3}(I_1\bar{\mathbb{C}}_1 + H_1\bar{\mathbb{C}}_2)(\mathbf{I}\mathbf{C}^{-1} + \mathbf{C}^{-1}\mathbf{I}) \\
& + J^{-4/3}\bar{\mathbb{C}}_3\mathbf{C}\mathbf{C} - \frac{J^{-4/3}}{3}(I_1\bar{\mathbb{C}}_2 + H_1\bar{\mathbb{C}}_3 + \bar{\mathbb{C}}_4)(\mathbf{C}\mathbf{C}^{-1} + \mathbf{C}^{-1}\mathbf{C}) \\
& + \frac{J^{-4/3}}{9}(I_1^2\bar{\mathbb{C}}_1 + 2I_1H_1\bar{\mathbb{C}}_2 + H_1^2\bar{\mathbb{C}}_3 + H_1\bar{\mathbb{C}}_4)\mathbf{C}^{-1}\mathbf{C}^{-1} + J^{-4/3}\bar{\mathbb{C}}_4\mathbf{I}\odot\mathbf{I}. \tag{2.233}
\end{aligned}$$

The second term of Eq. (2.228) with Eq. (2.196) is

$$\frac{2}{3}J^{-2/3}(\mathbf{C} : \bar{\mathbf{S}}) \left( \mathbf{C}^{-1} \odot \mathbf{C}^{-1} - \frac{1}{3}\mathbf{C}^{-1}\mathbf{C}^{-1} \right)$$

$$= \frac{2}{3} J^{-2/3} (\bar{S}_1 I_1 + J^{-2/3} \bar{S}_2 II_1) \left( \mathbf{C}^{-1} \odot \mathbf{C}^{-1} - \frac{1}{3} \mathbf{C}^{-1} \mathbf{C}^{-1} \right). \quad (2.234)$$

The third term of Eq. (2.228) with Eqs. (2.192), (2.196) and (2.181) is

$$\begin{aligned} & -\frac{2}{3} (\mathbf{C}^{-1} \mathbf{S}_{\text{iso}} + \mathbf{S}_{\text{iso}} \mathbf{C}^{-1}) \\ &= -\frac{2}{3} J^{-2/3} \left( \mathbf{C}^{-1} \bar{\mathbf{S}} - \frac{1}{3} (\mathbf{C} : \bar{\mathbf{S}}) \mathbf{C}^{-1} \mathbf{C}^{-1} + \bar{\mathbf{S}} \mathbf{C}^{-1} - \frac{1}{3} (\mathbf{C} : \bar{\mathbf{S}}) \mathbf{C}^{-1} \mathbf{C}^{-1} \right) \end{aligned} \quad (2.235)$$

$$= -\frac{2}{3} J^{-2/3} (\mathbf{C}^{-1} \bar{\mathbf{S}} + \bar{\mathbf{S}} \mathbf{C}^{-1}) + \frac{4}{9} J^{-2/3} (\bar{S}_1 I_1 + J^{-2/3} \bar{S}_2 II_1) \mathbf{C}^{-1} \mathbf{C}^{-1} \quad (2.236)$$

$$= -\frac{2}{3} J^{-2/3} \bar{S}_1 (\mathbf{I} \mathbf{C}^{-1} + \mathbf{C}^{-1} \mathbf{I}) - \frac{2}{3} J^{-4/3} \bar{S}_2 (\mathbf{C} \mathbf{C}^{-1} + \mathbf{C}^{-1} \mathbf{C})$$

$$+ \frac{4}{9} J^{-2/3} (\bar{S}_1 I_1 + J^{-2/3} \bar{S}_2 II_1) \mathbf{C}^{-1} \mathbf{C}^{-1}. \quad (2.237)$$

Here, Eqs. (2.212) and (2.237) are combined as

$$\frac{2}{3} J^{-2/3} (\mathbf{C} : \bar{\mathbf{S}}) \left( \mathbf{C}^{-1} \odot \mathbf{C}^{-1} - \frac{1}{3} \mathbf{C}^{-1} \mathbf{C}^{-1} \right) - \frac{2}{3} (\mathbf{C}^{-1} \mathbf{S}_{\text{iso}} + \mathbf{S}_{\text{iso}} \mathbf{C}^{-1}) \quad (2.238)$$

$$= \frac{2}{3} J^{-2/3} (\bar{S}_1 I_1 + J^{-2/3} \bar{S}_2 II_1) \left( \mathbf{C}^{-1} \odot \mathbf{C}^{-1} - \frac{1}{3} \mathbf{C}^{-1} \mathbf{C}^{-1} \right)$$

$$- \frac{2}{3} J^{-2/3} \bar{S}_1 (\mathbf{I} \mathbf{C}^{-1} + \mathbf{C}^{-1} \mathbf{I}) - \frac{2}{3} J^{-4/3} \bar{S}_2 (\mathbf{C} \mathbf{C}^{-1} + \mathbf{C}^{-1} \mathbf{C})$$

$$+ \frac{4}{9} J^{-2/3} (\bar{S}_1 I_1 + J^{-2/3} \bar{S}_2 II_1) \mathbf{C}^{-1} \mathbf{C}^{-1} \quad (2.239)$$

$$= \bar{S}_1 \left( \frac{2}{3} J^{-2/3} I_1 \mathbf{C}^{-1} \odot \mathbf{C}^{-1} - \frac{2}{9} J^{-2/3} I_1 \mathbf{C}^{-1} \mathbf{C}^{-1} - \frac{2}{3} J^{-2/3} (\mathbf{I} \mathbf{C}^{-1} + \mathbf{C}^{-1} \mathbf{I}) + \frac{4}{9} J^{-2/3} I_1 \mathbf{C}^{-1} \mathbf{C}^{-1} \right)$$

$$+ \bar{S}_2 \left( \frac{2}{3} J^{-4/3} \mathbb{I}_1 \mathbf{C}^{-1} \odot \mathbf{C}^{-1} - \frac{2}{9} J^{-4/3} \mathbb{I}_1 \mathbf{C}^{-1} \mathbf{C}^{-1} - \frac{2}{3} J^{-4/3} (\mathbf{I} \mathbf{C}^{-1} + \mathbf{C}^{-1} \mathbf{I}) + \frac{4}{9} J^{-4/3} \mathbb{I}_1 \mathbf{C}^{-1} \mathbf{C}^{-1} \right) \quad (2.240)$$

$$= \frac{2}{3} J^{-2/3} \bar{S}_1 \left( \mathbb{I}_1 \mathbf{C}^{-1} \odot \mathbf{C}^{-1} - (\mathbf{I} \mathbf{C}^{-1} + \mathbf{C}^{-1} \mathbf{I}) + \frac{1}{3} \mathbb{I}_1 \mathbf{C}^{-1} \mathbf{C}^{-1} \right) \\ + \frac{2}{3} J^{-4/3} \bar{S}_2 \left( \mathbb{I}_1 \mathbf{C}^{-1} \odot \mathbf{C}^{-1} - (\mathbf{C} \mathbf{C}^{-1} + \mathbf{C}^{-1} \mathbf{C}) + \frac{1}{3} \mathbb{I}_1 \mathbf{C}^{-1} \mathbf{C}^{-1} \right). \quad (2.241)$$

Eqs. (2.233) and (2.241) are put into Eq. (2.228):

$$\mathbf{C}_{\text{iso}} = J^{-4/3} \bar{\mathbf{C}}_1 \mathbf{I} \mathbf{I} + J^{-4/3} \bar{\mathbf{C}}_2 (\mathbf{I} \mathbf{C} + \mathbf{C} \mathbf{I}) - \frac{J^{-4/3}}{3} (\mathbb{I}_1 \bar{\mathbf{C}}_1 + \mathbb{I}_1 \bar{\mathbf{C}}_2) (\mathbf{I} \mathbf{C}^{-1} + \mathbf{C}^{-1} \mathbf{I}) \\ + J^{-4/3} \bar{\mathbf{C}}_3 \mathbf{C} \mathbf{C} - \frac{J^{-4/3}}{3} (\mathbb{I}_1 \bar{\mathbf{C}}_2 + \mathbb{I}_1 \bar{\mathbf{C}}_3 + \bar{\mathbf{C}}_4) (\mathbf{C} \mathbf{C}^{-1} + \mathbf{C}^{-1} \mathbf{C}) \\ + \frac{J^{-4/3}}{9} (\mathbb{I}_1^2 \bar{\mathbf{C}}_1 + 2 \mathbb{I}_1 \mathbb{I}_1 \bar{\mathbf{C}}_2 + \mathbb{I}_1^2 \bar{\mathbf{C}}_3 + \mathbb{I}_1 \bar{\mathbf{C}}_4) \mathbf{C}^{-1} \mathbf{C}^{-1} + J^{-4/3} \bar{\mathbf{C}}_4 \mathbf{I} \odot \mathbf{I} \\ + \frac{2}{3} J^{-2/3} \bar{S}_1 \left( \mathbb{I}_1 \mathbf{C}^{-1} \odot \mathbf{C}^{-1} - (\mathbf{I} \mathbf{C}^{-1} + \mathbf{C}^{-1} \mathbf{I}) + \frac{1}{3} \mathbb{I}_1 \mathbf{C}^{-1} \mathbf{C}^{-1} \right) \\ + \frac{2}{3} J^{-4/3} \bar{S}_2 \left( \mathbb{I}_1 \mathbf{C}^{-1} \odot \mathbf{C}^{-1} - (\mathbf{C} \mathbf{C}^{-1} + \mathbf{C}^{-1} \mathbf{C}) + \frac{1}{3} \mathbb{I}_1 \mathbf{C}^{-1} \mathbf{C}^{-1} \right) \quad (2.242)$$

$$= J^{-4/3} \bar{\mathbf{C}}_1 \mathbf{I} \mathbf{I} + J^{-4/3} \bar{\mathbf{C}}_2 (\mathbf{I} \mathbf{C} + \mathbf{C} \mathbf{I}) + J^{-4/3} \bar{\mathbf{C}}_3 \mathbf{C} \mathbf{C} + J^{-4/3} \bar{\mathbf{C}}_4 \mathbf{I} \odot \mathbf{I} \\ - \frac{J^{-2/3}}{3} (J^{-2/3} (\mathbb{I}_1 \bar{\mathbf{C}}_1 + \mathbb{I}_1 \bar{\mathbf{C}}_2) + 2 \bar{S}_1) (\mathbf{I} \mathbf{C}^{-1} + \mathbf{C}^{-1} \mathbf{I}) \\ - \frac{J^{-4/3}}{3} (\mathbb{I}_1 \bar{\mathbf{C}}_2 + \mathbb{I}_1 \bar{\mathbf{C}}_3 + \bar{\mathbf{C}}_4 + 2 \bar{S}_2) (\mathbf{C} \mathbf{C}^{-1} + \mathbf{C}^{-1} \mathbf{C}) \\ + \frac{J^{-2/3}}{9} (J^{-2/3} (\mathbb{I}_1^2 \bar{\mathbf{C}}_1 + 2 \mathbb{I}_1 \mathbb{I}_1 \bar{\mathbf{C}}_2 + \mathbb{I}_1^2 \bar{\mathbf{C}}_3 + \mathbb{I}_1 \bar{\mathbf{C}}_4) + 2 (\mathbb{I}_1 \bar{S}_1 + J^{-2/3} \mathbb{I}_1 \bar{S}_2)) \mathbf{C}^{-1} \mathbf{C}^{-1} \\ + \frac{2 J^{-2/3}}{3} (\mathbb{I}_1 \bar{S}_1 + J^{-2/3} \mathbb{I}_1 \bar{S}_2) \mathbf{C}^{-1} \odot \mathbf{C}^{-1} \quad (2.243)$$

$$\begin{aligned}
&= \bar{\bar{C}}_1 \mathbf{I} \mathbf{I} + \bar{\bar{C}}_2 (\mathbf{I} \mathbf{C} + \mathbf{C} \mathbf{I}) + \bar{\bar{C}}_3 \mathbf{C} \mathbf{C} + \bar{\bar{C}}_4 \mathbf{I} \odot \mathbf{I} \\
&\quad - \frac{1}{3} (I_1 \bar{\bar{C}}_1 + II_1 \bar{\bar{C}}_2 + 2\bar{\bar{S}}_1) (\mathbf{I} \mathbf{C}^{-1} + \mathbf{C}^{-1} \mathbf{I}) \\
&\quad - \frac{1}{3} (I_1 \bar{\bar{C}}_2 + II_1 \bar{\bar{C}}_3 + \bar{\bar{C}}_4 + 2\bar{\bar{S}}_2) (\mathbf{C} \mathbf{C}^{-1} + \mathbf{C}^{-1} \mathbf{C}) \\
&\quad + \frac{1}{9} (I_1^2 \bar{\bar{C}}_1 + 2I_1 II_1 \bar{\bar{C}}_2 + II_1^2 \bar{\bar{C}}_3 + II_1 \bar{\bar{C}}_4 + 2I_1 \bar{\bar{S}}_1 + 2II_1 \bar{\bar{S}}_2) \mathbf{C}^{-1} \mathbf{C}^{-1} \\
&\quad + \frac{2}{3} (I_1 \bar{\bar{S}}_1 + II_1 \bar{\bar{S}}_2) \mathbf{C}^{-1} \odot \mathbf{C}^{-1} \tag{2.244}
\end{aligned}$$

$$\begin{aligned}
&= \left( \bar{\bar{C}}_1 + \frac{2}{I_1} \bar{\bar{S}}_1 \right) \left( \mathbf{I} - \frac{1}{3} I_1 \mathbf{C}^{-1} \right) \left( \mathbf{I} - \frac{1}{3} I_1 \mathbf{C}^{-1} \right) \\
&\quad + \bar{\bar{C}}_2 \left( \left( \mathbf{I} - \frac{1}{3} I_1 \mathbf{C}^{-1} \right) \left( \mathbf{C} - \frac{1}{3} II_1 \mathbf{C}^{-1} \right) + \left( \mathbf{C} - \frac{1}{3} II_1 \mathbf{C}^{-1} \right) \left( \mathbf{I} - \frac{1}{3} I_1 \mathbf{C}^{-1} \right) \right) \\
&\quad + \left( \bar{\bar{C}}_3 + \frac{1}{II_1} \bar{\bar{C}}_4 + \frac{2}{II_1} \bar{\bar{S}}_2 \right) \left( \mathbf{C} - \frac{1}{3} II_1 \mathbf{C}^{-1} \right) \left( \mathbf{C} - \frac{1}{3} II_1 \mathbf{C}^{-1} \right) \\
&\quad + \bar{\bar{C}}_4 \mathbf{I} \odot \mathbf{I} + \frac{2}{3} (I_1 \bar{\bar{S}}_1 + II_1 \bar{\bar{S}}_2) \mathbf{C}^{-1} \odot \mathbf{C}^{-1} \\
&\quad - \frac{2}{I_1} \bar{\bar{S}}_1 \mathbf{I} \mathbf{I} - \frac{1}{II_1} (\bar{\bar{C}}_4 + 2\bar{\bar{S}}_2) \mathbf{C} \mathbf{C}, \tag{2.245}
\end{aligned}$$

where

$$\left. \begin{aligned}
\bar{\bar{C}}_1 &= J^{-4/3} \bar{C}_1, & \bar{\bar{C}}_2 &= J^{-4/3} \bar{C}_2, \\
\bar{\bar{C}}_3 &= J^{-4/3} \bar{C}_3, & \bar{\bar{C}}_4 &= J^{-4/3} \bar{C}_4
\end{aligned} \right\}. \tag{2.246}$$

Then, the contravariant components of  $\mathbf{C}_{\text{iso}}$  are:

$$\mathbf{C}_{\text{iso}}^{JKLM} = \left( \bar{\bar{C}}_1 + \frac{2}{I_1} \bar{\bar{S}}_1 \right) \left( G^{JJ} - \frac{1}{3} I_1 \bar{C}^{JJ} \right) \left( G^{KL} - \frac{1}{3} I_1 \bar{C}^{KL} \right)$$



$$\begin{aligned}
& + \bar{\bar{C}}_2 \left( \left( G^{IJ} - \frac{1}{3} I_1 \bar{C}^{IJ} \right) \left( C^{KL} - \frac{1}{3} II_1 \bar{C}^{KL} \right) + \left( C^{IJ} - \frac{1}{3} II_1 \bar{C}^{IJ} \right) \left( G^{KL} - \frac{1}{3} I_1 \bar{C}^{KL} \right) \right) \\
& + \left( \bar{\bar{C}}_3 + \frac{1}{II_1} \bar{\bar{C}}_4 + \frac{2}{II_1} \bar{\bar{S}}_2 \right) \left( C^{IJ} - \frac{1}{3} II_1 \bar{C}^{IJ} \right) \left( C^{KL} - \frac{1}{3} II_1 \bar{C}^{KL} \right) \\
& + \bar{\bar{C}}_4 G^{IJ} \odot G^{KL} + \frac{2}{3} (I_1 \bar{\bar{S}}_1 + II_1 \bar{\bar{S}}_2) \bar{C}^{IJ} \odot \bar{C}^{KL} \\
& - \frac{2}{I_1} \bar{\bar{S}}_1 G^{IJ} G^{KL} - \frac{1}{II_1} (\bar{\bar{C}}_4 + 2\bar{\bar{S}}_2) C^{IJ} C^{KL}. \tag{2.247}
\end{aligned}$$

## 2.8.2 Incompressible material

Incompressible material deforms with keeping its volume constant by the incompressibility constraint  $J = 1$ . The strain energy function for incompressible hyperelastic materials is assumed that consists of an elastic strain energy function and a constraint term with incompressibility,  $J = \det \mathbf{F} = 1$ :

$$\varphi = \varphi_{\text{el}}(\mathbf{C}) + \varphi_p(J). \tag{2.248}$$

The constraint term  $\varphi_p(J)$  is defined as:

$$\varphi_p(J) = -p(J - 1), \tag{2.249}$$

where the scalar  $p$  is hydrostatic pressure. With Eq. (2.91),  $\mathbf{S}$  can be written as

$$\mathbf{S} = 2 \frac{\partial \varphi_{\text{el}}(I_1, I_2)}{\partial \mathbf{C}} - 2p \frac{\partial J}{\partial \mathbf{C}} \tag{2.250}$$

$$= 2 \frac{\partial \varphi_{\text{el}}(I_1, I_2)}{\partial \mathbf{C}} - p J \mathbf{C}^{-1} \tag{2.251}$$

$$= S_1 \mathbf{I} + S_2 \mathbf{C} - p \mathbf{C}^{-1}. \tag{2.252}$$

where the strain energy function is assumed as a function with  $I_1$  and  $I_2$  because of incompressible constraint  $I_3 = 1$  and  $J = 1$ . With Eq. (2.93),  $\mathbf{C}$  is

$$\mathbf{C} = 4 \frac{\partial^2 \varphi_{\text{el}}(I_1, I_2)}{\partial \mathbf{C} \partial \mathbf{C}} - 2p \left( J \frac{\partial \mathbf{C}^{-1}}{\partial \mathbf{C}} + \frac{\partial J}{\partial \mathbf{C}} \mathbf{C}^{-1} \right) \quad (2.253)$$

$$= 4 \frac{\partial^2 \varphi_{\text{el}}(I_1, I_2)}{\partial \mathbf{C} \partial \mathbf{C}} - 2p \left( J \mathbf{C}^{-1} \odot \mathbf{C}^{-1} + J \mathbf{C}^{-1} \mathbf{C}^{-1} \right) \quad (2.254)$$

$$= \mathbb{C}_1 \mathbf{I} \mathbf{I} + \mathbb{C}_2 (\mathbf{I} \mathbf{C} + \mathbf{C} \mathbf{I}) + \mathbb{C}_4 \mathbf{C} \mathbf{C} + \mathbb{C}_8 \mathbf{S} - 2p \left( \mathbf{C}^{-1} \odot \mathbf{C}^{-1} + \mathbf{C}^{-1} \mathbf{C}^{-1} \right). \quad (2.255)$$

## 2.9 Constitutive equations

From above, generalized expressions of the strain energy functions for hyperelastic materials are described. In this section, Fung's model which is used in computations which will be shown in Chapters 4, 5, and 6 is introduced. For more hyperelastic models, see Appendix A. The isochoric part of the strain energy function for Fung's model [9] is written as:

$$(\varphi_{\text{iso}})_{\text{F}} = D_1 \left( e^{D_2 (\bar{I}_1 - 3)} - 1 \right) \quad (2.256)$$

where  $D_1$  and  $D_2$  are stress-like and dimensionless material constants, and the shear modulus at the undeformed shape is  $2D_1 D_2$ . With Eq. (2.183), the coefficients of  $\mathbf{S}$  for Fung's model are

$$\left( \bar{\bar{S}}_{\text{F}} \right)_1 = J^{-2/3} \left( \bar{S}_{\text{F}} \right)_1 = 2J^{-2/3} \frac{\partial (\varphi_{\text{iso}})_{\text{F}}}{\partial \bar{I}_1} = 2J^{-2/3} D_1 D_2 e^{D_2 (\bar{I}_1 - 3)}, \quad \left( \bar{\bar{S}}_{\text{F}} \right)_2 = 0. \quad (2.257)$$

The contravariant components of  $\mathbf{S}_{\text{iso}}$  for Fung's model can be expressed with Eqs. (2.202) and (2.257) as:

$$(\mathcal{S}_{\text{F}})_{\text{iso}}^{IJ} = (\bar{\bar{\mathcal{S}}}_{\text{F}})_1 \left( G^{IJ} - \frac{1}{3} I_1 \bar{C}^{IJ} \right) + (\bar{\bar{\mathcal{S}}}_{\text{F}})_2 \left( g_{KL} G^{IK} G^{JL} - \frac{1}{3} II_1 \bar{C}^{IJ} \right) \quad (2.258)$$

$$= (\bar{\bar{\mathcal{S}}}_{\text{F}})_1 \left( G^{IJ} - \frac{1}{3} I_1 g^{IJ} \right). \quad (2.259)$$

With Eq. (2.246), the coefficients of  $\mathbf{C}$  for Fung's model are

$$(\bar{\bar{\mathcal{C}}}_{\text{F}})_1 = J^{-4/3} (\bar{\mathcal{C}}_{\text{F}})_1 = 4J^{-4/3} D_1 D_2^2 e^{D_2(\bar{I}_1-3)}, \quad (\bar{\bar{\mathcal{C}}}_{\text{F}})_2 = (\bar{\bar{\mathcal{C}}}_{\text{F}})_3 = (\bar{\bar{\mathcal{C}}}_{\text{F}})_4 = 0. \quad (2.260)$$

The contravariant components of  $\mathbf{C}_{\text{iso}}$  for Fung's model can be expressed with Eqs. (2.247) and (2.260) as:

$$\begin{aligned} (\mathcal{C}_{\text{F}})_{\text{iso}}^{JKL} &= \left( (\bar{\bar{\mathcal{C}}}_{\text{F}})_1 + \frac{2}{I_1} (\bar{\bar{\mathcal{S}}}_{\text{F}})_1 \right) \left( G^{IJ} - \frac{1}{3} I_1 \bar{C}^{IJ} \right) \left( G^{KL} - \frac{1}{3} I_1 \bar{C}^{KL} \right) \\ &+ (\bar{\bar{\mathcal{C}}}_{\text{F}})_2 \left( \left( G^{IJ} - \frac{1}{3} I_1 \bar{C}^{IJ} \right) \left( C^{KL} - \frac{1}{3} II_1 \bar{C}^{KL} \right) + \left( C^{IJ} - \frac{1}{3} II_1 \bar{C}^{IJ} \right) \left( G^{KL} - \frac{1}{3} I_1 \bar{C}^{KL} \right) \right) \\ &+ \left( (\bar{\bar{\mathcal{C}}}_{\text{F}})_3 + \frac{1}{II_1} (\bar{\bar{\mathcal{C}}}_{\text{F}})_4 + \frac{2}{II_1} (\bar{\bar{\mathcal{S}}}_{\text{F}})_2 \right) \left( C^{IJ} - \frac{1}{3} II_1 \bar{C}^{IJ} \right) \left( C^{KL} - \frac{1}{3} II_1 \bar{C}^{KL} \right) \\ &+ (\bar{\bar{\mathcal{C}}}_{\text{F}})_4 G^{IJ} \odot G^{KL} + \frac{2}{3} (I_1 (\bar{\bar{\mathcal{S}}}_{\text{F}})_1 + II_1 (\bar{\bar{\mathcal{S}}}_{\text{F}})_2) \bar{C}^{IJ} \odot \bar{C}^{KL} \\ &- \frac{2}{I_1} (\bar{\bar{\mathcal{S}}}_{\text{F}})_1 G^{IJ} G^{KL} - \frac{1}{II_1} \left( (\bar{\bar{\mathcal{C}}}_{\text{F}})_4 + 2 (\bar{\bar{\mathcal{S}}}_{\text{F}})_2 \right) C^{IJ} C^{KL} \quad (2.261) \\ &= \left( (\bar{\bar{\mathcal{C}}}_{\text{F}})_1 + \frac{2}{I_1} (\bar{\bar{\mathcal{S}}}_{\text{F}})_1 \right) \left( G^{IJ} - \frac{1}{3} I_1 g^{IJ} \right) \left( G^{KL} - \frac{1}{3} I_1 g^{KL} \right) \end{aligned}$$

$$+ \frac{2}{3} I_1 (\bar{\bar{S}}_F)_1 g^{JJ} \odot g^{KL} - \frac{2}{I_1} (\bar{\bar{S}}_F)_1 G^{IJ} G^{KL}. \quad (2.262)$$

For the compressible shell model,

$$(S_F)_{\text{iso}}^{33} = (\bar{\bar{S}}_F)_1 \left( 1 - \frac{1}{3C_{33}} I_1 \right) + (\bar{\bar{S}}_F)_2 \left( C_{33} - \frac{1}{3C_{33}} II_1 \right) \quad (2.263)$$

$$= (\bar{\bar{S}}_F)_1 \left( 1 - \frac{1}{3C_{33}} I_1 \right), \quad (2.264)$$

$$\begin{aligned} (\mathbb{C}_F)_{\text{iso}}^{\alpha\beta 33} &= \left( (\bar{\bar{C}}_F)_1 \left( 1 - \frac{1}{3C_{33}} I_1 \right) + (\bar{\bar{C}}_F)_2 \left( C_{33} - \frac{1}{3C_{33}} II_1 \right) - \frac{2}{3C_{33}} (\bar{\bar{S}}_F)_1 \right) G^{\alpha\beta} \\ &+ \left( (\bar{\bar{C}}_F)_2 \left( 1 - \frac{1}{3C_{33}} I_1 \right) + (\bar{\bar{C}}_F)_3 \left( C_{33} - \frac{1}{3C_{33}} II_1 \right) - \frac{1}{3C_{33}} (\bar{\bar{C}}_F)_4 - \frac{2}{3C_{33}} (\bar{\bar{S}}_F)_2 \right) C^{\alpha\beta} \\ &- \frac{1}{3} \left( I_1 (\bar{\bar{C}}_F)_1 \left( 1 - \frac{1}{3C_{33}} I_1 \right) + (\bar{\bar{C}}_F)_2 \left( C_{33} I_1 + II_1 - \frac{2}{3C_{33}} I_1 II_1 \right) \right. \\ &\quad \left. + II_1 (\bar{\bar{C}}_F)_3 \left( C_{33} - \frac{1}{3C_{33}} II_1 \right) + (\bar{\bar{C}}_F)_4 \left( C_{33} - \frac{1}{3C_{33}} II_1 \right) \right. \\ &\quad \left. + 2 (\bar{\bar{S}}_F)_1 \left( 1 - \frac{1}{3C_{33}} I_1 \right) + 2 (\bar{\bar{S}}_F)_2 \left( C_{33} - \frac{1}{3C_{33}} II_1 \right) \right) \bar{C}^{\alpha\beta} \quad (2.265) \end{aligned}$$

$$\begin{aligned} &= \left( (\bar{\bar{C}}_F)_1 \left( 1 - \frac{1}{3C_{33}} I_1 \right) - \frac{2}{3C_{33}} (\bar{\bar{S}}_F)_1 \right) G^{\alpha\beta} \\ &- \frac{1}{3} \left( I_1 (\bar{\bar{C}}_F)_1 \left( 1 - \frac{1}{3C_{33}} I_1 \right) + 2 (\bar{\bar{S}}_F)_1 \left( 1 - \frac{1}{3C_{33}} I_1 \right) \right) g^{\alpha\beta} \quad (2.266) \end{aligned}$$

$$\begin{aligned}
&= \left( (\bar{\bar{C}}_F)_1 \left( 1 - \frac{1}{3C_{33}} I_1 \right) - \frac{2}{3C_{33}} (\bar{\bar{S}}_F)_1 \right) G^{\alpha\beta} \\
&\quad - \frac{1}{3} (I_1 (\bar{\bar{C}}_F)_1 + 2 (\bar{\bar{S}}_F)_1) \left( 1 - \frac{1}{3C_{33}} I_1 \right) g^{\alpha\beta}, \tag{2.267}
\end{aligned}$$

and

$$\begin{aligned}
(\mathbb{C}_F)_{\text{iso}}^{3333} &= (\bar{\bar{C}}_F)_1 \left( 1 - \frac{1}{3C_{33}} I_1 \right)^2 + 2 (\bar{\bar{C}}_F)_2 \left( 1 - \frac{1}{3C_{33}} I_1 \right) \left( C_{33} - \frac{1}{3C_{33}} II_1 \right) \\
&\quad + (\bar{\bar{C}}_F)_3 \left( C_{33} - \frac{1}{3C_{33}} II_1 \right)^2 + \frac{1}{3} (\bar{\bar{C}}_F)_4 \left( 1 + \frac{1}{3C_{33}^2} II_1 \right) \\
&\quad + \frac{4}{3C_{33}} (\bar{\bar{S}}_F)_1 \left( \frac{2}{3C_{33}} I_1 - 1 \right) + \frac{4}{3C_{33}} (\bar{\bar{S}}_F)_2 \left( \frac{2}{3C_{33}} II_1 - C_{33} \right) \tag{2.268}
\end{aligned}$$

$$= (\bar{\bar{C}}_F)_1 \left( 1 - \frac{1}{3C_{33}} I_1 \right)^2 + \frac{4}{3C_{33}} (\bar{\bar{S}}_F)_1 \left( \frac{2}{3C_{33}} I_1 - 1 \right), \tag{2.269}$$

are given.

## Chapter 3

### Isogeometric Discretization

In this chapter, the shape functions for discretization are given in [93]. They are for Bézier, B-splines, non-uniform rational B-splines (NURBS), and T-splines. A finite element (FE) analysis based on these functions is called isogeometric analysis (IGA). This representation is defined as “isogeometric discretization.” All the core functions can be represented by Bernstein polynomial functions with linear transformation matrices. Those matrices are constant within an element, and they are called “Bezier extraction operators.” This representation generalizes the discretization, and it makes easier to understand the shape of an element, and it simplifies the implementing algorithms.

#### 3.1 B-splines

B-splines description is the starting point of the isogeometric discretization in this chapter.

##### 3.1.1 Knot vectors

A knot vector in 1D is a non-decreasing set of coordinates in the parametric space, which is written as  $\Xi = \{\xi_1, \xi_2, \dots, \xi_{n+p+1}\}$ , where  $\xi_i \in \mathbb{R}$  is  $i^{th}$  knot,  $i$  is the knot index,  $i = 1, 2, \dots, n_k$ ,  $n_k$  is the number of knots in the knot vector,  $n_k = n_c + p + 1$ ,  $p$  is the polynomial order, and  $n_c$  is the number of basis functions used to construct the B-spline curve.

### 3.1.2 Basis functions

The B-spline basis functions are defined recursively with the knot vector, and starting with piecewise constants ( $p = 0$ ):

$$N_{i,0}(\xi) = \begin{cases} 1 & \text{if } \xi_i \leq \xi \leq \xi_{i+1}, \\ 0 & \text{otherwise.} \end{cases} \quad (3.1)$$

The basis functions corresponding to  $p = 1, 2, 3, \dots$ , are given by

$$N_{i,p}(\xi) = \frac{\xi - \xi_i}{\xi_{i+p} - \xi_i} N_{i,p-1}(\xi) + \frac{\xi_{i+p+1} - \xi}{\xi_{i+p+1} - \xi_{i+1}} N_{i+1,p-1}(\xi), \quad (3.2)$$

which is the Cox–de Boor recursion formula [94, 95].

### 3.1.3 Derivatives of B-spline basis functions

The derivative of B-spline basis functions are represented regarding B-spline lower order bases. It is the recursive definition of the basis in Eqs. (3.1) and (3.2). With given  $p$  and  $\Xi$ , the derivative of the  $i^{\text{th}}$  basis function is described as

$$\frac{d}{d\xi} N_{i,p}(\xi) = \frac{p}{\xi_{i+p} - \xi_i} N_{i,p-1}(\xi) - \frac{p}{\xi_{i+p+1} - \xi_{i+1}} N_{i+1,p-1}(\xi). \quad (3.3)$$

Higher derivatives also defined with Eq. (3.3) by

$$\frac{d^k}{d\xi^k} N_{i,p}(\xi) = \frac{p}{\xi_{i+p} - \xi_i} \left( \frac{d^{k-1}}{d\xi^{k-1}} N_{i,p-1}(\xi) \right) - \frac{p}{\xi_{i+p+1} - \xi_{i+1}} \left( \frac{d^{k-1}}{d\xi^{k-1}} N_{i+1,p-1}(\xi) \right). \quad (3.4)$$

## 3.2 NURBS

NURBS is a superset of B-splines, and a curve segment is described as NURBS basis function is able to represent an accurate arc by using weights. The position is represented

with shape functions and control points, and in 1D case, that is described as:

$$\mathbf{z}(\xi) = \sum_{a=1}^{n_{\text{en}}} R_a(\xi) \mathbf{z}_a, \quad (3.5)$$

where  $n_{\text{en}}$  is the number of control points within an element,  $\mathbf{z}_a$  is the position of the control point  $a$ , the NURBS shape function  $R_a(\xi)$  is written by

$$R_a(\xi) = \frac{N_a(\xi)w_a}{\sum_{b=1}^{n_{\text{en}}} N_b(\xi)w_b}. \quad (3.6)$$

Here,  $N_a(\xi)$  and  $w_a$  are the B-spline basis function and the NURBS weight regarding control point  $a$ . Eq. 3.5 can be converted by using the homogeneous coordinates [96].

With  $\mathbf{z}_a$  and  $w_a$ , the position with the homogeneous coordinates is described as

$$\mathbf{z}_a^w = \begin{bmatrix} w_a \mathbf{z}_a \\ w_a \end{bmatrix}. \quad (3.7)$$

With that, the curve segment is represented as

$$\mathbf{z}^w(\xi) = \sum_{a=1}^{n_{\text{en}}} N_a(\xi) \mathbf{z}_a^w, \quad (3.8)$$

and an equivalent form is given by Eqs. (3.5) and (3.9):

$$\mathbf{z}(\xi) = \begin{bmatrix} 1 & 0 & 0 & 0 \\ 0 & 1 & 0 & 0 \\ 0 & 0 & 1 & 0 \end{bmatrix} \frac{\mathbf{z}^w(\xi)}{\sum_{a=1}^{n_{\text{en}}} N_a(\xi)w_a}. \quad (3.9)$$

### 3.3 T-splines

T-spline [97] is a superset of NURBS. That allows geometrical high continuity even at unstructured parts. The core extensions are T-junctions and extraordinary points. The



T-junctions allows that a edge is inserted to an internal point of another edge with keeping its continuity. The extraordinary point is a point reached three or over four edges to keep the continuity in specific directions, which requires optimization methods [98]. Figure 3.1 shows T-spline control grids which have T-junctions and extraordinary points.

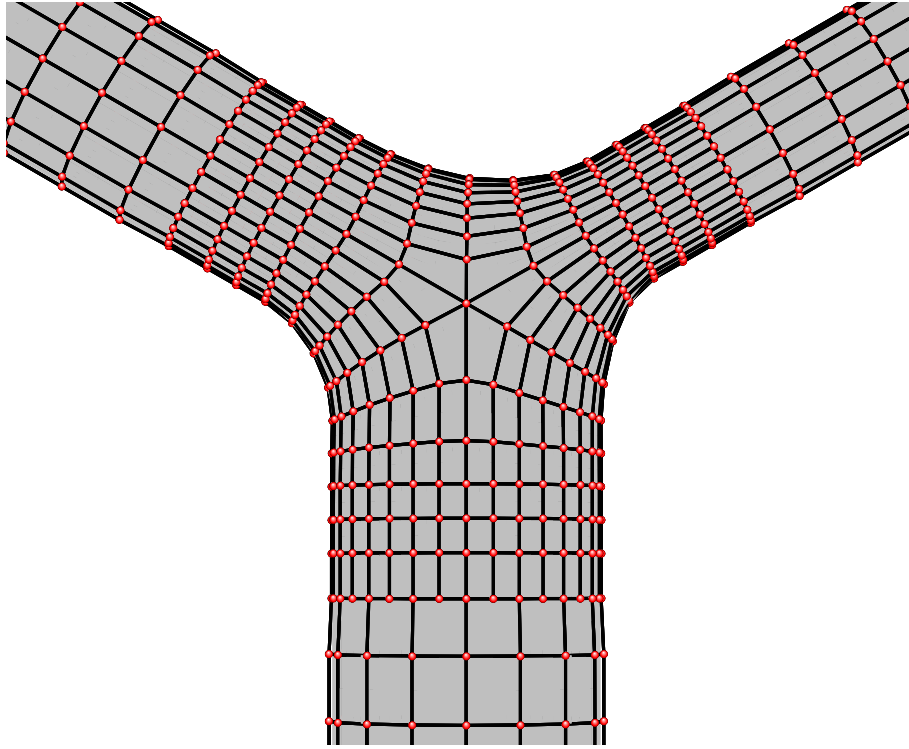


Figure 3.1: T-spline control grid. The center point is an extraordinary point. The cross points with three edges in the surface are T-junctions

### 3.4 Bézier extraction

As described in Eq. 3.1.2, a recursive way is one of the choices to generate corresponding B-spline basis function. As proposed in [96], the B-spline basis functions can be represented with the Bernstein basis functions  $B_b(\xi)$ :

$$N_a(\xi) = \sum_{b=1}^{n_{en}} C_{ab} B_b(\xi), \quad (3.10)$$

where  $C_{ab}$  is the components of the Bézier extraction operator. That indicates if  $C_{ab}$  is obtained once, the B-spline shape function is calculated with that and the given Bernstein function. See [96] for how to obtain  $C_{ab}$  from the B-spline knots vector. The position can be represented with the control points, the Bernstein function, and the components of the Bézier extraction operator:

$$\mathbf{z}^w(\xi) = \sum_{a=1}^{n_{en}} \sum_{b=1}^{n_{en}} C_{ab} B_b(\xi) \mathbf{z}_a^w. \quad (3.11)$$

By using that, the Bézier control points can be obtained:

$$\hat{\mathbf{z}}_b = \sum_{a=1}^{n_{en}} \mathbf{z}_a^w C_{ab}. \quad (3.12)$$

The extension to multi-dimensional parametric spaces is straightforward.

Here for more general purpose, array notations are represented:

$$\mathbf{Z} = [\mathbf{z}_a], \quad (3.13)$$

$$\mathbf{Z}^w = [\mathbf{z}_a^w], \quad (3.14)$$

$$\hat{\mathbf{Z}} = [\hat{\mathbf{z}}_a], \quad (3.15)$$

$$\mathbf{C} = [C_{ab}]. \quad (3.16)$$

Therefore, Eq. (3.12) can be written as

$$\hat{\mathbf{Z}} = \mathbf{Z}^w \cdot \mathbf{C}. \quad (3.17)$$

The opposite manipulation is also defined:

$$\mathbf{Z}^w = \hat{\mathbf{Z}} \cdot \mathbf{C}^{-1}. \quad (3.18)$$

## Chapter 4

### EBZSS with Isogeometric Discretization

The objective of this chapter is to apply higher-order shape functions to the EBZSS estimation method as the abovementioned (see Section 1.4). By using the isogeometric discretization, the process in the previous EBZSS method that is mapping between the artery and straight-tube segments is not needed. The higher-order shape functions give direct calculation of curvatures, and represent a convex-concave shape within an element. In this extension, the shape representation and the iterative method are modified.

2D test computations with straight-tube configurations are presented to show how the new EBZSS method works. The computations also aim to decide enough resolutions in the circumferential direction and the circumferential residual stretch as the ZSS design parameter. A 3D computation with matches the deformed shape to the medical-image-based geometry with the resolutions and the design parameters obtained in the 2D computations is also presented and represents how the method can be used.

In Section 4.1, the EBZSS concept with the isogeometric discretization is introduced. In Section 4.2, extracted from [88], an overview of the analytical relationship between the ZS and reference states of straight-tube segments is described, and here the relationship is referred to “straight-tube ZSS template.” The 2D test computations and the 3D computation are presented in Section 4.3 and Section 4.4, respectively. The concluding remarks are presented in Section 4.5. Most of the works in this chapter are already published in [99, 100].

## 4.1 EBTL method with isogeometric discretization

To design a ZSS from the corresponding reference state  $\mathbf{X}_{\text{REF}}$ , its control points  $(\mathbf{X}_{\text{REF}})_a$ , and the Bézier extraction operator corresponding to the element are used. Element-based coordinates  $(\mathbf{X}_{\text{REF}})_a^w$  is obtained and then converted to Bézier representation  $(\hat{\mathbf{X}}_{\text{REF}})_a$  by using the Bézier representation and the Bernstein basis functions. Then, the EBZSS initial guess can be designed as  $(\hat{\mathbf{X}}_0)_a$ . To adapt it for  $(\mathbf{X}_{\text{REF}})_a^w$ , the control points  $(\hat{\mathbf{X}}_0)_a$  to  $(\mathbf{X}_0)_a^w$  by using Eq. (3.18). In this process, the ZSS could have element-based weights  $w_a$  other than *one*, that would in general require using different basis functions between the ZS and reference states. This is not considered in this thesis.

The loaded configuration is needed to be matched to the target shape with the EBZSS, here  $\mathbf{X}_{\text{REF}}$  is taken as the target state. The iterative process is started from the ZSS initial guess  $(\mathbf{X}_0)^0$ , and kept continuing until the loaded configuration is matched to the target shape. In doing that, many pieces of the method described in [88] for linear elements are used.

In the previous iterative method,  $\mathbf{F}$  is estimated from the  $i^{\text{th}}$  solution. Here, the notation

$$\mathbf{F}(\mathbf{x}, \mathbf{X}) = \mathbf{R}(\mathbf{x}, \mathbf{X}) \cdot \mathbf{U}(\mathbf{x}, \mathbf{X}), \quad (4.1)$$

which is the polar decomposition with Eq. (2.12) is given. The arguments in the tensors represent the numerator and denominator in the partial derivatives, it means deformed from  $\mathbf{X}$  to  $\mathbf{x}$ . With the notation,  $\mathbf{F}$  at  $(i + 1)^{\text{th}}$  step can be described as

$$\mathbf{F}^{i+1} = \mathbf{R}(\mathbf{X}_{\text{REF}}, \mathbf{x}^i) \cdot \mathbf{F}^i \cdot \mathbf{R}((\mathbf{X}_0^e)^i, (\mathbf{X}_0^e)^{i+1}). \quad (4.2)$$

Here, the rotation between  $i^{\text{th}}$  and  $(i + 1)^{\text{th}}$  ZSS is assumed as

$$\mathbf{R}((\mathbf{X}_0^e)^i, (\mathbf{X}_0^e)^{i+1}) = \mathbf{I}. \quad (4.3)$$

With that and Eq. (4.2),

$$\mathbf{F}^{i+1} = \mathbf{R}(\mathbf{X}_{\text{REF}}, \mathbf{x}^i) \cdot \mathbf{F}^i, \quad (4.4)$$

is obtained and the inverse of that is described as

$$(\mathbf{F}^{i+1})^{-1} = (\mathbf{F}^i)^{-1} \cdot \mathbf{R}(\mathbf{x}^i, \mathbf{X}_{\text{REF}}), \quad (4.5)$$

$$= (\mathbf{U}^i)^{-1} \cdot \mathbf{R}((\mathbf{X}_0^e)^i, \mathbf{X}_{\text{REF}}). \quad (4.6)$$

The previous work calculates  $(\mathbf{X}_0^e)^{i+1}$  on the element center  $\boldsymbol{\xi} = \mathbf{0}$ , where  $\boldsymbol{\xi}$  is the parametric position. In this section, the tensor evaluations with integration is worked from  $\boldsymbol{\xi} = \mathbf{0}$  to the corresponding positions instead of  $\boldsymbol{\xi} = \mathbf{0}$  as

$$(\mathbf{X}_0^e)^{i+1} \Big|_{\boldsymbol{\xi}=\boldsymbol{\xi}_a} - (\mathbf{X}_0^e)^{i+1} \Big|_{\boldsymbol{\xi}=\mathbf{0}} = \int_{\mathbf{X}_{\text{REF}}^e \Big|_{\boldsymbol{\xi}=\mathbf{0}}}^{\mathbf{X}_{\text{REF}}^e \Big|_{\boldsymbol{\xi}=\boldsymbol{\xi}_a}} (\mathbf{F}^{i+1})^{-1} d\mathbf{X}_{\text{REF}}. \quad (4.7)$$

Here  $\boldsymbol{\xi}_a$  represents a parametric position assigned to the Bézier control point for  $a$  (see Figure 4.1), and a straight path is set from  $\mathbf{0}$  to  $\boldsymbol{\xi}_a$ . The representative parametric positions are equally spaced. The first approximation here is performing the integration with the midpoint rule:

$$\begin{aligned} & (\mathbf{X}_0^e)^{i+1} \Big|_{\boldsymbol{\xi}=\boldsymbol{\xi}_a} - (\mathbf{X}_0^e)^{i+1} \Big|_{\boldsymbol{\xi}=\mathbf{0}} \\ & \approx (\mathbf{F}^{i+1})^{-1} \Big|_{\boldsymbol{\xi}=\boldsymbol{\xi}_a/2} \cdot (\mathbf{X}_{\text{REF}}^e \Big|_{\boldsymbol{\xi}=\boldsymbol{\xi}_a} - \mathbf{X}_{\text{REF}}^e \Big|_{\boldsymbol{\xi}=\mathbf{0}}). \end{aligned} \quad (4.8)$$

The second approximation is to assume that the relationship given by Eq. (4.8) between  $(\mathbf{X}_0^e)^{i+1} \Big|_{\boldsymbol{\xi}=\boldsymbol{\xi}_a}$  and  $\mathbf{X}_{\text{REF}}^e \Big|_{\boldsymbol{\xi}=\boldsymbol{\xi}_a}$  can also be used between  $(\hat{\mathbf{X}}_0^e)_a^{i+1}$  and  $(\hat{\mathbf{X}}_{\text{REF}}^e)_a$ :

$$\begin{aligned} & (\hat{\mathbf{X}}_0^e)_a^{i+1} - (\mathbf{X}_0^e)^{i+1} \Big|_{\boldsymbol{\xi}=\mathbf{0}} \\ & \approx (\mathbf{F}^{i+1})^{-1} \Big|_{\boldsymbol{\xi}=\boldsymbol{\xi}_a/2} \cdot ((\hat{\mathbf{X}}_{\text{REF}}^e)_a - \mathbf{X}_{\text{REF}}^e \Big|_{\boldsymbol{\xi}=\mathbf{0}}). \end{aligned} \quad (4.9)$$

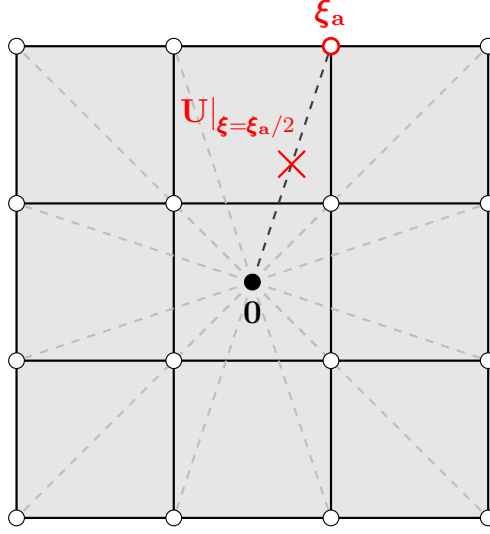


Figure 4.1: The position  $\times$  is the where  $(\mathbf{X}_0^e)^{i+1}$  is calculated in a Bézier element. The representative position  $\xi_a$  is assigned to the Bézier control point  $a$ . Straight paths are described from  $\mathbf{0}$  to  $\xi_a$ , and  $\times$  is the midpoint

This is the new version of the “direct-update (DU)” process instead of the original DU process in [88]. The “recursive-update (RU)” process is given as

$$\begin{aligned} & (\hat{\mathbf{X}}_0^e)_a^{i+1} - (\mathbf{X}_0^e)^{i+1}|_{\xi=0} \\ & \approx (\mathbf{F}^{i+1})^{-1}|_{\xi=\xi_a/2} \cdot \mathbf{F}(\mathbf{X}_{\text{REF}}, (\mathbf{X}_0^e)^i)|_{\xi=\xi_a/2} \cdot \left( (\hat{\mathbf{X}}_0^e)_a^i - (\mathbf{X}_0^e)^i|_{\xi=0} \right) \end{aligned} \quad (4.10)$$

$$= (\mathbf{U}^i)^{-1}|_{\xi=\xi_a/2} \cdot \mathbf{U}(\mathbf{X}_{\text{REF}}, (\mathbf{X}_0^e)^i)|_{\xi=\xi_a/2} \cdot \left( (\hat{\mathbf{X}}_0^e)_a^i - (\mathbf{X}_0^e)^i|_{\xi=0} \right). \quad (4.11)$$

Note that, the tensor–vector operations in Eqs. (4.9)–(4.11) actually involve the augmented versions of the tensors, where the augmented version of a tensor  $\mathbf{F}$  is defined as

$$\begin{bmatrix} \mathbf{F} & \mathbf{0} \\ \mathbf{0}^T & 1 \end{bmatrix}, \quad (4.12)$$

and the augmented versions of the vectors  $(\mathbf{X}_0^e)^{i+1}|_{\xi=0}$ ,  $\mathbf{X}_{\text{REF}}^e|_{\xi=0}$  and  $(\mathbf{X}_0^e)^i|_{\xi=0}$ , as defined by Eq. (3.8).

In the actual computations, the iteration is started from the “ZSS template”:  $(\mathbf{X}_0^e)^0 = (\mathbf{X}_0^e)_{\text{TEMP}}$  which is introduced in Section 4.2. In the steady-state structural mechanics computations, it is reasonable to start from displacement  $\mathbf{y} = \mathbf{0}$  with a given load and  $(\mathbf{X}_0^e)^0$ . However, sometime the deformed shape is far from the target state. To improve the convergence of the structural mechanics solution for  $i = 0$ , an incremental loading is applied and the initial guess is modified for the EBZSS based on that ramping:

$$((\mathbf{X}_0^e)^0)^j = (1 - t^j)\mathbf{X}_{\text{REF}} + t^j(\mathbf{X}_0^e)_{\text{TEMP}}. \quad (4.13)$$

Here  $0 < t^1 \leq t^2 \leq \dots \leq t^N = 1$ ,  $N$  is the number of nonlinear-iteration steps used in computing  $\mathbf{y}^0$ , and the iterations start with  $(\mathbf{y}^0)^0 = \mathbf{0}$ . The load is also ramped:

$$(\mathbf{h}^h)^j = t^j \mathbf{h}^h, \quad (4.14)$$

where  $\mathbf{h}^h$  is the target load. The ramping options include a ramping profile where the  $t^j$  values change at every certain number of nonlinear-iteration steps. With that, the steady-state solution  $\mathbf{y}^0$  for  $(\mathbf{X}_0^e)^0 = (\mathbf{X}_0^e)_{\text{TEMP}}$  based on the target load is obtained. For  $i = 1$  and beyond,  $(\mathbf{X}_0^e)^i$  is calculated from Eq. (4.11), and the nonlinear iterations used in computing  $\mathbf{y}^i$  start with  $(\mathbf{y}^i)^0 = \mathbf{0}$ .

## 4.2 Modeling the ZSS initial guess: straight-tube ZSS template

An analytical relationship between the ZS and reference states of straight-tube segments was given in [88]. Here that relationship is called “straight-tube ZSS template.” The straight tube in the target state, which is here the reference state, is described with three lengths:  $\bar{\ell}$ ,  $h$  and  $L$ . They are the circumferential length of the arterial-wall midsurface, wall thickness, and the longitudinal length, respectively. The tube volume is calculated as

$$V = \bar{\ell}hL. \quad (4.15)$$

The target shape which is from medical images give the three lengths, and three design parameters:  $\phi$ ,  $\alpha$ , and  $\lambda_z$ , have to be considered. They are the opening angle, the inverse value of the circumferential residual stretch, and the longitudinal residual stretch. The

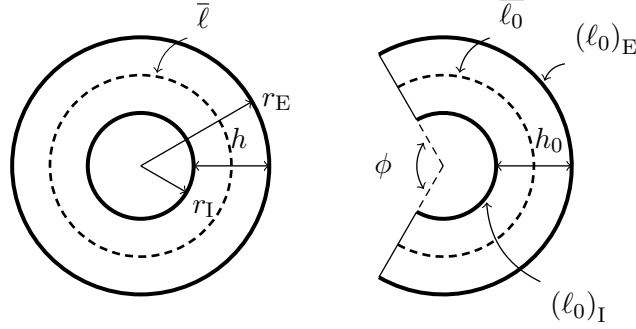


Figure 4.2: Straight tube in the target (*left*) and ZS (*right*) states. The dashed lines denote the arterial-wall midsurface in each state

parameter  $\alpha$  is explained as

$$\bar{\ell}_0 = \alpha \ell_1, \quad (4.16)$$

where  $\ell_1$  is the circumferential length of the inner tube surface in the target state. The task of calculating  $\bar{\ell}_0$  becomes the task of calculating  $\alpha$ . Figure 4.2 summarizes the template.

### 4.3 2D test computations

In this section, two objectives are set: 1. Find enough resolutions for the circumferential direction. 2. Find  $\alpha$  for the ZSS initial guess design with matches the deformed shape to the target shape. To simplify arterial geometries, ideal tube geometries are used.

In the 2D computations, two types of shape functions are prepared for the meshes: quadratic and cubic B-splines basis functions. Although NURBS can represent a circular arc exactly, it cannot do that throughout a full circle while retaining the  $C^1$  continuity of the basis functions. Therefore, to represent structure meshes uniform and periodic B-splines are used. Figures 4.3 and 4.4 show the meshes used. One element of the



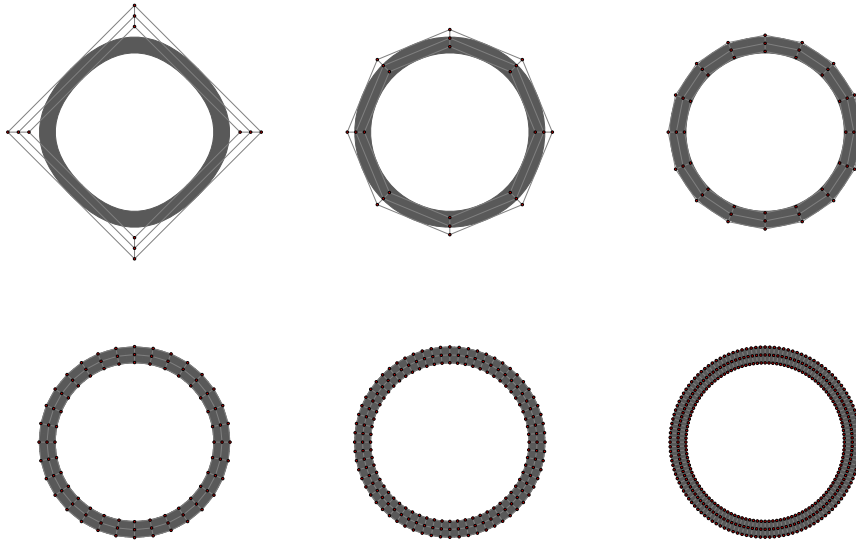


Figure 4.3: Quadratic B-spline meshes with 4, 8, 16, 32, 64, and 128 elements. The *red* circles are the control points and the *gray* part is the actual tube

quadratic meshes consists of three control points in each direction, on the other hand, cubic element consists of four control points in each direction. Here how well the meshes represent the circular arcs is evaluated. For that, the radius of curvature,  $\rho$ , is focused. Figures 4.5 shows  $\rho/\bar{\rho}$  as a function of the circumferential parametric coordinate,  $\xi$ , from  $-1$  to  $1$  in an element, where  $\bar{\rho}$  is the average radius. Quadratic representations have the lowest radius of curvature at  $\xi = 0$ , and cubic representations have the lowest radius of curvature at  $\xi = -1, 1$ . Figure 4.6 shows the  $1/4$  arcs of circles with quadratic and cubic B-spline representations. From the figure, the radius of curvature will be the lowest at points closest to the control points, and the highest between those points.

Figure 4.7 shows the standard deviation of  $\rho/\bar{\rho}$ , as a function of the arc angle  $\Delta\theta$  represented by an element, where  $\Delta\theta = 2\pi/n_{el}$ , and  $n_{el}$  is the number of elements. Note that, both quadratic and cubic B-splines have second-order accuracy. From the figure, quadratic 32 elements and cubic 16 elements have under 1 % standard deviations.

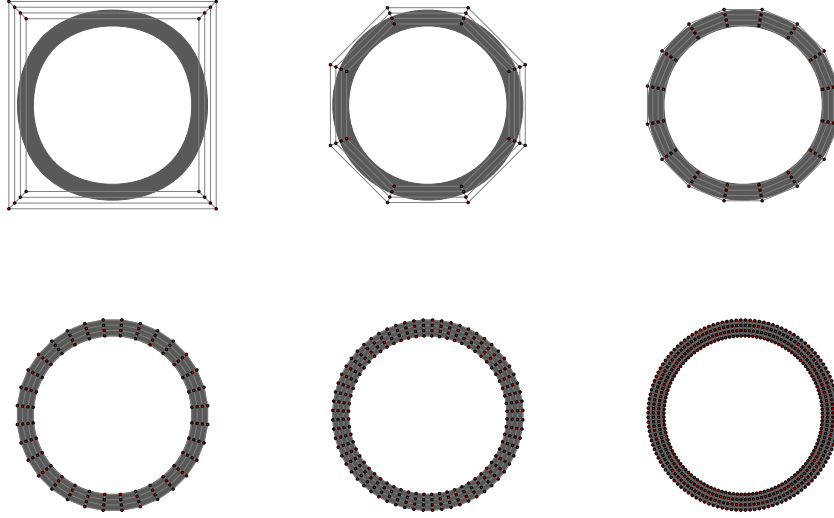


Figure 4.4: Cubic B-spline meshes with 4, 8, 16, 32, 64, and 128 elements. The *red* circles are the control points and the *gray* part is the actual tube

#### 4.3.1 Curvature matching in the ZSS

Curvature matching in the ZSS is done by first converting the B-spline element in the target state to Bézier representation. After that, for the specified  $\phi$ , element configurations are built with the objective of having a constant radius of curvature in the ZSS. Then the Bézier representation is converted back to B-spline representation. Figures 4.8 and 4.9 show examples of the process for  $\phi = 5\pi/2$  with quadratic and cubic representations, which results in Bézier elements with  $\Delta\theta = (2\pi - \phi)/n_{el} = -\pi/(2n_{el})$ , and for a given value of  $\alpha$ . In these cases, the outer surface is smaller than the inner surface.

In the case of quadratic Bézier functions, the middle control point is chosen to be on the tangents to the inner surface at the two other control points. This determines the curvature in the ZSS. For cubic Bézier functions, the control points are chosen to be also at equally-spaced angular positions with an additional degree of freedom. Figure 4.10 shows the convergence rate for the standard deviation of  $\rho_0/\bar{\rho}_0$  for the Bézier elements, where  $\bar{\rho}_0$  is the average radius. Note that from Figures 4.7 and 4.10, Bézier elements

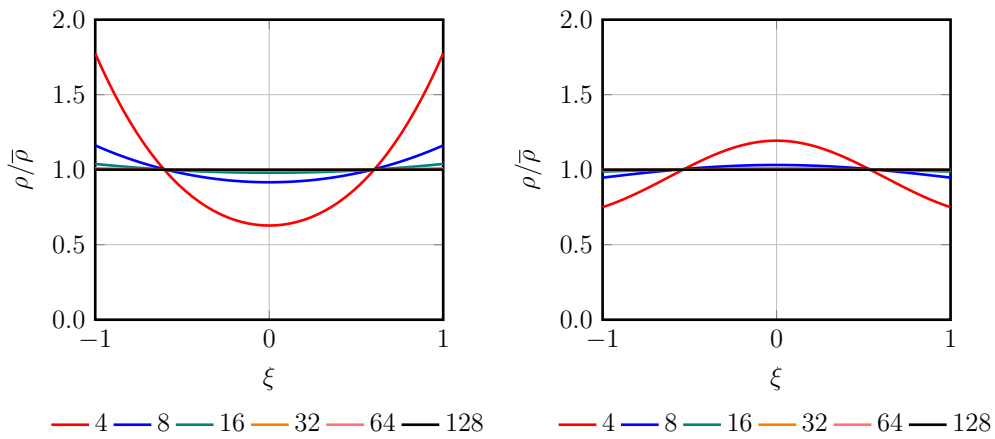


Figure 4.5: Representation of the radius of curvature within an element with quadratic (*left*) and cubic (*right*) B-splines. The curves are for the six meshes,  $\xi$  is the circumferential parametric coordinate, and  $\bar{\rho}$  is the average radius

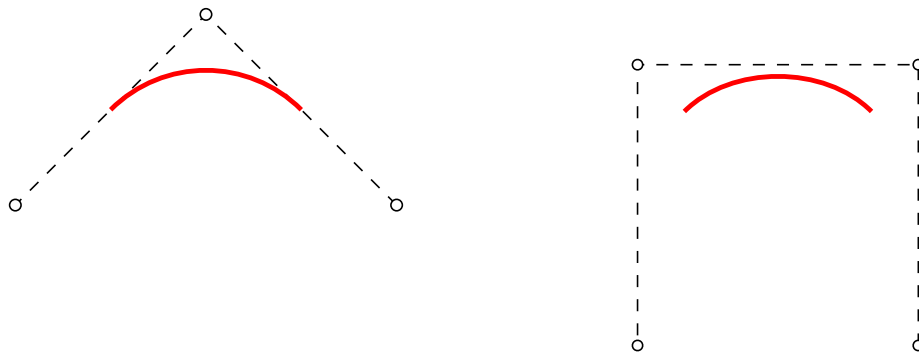


Figure 4.6: 1/4 arcs of circles. Quadratic (*left*) and cubic (*right*) B-spline representations. Circles are control points, red solid lines are physical arcs

have the same representation quality as the B-spline elements for quadratic functions, and slightly better quality for cubic functions.

### 4.3.2 Computational results

The results of the processes which is described in Section 4.3.1 with a range of  $\alpha$  values are shown in this section. The steady-state solutions corresponding to a constant pressure value of  $p_0 = 92$  mm Hg are obtained. In these computations, the arterial wall is made of Fung material (see Section 2.9) which is described in Section 2.9. The material constants

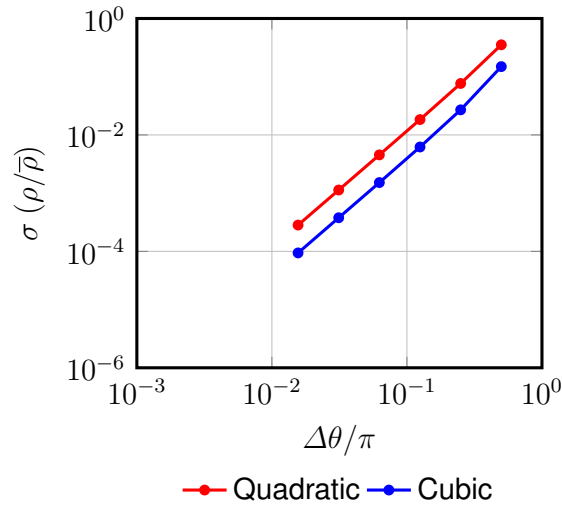


Figure 4.7: Standard deviation of  $\rho/\bar{\rho}$  as a function of the arc angle  $\Delta\theta$  represented by a B-spline element, where  $\bar{\rho}$  is the average radius

$D_1$  and  $D_2$  are  $2.6447 \times 10^3 \text{ N/m}^2$  and 8.365, and the penalty Poisson's ratio is 0.45.

The structural mechanics computations generate a relationship between the curvature to the deformed state and  $\alpha$ , and from that  $\alpha$  value can be selected with matches the curvature in the target state. Figures 4.11 and 4.12 show the average curvature of the inner surface in the deformed state as a function of  $\alpha$  for the six meshes with quadratic and cubic B-splines. The value of  $\alpha$  that matches the target curvature of the mesh made of 4 elements with quadratic functions is very different than the value obtained with the other meshes. For cubic functions, except for the mesh made of 4 elements, curves for all the meshes coincide. Figure 4.13 shows, for all the meshes,  $\alpha$  values that matches the target curvature. The values of  $\alpha$  are converged in the resolutions, and the mesh which consists of 16 elements with both quadratic cubic representations have enough convergence.

With all the meshes and  $\alpha$  values displayed in Figure 4.13, the steady-state structural mechanics solutions are computed to examine the stretches at the  $4 \times 4$  Gaussian quadrature points (see Figure 4.14). Note that, because the structural mechanics computations are done with quadratic functions, only  $3 \times 3$  quadrature points are used. Because of the circular symmetry, the stretches should depend only on the radial position. Here the

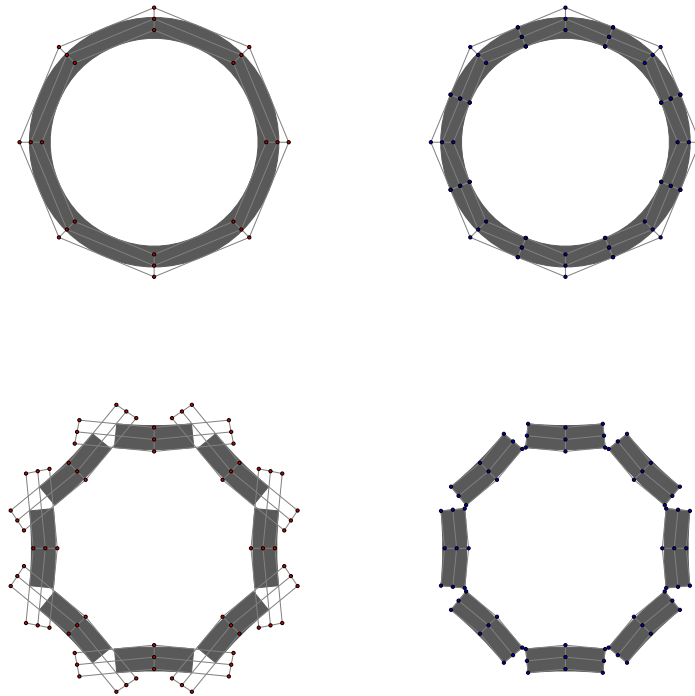


Figure 4.8: Curvature matching in the ZSS. Quadratic basis functions with 8 elements. The B-spline mesh in the target state (*top left*) is converted to Bézier representation (*top right*). From that, for the specified  $\phi$  and for a given value of  $\alpha$ , element configurations are built with the objective of having constant radius of curvature in the ZSS (*bottom right*). Then that is converted back to B-spline representation (*bottom left*)

stretches are observed by examining their values along different radial lines in the element, which are called “Inner” and “Outer” in Figure 4.14. Figure 4.15 shows the radial stretches for the meshes with 8 elements. For the meshes with 16 or more elements, the radial stretches along the inner and outer lines are basically indistinguishable. Figure 4.16 shows the circumferential stretches for the meshes with 16 elements. For the meshes with 32 or more elements, the circumferential stretches along the inner and outer lines are basically indistinguishable. Table 4.1 shows the stretch values at the integration points for the mesh with 128 elements and cubic B-splines. The values in Table 4.1 could be assumed to be the actual values and the relative error for the other meshes can be calculated. Figure 4.17 shows the relative error in the radial and circumferential stretches at all

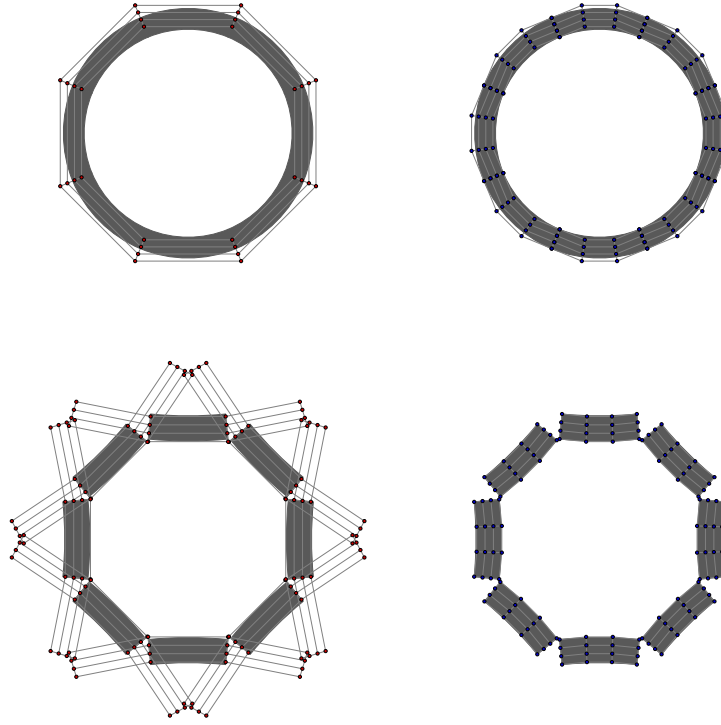


Figure 4.9: Curvature matching in the ZSS. Cubic basis functions with 8 elements. The B-spline mesh in the target state (*top left*) is converted to Bézier representation (*top right*). From that, for the specified  $\phi$  and for a given value of  $\alpha$ , element configurations are built with the objective of having constant radius of curvature in the ZSS (*bottom right*). Then that is converted back to B-spline representation (*bottom left*)

8 integration points for all those other meshes. From the results, quadratic representation has a limited error even though the resolution is increased. The mesh with 16 or more elements and cubic representation has under  $10^{-3}$  error on all of the integration points.

#### 4.4 3D computation

The objective of this section is to observe how the method works with the geometry extracted from medical images. The geometry has an uneven surface. Because it was difficult to obtain well converged results with the previous method in such a geometry, here the convergence will be observed. The first step of this test is to generate a mesh for the target geometry, and the volume mesh is generated in a special fashion, taking into

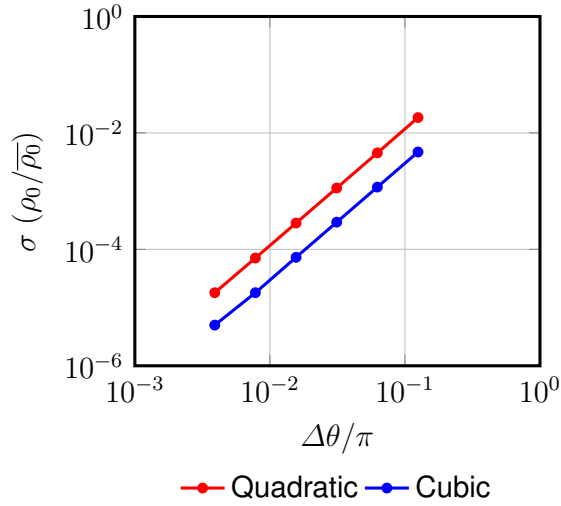


Figure 4.10: Curvature matching in the ZSS. Standard deviation of  $\rho_0/\bar{\rho}_0$  as a function of the arc angle  $\Delta\theta$  represented by a Bézier element, where  $\bar{\rho}_0$  is the average radius

Table 4.1: Stretch values at the integration points for the mesh with 128 elements and cubic B-splines. The values along the inner and outer lines are identical for the number of digits displayed

$\eta$	$\lambda_r$	$\lambda_\theta$
-0.86114	0.9481	1.044
-0.33998	0.8760	1.121
0.33998	0.7800	1.218
0.86114	0.7049	1.289

account the radial stretch. As seen in Figure 4.15, in the 2D computations  $\lambda_r$  was linear in  $\eta$ , the parametric coordinate in the radial direction in the ZSS. In that computational setting, in the ZSS, the parametric and physical coordinates in the radial direction also had a linear relationship. Consequently, in the ZSS,  $\lambda_r$  was linear in the physical coordinate in the radial direction. Based on these considerations, the volume mesh for the target geometry is generated with the objective of having in the ZSS a linear relationship between the parametric and physical coordinates in the radial direction. In this example, the mesh is with cubic B-spline representation and 16 elements for the circumferential direction.

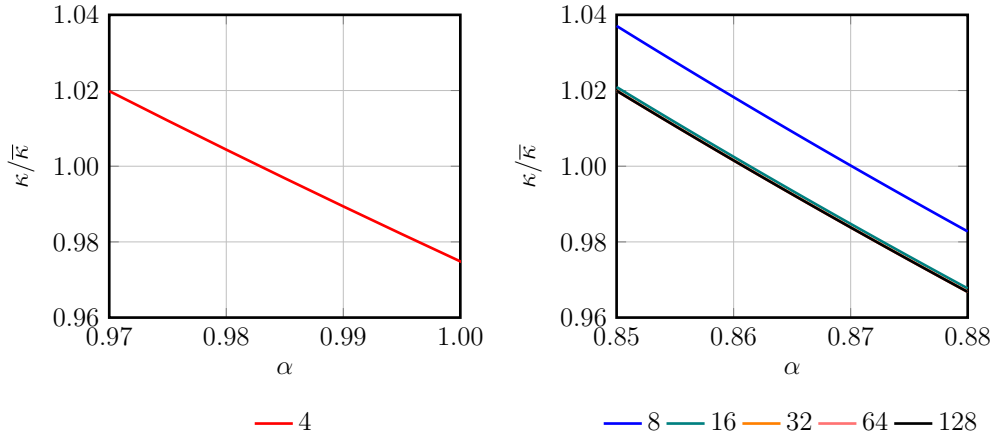


Figure 4.11: Average curvature in the deformed state as a function of  $\alpha$  for the six meshes with quadratic B-splines, where  $\bar{\kappa}$  is the curvature in the target state

#### 4.4.1 Surface and volume mesh generation for the target geometry

The surface geometry is obtained from the medical images using techniques described in [63]. Figure 4.18 shows a generated surface mesh. Next step is volume mesh generation. The mesh has only one element in the radial direction, with four control points. To locate the control points of the outer surface, for each control point of the inner surface, a distance is taken equal to the wall thickness in the direction normal to the surface at the collocation point corresponding to that control point. Figure 4.19 shows the volume geometry. In this example, the inner diameter at the inlet is about 27.3 mm, and use a constant wall thickness of 2.5 mm. The two interior control points do not effect the arterial volume geometry. However, as mentioned above, their locations in a special fashion are determined based on considerations related to the radial stretch. That will be explained in the next section.

#### 4.4.2 Mesh generation for $(\mathbf{X}_0^e)^0$

To obtain  $(\mathbf{X}_0^e)^0$ , the straight-tube ZSS template is applied with the data obtained in Section 4.3. Because the template is for the circumferential direction, each direction has to be determined on the geometry at first. Here, the principal curvature directions of the



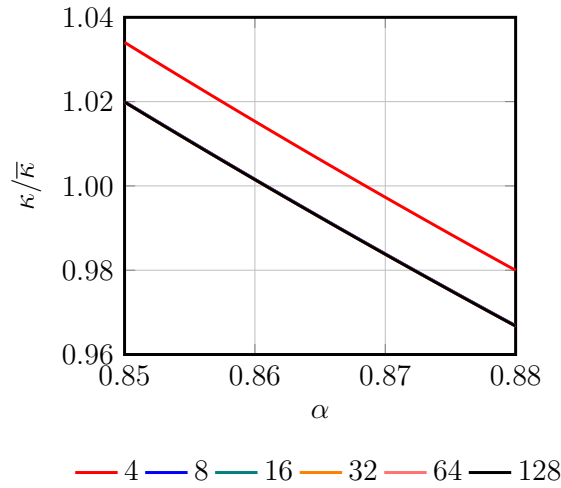


Figure 4.12: Average curvature in the deformed state as a function of  $\alpha$  for the six meshes with cubic B-splines, where  $\bar{\kappa}$  is the curvature in the target state

inner surface are assumed to be useful for the determination. Figures 4.20 and 4.21 show maximum principal curvatures and their directions. As expected, in most places, the direction of maximum principal curvature is toward to the circumferential direction.

Using those two directions including the minimum principal direction, and their cross product, “ideal element” can be created as shown in Figure 4.22. The direction of maximum principal curvature is set as the circumferential direction  $\theta$ , the other principal direction is set as the longitudinal direction  $z$ , and the cross-product direction is set as the radial direction  $r$ . The ideal element is defined with its inner surface having those principal curvatures in the  $\theta$  and  $z$  directions, and expanding in all three directions to cover the physical element. The curvature in the circumferential direction comes from  $\phi = 5\pi/2$  and  $\alpha = 0.870$ , and for the  $z$  direction  $\lambda_z = 1.0$  (no stretch) is assumed in this example. The radial direction is based on having the  $\lambda_r$  distribution from Figure 4.15.

With the ideal elements from the target state and ZSS, by using a least-squares projection, the physical element is mapped from the target state to the ZSS. Here a second choice to make is faced, and that is for the control-point spacing in the radial direction for the physical element in the target state and ZSS. The spacing in the target state is chosen to be proportional to the spacing for the ideal element in the target state, leading to a

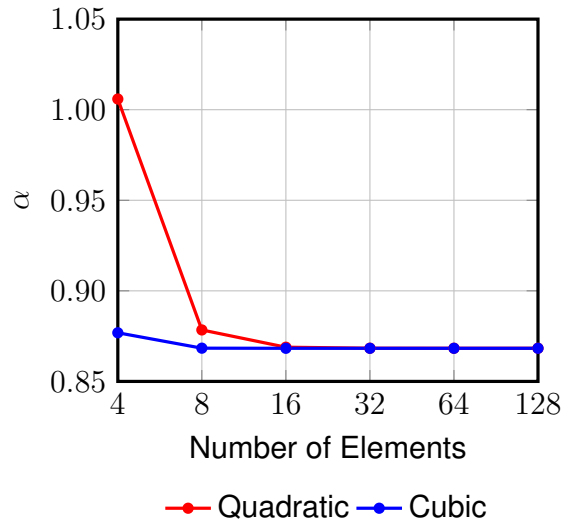


Figure 4.13: For all the meshes,  $\alpha$  value that matches the target curvature

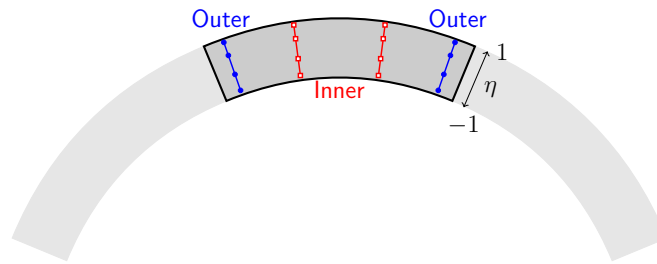


Figure 4.14: Schematic display of the integration points

distribution in the ZSS that is not far from being equally spaced. Figure 4.23 shows the control mesh in the target state.

Figure 4.24 shows the element representation of  $(\mathbf{X}_0^e)^0$  obtained with the process, curvature-based cut. From  $(\mathbf{X}_0^e)^0$  and  $\mathbf{X}_{\text{REF}}$ , maximum and minimum principal stretches, and the stretch in the radial direction are calculated. Figures 4.25–4.27 show those stretches.

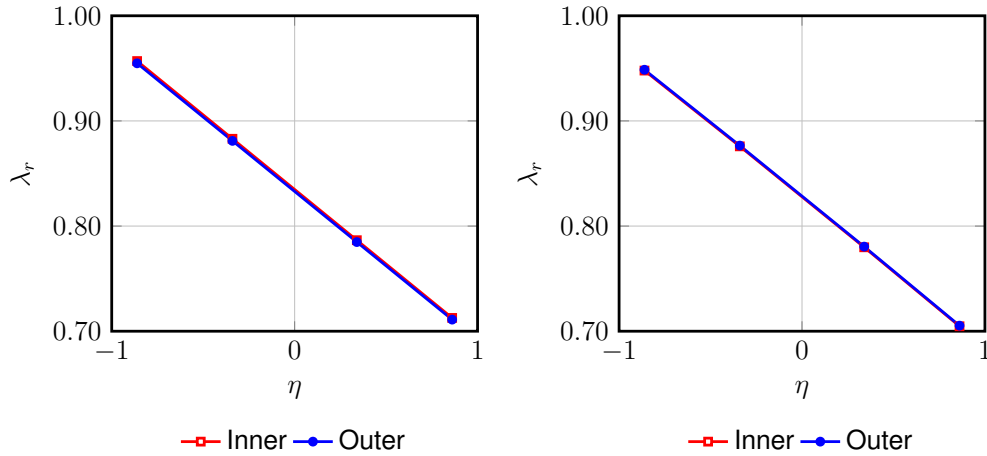


Figure 4.15: Radial stretches for the meshes with 8 elements and quadratic (*left*) and cubic (*right*) B-splines

#### 4.4.3 Iterations to calculate $\mathbf{X}_0^e$

In computation of  $\mathbf{y}^0$  from  $(\mathbf{X}_0^e)^0$ , the ramping method described in Section 4.1 is used, for reasons also described in that section. Figure 4.28 shows  $(\mathbf{X}_0^e)^0$  and  $\mathbf{y}^0$ . Figures 4.29–4.32 show  $(\mathbf{X}_0^e)^i$  and  $\mathbf{y}^i$  for iteration step  $i = 1, 2, 300,$  and  $1000$ . Figure 4.33 shows the maximum of  $\|\mathbf{y}^i\|$  as a function of  $i$ . There are some very-low-magnitude oscillations, but the solution converges very well.

#### 4.4.4 Observations on the results

From converged  $\mathbf{X}_0^e$  and  $\mathbf{X}_{\text{REF}}$ , the maximum and minimum principal stretches and radial stretch are calculated. The stretches are shown in Figures 4.34–4.36. In most places the stretches are very comparable to what we obtained from  $(\mathbf{X}_0^e)^0$  and  $\mathbf{X}_{\text{REF}}$  (see Figures 4.25–4.27), such as high-stretch (tension) regions and low-stretch (compression) regions. However, there are some differences locally, such as at the high-curvature region of the descending aorta. The maximum values of the maximum principal stretches with  $(\mathbf{X}_0^e)^0$  and  $(\mathbf{X}_0^e)^{1000}$  are 1.134 and 1.916. The average values of the maximum principal stretches with  $(\mathbf{X}_0^e)^0$  and  $(\mathbf{X}_0^e)^{1000}$  are 1.045 and 1.215. The minimum values of the minimum principal stretches with  $(\mathbf{X}_0^e)^0$  and  $(\mathbf{X}_0^e)^{1000}$  are 0.8635 and 0.5764. The average

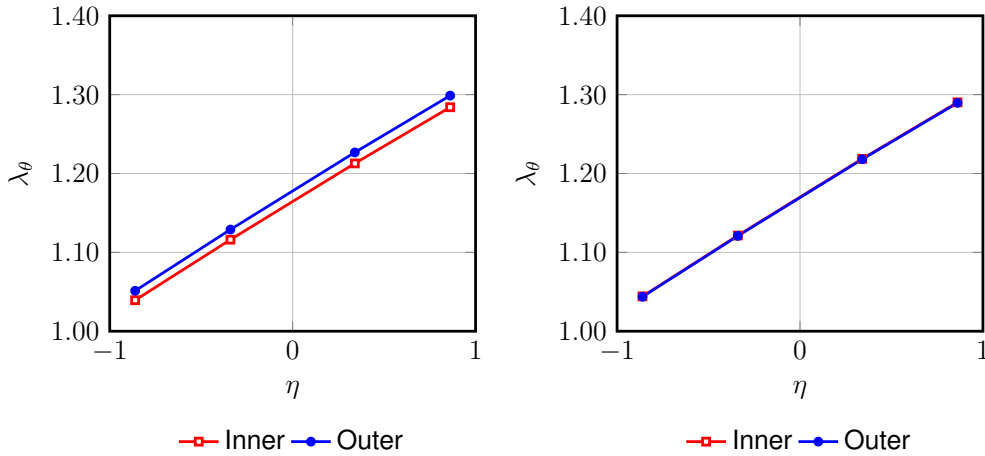


Figure 4.16: Circumferential stretches for the meshes with 16 elements and quadratic (*left*) and cubic (*right*) B-splines

values of the minimum principal stretches with  $(\mathbf{X}_0^\epsilon)^0$  and  $(\mathbf{X}_0^\epsilon)^{1000}$  are 0.9547 and 0.8562. The differences of the values indicate the ZSS initial guess is far from the converged ZSS. To thinking reasons for the results, the high curvature might have other choices of set of the design values. Also, note that the template used in the computation was based on the straight-tube part of the aorta. Although T-spline (see Section 3.3) is a useful representation for geometrical complexities, the control mesh structure could be complicated like Figure 3.1. Since the iterative method (see Section 4.1) imposes modifications on element-based control points (see Figure 4.1), T-spline representation with the EBZSS could have convergence difficulty.

## 4.5 Concluding remarks

The objective of this chapter was to apply higher-order shape functions to the EBZSS estimation method as the abovementioned (see Section 1.4). The extension of the EBZSS estimation method by applying the isogeometric discretization was introduced and has been successfully applied to a patient-specific modeling of a human aorta, which has convex-concave regions. 2D test computations with straight-tube configurations showed how the new EBZSS method works, and decided enough resolutions in the circumferential

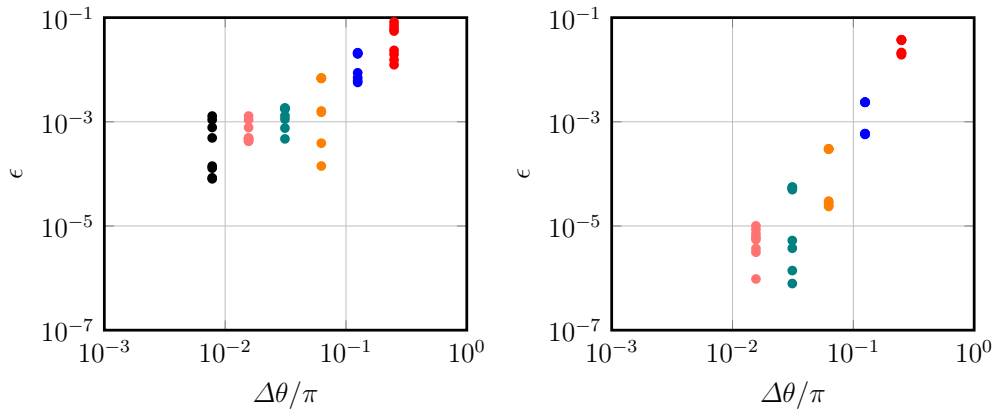


Figure 4.17: Relative error in the radial and circumferential stretches at all 8 integration points for the meshes with quadratic (*left*) and cubic (*right*) B-splines. The colors represent different meshes, with the same color convention used in Figure 4.11. The relative error is calculated based on the value obtained from the mesh with 128 elements and cubic B-splines



Figure 4.18: Surface geometry

direction and the circumferential residual stretch as the ZSS design parameter. In addition, a 3D computation with matches the deformed shape to the medical-image-based geometry represented well-converged results.

From above results, the following challenges remained. The first challenge is the ZSS initial guess was far from the converged ZSS. It means the anatomical ZSS design was not applied well on the converged ZSS. The second challenge is that the EBZSS iterative method depends on the control mesh structure. The method imposes displacements, calculated from the stretch on the surface, on element-based control points. T-spline is

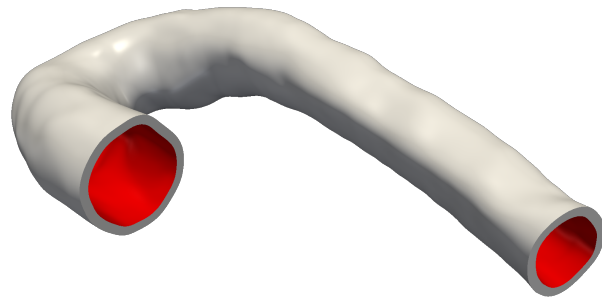


Figure 4.19: Volume geometry. *Red* surface indicates the inner surface. The left is inlet, and the right is outlet of blood flow

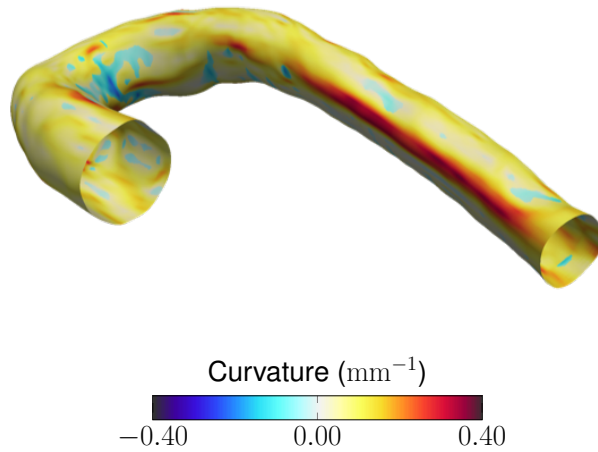


Figure 4.20: Distribution of the maximum principal curvature

a useful representation for more complex geometry, but the control mesh could be unstructured connections. Since that connections could set the point far from the physical surface, T-spline representation with the EBZSS has convergence difficulty.

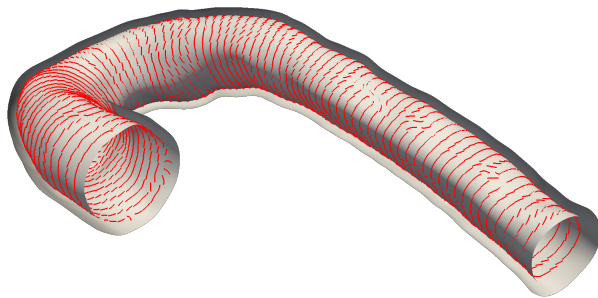


Figure 4.21: Directions of maximum principal curvature

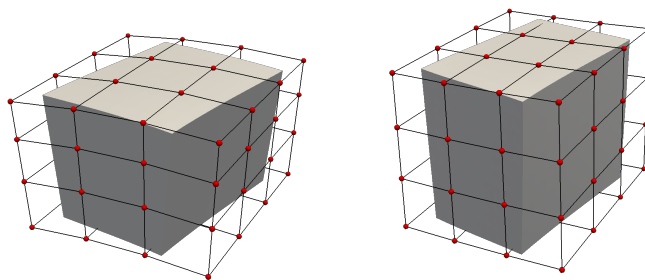


Figure 4.22: Physical and ideal elements. The gray colored shape represents the physical element, and the lines and points represent the corresponding ideal Bézier control element. Target state (*left*) and ZSS (*right*)

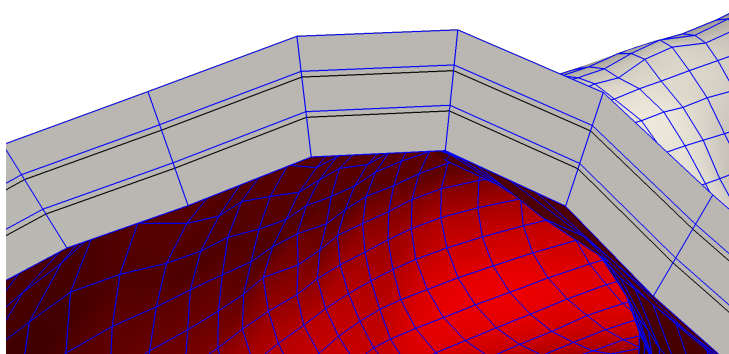


Figure 4.23: Control mesh in the target state, with the blue lines representing the mesh we use, which is based on the control-point spacing we chose in the radial direction, and with the black lines representing equal spacing of control points in the radial direction

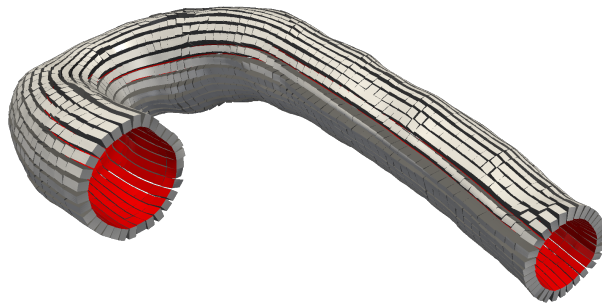


Figure 4.24: Element representation of  $(\mathbf{X}_0^e)^0$

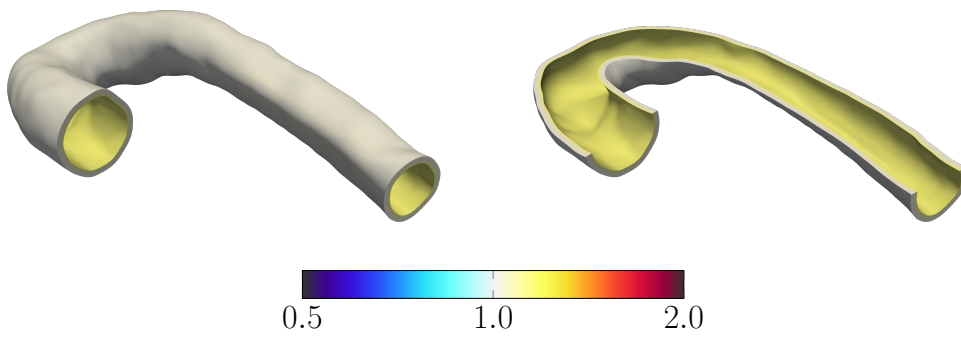


Figure 4.25: Maximum principal stretch from  $(\mathbf{X}_0^e)^0$  and  $\mathbf{X}_{\text{REF}}$  The whole domain (*left*) and the clipped view (*right*)

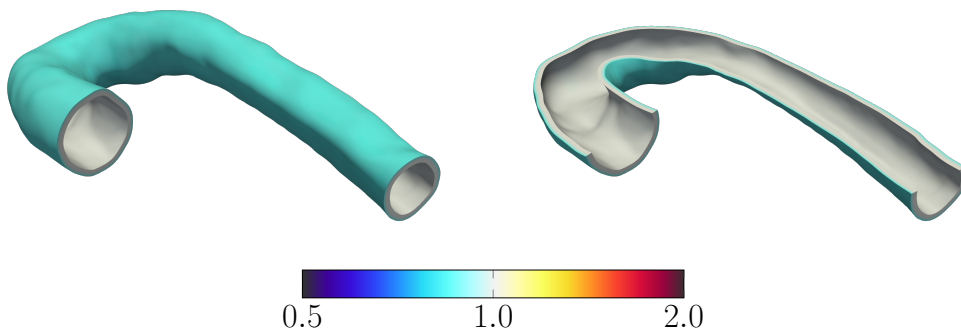


Figure 4.26: Minimum principal stretch from  $(\mathbf{X}_0^e)^0$  and  $\mathbf{X}_{\text{REF}}$  The whole domain (*left*) and the clipped view (*right*)



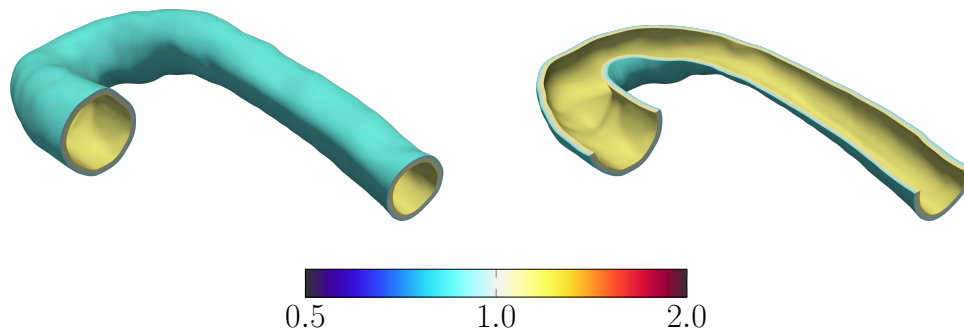


Figure 4.27: Radial stretch from  $(\mathbf{X}_0^e)^0$  and  $\mathbf{X}_{\text{REF}}$  The whole domain (*left*) and the clipped view (*right*)

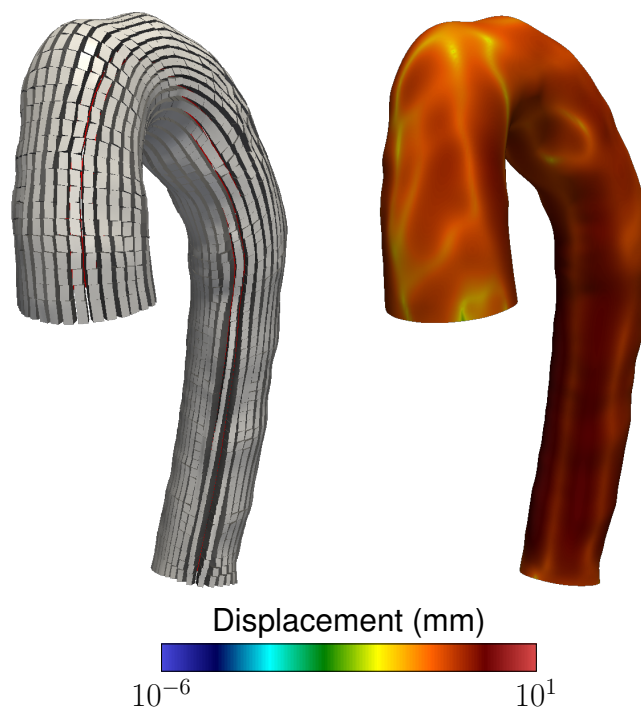


Figure 4.28: Elements of  $(\mathbf{X}_0^e)^0$  (*left*) and  $\mathbf{y}^0$  (*right*)

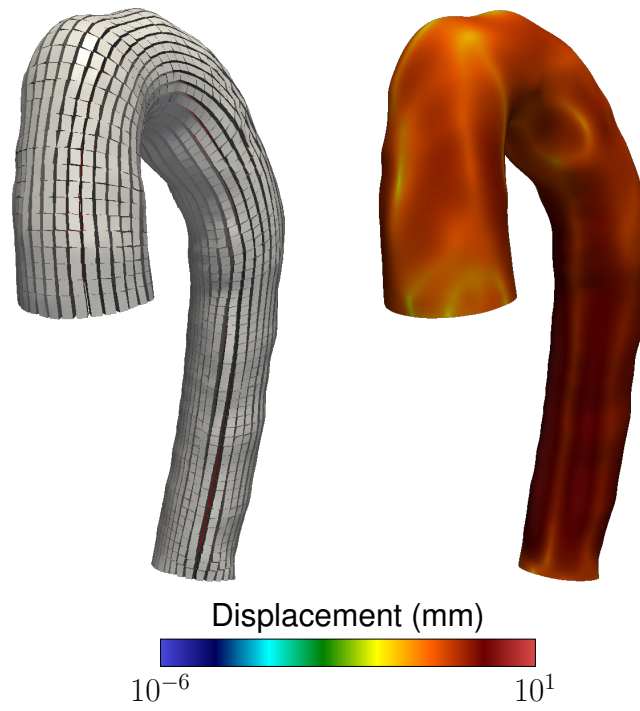


Figure 4.29: Elements of  $(\mathbf{X}_0^\epsilon)^1$  (left) and  $\mathbf{y}^1$  (right)

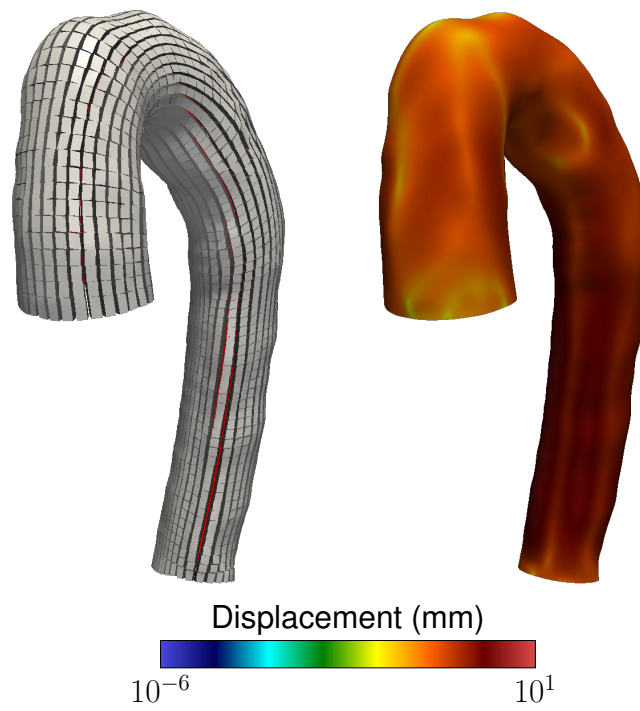


Figure 4.30: Elements of  $(\mathbf{X}_0^\epsilon)^2$  (left) and  $\mathbf{y}^2$  (right)

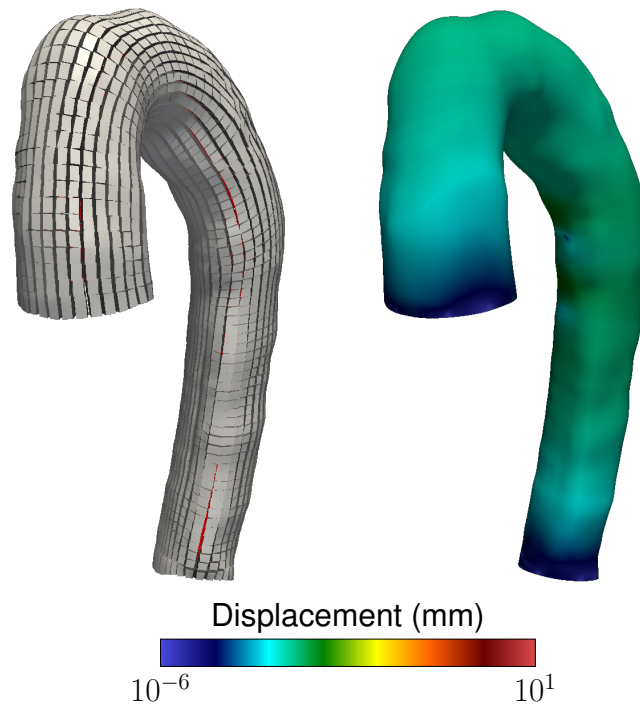


Figure 4.31: Elements of  $(\mathbf{X}_0^\epsilon)^{300}$  (left) and  $\mathbf{y}^{300}$  (right)

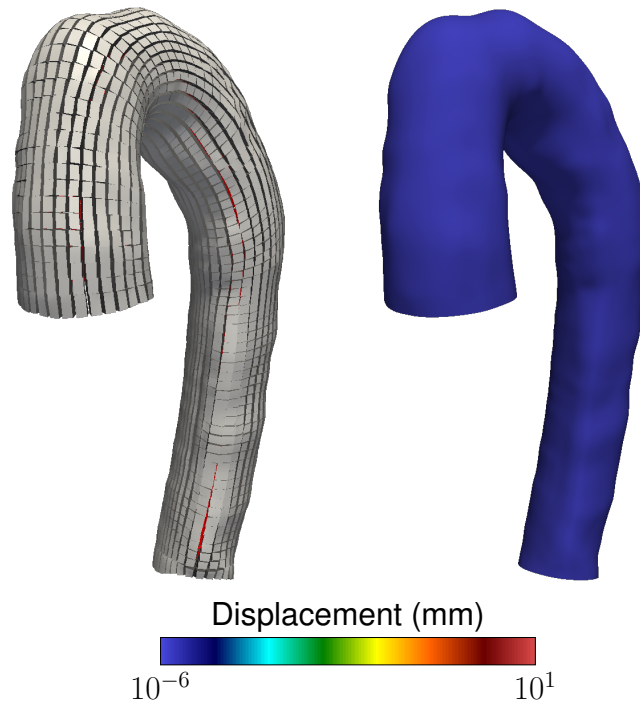


Figure 4.32: Elements of  $(\mathbf{X}_0^\epsilon)^{1000}$  (left) and  $\mathbf{y}^{1000}$  (right)

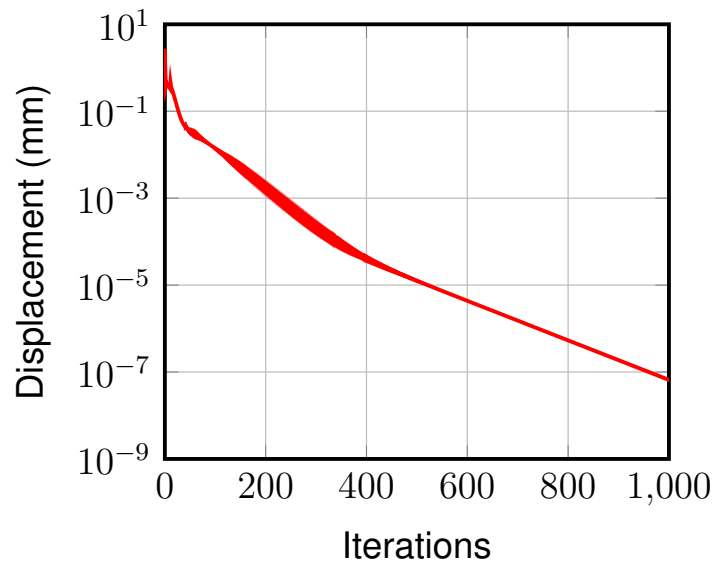


Figure 4.33: Maximum of  $\|y^i\|$  as a function of  $i$  (EBZSS iteration counter)

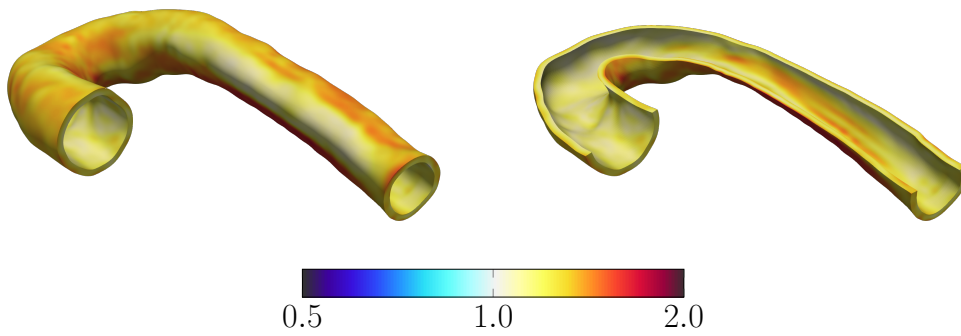


Figure 4.34: Maximum principal stretch from converged  $\mathbf{X}_0^e$  and  $\mathbf{X}_{\text{REF}}$ . The whole domain (*left*) and the clipped view (*right*)

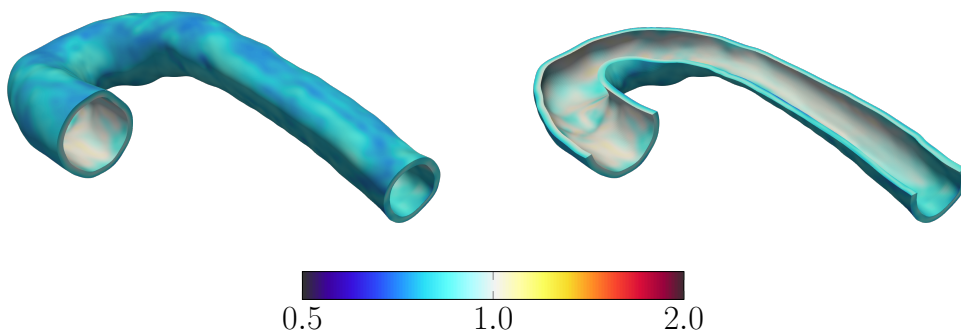


Figure 4.35: Minimum principal stretch from converged  $\mathbf{X}_0^e$  and  $\mathbf{X}_{\text{REF}}$ . The whole domain (*left*) and the clipped view (*right*)

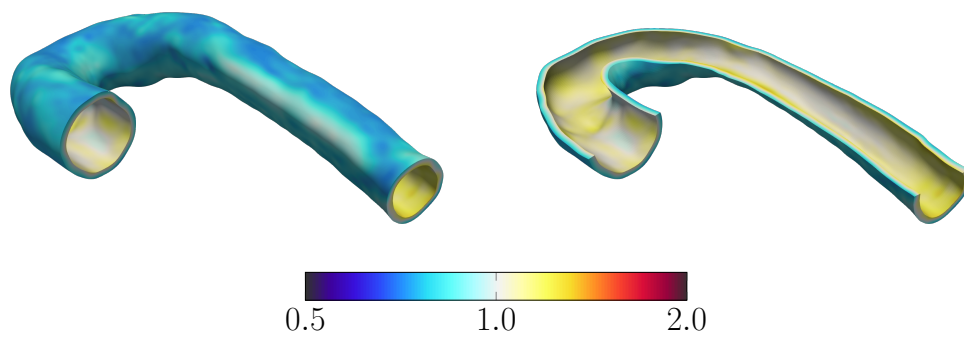


Figure 4.36: Radial stretch stretch from converged  $\mathbf{X}_0^e$  and  $\mathbf{X}_{\text{REF}}$ . The whole domain (*left*) and the clipped view (*right*)

## Chapter 5

### IPBZSS Estimation

With the results obtained in Chapter 4, the EBZSS process imposes modifications on element-based control points, and it was succeeded with geometries without branches. For more complex geometries, the EBZSS with control mesh complexity has convergence difficulty as abovementioned in Section 4.4.

The objective of this chapter is to impose integration-point-based strain using the components of its metric tensor. The method which is introduced in this chapter tries to directly impose the residual strain at each integration point, which is on the physical position on the geometry, instead of element-based control points. This is the reason why the new ZSS is called IPBZSS. Metric tensors with the natural coordinate system, which are introduced in Chapter 2, are effective ways to describe geometrical information without its control mesh.

In particular to the ZSS initial guess, the ZSS is based on an inner-surface geometry and its design parameters. Therefore, how to extend the information to the radial direction is needed. With the method, conversion between T-spline and Bézier representations is not needed. To show how the new method for estimating the ZSS performs, a 3D test computation with a Y-shaped tube is first presented. Then, the 3D computation where the target geometry is coming from medical images of a human aorta, which includes branches is presented.

The IPBZSS concept for the EBTL method is introduced in Section 5.1, The ZSS initial guess modeling based on the shell model is introduced in Section 5.2. The numerical examples are presented in Section 5.3. Finally, the concluding remarks are presented in Section 5.4. Most of the works in this chapter are already published in [101].

## 5.1 EBTL method with IPBZSS

In this section, the EBTL method with IPBZSS is introduced instead of by using the EBZSS. The IPBZSS can be converted from the EBZSS, so the conversions between the EBZSS and the IPBZSS are also introduced here.

### 5.1.1 IPBZSS

The key idea behind the EBZSS method was that, due to the objectivity, all the quantities seen in Eq. (2.84) can be computed with any orientations of the ZSS. The way  $\mathbf{X}_0^e$  can be extended to integration-point counterpart of  $\mathbf{X}_0^e$ . The manipulation is worked with the reference domain. With the reference Jacobian

$$J_{\text{REF}} = \det\left(\frac{\partial \mathbf{X}_{\text{REF}}}{\partial \mathbf{X}_0}\right), \quad (5.1)$$

Eq. (2.84) can be rearranged as

$$\int_{\Omega_{\text{REF}}} \mathbf{w} \cdot \rho_0 \mathbf{a} J_{\text{REF}}^{-1} d\Omega + \int_{\Omega_{\text{REF}}} \delta \mathbf{E} : \mathbf{S} J_{\text{REF}}^{-1} d\Omega - \int_{\Omega_{\text{REF}}} \mathbf{w} \cdot \rho_0 \mathbf{f} J_{\text{REF}}^{-1} d\Omega = \int_{(\Gamma_t)_h} \mathbf{w} \cdot \mathbf{h} d\Gamma. \quad (5.2)$$

In this implementation at first, the Jacobian in Eq. (2.18), can be also expressed as

$$J^2 = \det \mathbf{C}. \quad (5.3)$$

The  $\det \mathbf{C}$  is described by using the natural coordinates as,

$$\det \mathbf{C} = \frac{\det [g_{IJ}]}{\det [G_{IJ}]}, \quad (5.4)$$

and from that

$$J = \left( \frac{\det [g_{IJ}]}{\det [G_{IJ}]} \right)^{\frac{1}{2}}, \quad (5.5)$$

is obtained. With Eq. (5.5),  $\mathbf{g}_I$  is replaced to  $(\mathbf{G}_{\text{REF}})_I$  and an alternative expression is given by Eq. (5.1):

$$J_{\text{REF}} = \left( \frac{\det [(G_{\text{REF}})_{IJ}]}{\det [G_{IJ}]} \right)^{\frac{1}{2}}. \quad (5.6)$$

Eq. (2.6) can be rewritten with the contravariant basis vectors as

$$\mathbf{E} = \frac{1}{2} (g_{IJ} - G_{IJ}) \mathbf{G}^I \mathbf{G}^J. \quad (5.7)$$

The stress tensor  $\mathbf{S}$  can be expressed with the covariant basis vectors as

$$\mathbf{S} = S^{IJ} \mathbf{G}_I \mathbf{G}_J, \quad (5.8)$$

where  $S^{IJ}$  can be expressed with the components of the metric tensors. Thus, the inner product  $\delta \mathbf{E} : \mathbf{S}$ , and all the other quantities, in the weak form given by Eq. (5.2) can be evaluated without actually using the basis vectors  $\mathbf{G}_I$  because  $\mathbf{E}$  is described with contravariant basis vectors, and  $\mathbf{S}$  is described with covariant basis vectors. This justifies using  $(G_{IJ})_k$  as the integration-point counterpart of  $\mathbf{X}_0^e$ , with  $k = 1, \dots, n_{\text{int}}$ , where  $n_{\text{int}}$  is the number of integration points. Note that  $G_{IJ}$  is symmetric, and therefore the IPBZSS representation will in 3D have  $6 \times n_{\text{int}}$  parameters for each element.



### 5.1.2 EBZSS to IPBZSS

Converting the EBZSS representation to IPBZSS representation is straightforward. From given  $\mathbf{X}_0^e$  the covariant basis vectors at each integration point  $\xi_k$  can be calculated as:

$$(\mathbf{G}_I)_k = \left. \frac{\partial \mathbf{X}_0^e}{\partial \xi^I} \right|_{\xi=\xi_k}, \quad (5.9)$$

and the components of the metric tensor is obtained from Eq. (2.31).

### 5.1.3 IPBZSS to EBZSS

Converting the IPBZSS representation to EBZSS representation will, in general, not be exact because the IPBZSS has more parameters than the EBZSS. Given  $(G_{IJ})_k$ , a steady-state element-based problem (with  $\mathbf{f} = \mathbf{0}$  and  $\mathbf{h} = \mathbf{0}$ ) has to be solved:

$$\int_{\Omega_{\text{REF}}^e} \delta \mathbf{E} : \mathbf{S} J_{\text{REF}}^{-1} d\Omega = 0, \quad (5.10)$$

and the solution to that, in the form  $\mathbf{X}_{\text{REF}} + \mathbf{y}$ , will be the EBZSS representation. If the stress calculated from the solution is zero, then the conversion will be exact. Note that, to obtain a steady-state solution, to preclude translation and rigid-body rotation by imposing 6 appropriate constraints is required. To do that here three control points:  $A$ ,  $B$  and  $C$  are selected. All three components of  $\mathbf{y}_A$  is set to be zero and  $\mathbf{y}_B$  is constrained to be in the direction  $(\mathbf{X}_{\text{REF}})_B - (\mathbf{X}_{\text{REF}})_A$ . The last constraint is  $\mathbf{y}_C$  to be on the plane defined by the vector  $((\mathbf{X}_{\text{REF}})_B - (\mathbf{X}_{\text{REF}})_A) \times ((\mathbf{X}_{\text{REF}})_C - (\mathbf{X}_{\text{REF}})_A)$ .

### 5.1.4 An iterative method

Here it is assumed that there is a reasonably good initial guess for the IPBZSS (see Section 5.2). The iterative method below is used in calculating the IPBZSS that results in the target state associated with the given load. In the iterative method,  $\mathbf{F}$  is estimated from

the  $i^{\text{th}}$  solution. Simply,

$$\mathbf{F}^{i+1} = \mathbf{F}^i, \quad (5.11)$$

is assumed, and that means

$$\left(\mathbf{F}^{i+1}\right)^{-1} = \left(\mathbf{F}^i\right)^{-1}. \quad (5.12)$$

The inverse of the deformation gradient tensor from the  $i^{\text{th}}$  solution can be written as

$$\left(\mathbf{F}^i\right)^{-1} = \left(\mathbf{G}_I\right)^i \left(\mathbf{g}^I\right)^i. \quad (5.13)$$

Similarly, the inverse of the target deformation gradient tensor is

$$\left(\mathbf{F}^{i+1}\right)^{-1} = \left(\mathbf{G}_I\right)^{i+1} \left(\mathbf{G}_{\text{REF}}\right)^I. \quad (5.14)$$

Thus, the following equation is obtained:

$$\left(\mathbf{G}_K\right)^{i+1} \left(\mathbf{G}_{\text{REF}}\right)^K = \left(\mathbf{G}_K\right)^i \left(\mathbf{g}^K\right)^i. \quad (5.15)$$

Inner-producting both sides of this equation from the right with the covariant basis vectors corresponding to  $\mathbf{X}_{\text{REF}}$ ,

$$\left(\mathbf{G}_K\right)^{i+1} \left(\mathbf{G}_{\text{REF}}\right)^K \cdot \left(\mathbf{G}_{\text{REF}}\right)_I = \left(\mathbf{G}_K\right)^i \left(\mathbf{g}^K\right)^i \cdot \left(\mathbf{G}_{\text{REF}}\right)_I, \quad (5.16)$$

is obtained, and that results in

$$\left(\mathbf{G}_I\right)^{i+1} = \left(\mathbf{G}_K\right)^i \left(\mathbf{g}^K\right)^i \cdot \left(\mathbf{G}_{\text{REF}}\right)_I. \quad (5.17)$$

The components of the metric tensor are

$$(G_{IJ})^{i+1} = \left( (\mathbf{G}_K)^i (\mathbf{g}^K)^i \cdot (\mathbf{G}_{\text{REF}})_I \right) \cdot \left( (\mathbf{G}_L)^i (\mathbf{g}^L)^i \cdot (\mathbf{G}_{\text{REF}})_J \right). \quad (5.18)$$

Rearranging the terms,

$$(G_{IJ})^{i+1} = (G_{KL})^i \left( (\mathbf{g}^K)^i \cdot (\mathbf{G}_{\text{REF}})_I \right) \left( (\mathbf{g}^L)^i \cdot (\mathbf{G}_{\text{REF}})_J \right), \quad (5.19)$$

is obtained. Thus, the components of the metric tensor can be updated without actually knowing the orientation, which mean the basis vectors  $\mathbf{G}_I$ .

## 5.2 ZSS Initial guess based on the shell model of the artery

An analytical relationship between the ZS and reference states of straight-tube segments was given in [88]. The relationship is called “straight-tube ZSS template” in Chapter 4 and was extended to curved tubes. These were for the EBZSS. Here the IPBZSS is directly built instead of the EBZSS first. This is simpler because with the isogeometric discretization, especially with T-spline discretization, specifying conditions at integration points is far more straightforward than imposing conditions on control points.

The ZSS is built with the artery inner surface, which is what the medical images show. Typically, the wall thickness cannot be obtained from the medical image. Therefore the inner-surface mesh is first built with T-splines. Then a T-spline volume mesh is built by extruding the surface elements by an estimated thickness.

In this notation here,  $\mathbf{x}$  will now imply  $\mathbf{X}_{\text{REF}}$ , which is the target shape, and  $\mathbf{X}$  will imply  $\mathbf{X}_0$ . The method is explained in the context of one element in the thickness direction. Extending the method to multiple elements is straightforward.

### 5.2.1 Inner-surface coordinates in the target state

The coordinate system is similar to the one used for the shell modeling in [102]. Note that the “midsurface” of the shell formulation has been shifted to the inner surface here, and  $\bar{\bullet}$  indicates the inner surface. The basis vectors are

$$\bar{\mathbf{g}}_\alpha = \frac{\partial \bar{\mathbf{x}}}{\partial \xi^\alpha}, \quad (5.20)$$

where  $\alpha = 1, \dots, n_{\text{sd}} - 1$ , and the third direction is

$$\mathbf{n} = \frac{\bar{\mathbf{g}}_1 \times \bar{\mathbf{g}}_2}{\|\bar{\mathbf{g}}_1 \times \bar{\mathbf{g}}_2\|}. \quad (5.21)$$

The second fundamental form is defined as

$$\bar{b}_{\alpha\beta} = \frac{\partial \bar{\mathbf{g}}_\alpha}{\partial \xi^\beta} \cdot \mathbf{n}, \quad (5.22)$$

and the curvature tensor is

$$\hat{\mathbf{k}} = \underbrace{-\bar{b}_{\alpha\beta}}_{\hat{\kappa}_{\alpha\beta}} \bar{\mathbf{g}}^\alpha \bar{\mathbf{g}}^\beta. \quad (5.23)$$

Clearly,  $\hat{\mathbf{k}}$  is symmetric.

For a given unit vector  $\mathbf{t}$  on the surface, the curvature  $\hat{\kappa}$  is obtained as

$$\hat{\kappa} = \mathbf{t} \cdot \hat{\mathbf{k}} \cdot \mathbf{t}. \quad (5.24)$$

If  $\mathbf{t}$  is a principal direction,

$$\hat{\mathbf{k}} \cdot \mathbf{t} = \hat{\kappa} \mathbf{t}, \quad (5.25)$$

and  $\hat{k}$  is the corresponding principal curvature. The eigenvector can be expressed as

$$\mathbf{t} = t^\beta \bar{\mathbf{g}}_\beta. \quad (5.26)$$

Substituting this into Eq. (5.25) and inner-producting with  $\bar{\mathbf{g}}^\alpha$ ,

$$\bar{g}_{\gamma\alpha} (\hat{k}_{\bullet\beta}^\alpha - \hat{k} \delta_\beta^\alpha) t^\beta = 0, \quad (5.27)$$

is obtained, and the mixed components indicate

$$\hat{\mathbf{k}} = \hat{k}_{\bullet\beta}^\alpha \bar{\mathbf{g}}_\alpha \bar{\mathbf{g}}^\beta. \quad (5.28)$$

Since the inverse of  $[\bar{g}_{\gamma\alpha}]$  exists,

$$\det [\hat{k}_{\bullet\beta}^\alpha - \hat{k} \delta_\beta^\alpha] = 0, \quad (5.29)$$

where  $\hat{k}$  is an eigenvalue of the matrix defined by the mixed components  $\hat{k}_{\bullet\beta}^\alpha$ , and the two eigenvalues are called  $\hat{k}_1$  and  $\hat{k}_2$ . For  $\hat{k}_1 > \hat{k}_2$  the corresponding eigenvectors are obtained:

$$\mathbf{t}_1 = (t_1)^\beta \bar{\mathbf{g}}_\beta, \quad (5.30)$$

$$\mathbf{t}_2 = (t_2)^\beta \bar{\mathbf{g}}_\beta, \quad (5.31)$$

where  $\mathbf{t}_1$  and  $\mathbf{t}_2$  are unit vectors. From Eq. (5.25),

$$\hat{\mathbf{k}} \cdot \mathbf{t}_1 = \hat{k}_1 \mathbf{t}_1, \quad (5.32)$$

$$\hat{\mathbf{k}} \cdot \mathbf{t}_2 = \hat{k}_2 \mathbf{t}_2, \quad (5.33)$$

are described. Since  $\hat{\mathbf{k}}$  is symmetric,

$$\mathbf{t}_2 \cdot \hat{\mathbf{k}} \cdot \mathbf{t}_1 = \mathbf{t}_1 \cdot \hat{\mathbf{k}} \cdot \mathbf{t}_2. \quad (5.34)$$

Substituting Eqs. (5.32) and (5.33) into this,

$$\hat{\kappa}_1 \mathbf{t}_1 \cdot \mathbf{t}_2 = \hat{\kappa}_2 \mathbf{t}_1 \cdot \mathbf{t}_2, \quad (5.35)$$

are obtained. Thus, the two vectors are orthonormal, and the curvature tensor can be expressed as

$$\hat{\mathbf{k}} = \hat{\kappa}_1 \mathbf{t}_1 \mathbf{t}_1 + \hat{\kappa}_2 \mathbf{t}_2 \mathbf{t}_2. \quad (5.36)$$

When  $\hat{\kappa}_1 = \hat{\kappa}_2$ , an arbitrary orthonormal set of  $\mathbf{t}_1$  and  $\mathbf{t}_2$  can be used in the above equation.

### 5.2.2 Inner-surface coordinates in the ZSS

Since the principal curvature directions  $\mathbf{t}_1$  and  $\mathbf{t}_2$  of the target shape are orthogonal to each other, the ZSS shape can be built using those directions. The basis vectors on the inner surface in the ZSS are

$$\bar{\mathbf{G}}_\alpha = \frac{\partial \bar{\mathbf{X}}}{\partial \xi^\alpha}, \quad (5.37)$$

and the third direction is

$$\mathbf{N} = \frac{\bar{\mathbf{G}}_1 \times \bar{\mathbf{G}}_2}{\|\bar{\mathbf{G}}_1 \times \bar{\mathbf{G}}_2\|}. \quad (5.38)$$

The stretches corresponding to those directions will be  $\hat{\lambda}_1$  and  $\hat{\lambda}_2$ . Then the ZSS basis vectors are calculated from

$$\hat{\lambda}_1 \mathbf{t}_1 = \mathbf{F} \cdot \mathbf{t}_1, \quad (5.39)$$

$$\hat{\lambda}_2 \mathbf{t}_2 = \mathbf{F} \cdot \mathbf{t}_2. \quad (5.40)$$

That is

$$\hat{\lambda}_1 \mathbf{F}^{-1} \cdot \mathbf{t}_1 = \mathbf{t}_1, \quad (5.41)$$

$$\hat{\lambda}_2 \mathbf{F}^{-1} \cdot \mathbf{t}_2 = \mathbf{t}_2. \quad (5.42)$$

Because the third direction is orthogonal to  $\mathbf{t}_1$  and  $\mathbf{t}_2$ , these equations can be reduced to

$$\hat{\lambda}_1 \bar{\mathbf{G}}_\beta \bar{\mathbf{g}}^\beta \cdot \mathbf{t}_1 = \mathbf{t}_1, \quad (5.43)$$

$$\hat{\lambda}_2 \bar{\mathbf{G}}_\beta \bar{\mathbf{g}}^\beta \cdot \mathbf{t}_2 = \mathbf{t}_2. \quad (5.44)$$

Substituting Eqs. (5.30) and (5.31) into these,

$$\hat{\lambda}_1 (t_1)^\alpha \bar{\mathbf{G}}_\alpha = (t_1)^\alpha \bar{\mathbf{g}}_\alpha, \quad (5.45)$$

$$\hat{\lambda}_2 (t_2)^\alpha \bar{\mathbf{G}}_\alpha = (t_2)^\alpha \bar{\mathbf{g}}_\alpha, \quad (5.46)$$

are obtained. This can also be written as

$$\begin{bmatrix} \hat{\lambda}_1 & 0 \\ 0 & \hat{\lambda}_2 \end{bmatrix} \begin{bmatrix} (t_1)^1 & (t_1)^2 \\ (t_2)^1 & (t_2)^2 \end{bmatrix} \begin{bmatrix} \bar{\mathbf{G}}_1 \\ \bar{\mathbf{G}}_2 \end{bmatrix} = \begin{bmatrix} (t_1)^1 & (t_1)^2 \\ (t_2)^1 & (t_2)^2 \end{bmatrix} \begin{bmatrix} \bar{\mathbf{g}}_1 \\ \bar{\mathbf{g}}_2 \end{bmatrix}, \quad (5.47)$$

and from that the basis vectors is calculated as

$$\begin{bmatrix} \bar{\mathbf{G}}_1 \\ \bar{\mathbf{G}}_2 \end{bmatrix} = \begin{bmatrix} (t_1)^1 & (t_1)^2 \\ (t_2)^1 & (t_2)^2 \end{bmatrix}^{-1} \begin{bmatrix} \frac{1}{\lambda_1} & 0 \\ 0 & \frac{1}{\lambda_2} \end{bmatrix} \begin{bmatrix} (t_1)^1 & (t_1)^2 \\ (t_2)^1 & (t_2)^2 \end{bmatrix} \begin{bmatrix} \bar{\mathbf{g}}_1 \\ \bar{\mathbf{g}}_2 \end{bmatrix}. \quad (5.48)$$

### 5.2.3 Wall coordinates in the target state

The position in the target configuration is

$$\mathbf{x} = \bar{\mathbf{x}} + \mathbf{n}\vartheta, \quad (5.49)$$

where  $0 \leq \vartheta \leq h_{\text{th}}$ , and  $h_{\text{th}}$  is the wall thickness in the target configuration. The basis vectors will vary along the thickness direction as

$$\mathbf{g}_\alpha = \frac{\partial \mathbf{x}}{\partial \xi^\alpha} \quad (5.50)$$

$$= \bar{\mathbf{g}}_\alpha + \frac{\partial \mathbf{n}}{\partial \xi^\alpha} \vartheta \quad (5.51)$$

$$= \bar{\mathbf{g}}_\alpha - \bar{b}_{\alpha\gamma} \bar{\mathbf{g}}^\gamma \vartheta. \quad (5.52)$$

The third coordinate is mapped as

$$\vartheta = \frac{1 + \xi^3}{2} h_{\text{th}}, \quad (5.53)$$

where  $-1 \leq \xi^3 \leq 1$ . The basis vector in the third direction is constant as

$$\mathbf{g}_3 = \frac{h_{\text{th}}}{2} \mathbf{n}, \quad (5.54)$$

and

$$\mathbf{g}^3 = \frac{2}{h_{\text{th}}} \mathbf{n}. \quad (5.55)$$



With that, the components of the metric tensor are

$$g_{\alpha\beta} = \bar{g}_{\alpha\beta} - 2\bar{b}_{\alpha\beta}\vartheta + \bar{b}_{\alpha\gamma}\bar{g}^{\gamma\delta}\bar{b}_{\beta\delta}\vartheta^2, \quad (5.56)$$

$$g_{3\alpha} = 0, \quad (5.57)$$

$$g_{\alpha 3} = 0, \quad (5.58)$$

$$g_{33} = \frac{h_{\text{th}}^2}{4}. \quad (5.59)$$

#### 5.2.4 Wall coordinates in the ZSS

The position in the ZSS configuration is

$$\mathbf{X} = \bar{\mathbf{X}} + \mathbf{N}\vartheta_0, \quad (5.60)$$

where  $0 \leq \vartheta_0 \leq (h_{\text{th}})_0$ , and  $(h_{\text{th}})_0$  is the wall thickness in the ZSS configuration. The basis vectors will vary along the thickness direction as

$$\mathbf{G}_\alpha = \frac{\partial \mathbf{X}}{\partial \xi^\alpha} \quad (5.61)$$

$$= \bar{\mathbf{G}}_\alpha + \frac{\partial \mathbf{N}}{\partial \xi^\alpha} \vartheta_0 \quad (5.62)$$

$$= \bar{\mathbf{G}}_\alpha - \bar{B}_{\alpha\gamma} \bar{\mathbf{G}}^\gamma \vartheta_0. \quad (5.63)$$

The curvature tensor in the ZSS configuration is

$$\hat{\boldsymbol{\kappa}}_0 = (\hat{\kappa}_0)_1 \mathbf{t}_1 \mathbf{t}_1 + (\hat{\kappa}_0)_2 \mathbf{t}_2 \mathbf{t}_2. \quad (5.64)$$

From that,

$$\bar{B}_{\alpha\beta} = -\hat{\boldsymbol{\kappa}}_0 : \bar{\mathbf{G}}_\alpha \bar{\mathbf{G}}_\beta \quad (5.65)$$

$$= -(\hat{\kappa}_0)_1 (\mathbf{t}_1 \cdot \bar{\mathbf{G}}_\alpha) (\mathbf{t}_1 \cdot \bar{\mathbf{G}}_\beta) - (\hat{\kappa}_0)_2 (\mathbf{t}_2 \cdot \bar{\mathbf{G}}_\alpha) (\mathbf{t}_2 \cdot \bar{\mathbf{G}}_\beta). \quad (5.66)$$

Similar to what we had for  $\mathbf{t}_1$  and  $\mathbf{t}_2$ ,

$$\lambda_3 \mathbf{F}^{-1} \cdot \mathbf{n} = \mathbf{n}, \quad (5.67)$$

which becomes

$$\lambda_3 \mathbf{G}_3 \mathbf{g}^3 \cdot \mathbf{n} = \mathbf{n}. \quad (5.68)$$

Eq. (5.55) is substituted into this and

$$\mathbf{G}_3 = \frac{h_{\text{th}}}{2\lambda_3} \mathbf{n}, \quad (5.69)$$

and

$$\mathbf{G}^3 = \frac{2\lambda_3}{h_{\text{th}}} \mathbf{n}, \quad (5.70)$$

are obtained.

### 5.2.5 Calculating the components of the ZSS metric tensor at each integration point

For an integration point  $\xi$ , the components of the metric tensor can be obtained as

$$G_{\alpha\beta} = \bar{G}_{\alpha\beta} - 2\bar{B}_{\alpha\beta}\vartheta_0 + \bar{B}_{\alpha\gamma}\bar{G}^{\gamma\delta}\bar{B}_{\beta\delta}\vartheta_0^2, \quad (5.71)$$

$$G_{3\alpha} = 0, \quad (5.72)$$

$$G_{\alpha 3} = 0, \quad (5.73)$$

$$G_{33} = \frac{h_{\text{th}}^2}{4\lambda_3^2}. \quad (5.74)$$

The third coordinate can be obtained from

$$\vartheta_0 = \int_{-1}^{\xi^3} \frac{h_{\text{th}}}{2\lambda_3} d\xi^3. \quad (5.75)$$

Assuming incompressible material,  $J = 1$ ,

$$\lambda_3 = \frac{A_0}{A}, \quad (5.76)$$

where

$$A^2 = \det [g_{\alpha\beta}], \quad (5.77)$$

$$A_0^2 = \det [G_{\alpha\beta}]. \quad (5.78)$$

The components of the matrix tensors are given by Eqs. (5.56) and (5.71).

### 5.2.6 Design of the ZSS

The design parameters are the principal curvatures  $(\hat{\kappa}_0)_1$  and  $(\hat{\kappa}_0)_2$ , and the stretches  $\hat{\lambda}_1$  and  $\hat{\lambda}_2$  for each principal curvature direction. Those parameters can be determined from given shape parameters of the target configuration, especially  $\hat{\kappa}_1$ ,  $\hat{\kappa}_2$ ,  $h_{\text{th}}$ , and its basis vectors.

As proposed in Chapter 4, the two principal directions are seen as circumferential and longitudinal directions, and  $\hat{\kappa}_1$  is in the circumferential direction, giving

$$(\hat{\kappa}_0)_1 = \frac{2\pi - \phi}{2\pi} \hat{\kappa}_1. \quad (5.79)$$

Here  $\phi$  is the opening angle, which is seen after a longitudinal cut, based on artery experimental data [16]. The stretch in that direction,  $\hat{\lambda}_1$ , corresponds to  $\lambda_\theta$  in Chapter 4 and that is determined from the 2D computations in Chapter 4. It is assumed that in the longitudinal direction the ZSS configuration has zero curvature,  $(\hat{\kappa}_0)_2 = 0$ . The stretch

in that direction,  $\hat{\lambda}_2$ , corresponds to  $\lambda_z$  in Chapter 4. If at an integration point  $\hat{k}_2 \approx \hat{k}_1$ ,  $(\hat{k}_0)_2 = (\hat{k}_0)_1$  and  $\hat{\lambda}_2 = \hat{\lambda}_1$  are set. That makes the assignment of the principal directions less consequential. Thus, including wall coordinates, there are given shape parameters  $\hat{k}_1$ ,  $\hat{k}_2$ ,  $h_{th}$ , and the basis vectors, and given ZSS design parameters  $\hat{\lambda}_1$ ,  $\hat{\lambda}_2$  and  $\phi$ , then other design parameters  $(\hat{k}_0)_1$  and  $(\hat{k}_0)_2$  are calculated.

### 5.3 Numerical examples

In the numerical examples The Fung's model described in Section 2.9 is used with  $D_1 = 2.6447 \times 10^3$  Pa,  $D_2 = 8.365$ , and the Poisson's ratio  $\nu = 0.45$ . The pressure associated with the target shape is assumed as 92 mm Hg.

The initial guess for the iterations is determined as described in Section 5.2, with  $\phi = \frac{5}{2}\pi$  and  $\hat{\lambda}_2 = 1.05$ . After the iterations, explained in Section 5.1.4, for comparison purposes, the IPBZSS representation is converted to EBZSS representation, with the method described in Section 5.1.3. With the EBZSS,  $\mathbf{y}$  is computed again, and compare that to the IPBZSS.

#### 5.3.1 Y-shaped tube

The target state of the Y-shaped tube is shown in Figure 5.1. The end diameters of the tube are 20, 14 and 10 mm. Figure 5.2 shows the T-spline mesh. The mesh is based on a mixture of cubic and quartic T-splines. The wall thickness distribution is smooth, outcome of solving the Laplace's equation over the inner surface, with Dirichlet boundary conditions at the tube ends [39], where the value specified is 0.1 times the end diameter. Figure 5.3 shows the thickness distribution. The volume mesh is built with one element (cubic Bézier element) in the thickness direction. The number of control points and elements are 5,180 and 2,592. Since the IPBZSS cannot be visualized, the EBZSS representation is used for that. Figure 5.4 shows the initial guess for the IPBZSS. Figure 5.5 shows an element in the target state and the corresponding IPBZSS initial guess.

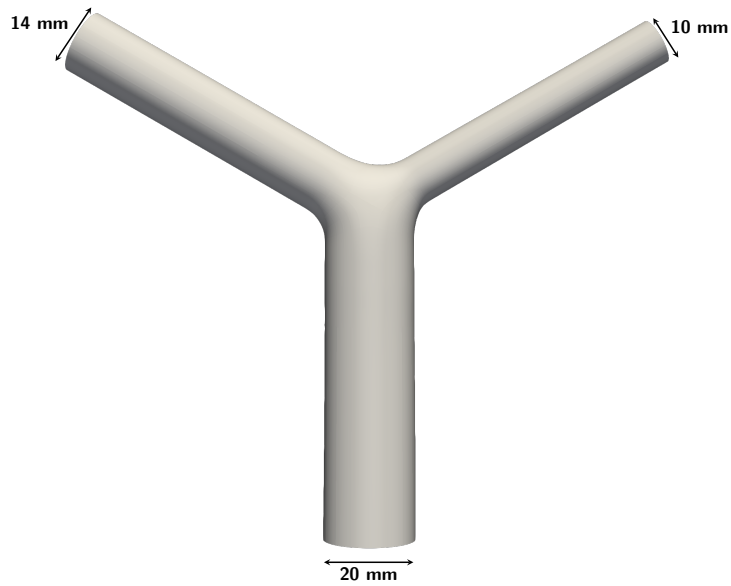


Figure 5.1: Y-shaped tube. Target state. The end diameters are 20, 14 and 10 mm

The IPBZSS is iterated to be converged with the method in Section 5.1.4. Figure 5.6 shows  $\|\mathbf{y}\|$  computed from that. The maximum value of  $\|\mathbf{y}\|$  is  $1.279 \times 10^{-14}$  mm. Figures 5.7 and 5.8 shows the principal stretches, computed from the IPBZSS initial guess and from the converged IPBZSS. The converged IPBZSS element is shown in Figure 5.9. Figure 5.9 shows that the opening angle and the longitudinal stretch do not change much between the IPBZSS initial guess (see the left one in Figure 5.5) and the converted IPBZSS. However, the circumferential stretches are somewhat different. The initial guess for the circumferential stretch was based on the 2D computations reported in Chapter 4. Alternatively, the stretch can be estimated by an analytical solution, similar to the one described in [102].

Displacement  $\mathbf{y}$  is also computed after converting the converged IPBZSS to EBZSS. Figure 5.10 shows  $\|\mathbf{y}\|$  computed that way. The maximum value of  $\|\mathbf{y}\|$  is  $1.626 \times 10^{-2}$  mm. Figure 5.11 shows the maximum principal stretch. There is no visible difference between the strains obtained from the IPBZSS directly (see Figure 5.7) and after conversion to

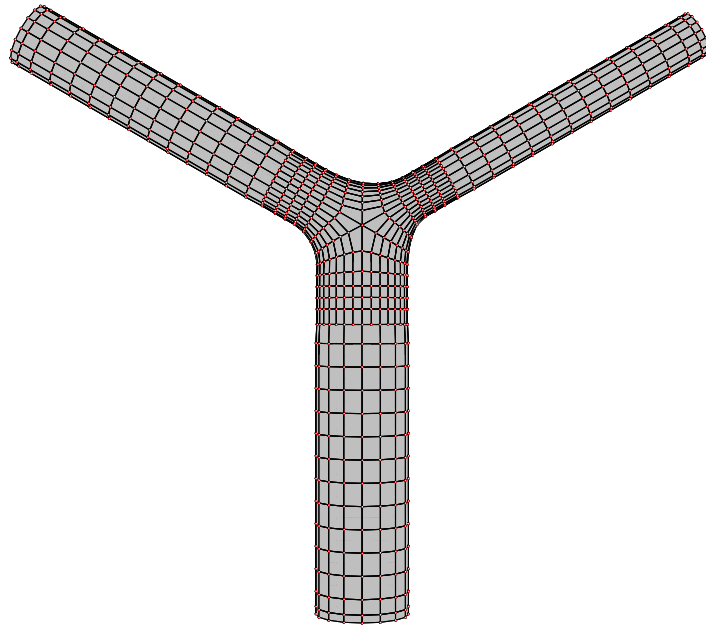


Figure 5.2: Y-shaped tube. Mesh made of cubic and quartic T-splines. *Red* circles represent the control points. The parts with the quartic T-splines, obtained by order elevation, are around the two extraordinary points, each connected to six edges

EBZSS (see Figure 5.11) .

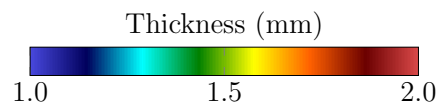
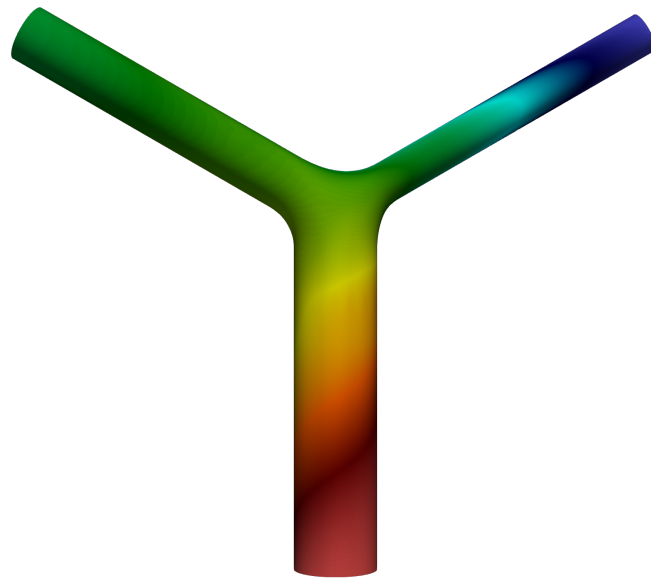


Figure 5.3: Y-shaped tube. Wall thickness distribution

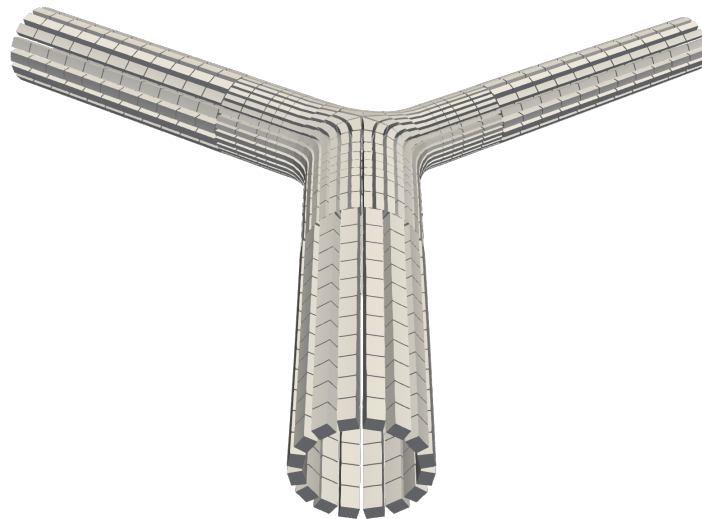


Figure 5.4: Y-shaped tube. The IPBZSS initial guess, shown using the EBZSS representation

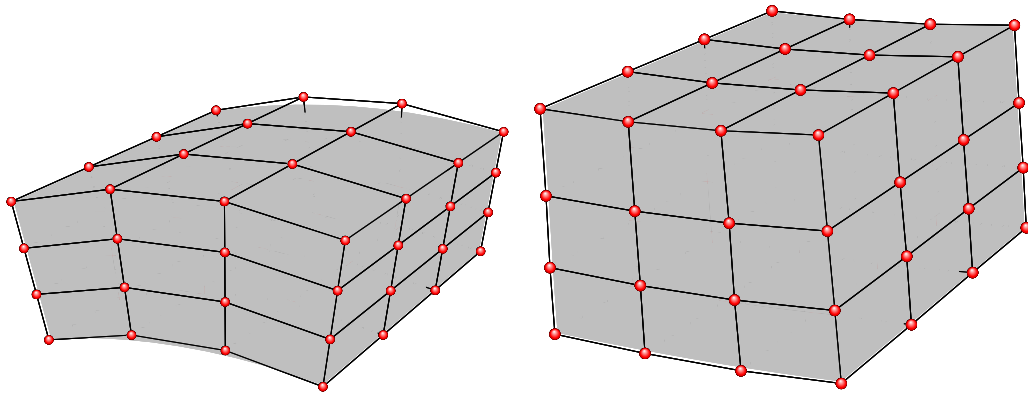


Figure 5.5: Y-shaped tube. An element in the target state (*left*) and the corresponding IPBZSS initial guess, shown using the EBZSS representation (*right*)

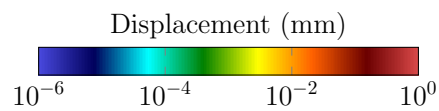
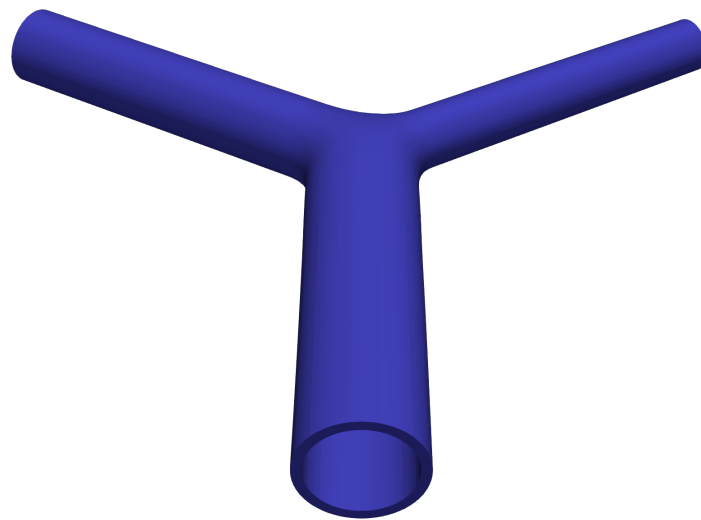


Figure 5.6: Y-shaped tube. Colored by  $\|\mathbf{y}\|$  computed from the converged IPBZSS



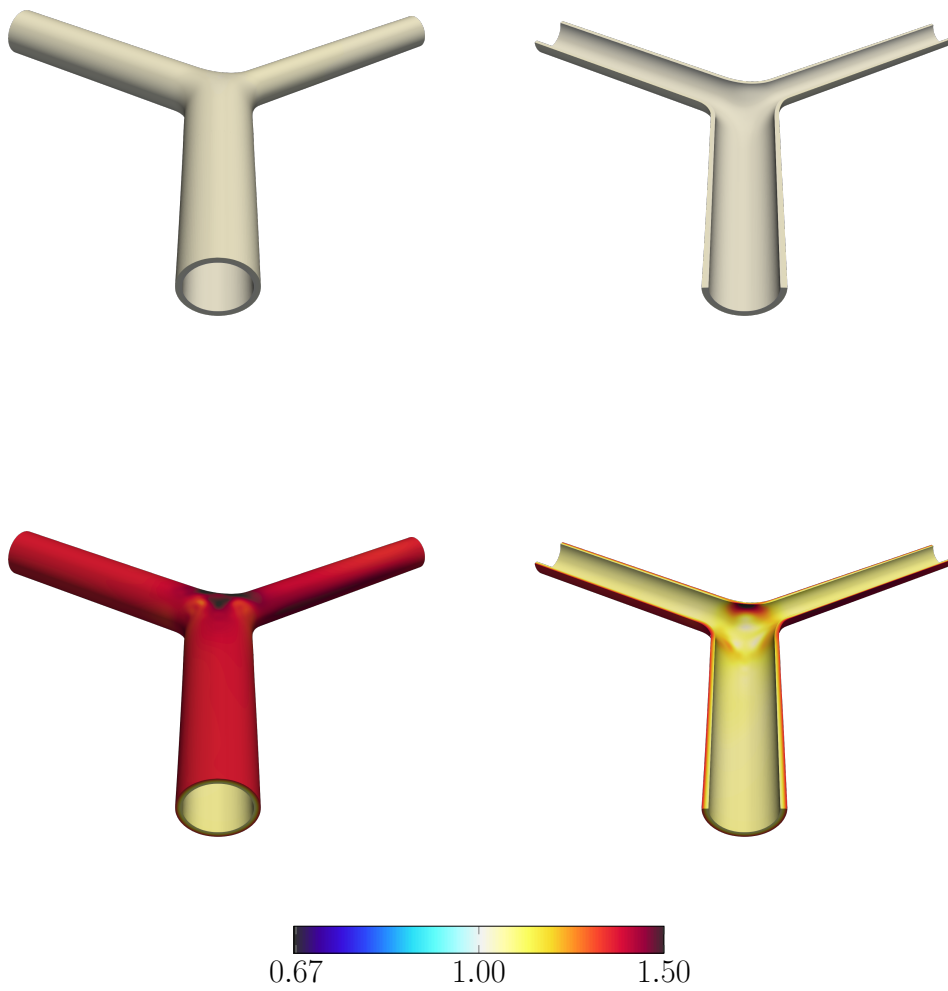


Figure 5.7: Y-shaped tube. The maximum principal stretch, from the IPBZSS initial guess (*top*) and from the converged IPBZSS (*bottom*). Whole elements (*left*) and the clipped view (*right*)

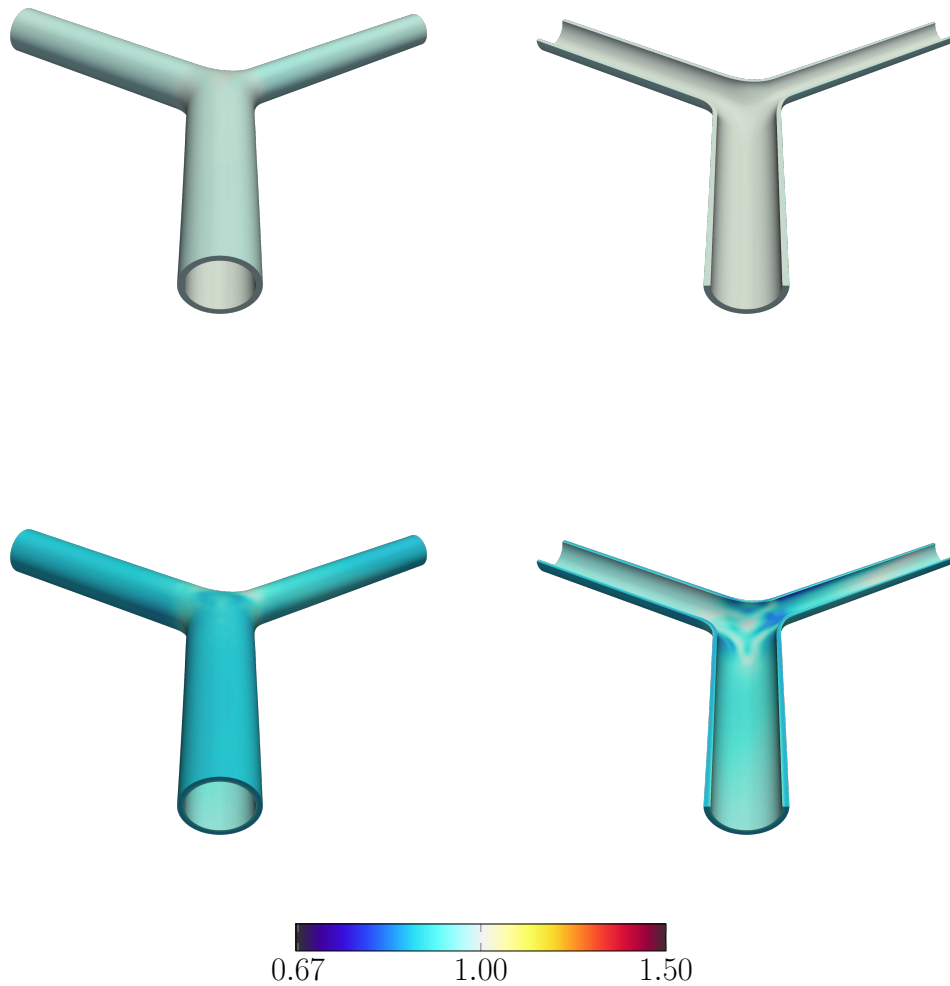


Figure 5.8: Y-shaped tube. The minimum principal stretch, from the IPBZSS initial guess (*top*) and from the converged IPBZSS (*bottom*). Whole elements (*left*) and the clipped view (*right*)

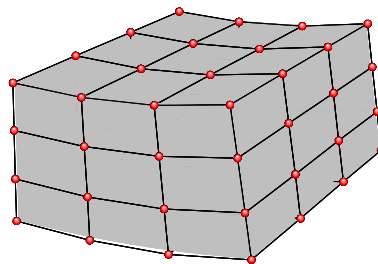


Figure 5.9: Y-shaped tube. The converged IPBZSS element corresponding to the element in Figure 5.5, shown using the EBZSS representation

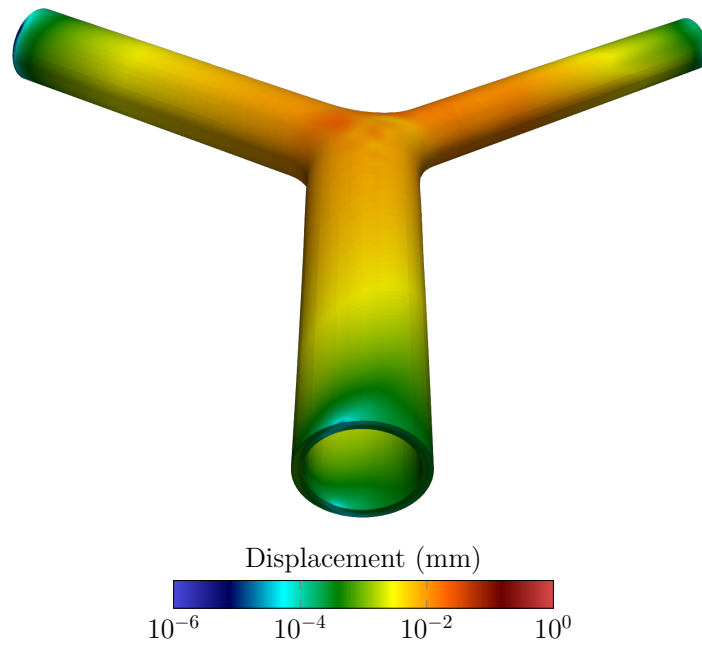


Figure 5.10: Y-shaped tube. Colored by  $\|y\|$  computed after converting the converged IPBZSS to EBZSS

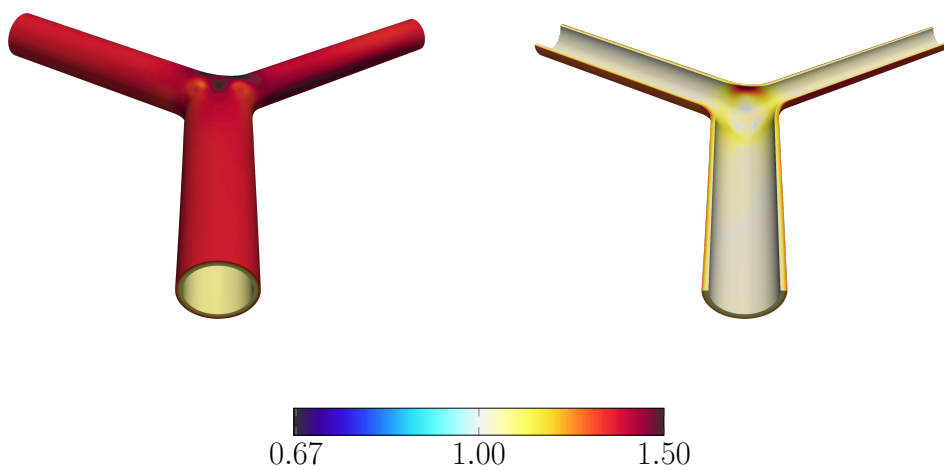


Figure 5.11: Y-shaped tube. The maximum principal stretch, obtained after converting the converged IPBZSS to EBZSS. Whole geometry (*left*) and clipped view (*right*)

### 5.3.2 Patient-specific aorta geometry

The target state of the patient-specific geometry and the T-spline mesh are shown in Figure 5.12. The inlet diameter is about 25 mm. The wall thickness distribution is smooth,

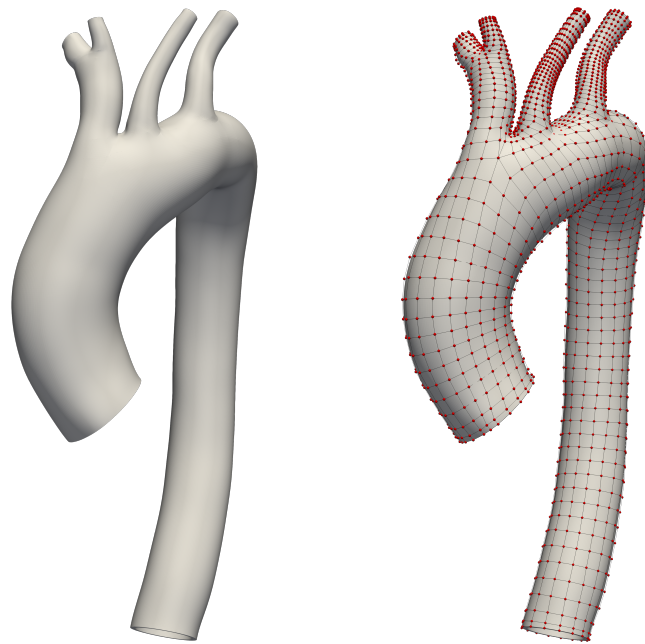


Figure 5.12: Patient-specific aorta geometry. Target state, extracted from medical images (*left*). The inlet diameter is about 25 mm. Mesh made of cubic and quartic T-splines (*right*). Red circles represent the control points. The parts with the quartic T-splines, obtained by order elevation [98], are around the eight extraordinary points

outcome of solving the Laplace's equation over the inner surface, with Dirichlet boundary conditions at the tube ends [39], where the value specified is 0.08 times the end diameter. In some parts of the branched area the thickness exceeds the radius of curvature, and there we reduce the thickness to 0.8 times the radius of curvature. Figure 5.13 shows the thickness distribution. The volume mesh is built again with one element (cubic Bézier element) in the thickness direction. The number of control points and elements are 9,244 and 4,360.

Figure 5.14 shows the initial guess for the IPBZSS. The IPBZSS is iterated to be

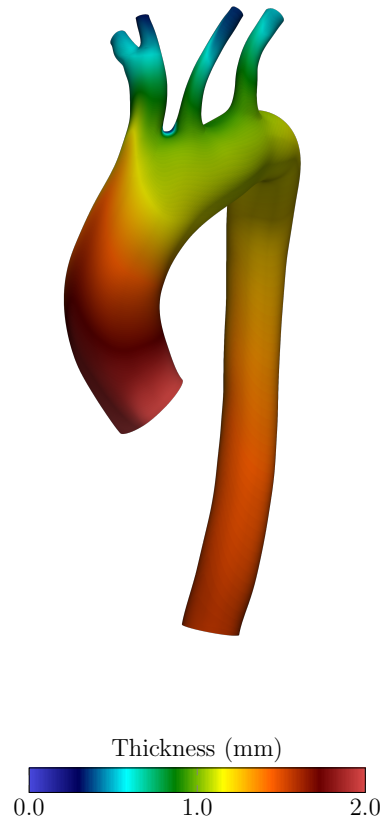


Figure 5.13: Patient-specific aorta geometry. Wall thickness distribution

converged with the method in Section 5.1.4. Figure 5.15 shows  $\|\mathbf{y}\|$  computed from that. The maximum value of  $\|\mathbf{y}\|$  is  $1.163 \times 10^{-13}$  mm. Figures 5.16 and 5.17 shows the principal stretches, computed from the IPBZSS initial guess and from the converged IPBZSS.

Displacement  $\mathbf{y}$  is also computed after converting the converged IPBZSS to EBZSS. Figure 5.18 shows  $\|\mathbf{y}\|$  computed that way. The maximum value of  $\|\mathbf{y}\|$  is  $1.057 \times 10^{-1}$  mm. Figures 5.19 shows the maximum principal stretch. There is a visible difference at the region which has high stretch values between the strains obtained from the IPBZSS directly (see Figure 5.16) and after conversion to EBZSS (see Figure 5.19). However, the inclination of high or low stretch distribution can be recognized with the EBZSS. These results indicate that the EBZSS obtained by conversion from the IPBZSS is also a reasonable representation of the aorta ZSS, regarding observing the inclination of high or low stretch distribution. Moreover, as focusing on the stretch values, 4.0 is too high. Given that the

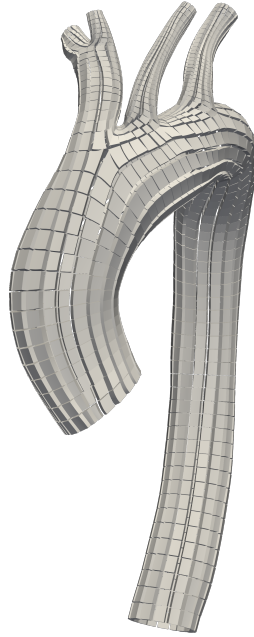


Figure 5.14: Patient-specific aorta geometry. The IPBZSS initial guess, shown using the EBZSS representation

comparison of the stretch values between the ZSS initial guess and the converged ZSS is far from Figures 5.16 and 5.17, the ZSS might be converged to unphysical solutions. From the result observation, the design of the ZSS initial guess is required to be modified for observing more anatomical conditions.

## 5.4 Concluding remarks

The objective of this chapter was to impose integration-point-based strain using the components of its metric tensor. That is called IPBZSS, especially the method is applied with T-spline representation for unstructured geometries such as branched points. The method which was introduced in this chapter tried to directly impose the residual strain at each integration point, which is on the physical position on the geometry, instead of element-based control points. In the EBTL method with IPBZSS, the conversion between IPBZSS

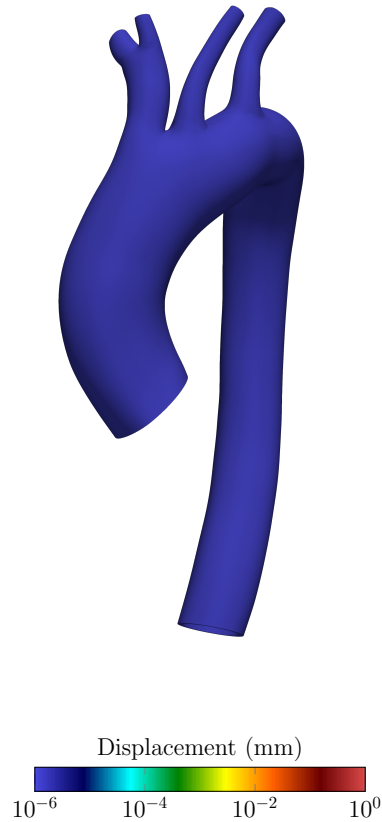


Figure 5.15: Patient-specific aorta geometry. Colored by  $\|\mathbf{y}\|$  computed from the converged IPBZSS

and EBZSS was also introduced. In particular to the ZSS initial guess, the ZSS is based on an inner-surface geometry and its design parameters. Therefore, the ZSS initial guess modeling based on the shell model was introduced.

3D test computations with a Y-shaped tube and patient-specific aorta geometry is coming from medical images resulted well convergence even at the branched points. This is the outcome of the IPBZSS. With the result of the EBZSS converted from the IPBZSS, the EBZSS is also a reasonable representation regarding observing the inclination of high or low stretch distribution. Here, two challenges remained. First, unphysical stretch values were observed at branched points of the patient-specific aorta geometry. Second, the ZSS initial guess was far from the converged ZSS: it means the anatomical ZSS design was not applied well on the converged ZSS. Given that these problems might be related each

other, more anatomical ZSS initial modeling could estimate more reasonable results.



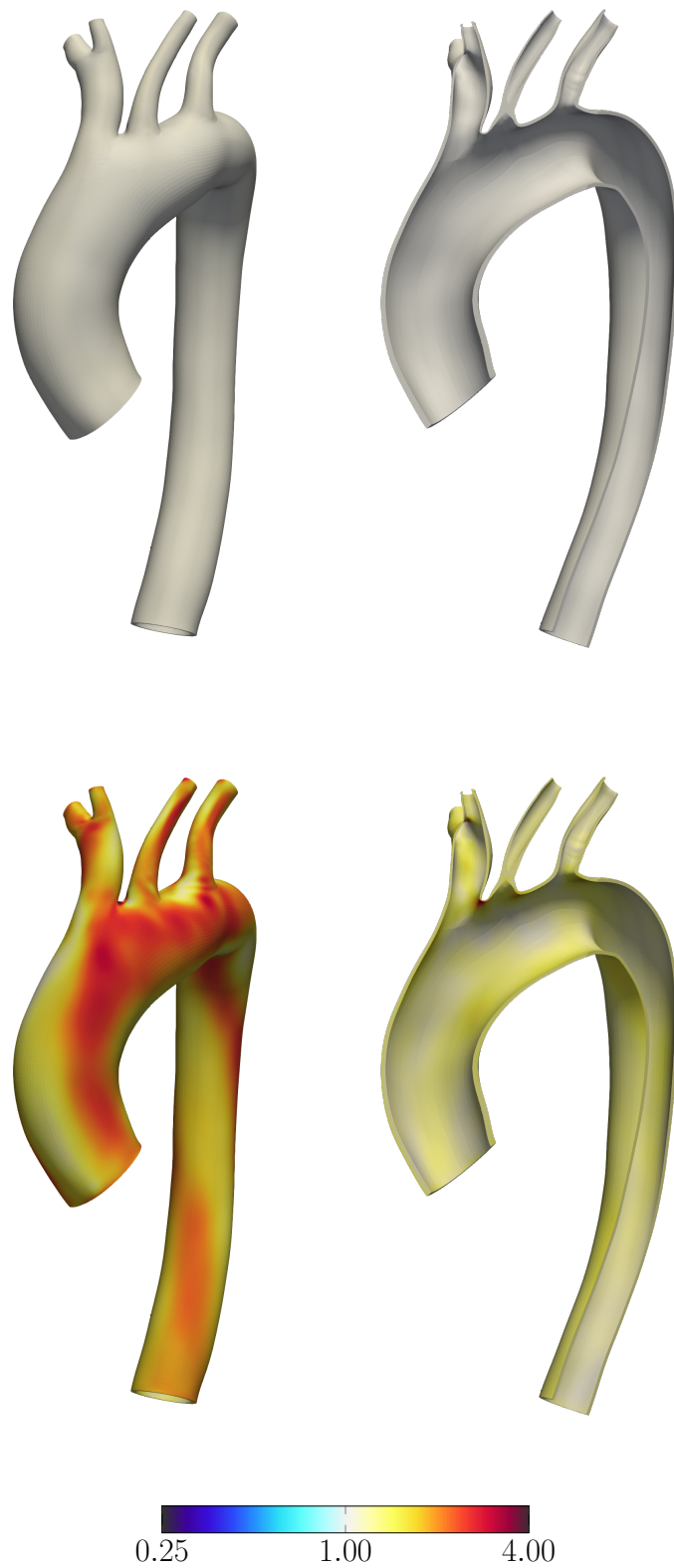


Figure 5.16: Patient-specific aorta geometry. The maximum principal stretch, from the IPBZSS initial guess (*top*) and from the converged IPBZSS (*bottom*) Whole elements (*left*) and the clipped view (*right*)

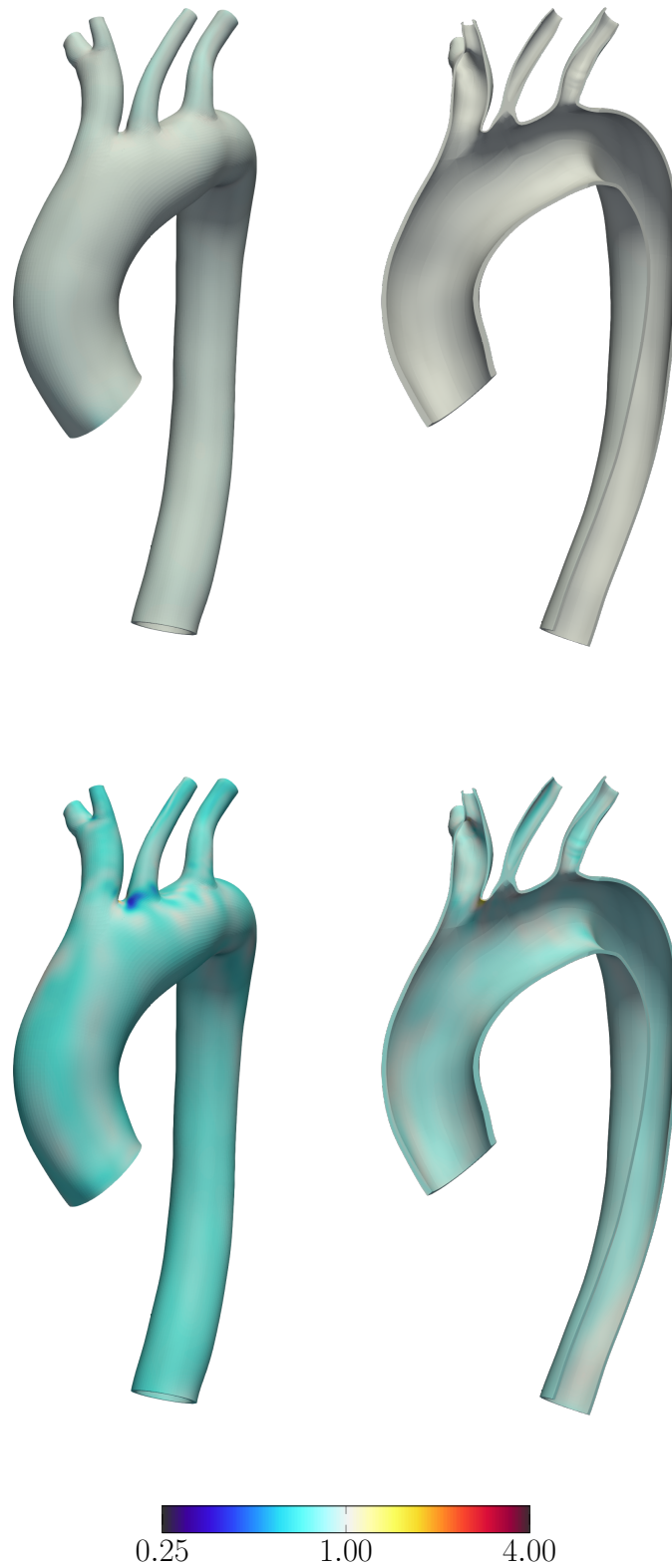


Figure 5.17: Patient-specific aorta geometry. The minimum principal stretch, from the IPBZSS initial guess (*top*) and from the converged IPBZSS (*bottom*) Whole elements (*left*) and the clipped view (*right*)

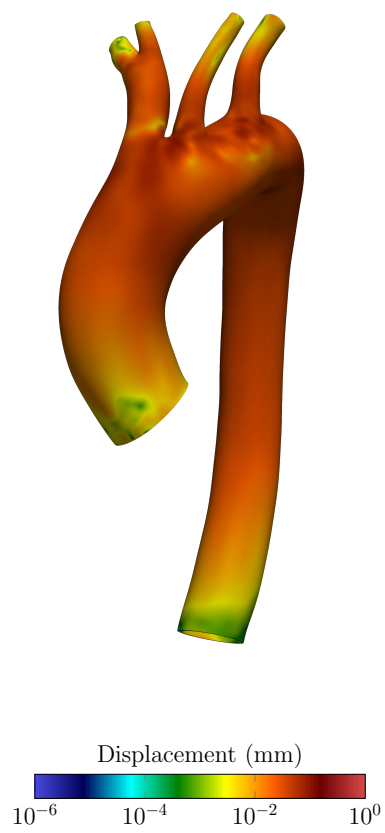


Figure 5.18: Patient-specific aorta geometry. Colored by  $\|y\|$  computed after converting the converged IPBZSS to EBZSS

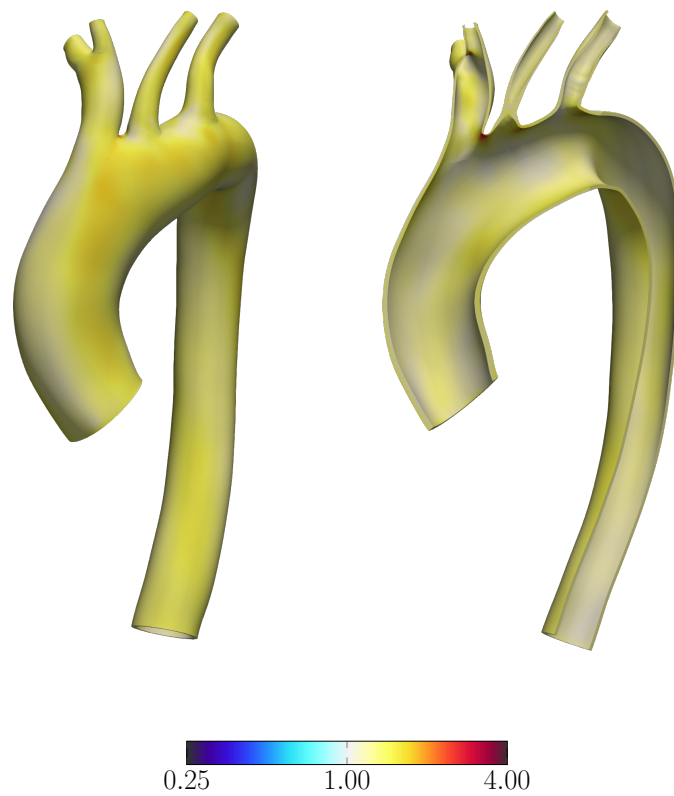


Figure 5.19: Patient-specific aorta geometry. The maximum principal stretch, obtained after converting the converged IPBZSS to EBZSS. Whole geometry (*left*) and clipped view (*right*)

## Chapter 6

### ZSS Estimation with Anatomical Observation

With the results obtained in Chapters 4 and 5, both the EBZSS and the IPBZSS have a challenge which is a gap between an initial-guess and converged solutions. That indicates the converged ZSS might not be based on anatomical observation even though the ZSS initial guess was defined based on the observation. Therefore, the objective of this chapter is to design the ZSS initial guess with analytical solutions of the force equilibrium. The force equilibrium in the normal direction is based on Kirchhoff–Love shell theory and the plane-stress condition, which gives proper constraints of the ZSS design parameters. Calculating the ZSS initial guess based on the analysis solution could improve estimation accuracy, and that makes converged ZSS reaching the ZSS target design quite well. In addition, given that a convergence difficulty is observed at the branched point which described in Chapter 5, an update of the wall coordinate system, which is introduced in Section 5.1, is required. To show how the new ZSS initial guess techniques perform, 3D test computations with straight-tube configurations are first presented. The computations also aim to observe the effects of the modified wall coordinate system. A Y-shaped tube computation is present to observe the perform at the branched points. Then, the 3D computation where the target geometry is coming from medical images of a human aorta is also presented. After how the method works is shown, the results are compared to the last results in Chapters 5.

The coordinate systems and mesh generation is introduced in Section 6.1. The ZSS initial guess based on the Kirchhoff–Love shell theory and the design strategies of the ZSS are introduced in Section 6.2. The numerical examples are presented in Section 6.3. The comparisons and discussions are given in Section 6.4. Finally, the concluding remarks

are presentend in Section 6.5. Most of the works in this chapter are already published in [103].

## **6.1 Coordinate systems for the artery inner surface and wall**

A geometrical relationship between the ZS and reference states, for a straight tube, was described in Chapter 5. It was based on the shell model, where it is assumed that the inner-surface elements are extruded in the normal direction. Here the method is extended to general parametrization in the computational space. A shell-like coordinate system is used specific to each integration point of the computational space, That coordinate system is explained later in this section, after explaining how the mesh is generated first.

In the notation here,  $\mathbf{x}$  will now imply  $\mathbf{X}_{\text{REF}}$ , which is the target shape, and  $\mathbf{X}$  will imply  $\mathbf{X}_0$  as same as the earlier chapters. The method is explained in the context of one element across the wall. Extending the method to multiple elements is straightforward.

### **6.1.1 Mesh generation**

As same as the previous methods, the artery inner surface is the first point of the process, and the wall is built in some fashion. Here a T-spline inner-surface mesh is first built. Then it is expanded with an estimated thickness to the outer surface. After that the outer-surface mesh manually modified by moving the control points, when the thickness is larger than the radius of curvature away from parts of the outer surface overlap. Because this might happen near the branches, a simple extrusion does not work at the point. Since the outer surface cannot be obtained from medical images, the design of the outer surface has to be based on other anatomical knowledge. This is the reason why currently meshes are generated manually rather than by an automated process. After defining the outer-surface mesh, which will have a control point corresponding to every control point on the inner surface, two control points are added for each pair. So the four control points are used to form a cubic Bézier element across the wall. This is the way that a T-spline volume mesh

is obtained.

### 6.1.2 Wall coordinates in the target state

The natural coordinate system is also applied to a target volume element. The position in the target state is  $\mathbf{x}(\boldsymbol{\xi})$ , and the total differential of the position is

$$d\mathbf{x} = \mathbf{g}_I d\xi^I. \quad (6.1)$$

Here coordinate  $\vartheta$  in a “normal” direction is defined as:

$$d\vartheta = \hat{\mathbf{n}} \cdot \mathbf{g}_I d\xi^I, \quad (6.2)$$

where  $\hat{\mathbf{n}}$  is the unit normal vector inside the wall. As the integration  $\int d\vartheta$  is performed, the difference between the inner and outer surfaces will be the formal definition of the thickness  $h_{\text{th}}$ . There are two options for defining the normal vector.

First option is that the closest point  $\bar{\mathbf{x}}^\perp$  on the inner surface is found from a given position  $\mathbf{x}$ :

$$\hat{\mathbf{n}}(\boldsymbol{\xi}) = \frac{\mathbf{x}(\boldsymbol{\xi}) - \bar{\mathbf{x}}^\perp}{\|\mathbf{x}(\boldsymbol{\xi}) - \bar{\mathbf{x}}^\perp\|}, \quad (6.3)$$

assuming a reasonable geometry for the purpose of calculating  $\hat{\mathbf{n}}$ . For  $\|\mathbf{x}(\boldsymbol{\xi}) - \bar{\mathbf{x}}^\perp\| = 0$ , Eq. (5.21) is obtained. Figure 6.1 shows the normal definition.

The second option is

$$\hat{\mathbf{n}}(\boldsymbol{\xi}) = \frac{\mathbf{g}_1 \times \mathbf{g}_2}{\|\mathbf{g}_1 \times \mathbf{g}_2\|}, \quad (6.4)$$

which naturally gives to Eq. (5.21) at the surface. Figure 6.2 shows the normal definition. The other two components of the new coordinate system is represented by the vector

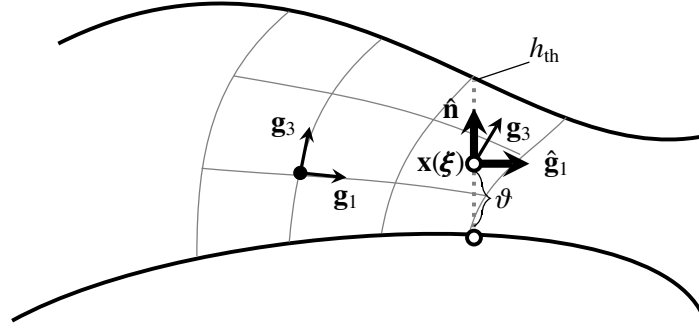


Figure 6.1: The coordinate system with the normal based on the closest point

$\hat{\xi} \in \mathbb{R}^{n_{sd}-1}$ , and the corresponding basis vectors are  $\hat{\mathbf{g}}_\alpha$ :

$$\hat{\mathbf{g}}_\alpha(\hat{\xi}(\xi), \vartheta(\xi)) = (\mathbf{I} - \hat{\mathbf{n}}(\xi)\hat{\mathbf{n}}(\xi)) \cdot \mathbf{g}_\alpha(\xi). \quad (6.5)$$

For the normal-vector definition of Eq. (6.4), it simplifies to

$$\hat{\mathbf{g}}_\alpha(\hat{\xi}(\xi), \vartheta(\xi)) = \mathbf{g}_\alpha(\xi). \quad (6.6)$$

Note that, even if  $\hat{\mathbf{g}}_\alpha = \mathbf{g}_\alpha$ ,  $\hat{\mathbf{g}}^\gamma$  and  $\mathbf{g}^\gamma$  are not the same in general, because  $\mathbf{g}_3$  is not perpendicular to  $\mathbf{g}_1$  and  $\mathbf{g}_2$  and  $\mathbf{g}^\gamma$  will have an out-of-plane component. The total differential of the position is expressed as

$$d\mathbf{x} = \hat{\mathbf{g}}_\alpha d\hat{\xi}^\alpha + \hat{\mathbf{n}} d\vartheta. \quad (6.7)$$

The first normal-vector option is closer to the shell theory. The second option does not suffer from that problem and gives us the possibility of coming up with an  $\hat{\mathbf{n}}$  design that would make the method better. However its quality depends on the mesh, such as the smoothness of the constant- $\xi^3$  surfaces.

At  $k$ th integration point a shell-like coordinate system is defined as

$$\mathbf{x}(\xi) = \hat{\mathbf{x}}(\hat{\xi}(\xi)) + \hat{\mathbf{n}}(\xi) (\vartheta - \vartheta_k), \quad (6.8)$$



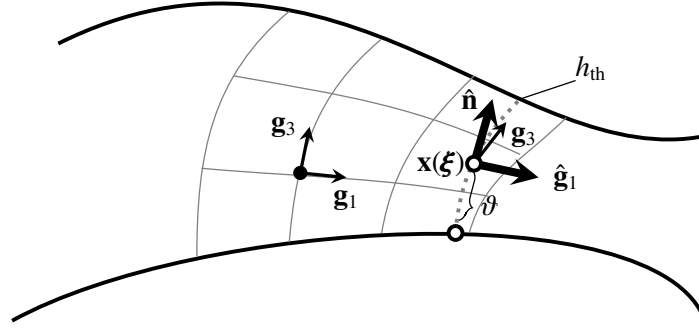


Figure 6.2: The coordinate system with the normal based on the two axis of the natural coordinates,  $\mathbf{g}_1$  and  $\mathbf{g}_2$

where  $\vartheta_k$  is an offset defined such that  $\mathbf{x}(\hat{\xi}(\hat{\xi}, 0))$  is  $\bar{\mathbf{x}}$  on the surface. To find the value, the following expression is used:

$$\vartheta_k = \|\mathbf{x}(\hat{\xi}_k) - \bar{\mathbf{x}}^\perp\|. \quad (6.9)$$

In generating the ZSS, for each integration point,  $h_{th}$  is calculated as

$$h_{th} = \|\mathbf{x}^\top - \mathbf{x}\| + \|\mathbf{x} - \bar{\mathbf{x}}^\perp\|, \quad (6.10)$$

where  $\mathbf{x}^\top$  is the closest point on the outer surface. By differentiating  $\mathbf{x}$  from Eq. (6.8) with respect to  $\hat{\xi}^\alpha$ , the covariant basis vectors along the thickness direction is obtained:

$$\hat{\mathbf{g}}_\alpha(\hat{\xi}, \vartheta) = \hat{\mathbf{g}}_\alpha|_{\vartheta_k} + \left. \frac{\partial \hat{\mathbf{n}}}{\partial \hat{\xi}^\alpha} \right|_{\xi(\hat{\xi}, \vartheta_k)} (\vartheta - \vartheta_k) \quad (6.11)$$

$$= \hat{\mathbf{g}}_\alpha|_{\vartheta_k} - \left( \hat{b}_{\alpha\gamma} \hat{\mathbf{g}}^\gamma \right) \Big|_{\vartheta_k} (\vartheta - \vartheta_k). \quad (6.12)$$

Here  $\hat{b}_{\alpha\gamma}$  is the second fundamental form:

$$\hat{b}_{\alpha\gamma}(\hat{\xi}, \vartheta) = \frac{\partial \hat{\mathbf{g}}_\alpha(\hat{\xi}, \vartheta)}{\partial \hat{\xi}^\gamma} \cdot \hat{\mathbf{n}}(\hat{\xi}(\hat{\xi}, \vartheta)), \quad (6.13)$$

which can be calculated by using the natural coordinates:

$$\hat{b}_{\alpha\gamma} = \frac{\partial \mathbf{g}_I}{\partial \xi^J} \frac{\partial \xi^I}{\partial \hat{\xi}^\alpha} \frac{\partial \xi^J}{\partial \hat{\xi}^\gamma} \cdot \hat{\mathbf{n}}. \quad (6.14)$$

To obtain  $\frac{\partial \xi^I}{\partial \hat{\xi}^\alpha}$ , the right-hand sides of Eqs (6.1) and (6.7) are done inner-product with  $\mathbf{g}^J$  and the two:

$$d\xi^J = \underbrace{\mathbf{g}^J \cdot \hat{\mathbf{g}}_\alpha}_{=\frac{\partial \xi^J}{\partial \hat{\xi}^\alpha}} d\hat{\xi}^\alpha + \mathbf{g}^J \cdot \hat{\mathbf{n}} d\vartheta, \quad (6.15)$$

are equated. Therefore,

$$\frac{\partial \xi^J}{\partial \hat{\xi}^\alpha} = \mathbf{g}^J \cdot \hat{\mathbf{g}}_\alpha. \quad (6.16)$$

For the normal-vector definition of Eq. (6.4), the expression given by Eq. (6.14) simplifies to

$$\hat{b}_{\alpha\gamma} = \frac{\partial \mathbf{g}_\alpha}{\partial \xi^\gamma} \cdot \hat{\mathbf{n}}. \quad (6.17)$$

From Eqs. (6.12) and (6.13),

$$\begin{aligned} \hat{b}_{\alpha\beta}(\hat{\boldsymbol{\xi}}, \vartheta) &= \hat{b}_{\alpha\beta}|_{\vartheta_k} - \frac{\partial \hat{b}_{\alpha\gamma}}{\partial \hat{\xi}^\beta} \Big|_{\vartheta_k} \underbrace{\hat{\mathbf{g}}^\gamma|_{\vartheta_k} \cdot \hat{\mathbf{n}}}_{=0} (\vartheta - \vartheta_k) \\ &\quad - \hat{b}_{\alpha\gamma}|_{\vartheta_k} \frac{\partial \hat{\mathbf{g}}^\gamma}{\partial \hat{\xi}^\beta} \Big|_{\vartheta_k} \cdot \hat{\mathbf{n}} (\vartheta - \vartheta_k) \end{aligned} \quad (6.18)$$

$$= \hat{b}_{\alpha\beta}|_{\vartheta_k} - \left( \hat{b}_{\alpha\gamma} \hat{g}^{\gamma\delta} \right) \Big|_{\vartheta_k} \underbrace{\frac{\partial \hat{\mathbf{g}}_\delta}{\partial \hat{\xi}^\beta} \Big|_{\vartheta_k}}_{\hat{b}_{\delta\beta}|_{\vartheta_k}} \cdot \hat{\mathbf{n}} (\vartheta - \vartheta_k) \quad (6.19)$$

$$= \hat{b}_{\alpha\beta}|_{\vartheta_k} - \left( \hat{b}_{\alpha\gamma} \hat{g}^{\gamma\delta} \hat{b}_{\delta\beta} \right) \Big|_{\vartheta_k} (\vartheta - \vartheta_k). \quad (6.20)$$

is obtained.

### 6.1.3 Wall coordinates in the ZSS

Once the shell-like coordinate system on  $k$ th integration point is defined, the corresponding ZSS coordinate system can be used as described in Chapter 5. From that the components of the metric tensor corresponding to the natural coordinates are computed.

Here the method is redescribed by using the notation from the earlier parts of Section 5.2. The position in the ZSS configuration is

$$\mathbf{X}(\hat{\xi}, \vartheta) = \bar{\mathbf{X}}(\hat{\xi}) + \hat{\mathbf{N}}(\hat{\xi})\vartheta_0(\vartheta), \quad (6.21)$$

where  $0 \leq \vartheta_0 \leq (h_{\text{th}})_0$ , and  $(h_{\text{th}})_0$  is the wall thickness in the ZSS configuration. This thickness will be expressed as  $(h_{\text{th}})_0(\hat{\xi})$ . The position  $\bar{\mathbf{X}}$  on the inner surface is an arbitrary position, and  $\hat{\mathbf{N}} = \mathbf{N}$  as given in Eq. (5.38):

$$\hat{\mathbf{N}} = \mathbf{N} = \frac{\bar{\mathbf{G}}_1 \times \bar{\mathbf{G}}_2}{\|\bar{\mathbf{G}}_1 \times \bar{\mathbf{G}}_2\|}. \quad (6.22)$$

The covariant basis vectors are

$$\hat{\mathbf{G}}_\alpha(\hat{\xi}, \vartheta) = \frac{\partial \mathbf{X}}{\partial \hat{\xi}^\alpha} \quad (6.23)$$

$$= \bar{\mathbf{G}}_\alpha + \frac{\partial \hat{\mathbf{N}}}{\partial \hat{\xi}^\alpha} \vartheta_0(\vartheta) \quad (6.24)$$

$$= \bar{\mathbf{G}}_\alpha - \hat{B}_{\alpha\gamma} \bar{\mathbf{G}}^\gamma \vartheta_0(\vartheta), \quad (6.25)$$

where  $\bar{\mathbf{G}}_\alpha$  is obtained from Eq. (5.47) with

$$\bar{\mathbf{g}}_\alpha = \hat{\mathbf{g}}_\alpha|_{\vartheta_k} + \left( \hat{b}_{\alpha\gamma} \hat{\mathbf{g}}^\gamma \right) \Big|_{\vartheta_k} \vartheta_k, \quad (6.26)$$

which is from Eq. (6.12) at  $\vartheta = 0$ . The curvature tensor in the ZSS configuration is

$$\hat{\mathbf{k}}_0 = (\hat{k}_0)_1 \mathbf{t}_1 \mathbf{t}_1 + (\hat{k}_0)_2 \mathbf{t}_2 \mathbf{t}_2, \quad (6.27)$$

and the second fundamental form  $\hat{B}_{\alpha\beta}$  can be obtained from that as

$$\hat{B}_{\alpha\beta} = -\hat{\mathbf{k}}_0 : \bar{\mathbf{G}}_\alpha \bar{\mathbf{G}}_\beta \quad (6.28)$$

$$= -(\hat{\kappa}_0)_1 (\mathbf{t}_1 \cdot \bar{\mathbf{G}}_\alpha) (\mathbf{t}_1 \cdot \bar{\mathbf{G}}_\beta) - (\hat{\kappa}_0)_2 (\mathbf{t}_2 \cdot \bar{\mathbf{G}}_\alpha) (\mathbf{t}_2 \cdot \bar{\mathbf{G}}_\beta). \quad (6.29)$$

Typically, the curvature in the ZSS is a function of the curvature at the inner surface. The inner-surface curvature tensor can be calculated as

$$\hat{\mathbf{k}}|_{\vartheta=0} = - \left( \hat{b}_{\alpha\beta} \Big|_{\vartheta_k} + \left( \hat{b}_{\alpha\gamma} \hat{g}^{\gamma\delta} \hat{b}_{\delta\beta} \right) \Big|_{\vartheta_k} \vartheta_k \right) \bar{\mathbf{g}}^\alpha \bar{\mathbf{g}}^\beta, \quad (6.30)$$

where the basis vectors are obtained from the covariant basis vectors given by Eq. (6.26).

The relationship  $\vartheta_0(\vartheta)$  is given by

$$\frac{d\vartheta_0}{d\vartheta} = \frac{1}{\lambda_3}. \quad (6.31)$$

The stretch  $\lambda_3$  can be obtained by the in-plane deformation and the constitutive law.

With all from the earlier parts of Section 6.1,  $\mathbf{F}^{-1}$  at  $\boldsymbol{\xi}_k$  is obtained:

$$\mathbf{F}^{-1} = \hat{\mathbf{G}}_\alpha \hat{\mathbf{g}}^\alpha + \frac{1}{\lambda_3} \hat{\mathbf{N}} \hat{\mathbf{n}}. \quad (6.32)$$

With

$$\mathbf{F}^{-1} = \mathbf{G}_I \mathbf{g}^I \quad (6.33)$$

and

$$\mathbf{F}^{-T} \cdot \mathbf{F}^{-1} = G_{IJ} \mathbf{g}^I \mathbf{g}^J, \quad (6.34)$$

$G_{IJ}$  is extracted from

$$G_{IJ} = (\mathbf{F}^{-T} \cdot \mathbf{F}^{-1}) : \mathbf{g}_I \mathbf{g}_J, \quad (6.35)$$

while obtaining  $\mathbf{F}^{-T} \cdot \mathbf{F}^{-1}$  from Eq. (6.32):

$$\mathbf{F}^{-T} \cdot \mathbf{F}^{-1} = \hat{G}_{\alpha\beta} \hat{\mathbf{g}}^\alpha \hat{\mathbf{g}}^\beta + \lambda_3^{-2} \hat{\mathbf{n}} \hat{\mathbf{n}}. \quad (6.36)$$

More explicitly,

$$G_{IJ} = (\hat{G}_{\alpha\beta} \hat{\mathbf{g}}^\alpha \hat{\mathbf{g}}^\beta + \lambda_3^{-2} \hat{\mathbf{n}} \hat{\mathbf{n}}) : \mathbf{g}_I \mathbf{g}_J, \quad (6.37)$$

can be described.

## 6.2 Analytical expression and the ZSS initial guess design

As explained in Chapter 5, the design parameters are the principal curvatures  $(\hat{\kappa}_0)_1$  and  $(\hat{\kappa}_0)_2$ , and the stretches  $\hat{\lambda}_1$  and  $\hat{\lambda}_2$  for each principal curvature direction. However, they are not a set of independent values because there are constraints for the ZSS to give us the target shape for the given load, and the initial guess is desirable to be close to that. To do that, the force equilibrium in the normal direction is introduced by using a local analytical solution for each integration point. After that, the overview of the ZSS initial guess design is described.

### 6.2.1 Analytical solution based Kirchhoff–Love shell theory

The Kirchhoff–Love shell theory with plane-stress condition is applied to obtain the analytical solution. That is the generalized version of the solutions given in [102] for pressurized sphere and cylinder.

To deal with an arbitrary geometry, the shape is assumed that is given in terms of the

principal curvatures. That is the reason the equilibrium equation in the normal direction is used only and focus on a small surface area  $\delta\bar{\Gamma}$ . From that, the surface area is extruded in the normal direction by  $h_{\text{th}}$  to define a volume:  $\delta\Omega = \int_0^{h_{\text{th}}} \delta\Gamma(\vartheta) d\vartheta$ .

The force equilibrium in the normal direction is

$$-\mathbf{n} \cdot \int_0^{h_{\text{th}}} \int_{\delta\Gamma(\vartheta)} \nabla \cdot \boldsymbol{\sigma} d\Gamma d\vartheta = p\delta\bar{\Gamma}, \quad (6.38)$$

where  $\boldsymbol{\sigma}$  is the Cauchy stress tensor. Here this equation can be described by using the shell-coordinate system. By using the plane-stress condition,

$$\boldsymbol{\sigma} = \hat{\sigma}^{\alpha\beta} \hat{\mathbf{g}}_\alpha \hat{\mathbf{g}}_\beta, \quad (6.39)$$

can be written and its divergence is

$$\nabla \cdot \boldsymbol{\sigma} = \frac{\partial \boldsymbol{\sigma}}{\partial \hat{\xi}^\gamma} \cdot \hat{\mathbf{g}}^\gamma \quad (6.40)$$

$$= \frac{\partial (\hat{\sigma}^{\alpha\beta} \hat{\mathbf{g}}_\alpha \hat{\mathbf{g}}_\beta)}{\partial \hat{\xi}^\gamma} \cdot \hat{\mathbf{g}}^\gamma \quad (6.41)$$

$$= \frac{\partial \hat{\sigma}^{\alpha\gamma}}{\partial \hat{\xi}^\gamma} \hat{\mathbf{g}}_\alpha + \hat{\sigma}^{\alpha\gamma} \frac{\partial \hat{\mathbf{g}}_\alpha}{\partial \hat{\xi}^\gamma} + \hat{\sigma}^{\alpha\beta} \hat{\mathbf{g}}_\alpha \frac{\partial \hat{\mathbf{g}}_\beta}{\partial \hat{\xi}^\gamma} \cdot \hat{\mathbf{g}}^\gamma. \quad (6.42)$$

Because  $\delta\Gamma \rightarrow 0$ ,  $\mathbf{n} \cdot \hat{\mathbf{g}}_\alpha \rightarrow 0$ . Thus, what is left in the normal direction is

$$\mathbf{n} \cdot (\nabla \cdot \boldsymbol{\sigma}) = \hat{\sigma}^{\alpha\gamma} \mathbf{n} \cdot \frac{\partial \hat{\mathbf{g}}_\alpha}{\partial \hat{\xi}^\gamma} \quad (6.43)$$

$$= \hat{\sigma}^{\alpha\gamma} \hat{b}_{\alpha\gamma}. \quad (6.44)$$

The small area can be expressed as

$$\delta\Gamma(\vartheta) = \hat{A}(\vartheta) \delta\hat{\xi}^1 \delta\hat{\xi}^2, \quad (6.45)$$

where

$$\hat{A}(\vartheta) = \|\hat{\mathbf{g}}_1 \times \hat{\mathbf{g}}_2\|. \quad (6.46)$$

At the inner surface,

$$\bar{A} = \|\bar{\mathbf{g}}_1 \times \bar{\mathbf{g}}_2\|, \quad (6.47)$$

is described. With all above, Eq. (6.38) becomes

$$-\int_0^{h_{\text{th}}} \hat{\sigma}^{\alpha\gamma} \hat{b}_{\alpha\gamma} \hat{A} \delta\hat{\xi}^1 \delta\hat{\xi}^2 d\vartheta = p \bar{A} \delta\hat{\xi}^1 \delta\hat{\xi}^2. \quad (6.48)$$

Thus, the relationship is obtained as:

$$p = -\frac{1}{\bar{A}} \int_0^{h_{\text{th}}} \hat{\sigma}^{\alpha\gamma} \hat{b}_{\alpha\gamma} \hat{A} d\vartheta, \quad (6.49)$$

where

$$\hat{b}_{\alpha\beta} = \bar{b}_{\alpha\beta} - \bar{b}_{\alpha\gamma} \bar{g}^{\gamma\delta} \bar{b}_{\delta\beta} \vartheta, \quad (6.50)$$

which can be obtained from Eq. (6.20) with  $\vartheta_k = 0$ . To express the stress components, the basis vectors is needed for all  $\vartheta$ , which are

$$\hat{\mathbf{g}}_\alpha = \bar{\mathbf{g}}_\alpha - \bar{b}_{\alpha\gamma} \bar{\mathbf{g}}^\gamma \vartheta. \quad (6.51)$$

The expressions come from Eq. (6.12) with  $\vartheta_k = 0$ .

Now the orthonormal vectors corresponding to the principal curvatures are used to be the covariant basis vectors at the inner surface:  $\bar{\mathbf{g}}_\alpha = \mathbf{t}_\alpha$ , and the second fundamental form

becomes diagonal:  $b_{\alpha\alpha} = -\hat{k}_\alpha$  (no sum). Thus, Eqs. (6.50) and (6.51) become

$$\hat{b}_{\alpha\alpha} = -\hat{k}_\alpha (1 + \hat{k}_\alpha \vartheta) \quad (\text{no sum}), \quad (6.52)$$

$$\hat{\mathbf{g}}_\alpha = (1 + \hat{k}_\alpha \vartheta) \mathbf{t}_\alpha \quad (\text{no sum}). \quad (6.53)$$

From that,  $\bar{A} = 1$  is also obtained,

$$\hat{A} = (1 + \hat{k}_1 \vartheta) (1 + \hat{k}_2 \vartheta), \quad (6.54)$$

and

$$\hat{\mathbf{g}}^\alpha = \frac{1}{1 + \hat{k}_\alpha \vartheta} \mathbf{t}_\alpha \quad (\text{no sum}). \quad (6.55)$$

Here the coefficients of the Cauchy stress tensor based on the orthonormal vectors are introduced as:

$$\boldsymbol{\sigma} = \tilde{\sigma}_{\gamma\delta} \mathbf{t}_\gamma \mathbf{t}_\delta, \quad (6.56)$$

and obtain

$$\hat{\sigma}^{\alpha\beta} = \tilde{\sigma}_{\gamma\delta} \mathbf{t}_\gamma \mathbf{t}_\delta : \hat{\mathbf{g}}^\alpha \hat{\mathbf{g}}^\beta. \quad (6.57)$$

That can be simplified as

$$\hat{\sigma}^{\alpha\beta} = \frac{\tilde{\sigma}_{\alpha\beta}}{(1 + \hat{k}_\alpha \vartheta) (1 + \hat{k}_\beta \vartheta)} \quad (\text{no sum}). \quad (6.58)$$

Thus, Eq. (6.49) becomes

$$p = \int_0^{t_{\text{in}}} \left( \tilde{\sigma}_{11} \hat{k}_1 (1 + \hat{k}_2 \vartheta) + \tilde{\sigma}_{22} \hat{k}_2 (1 + \hat{k}_1 \vartheta) \right) d\vartheta \quad (6.59)$$



$$\begin{aligned}
&= \hat{\kappa}_1 \int_0^{h_{th}} \tilde{\sigma}_{11} d\vartheta + \hat{\kappa}_2 \int_0^{h_{th}} \tilde{\sigma}_{22} d\vartheta \\
&\quad + \hat{\kappa}_1 \hat{\kappa}_2 \int_0^{h_{th}} (\tilde{\sigma}_{11} + \tilde{\sigma}_{22}) \vartheta d\vartheta.
\end{aligned} \tag{6.60}$$

To calculate  $\tilde{\sigma}_{\alpha\beta}$ , the ZSS is required. For that,  $\bar{\mathbf{g}}_\alpha = \mathbf{t}_\alpha$  is substituted into Eq. (5.47) and obtain the covariant basis vectors of the ZSS:

$$\bar{\mathbf{G}}_\alpha = \frac{1}{\hat{\lambda}_\alpha} \mathbf{t}_\alpha \quad (\text{no sum}), \tag{6.61}$$

and from  $\vartheta_0(\vartheta)$ , yet to be calculated, the covariant basis vectors are obtained as:

$$\hat{\mathbf{G}}_\alpha = \frac{1}{\hat{\lambda}_\alpha} (1 + (\hat{\kappa}_0)_\alpha \vartheta_0(\vartheta)) \mathbf{t}_\alpha \quad (\text{no sum}). \tag{6.62}$$

From that, the contravariant basis vectors are obtained as:

$$\hat{\mathbf{G}}^\alpha = \frac{\hat{\lambda}_\alpha}{1 + (\hat{\kappa}_0)_\alpha \vartheta_0(\vartheta)} \mathbf{t}_\alpha \quad (\text{no sum}). \tag{6.63}$$

Because it is assumed that the principal stretches are also in the principal curvature directions, the principal stretch in  $\alpha$  direction is obtained as

$$(\lambda_\alpha)^2 = \mathbf{F}^T \cdot \mathbf{F} : \mathbf{t}_\alpha \mathbf{t}_\alpha \quad (\text{no sum}) \tag{6.64}$$

$$= \hat{g}_{\gamma\delta} \hat{\mathbf{G}}^\gamma \hat{\mathbf{G}}^\delta : \mathbf{t}_\alpha \mathbf{t}_\alpha \quad (\text{no sum over } \alpha) \tag{6.65}$$

$$= (1 + \hat{\kappa}_\alpha \vartheta)^2 \left( \frac{\hat{\lambda}_\alpha}{1 + (\hat{\kappa}_0)_\alpha \vartheta_0} \right)^2 \quad (\text{no sum}). \tag{6.66}$$

From that,

$$\lambda_\alpha = \frac{1 + \hat{\kappa}_\alpha \vartheta}{1 + (\hat{\kappa}_0)_\alpha \vartheta_0} \hat{\lambda}_\alpha \quad (\text{no sum}), \tag{6.67}$$

is obtained. To obtain  $\vartheta_0(\vartheta)$ ,  $\vartheta = \vartheta_0 = 0$  is prepared and integrated by using Eq. (6.31).

This requires numerical integration, unless the constitutive law is very simple.

### 6.2.2 The ZSS initial guess design

As proposed in Chapters 4 and 5, the two principal directions are seen as circumferential and longitudinal directions, and  $\hat{\kappa}_1$  is in the circumferential direction, giving us

$$(\hat{\kappa}_0)_1 = \frac{2\pi - \phi}{2\pi} \hat{\kappa}_1. \quad (6.68)$$

Here  $\phi$  is the opening angle, which is seen after a longitudinal cut, based on artery experimental data [16]. The wall thickness is about 8–10 % of the diameter at the target configuration. This means that  $\hat{\kappa}_1 h_{\text{th}}$  is 0.16–0.20, and  $\hat{\kappa}_2 h_{\text{th}}$  is nearly equal to zero but that could be negative.

Patient-specific geometries are more complicated than that. To classify the local shapes, the quadrants of the space formed is considered by  $\hat{\kappa}_1 h_{\text{th}}$  and  $\hat{\kappa}_2 h_{\text{th}}$ . In the first quadrant, a balloon-like shape, which may be seen at a branch or an aneurysm is there. In the second and fourth quadrants, saddle points, which may be seen near branches are there. In the third quadrant, both curvatures negative, which may be seen also near branches are there. Note that, because of the Kirchhoff–Love shell assumption, the following conditions (for  $\alpha = 1$  or 2) are out of scope:

$$\hat{\kappa}_\alpha h_{\text{th}} < -1, \quad (6.69)$$

or

$$(\hat{\kappa}_0)_\alpha (h_{\text{th}})_0 < -1. \quad (6.70)$$

### 6.3 Numerical examples

All the computations here are based on the Fung's model (see Section 2.9) with  $D_1 = 2.6447 \times 10^3$  Pa,  $D_2 = 8.365$ , and the Poisson's ratio  $\nu = 0.49$ . The load is  $p = 92$  mm Hg. In this example section, the normal-vector definition of Eq. (6.4) is used.

#### 6.3.1 Analytical solution for constant stretch on the inner surface

There are four design parameters,  $\hat{\lambda}_1$ ,  $\hat{\lambda}_2$ ,  $\phi_1$ , and  $\phi_2$  which should be selected. Here, the stretches are assumed as  $\hat{\lambda}_1 = \hat{\lambda}_2 = 1.05$  and the opening angles  $\phi_1$  and  $\phi_2$  are found in terms of  $\hat{\kappa}_1 h_{\text{th}}$  and  $\hat{\kappa}_2 h_{\text{th}}$ . An opening angle for each direction is defined as:

$$\phi_\alpha = 2\pi \left( 1 - \frac{(\hat{\kappa}_0)_\alpha}{\hat{\kappa}_\alpha} \right) \quad (\text{no sum}), \quad (6.71)$$

where  $\alpha = 1, 2$ . Here, the stretch value 1.05 gives  $\phi_1 = 410^\circ$  for straight tube with  $\hat{\kappa}_1 h_{\text{th}} = 0.16$ , and  $\phi_1 = 310^\circ$  with  $\hat{\kappa}_1 h_{\text{th}} = 0.20$ . In this section, the rest of the design parameters  $\phi_1$  and  $\phi_2$  are searched with  $\hat{\kappa}_1 h_{\text{th}}$  and  $\hat{\kappa}_2 h_{\text{th}}$ .

Figure 6.3 shows  $\phi_1$ , which is obtained iteratively and may not be unique. The figure also gives us  $\phi_2$  when  $\hat{\kappa}_1 h_{\text{th}}$  and  $\hat{\kappa}_2 h_{\text{th}}$  are interchanged. In many regions, there are symmetric values with respect to  $\hat{\kappa}_1 h_{\text{th}} = \hat{\kappa}_2 h_{\text{th}}$ . In regions where  $\hat{\kappa}_1 \hat{\kappa}_2 < 0$ , which are the saddle points, large departure from symmetry is observed. This map is used for generating the initial guess. When the geometry is out of scope,  $\phi_\alpha = 0$  is set.

#### 6.3.2 Straight tube

The tube has  $\hat{\kappa}_1 h_{\text{th}} = 0.20$ . The meshes used in the computations are shown in Figures 6.4 and 6.5. They are cubic B-splines with 16, 8 and 1 elements in the circumferential, longitudinal and thickness directions. For the first mesh,  $\mathbf{g}_3$  is in  $\mathbf{n}$  direction, and for the second mesh,  $\mathbf{g}_3$  is skew to  $\mathbf{n}$  direction. Therefore, the meshes for observing how the wall coordinate in Section 6.1 works. As can be clearly seen in the left of Figure 6.5, the mesh

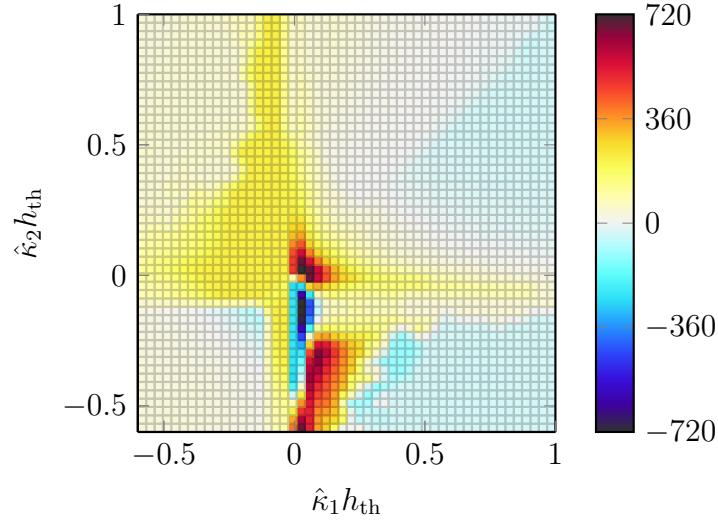


Figure 6.3: Opening angle  $\phi_1$  over the space formed by  $\hat{\kappa}_1 h_{\text{th}}$  and  $\hat{\kappa}_2 h_{\text{th}}$

is twisted. Figures 6.6 and 6.7 show, for the mesh in Figure 6.4, the principal stretches from the ZSS initial guess and the converged ZSS. Figures 6.8 and 6.9 do the same for the mesh in Figure 6.5. From all these results the principal stretches with ZSS initial guess is very close to the converged result, even for the mesh where  $\mathbf{g}_3$  is skew to  $\mathbf{n}$  direction.

### 6.3.3 Y-shaped tube

This geometry was motivated by branched arteries. The tube parts have  $\hat{\kappa}_1 h_{\text{th}} = 0.16$ , with constant thickness. Figure 6.10 shows the shape and  $\hat{\kappa}_1 h_{\text{th}}$  and  $\hat{\kappa}_2 h_{\text{th}}$ . The geometry has two umbilical points, where  $\hat{\kappa}_1 = \hat{\kappa}_2$ , and three saddle-point regions. The mesh is shown in Figure 6.11.

Figure 6.12 shows the IPBZSS, using the EBZSS representation, from the ZSS initial guess and the converged ZSS, and their clipped views. The stretches are shown in Figures 6.13 and 6.14. The initial guess has nearly uniform stretch on the inner surface because the stretches are assumed as  $\hat{\lambda}_1 = \hat{\lambda}_2 = 1.05$  in its design. However, at the saddle point, the maximum stretch on the converged result is higher than the result of the ZSS initial guess. This affects the stretch on the outer surface too. There is less effect at the umbilical points. Figure 6.15 shows the stretch in  $\hat{\mathbf{n}}$  direction. Again, there is less effect

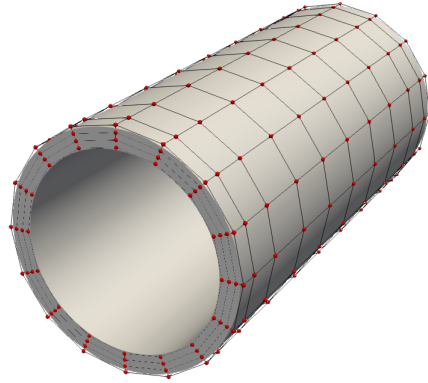


Figure 6.4: Straight tube. The mesh has  $\mathbf{g}_3$  in  $\mathbf{n}$  direction

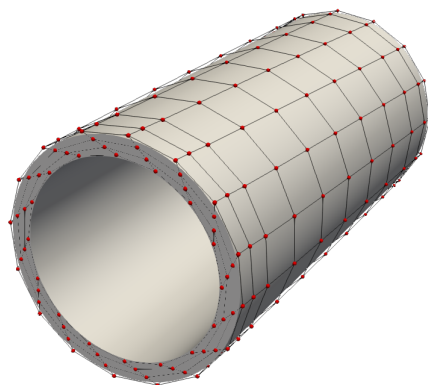


Figure 6.5: Straight tube. The mesh has  $\mathbf{g}_3$  skew to  $\mathbf{n}$  direction

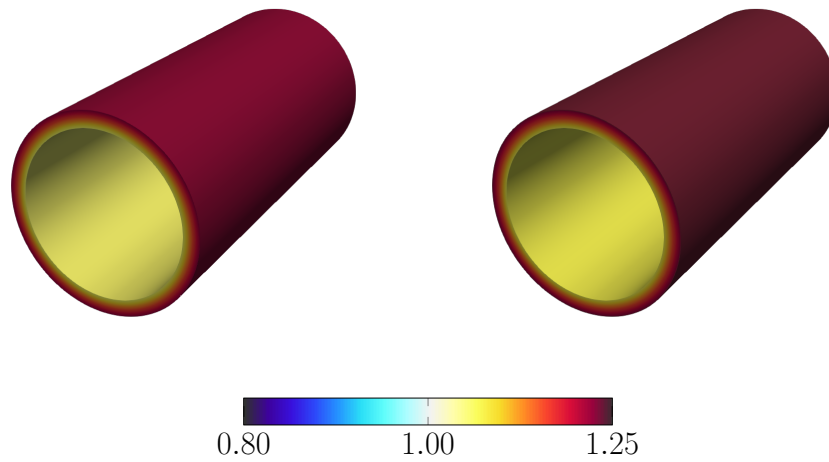


Figure 6.6: Straight tube. Maximum principal stretch for the mesh in Figure 6.4. From the ZSS initial guess (*left*) and the converged ZSS (*right*)

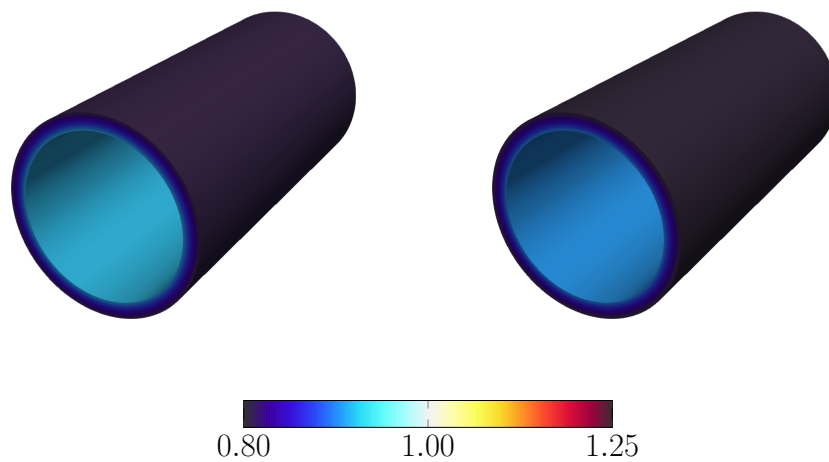


Figure 6.7: Straight tube. Minimum principal stretch for the mesh in Figure 6.4. From the ZSS initial guess (*left*) and the converged ZSS (*right*)

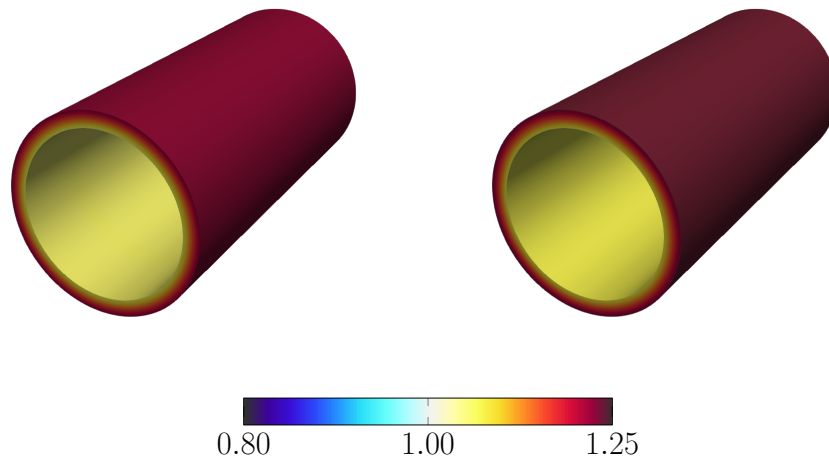


Figure 6.8: Straight tube. Maximum principal stretch for the mesh in Figure 6.5. From the ZSS initial guess (*left*) and the converged ZSS (*right*)

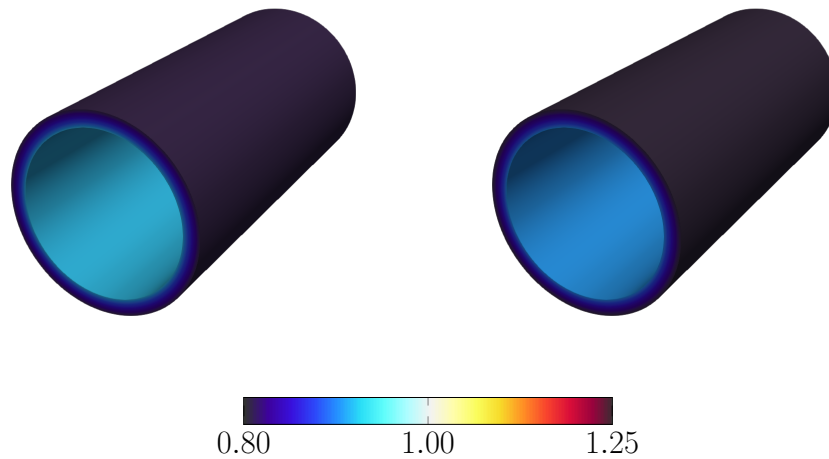


Figure 6.9: Straight tube. Minimum principal stretch for the mesh in Figure 6.5. From the ZSS initial guess (*left*) and the converged ZSS (*right*)

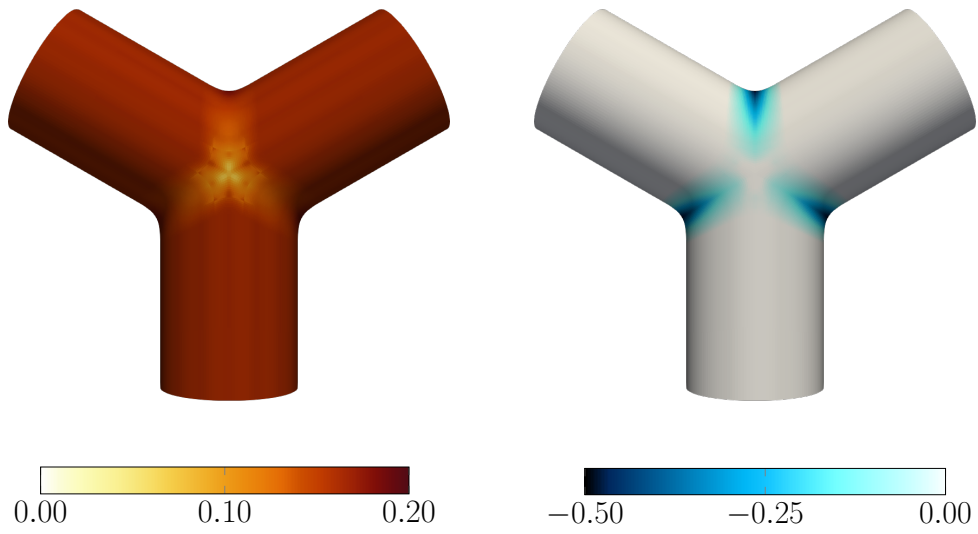


Figure 6.10: Y-shaped tube.  $\hat{\kappa}_1 h_{\text{th}}$  (*left*) and  $\hat{\kappa}_2 h_{\text{th}}$  (*right*)

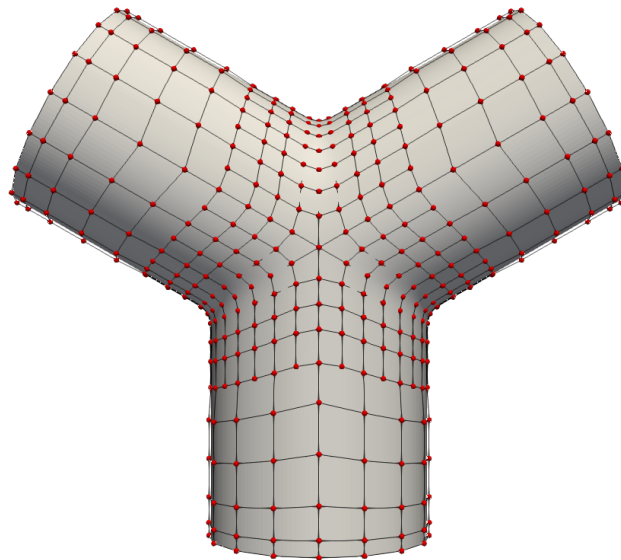


Figure 6.11: Y-shaped tube. Inner-surface mesh made of cubic and quartic T-splines. *Red* circles represent the control points. The parts with the quartic T-splines, obtained by order elevation [98], are around the two extraordinary points, each connected to six edges



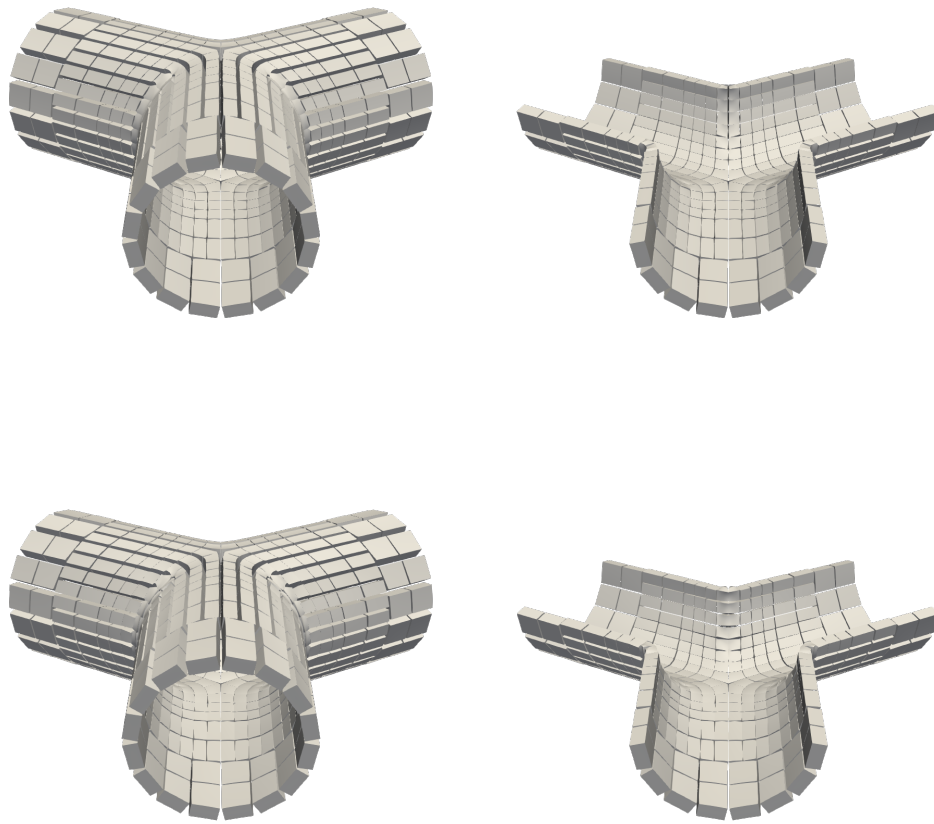


Figure 6.12: Y-shaped tube. The IPBZSS, shown using the EBZSS representation. From the ZSS initial guess (*top*) and the converged ZSS (*bottom*)

at the umbilical points.

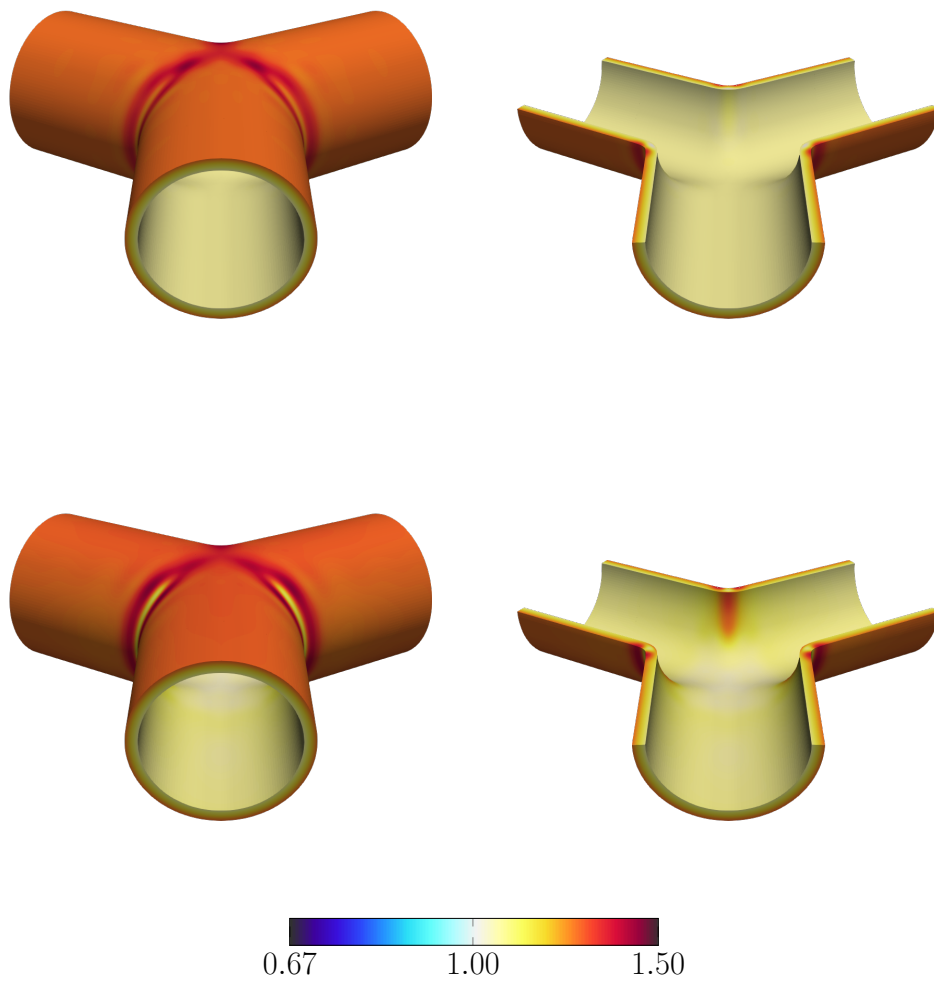


Figure 6.13: Y-shaped tube. Maximum principal stretch. From the ZSS initial guess (*top*) and the converged ZSS (*bottom*)

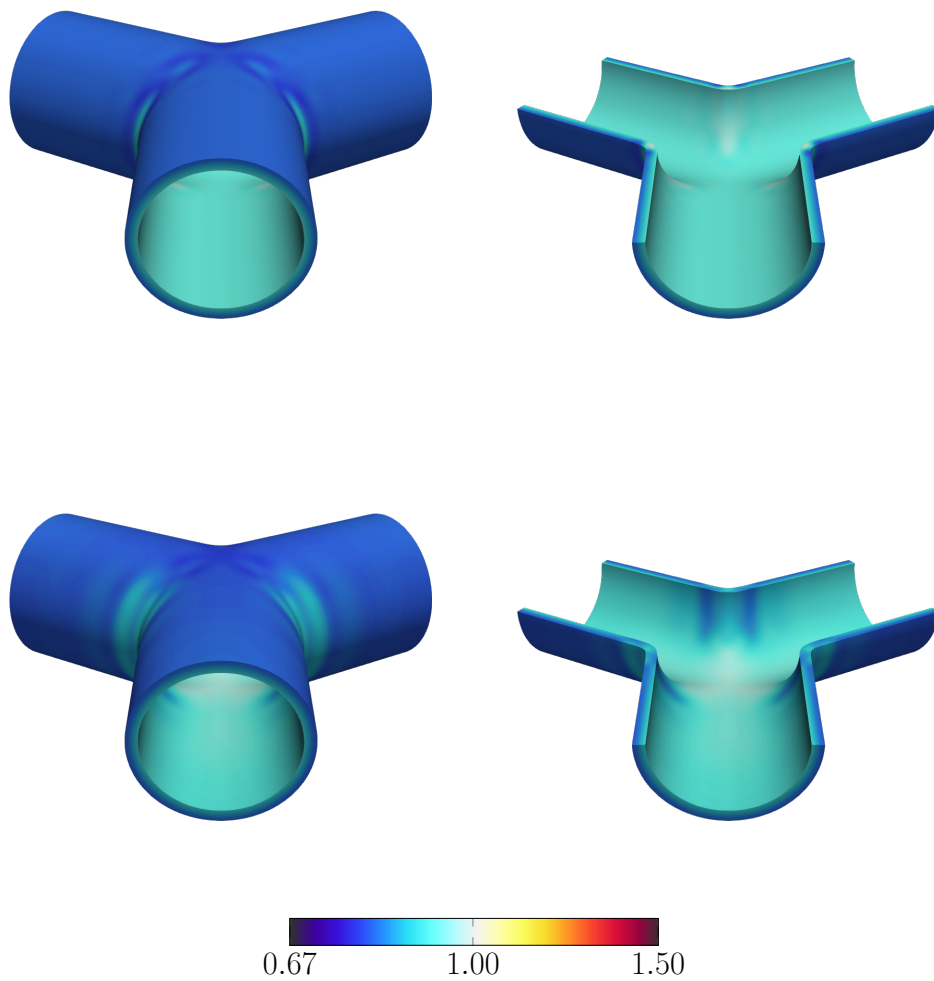


Figure 6.14: Y-shaped tube. Minimum principal stretch. From the ZSS initial guess (*top*) and the converged ZSS (*bottom*)

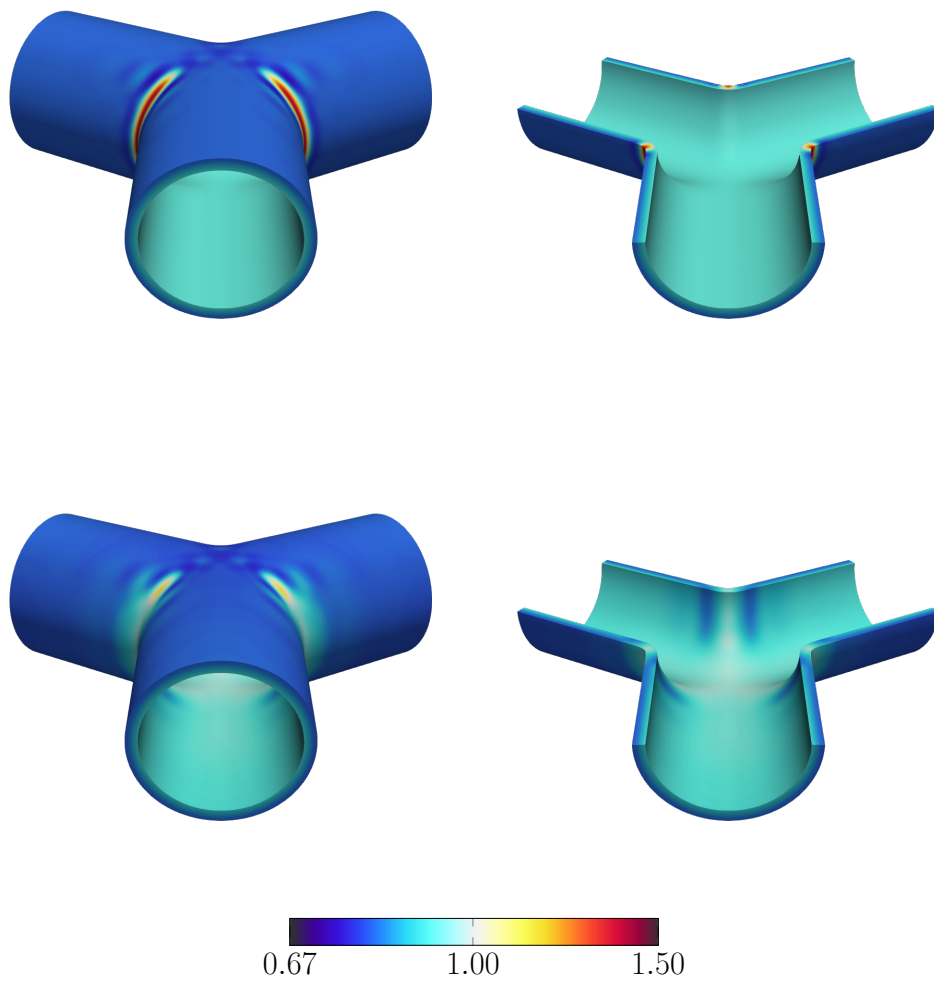


Figure 6.15: Y-shaped tube. Stretch in  $\hat{n}$  direction. From the ZSS initial guess (*top*) and the converged ZSS (*bottom*)

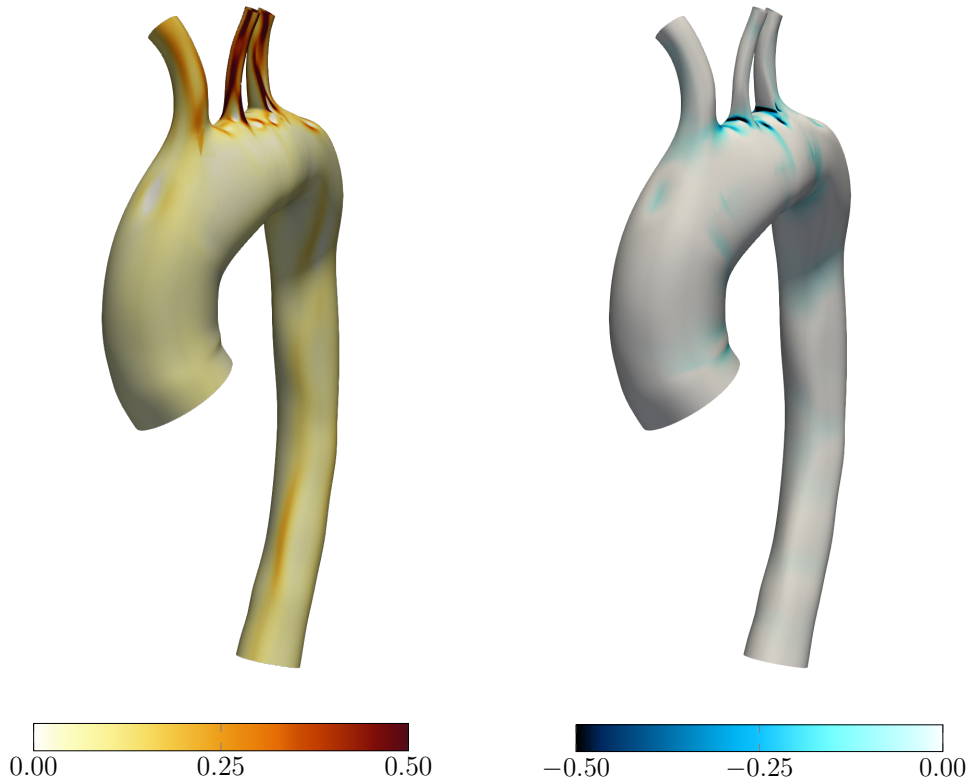


Figure 6.16: Patient-specific aorta.  $\hat{\kappa}_1$  ( $\text{mm}^{-1}$ ) (*left*) and  $\hat{\kappa}_2$  ( $\text{mm}^{-1}$ ) (*right*). The maximum and minimum values are  $1.822 \text{ mm}^{-1}$  and  $-0.2810 \text{ mm}^{-1}$  with  $\hat{\kappa}_1$  ( $\text{mm}^{-1}$ ), and the maximum and minimum values are  $0.1973 \text{ mm}^{-1}$  and  $-1.543 \text{ mm}^{-1}$  with  $\hat{\kappa}_2$  ( $\text{mm}^{-1}$ )

### 6.3.4 Patient-specific aorta

The largest diameter is about 30 mm. Figure 6.16 shows the shape and  $\hat{\kappa}_1$  and  $\hat{\kappa}_2$ . The inner-surface mesh and the volume mesh are shown in Figure 6.17. Laplace's equation is used to determine a smooth thickness distribution [39], setting the values at the boundaries to result in  $\hat{\kappa}_1 h_{\text{th}} = 0.20$ . The volume mesh is generated as described in Section 6.1.1, which involves modification of the outer surface and consequently the thickness. The measured thickness is displayed on the inner-surface mesh in Figures 6.18, with an average value of  $\hat{\kappa}_1 h_{\text{th}} = 0.18$ .

From the results of the Y-shaped tube, the initial guess should have had, on the outer surface, less variation in the stretch in  $\hat{\mathbf{n}}$  direction. Based on that, the initial guess is improved in parts of the region where both curvatures are not positive. For a straight tube

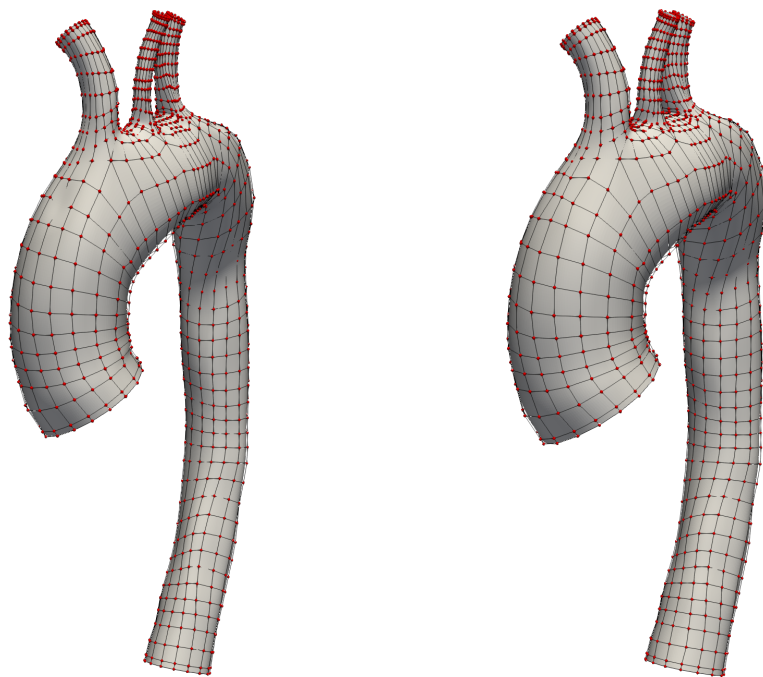


Figure 6.17: Patient-specific aorta. Inner-surface mesh (*left*) and Volume mesh (*right*), made of cubic and quartic T-splines. *Red* circles represent the control points. The parts with the quartic T-splines, obtained by order elevation [98], are around the two extraordinary points, each connected to six edges



Figure 6.18: Patient-specific aorta.  $h_{\text{th}}$  (mm)

with  $\hat{\kappa}_1 h_{\text{th}} = 0.18$ , on the outer surface, the stretch in  $\hat{\mathbf{n}}$  direction is 0.80. The value is set as the target in improving the initial guess.

Here, four cases are defined in deciding how to do the improvement, and the order is given below:

1.  $\hat{\kappa}_1 h_{\text{th}} < -0.6$  or  $\hat{\kappa}_2 h_{\text{th}} < -0.6$
2.  $\hat{\kappa}_1 h_{\text{th}} < -0.4$  or  $\hat{\kappa}_2 h_{\text{th}} < -0.4$
3.  $\hat{\kappa}_1 h_{\text{th}} + \hat{\kappa}_2 h_{\text{th}} < 0$
4. Elsewhere

Actions for each case are the followings:

1. Set  $\phi_1 = \phi_2 = 0$  and  $\hat{\lambda}_1 = \hat{\lambda}_2 = 1$ .

2. Set  $\phi_1 = \phi_2 = 0$ . Assume that  $\hat{\lambda}_1$  and  $\hat{\lambda}_2$  are the same. Determine them in such a way that, on the outer surface, the stretch in  $\hat{\mathbf{n}}$  direction is 0.80.
3. Leave  $\hat{\lambda}_1 = \hat{\lambda}_2 = 1.05$  unchanged. Assume  $\phi_1$  and  $\phi_2$  are the same. Determine them in such a way that, on the outer surface, the stretch in  $\hat{\mathbf{n}}$  direction is 0.80.
4. No modification.

Figure 6.19 shows the IPBZSS, using the EBZSS representation, from the ZSS initial guess and the converged ZSS. The stretches are shown in Figures 6.20 and 6.21. Figure 6.22 shows the stretch in  $\hat{\mathbf{n}}$  direction. Overall, the ZSS initial guess and the converged ZSS are very similar. This indicates that reaching the ZSS design targets based on the analytical solution works well.

## 6.4 Evaluations

This section introduces how the new ZSS design works with comparing to the past results, and the results of stretches distributions are observed.

### 6.4.1 Comparison between the initial guess and the converged ZSS

The method is applied the shapes which are used in Chapter 5. In the case of the Y-shaped tube, the stretches are shown in Figures 6.23 and 6.24. From the result, the stretches on the ZSS initial guess and the converged ZSS are very close to each other with compared to Figures 5.7 and 5.8. Similarly, in the case of the patient-specific aorta geometry, the stretches are shown in Figures 6.25 and 6.26. From the result, stretches on the ZSS initial guess and the converged ZSS are very close to each other with compared to Figures 5.16 and 5.17 as similar to the Y-shaped tube. For more specific observation, set the difference value of  $(\lambda_\alpha)^0$  and  $(\lambda_\alpha)^\infty$ , where  $(\lambda_\alpha)^0$  and  $(\lambda_\alpha)^\infty$  are calculated from the ZSS initial and the converged ZSS, as  $|1 - (\lambda_\alpha)^0/(\lambda_\alpha)^\infty|$ . Figures 6.27 and 6.28 show  $|1 - (\lambda_\alpha)^0/(\lambda_\alpha)^\infty|$  on the Y-shaped tube with the method in Chapter 5 and in this chapter.



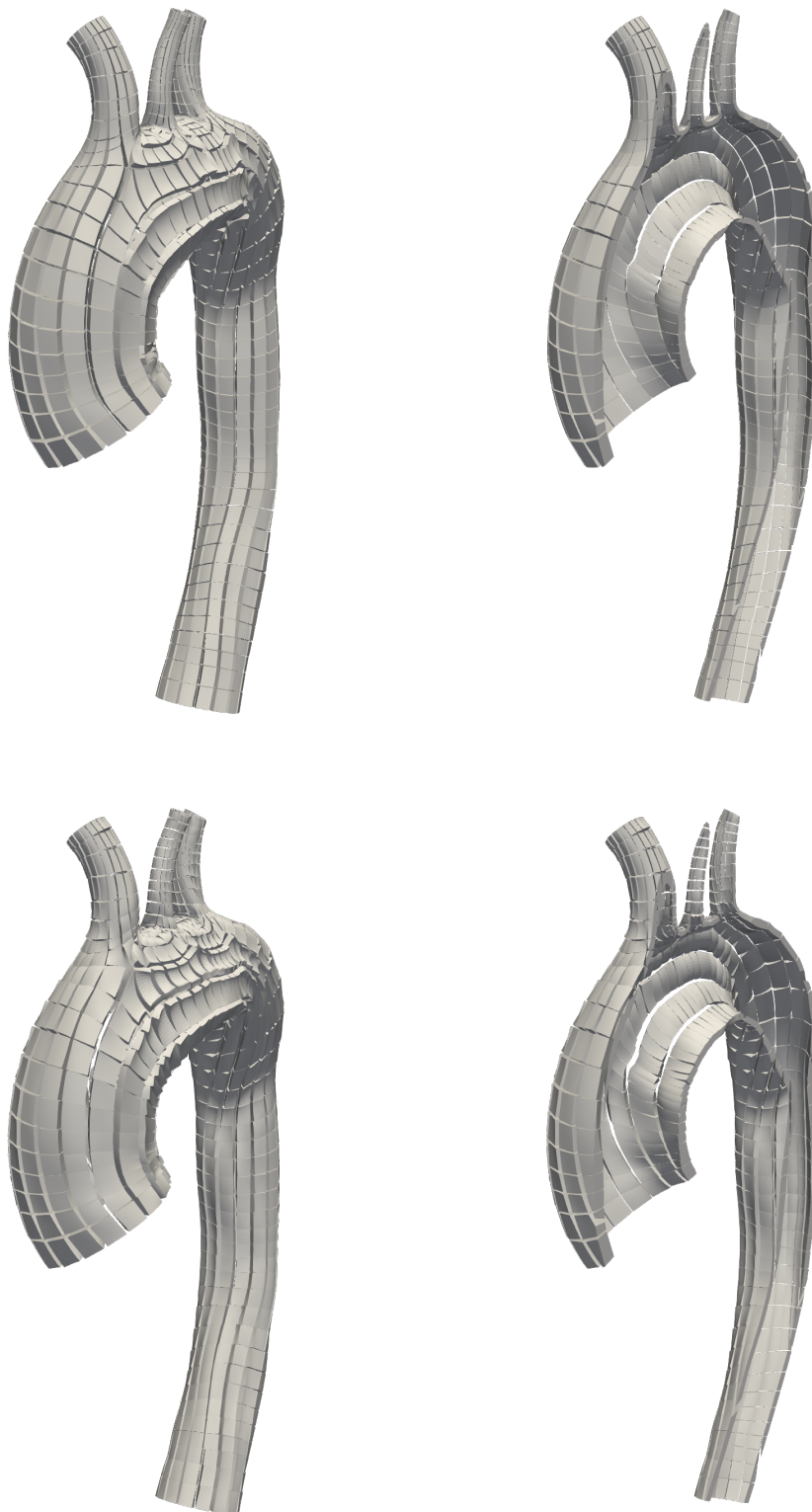


Figure 6.19: Patient-specific aorta. The IPBZSS, shown using the EBZSS representation. From the ZSS initial guess (*top*) and the converged ZSS (*bottom*)

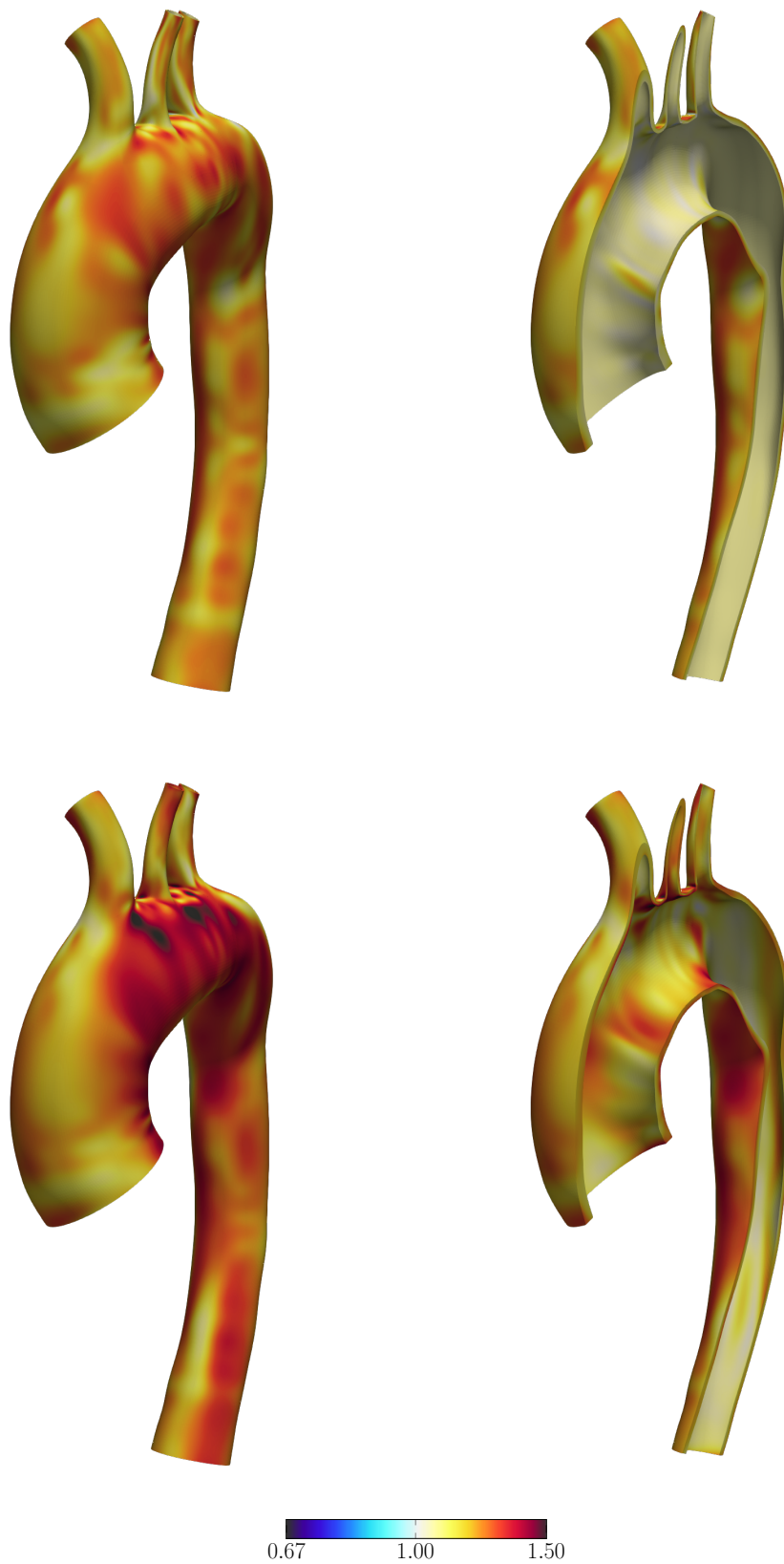


Figure 6.20: Patient-specific aorta. Maximum principal stretch. From the ZSS initial guess (*top*) and the converged ZSS (*bottom*)

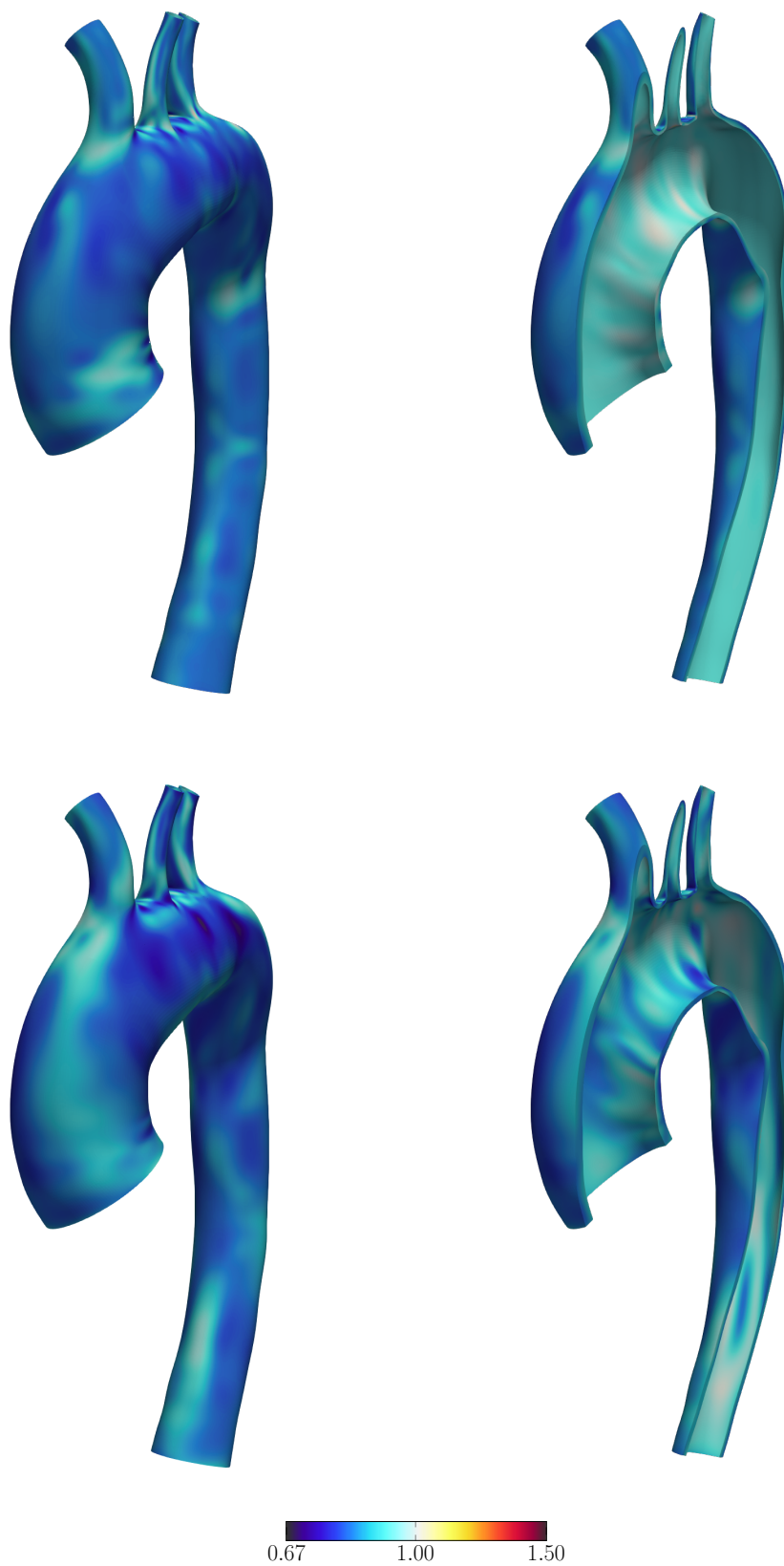


Figure 6.21: Patient-specific aorta. Minimum principal stretch. From the ZSS initial guess (*top*) and the converged ZSS (*bottom*)

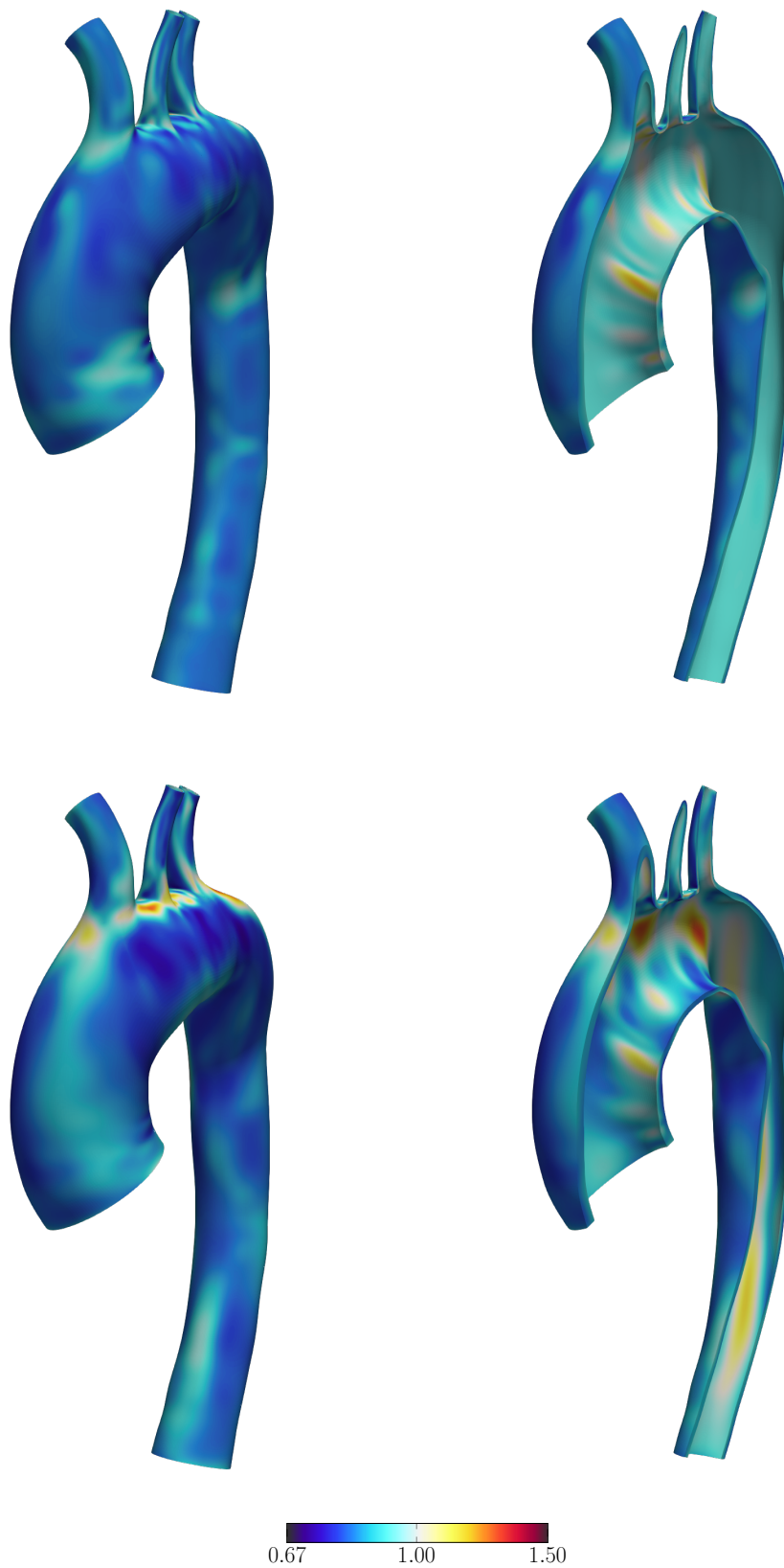


Figure 6.22: Patient-specific aorta. Stretch in  $\hat{n}$  direction. From the ZSS initial guess (*top*) and the converged ZSS (*bottom*)

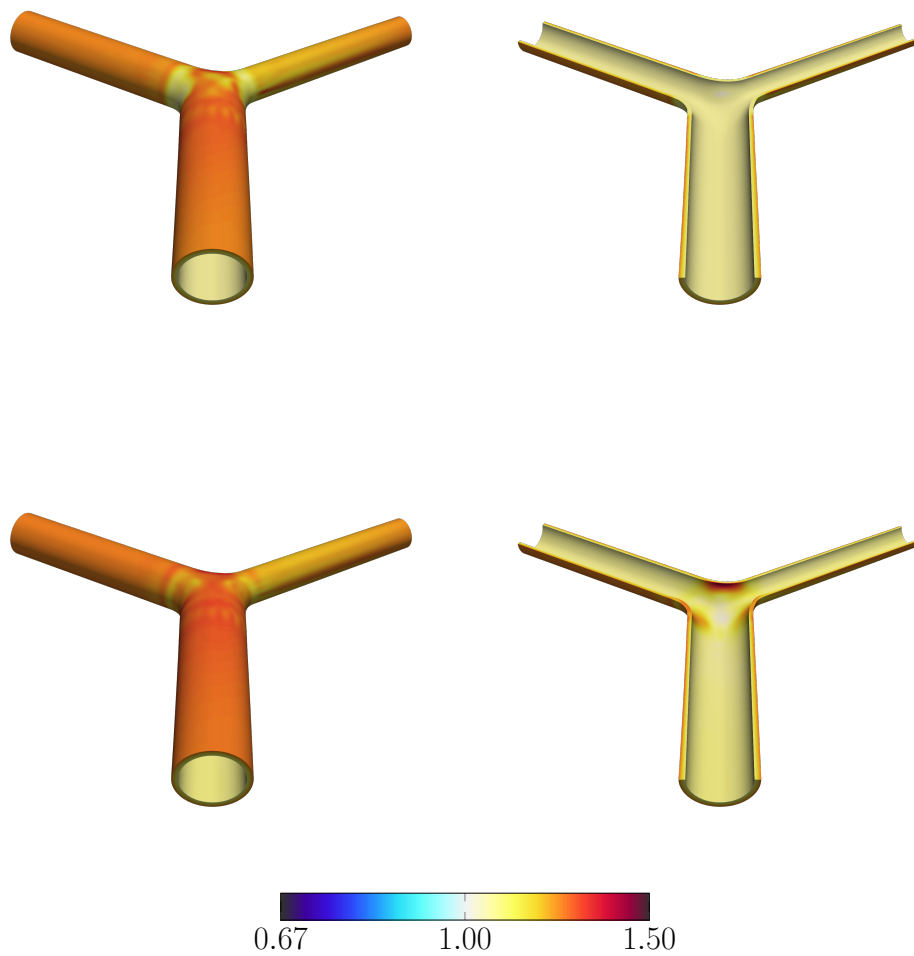


Figure 6.23: Y-shaped tube. Maximum principal stretch for the mesh in Figure 5.2. From the ZSS initial guess (*top*) and the converged ZSS (*bottom*)

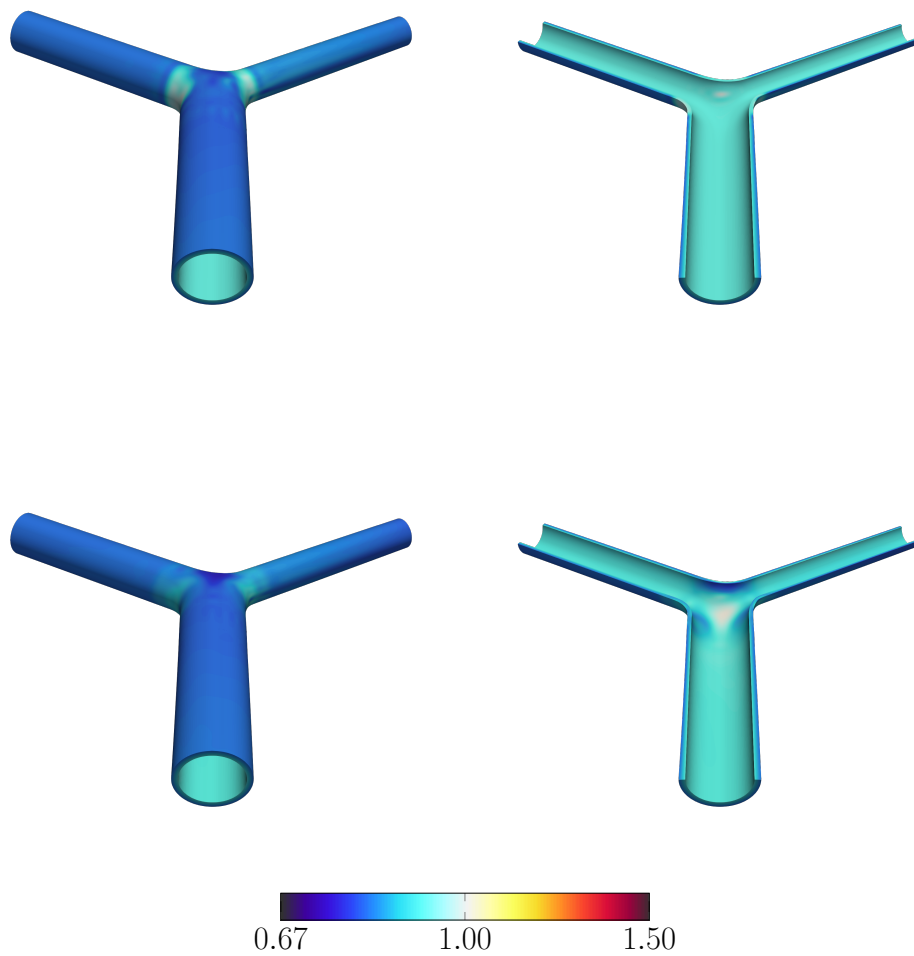


Figure 6.24: Y-shaped tube. Minimum principal stretch for the mesh in Figure 5.2. From the ZSS initial guess (*top*) and the converged ZSS (*bottom*)

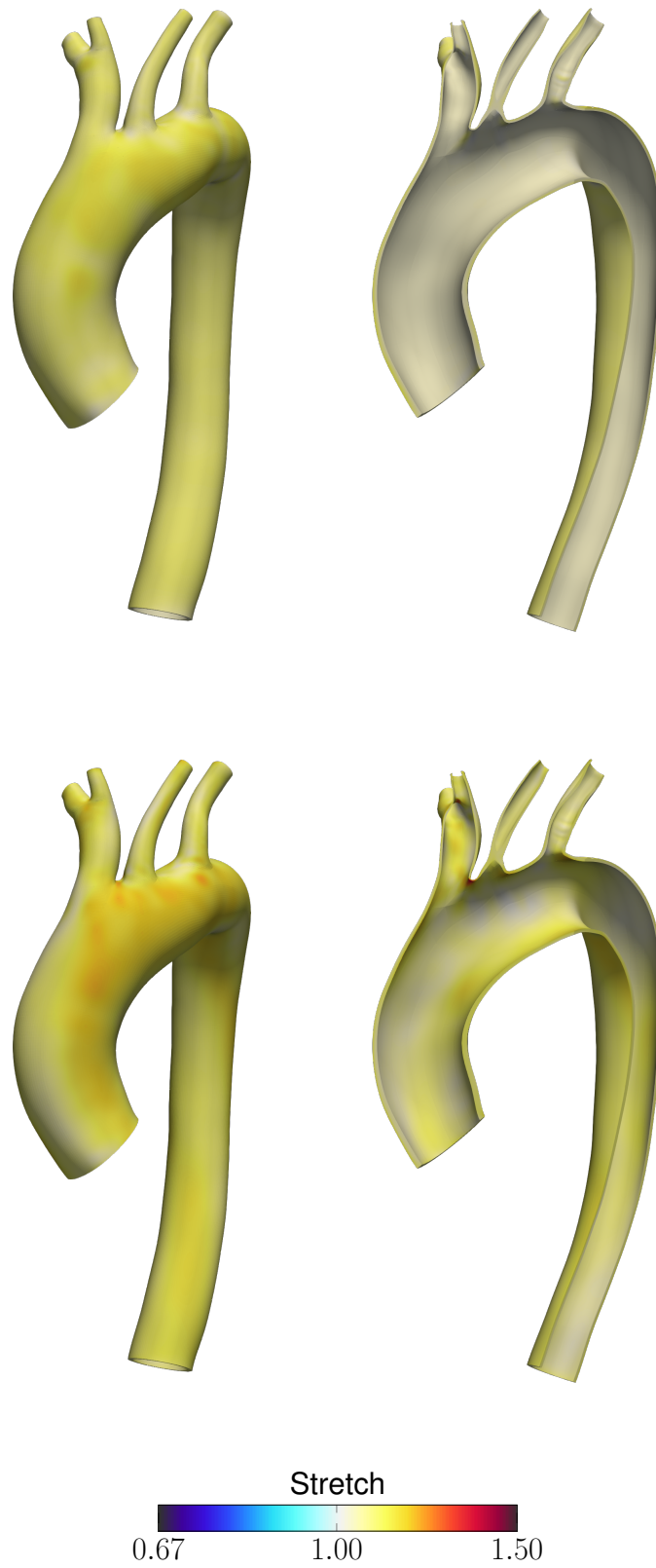


Figure 6.25: Patient-specific aorta. Maximum principal stretch for the mesh in Figure 5.12. From the ZSS initial guess (*top*) and the converged ZSS (*bottom*)

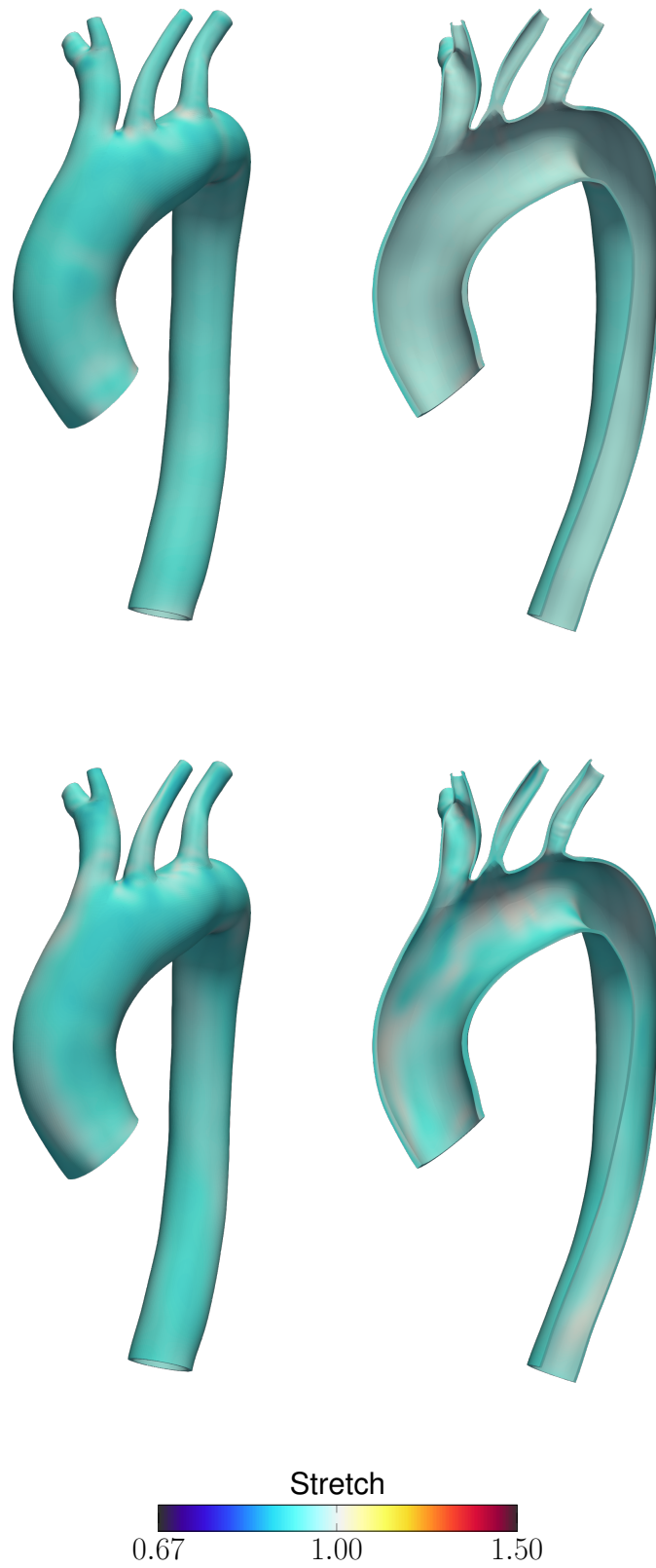


Figure 6.26: Patient-specific aorta. Minimum principal stretch for the mesh in Figure 5.12. From the ZSS initial guess (*top*) and the converged ZSS (*bottom*)



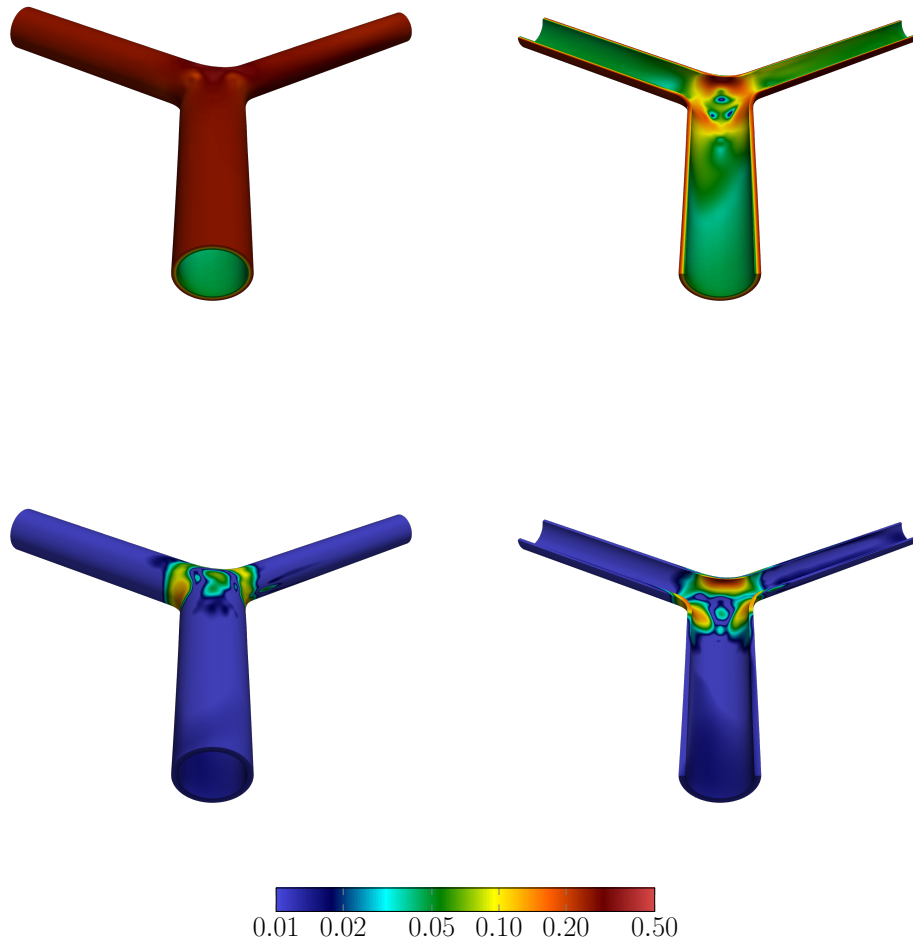


Figure 6.27: Y-shaped tube. The  $|1 - (\lambda_1)^0 / (\lambda_1)^\infty|$  with the method in Chapter 5 (*top*) and this chapter (*bottom*)

Figures 6.29 and 6.30 show  $|1 - (\lambda_\alpha)^0 / (\lambda_\alpha)^\infty|$  on the patient-specific aorta geometry with the method in Chapter 5 and in this chapter. From the results it is recognized visually that the new method has better initial guess. There are still far result at saddle points. To compare with quantitative way, the averaged  $|1 - (\lambda_1)^0 / (\lambda_1)^\infty|$  with the Y-shaped tube and the patient-specific aorta geometry are shown in Figure 6.31. From the figure, differences are decreased by using the improved method.

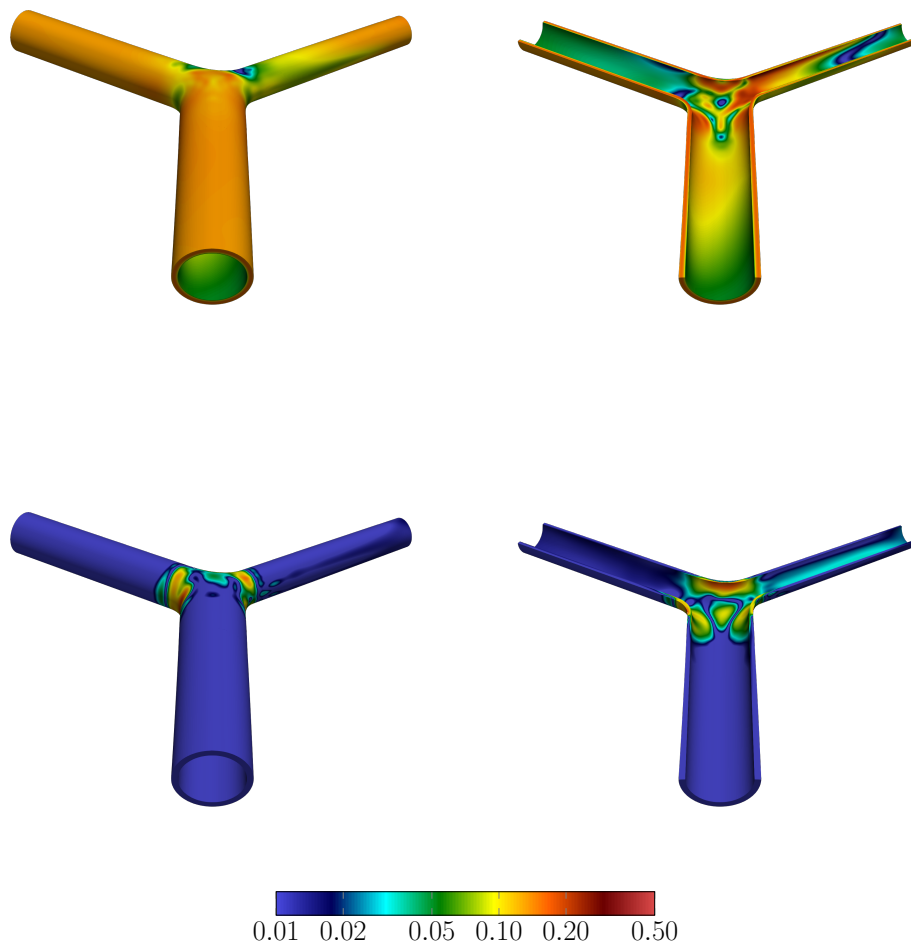


Figure 6.28: Y-shaped tube. The  $|1 - (\lambda_2)^0 / (\lambda_2)^\infty|$  with the method in Chapter 5 (*top*) and this chapter (*bottom*)

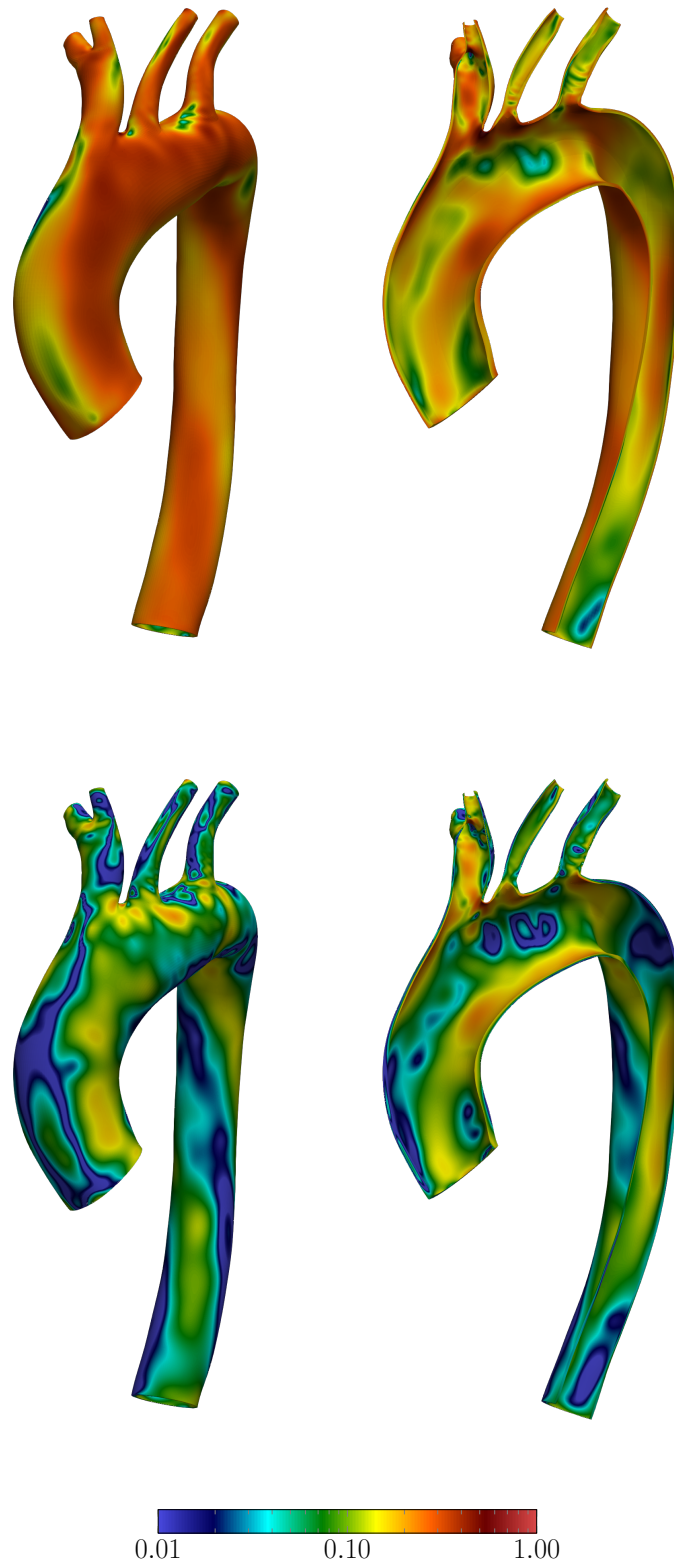


Figure 6.29: Patient-specific aorta geometry. The  $|1 - (\lambda_1)^0 / (\lambda_1)^\infty|$  with the method in Chapter 5 (*top*) and this chapter (*bottom*)

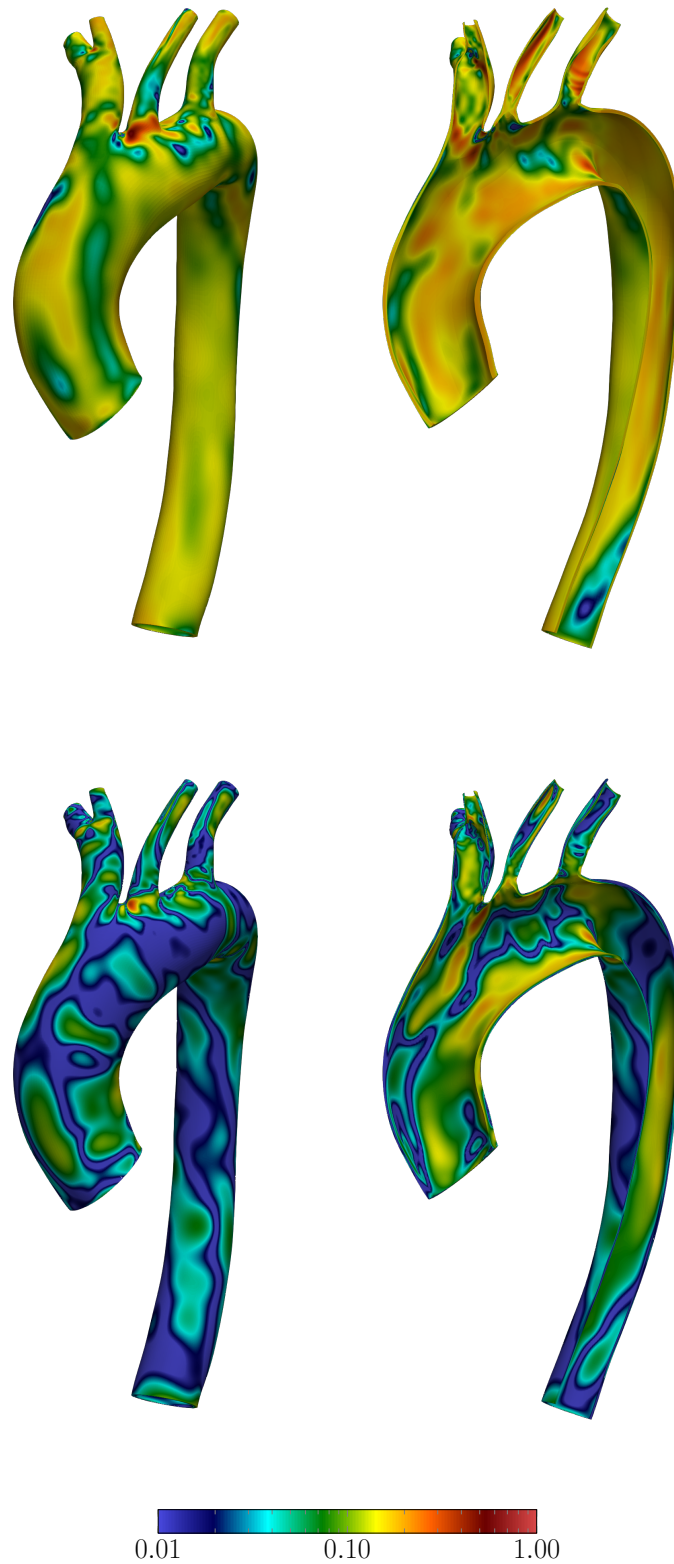


Figure 6.30: Patient-specific aorta geometry. The  $|1 - (\lambda_2)^0 / (\lambda_2)^\infty|$  with the method in Chapter 5 (*top*) and this chapter (*bottom*)

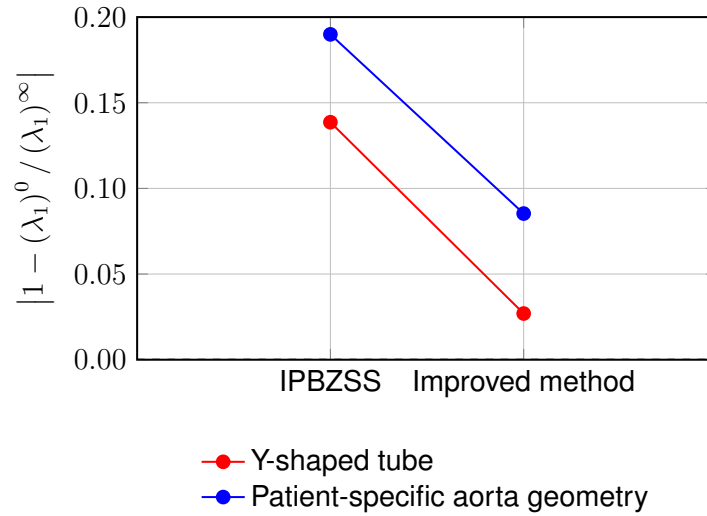


Figure 6.31: Average  $|1 - (\lambda_1)^0 / (\lambda_1)^\infty|$ . Y-shaped tube (*red*) and the patient-specific aorta geometry (*blue*)

### 6.4.2 Stretch distribution

From Figure 6.20, there are non-uniform stretch distributions even at non-branched regions. Gaussian curvature distribution is shown in Figure 6.32, and it is good way to recognize the distributions. The negative Gaussian curvature regions mean saddle points. The distribution is similar to the stretch distribution in Figure 6.20. Given that the initial guess design is based on the current  $\hat{k}_1 h_{th}$  and  $\hat{k}_2 h_{th}$  in Figure 6.3, especially in the saddle points, a large departure from symmetry is observed. That may be caused by searching two unknowns,  $\phi_1$  and  $\phi_2$ . In most cases, the initial guess theory gives smooth and symmetric solutions in Figure 6.3. However, the values are especially sensitive at the saddle-point regions. Given that the theory is based on the force equilibrium in the normal direction, the local equilibrium is assumed as satisfied. In focus on the force equilibrium in the tangential direction, it should be considered as a global problem such as the relationships of neighbors. Here, since the aorta geometry almost has positive curvatures, most of the regions are under tension. However the negative curvature regions such as the saddle points, it is difficult to satisfy the tangential equilibrium with the other positive curvature regions. Of course, regions both curvatures negative should have the

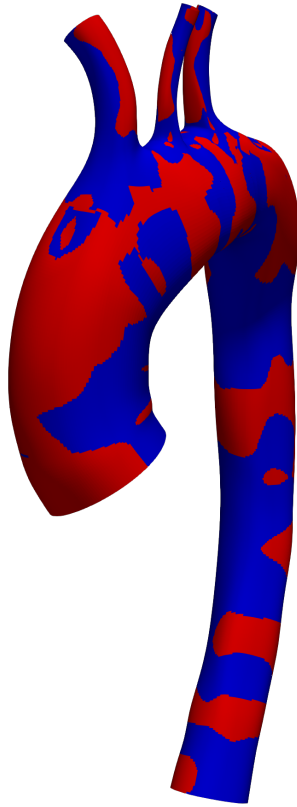


Figure 6.32: Patient-specific aorta geometry. Gaussian curvature. Positive value regions (*red*) and negative value regions (*blue*)

same difficulty. This is the reason why the Gaussian curvature distribution is similar to the stretch distribution, and the design could be improved with other additional equilibrium assumptions.

## 6.5 Concluding remarks

The objective of this chapter was to design the ZSS initial guess with analytical solutions of the force equilibrium. The force equilibrium in the normal direction was based on Kirchhoff–Love shell theory and the plane-stress condition, which gives proper constraints of the ZSS design parameters. In addition, an update of the wall coordinate system, which is introduced in Section 5.1, was introduced.

3D test computations with straight-tube configurations gave results that the initial guess was very similar to the converged results on both  $\mathbf{g}_3$  directions: normal and skewed. That means that both the new design of the ZSS initial guess and the modified wall coordinate system were worked well on the configurations. Given that the new design of the ZSS initial guess is based on the Kirchhoff–Love shell theory and the plane-stress condition, such an ideal tube and sphere configurations satisfy the assumptions well. The 3D computation with a Y-shaped tube resulted that the initial guess is very similar to the converged results with few errors at saddle points. With observing the result, an additional improvement depends on a relationship between  $\hat{k}_1 h_{th}$  and  $\hat{k}_2 h_{th}$  is newly introduced. With the improvement, a 3D computation with a patient-specific aorta geometry resulted that the ZSS initial guess is similar to the converged result. After how the method works were shown, the results were compared to the past results in Chapters 5. It was recognized visually and quantitatively that the new method has better initial guess with compared to the earlier method described in Chapter 5. In addition, the stretch values were in the reasonable range. The possibility for more anatomical modification was revealed with the observation about the force equilibrium.

## Chapter 7

### Concluding Remarks

The objective of this thesis was to introduce medical-image-based aorta modeling with ZSS estimation with anatomical observation. For the objective, the following challenges obtained from the existing researches were focused.

**Challenge 1:** Convergence incompleteness according to the geometry complexity

**Challenge 2:** The converged ZSS without anatomical observation

The following three approaches were set for the challenges:

**Approach A:** Apply higher-order shape functions to the EBZSS

**Approach B:** Impose integration-point-based strain

**Approach C:** Design a ZSS initial guess with analytical solutions of the force equilibrium

In Chapters 4 and 5, the ZSS estimation was successfully adapted to the geometries which have convex-concave and branched regions. In particular, the IPBZSS estimation method described in Chapter 5 was successfully applied to patient-specific aorta geometries which have branches with well-converged results. In Chapter 6, the ZSS initial guess was improved with analytical solutions of the force equilibrium based on the Kirchhoff–Love shell theory and the plane-stress condition. Given that the converged result was very similar to the initial guess, we could conclude that the converged ZSS was successfully based on the anatomical observation. From the results in Chapters 4–6, both Challenge 1: convergence incompleteness according to the geometry complexity and Challenge 2: the converged ZSS without anatomical observation, were solved. Thus, the ZSS modeling



with anatomical observation was successfully introduced, finally. The following sections present concluding remarks in each chapter.

## **7.1 EBZSS estimation with isogeometric discretization**

In Chapter 4, the objective was to apply higher-order shape functions to the EBZSS estimation method as the abovementioned (see Section 1.4). The extension of the EBZSS estimation method by applying the isogeometric discretization was introduced and has been successfully applied to a patient-specific modeling of a human aorta, which has convex-concave regions. 2D test computations with straight-tube configurations showed how the new EBZSS method works, and decided enough resolutions in the circumferential direction and the circumferential residual stretch as the ZSS design parameter. In addition, a 3D computation with matches the deformed shape to the medical-image-based geometry represented well-converged results.

From above results, the following challenges remained. The first challenge is the ZSS initial guess was far from the converged ZSS. It means the anatomical ZSS design was not applied well on the converged ZSS. The second challenge is that the EBZSS iterative method depends on the control mesh structure. The method imposes displacements, calculated from the stretch on the surface, on element-based control points. T-spline is a useful representation for more complex geometry, but the control mesh could be unstructured connections. Since that connections could set the point far from the physical surface, T-spline representation with the EBZSS has convergence difficulty.

## **7.2 IPBZSS estimation**

In Chapter 5, the objective was to impose integration-point-based strain using the components of its metric tensor. That is called IPBZSS, especially the method is applied with T-spline representation for unstructured geometries such as branched points. The method which was introduced in this chapter tried to directly impose the residual strain at each

integration point, which is on the physical position on the geometry, instead of element-based control points. In the EBTL method with IPBZSS, the conversion between IPBZSS and EBZSS was also introduced. In particular to the ZSS initial guess, the ZSS is based on an inner-surface geometry and its design parameters. Therefore, the ZSS initial guess modeling based on the shell model was introduced.

3D test computations with a Y-shaped tube and patient-specific aorta geometry is coming from medical images resulted well convergence even at the branched points. This is the outcome of the IPBZSS. With the result of the EBZSS converted from the IPBZSS, the EBZSS is also a reasonable representation regarding observing the inclination of high or low stretch distribution. Here, two challenges remained. First, unphysical stretch values were observed at branched points of the patient-specific aorta geometry. Second, the ZSS initial guess was far from the converged ZSS: it means the anatomical ZSS design was not applied well on the converged ZSS. Given that these problems might be related each other, more anatomical ZSS initial modeling could estimate more reasonable results.

### **7.3 ZSS estimation with anatomical observation**

In Chapter 6, the objective was to design ZSS initial guess with analytical solutions of the force equilibrium. The force equilibrium in the normal direction was based on Kirchhoff–Love shell theory and the plane-stress condition, which gives proper constraints of the ZSS design parameters. In addition, an update of the wall coordinate system, which is introduced in Section 5.1, was introduced.

3D test computations with straight-tube configurations gave results that the initial guess was very similar to the converged results on both  $\mathbf{g}_3$  directions: normal and skewed. That means that both the new design of the ZSS initial guess and the modified wall coordinate system were worked well on the configurations. Given that the new design of the ZSS initial guess is based on the Kirchhoff–Love shell theory and the plane-stress condition, such an ideal tube and sphere configurations satisfy the assumptions well. The 3D

computation with a Y-shaped tube resulted that the initial guess is very similar to the converged results with few errors at saddle points. With observing the result, an additional improvement depends on a relationship between  $\hat{k}_1 h_{th}$  and  $\hat{k}_2 h_{th}$  is newly introduced. With the improvement, a 3D computation with a patient-specific aorta geometry resulted that the ZSS initial guess is similar to the converged result. After how the method works were shown, the results were compared to the past results in Chapters 5. It was recognized visually and quantitatively that the new method has better initial guess with compared to the earlier method described in Chapter 5. In addition, the stretch values were in the reasonable range. The possibility for more anatomical modification was revealed with the observation about the force equilibrium.

# Appendix A

## Constitutive models

### A.1 Neo-Hookean model

The isochoric part of the strain energy function for the neo-Hookean model [104, 105] is written as:

$$(\varphi_{\text{iso}})_{\text{NH}} = c_{10}(\bar{I}_1 - 3), \quad (\text{A.1})$$

where  $c_{10}$  is the material constant, and the shear modulus at the undeformed shape is  $2c_{10}$ .

With Eq. (2.183), the coefficients of  $\mathbf{S}$  for the neo-Hookean model are

$$\left(\bar{\bar{S}}_{\text{NH}}\right)_1 = J^{-2/3} \left(\bar{S}_{\text{NH}}\right)_1 = 2J^{-2/3} \frac{\partial(\varphi_{\text{iso}})_{\text{NH}}}{\partial \bar{I}_1} = 2J^{-2/3} c_{10}, \quad \left(\bar{\bar{S}}_{\text{NH}}\right)_2 = 0. \quad (\text{A.2})$$

The contravariant components of  $\mathbf{S}_{\text{iso}}$  for the neo-Hookean model can be expressed with Eqs. (2.202) and (A.2) as:

$$(S_{\text{NH}})_{\text{iso}}^{IJ} = \left(\bar{\bar{S}}_{\text{NH}}\right)_1 \left( G^{IJ} - \frac{1}{3} I_1 \bar{C}^{IJ} \right) + \left(\bar{\bar{S}}_{\text{NH}}\right)_2 \left( C^{IJ} - \frac{1}{3} II_1 \bar{C}^{IJ} \right) \quad (\text{A.3})$$

$$= \left(\bar{\bar{S}}_{\text{NH}}\right)_1 \left( G^{IJ} - \frac{1}{3} I_1 g^{IJ} \right). \quad (\text{A.4})$$

With Eq. (2.246), the coefficients for the elastic moduli for the neo-Hookean model are

$$\left(\bar{\bar{\bar{C}}}_{\text{NH}}\right)_1 = \left(\bar{\bar{\bar{C}}}_{\text{NH}}\right)_2 = \left(\bar{\bar{\bar{C}}}_{\text{NH}}\right)_3 = \left(\bar{\bar{\bar{C}}}_{\text{NH}}\right)_4 = 0. \quad (\text{A.5})$$

The contravariant components of  $\mathbb{C}_{\text{iso}}$  for the neo-Hookean model can be expressed with Eqs. (2.247) and (A.5) as:

$$\begin{aligned}
(\mathbb{C}_{\text{NH}})_{\text{iso}}^{IJKL} &= \left( (\bar{\bar{\mathbb{C}}}_{\text{NH}})_1 + \frac{2}{I_1} (\bar{\bar{\mathcal{S}}}_{\text{NH}})_1 \right) \left( G^{IJ} - \frac{1}{3} I_1 \bar{C}^{IJ} \right) \left( G^{KL} - \frac{1}{3} I_1 \bar{C}^{KL} \right) \\
&\quad + (\bar{\bar{\mathbb{C}}}_{\text{NH}})_2 \left( \left( G^{IJ} - \frac{1}{3} I_1 \bar{C}^{IJ} \right) \left( C^{KL} - \frac{1}{3} II_1 \bar{C}^{KL} \right) + \left( C^{IJ} - \frac{1}{3} II_1 \bar{C}^{IJ} \right) \left( G^{KL} - \frac{1}{3} I_1 \bar{C}^{KL} \right) \right) \\
&\quad + \left( (\bar{\bar{\mathbb{C}}}_{\text{NH}})_3 + \frac{1}{II_1} (\bar{\bar{\mathbb{C}}}_{\text{NH}})_4 + \frac{2}{II_1} (\bar{\bar{\mathcal{S}}}_{\text{NH}})_2 \right) \left( C^{IJ} - \frac{1}{3} II_1 \bar{C}^{IJ} \right) \left( C^{KL} - \frac{1}{3} II_1 \bar{C}^{KL} \right) \\
&\quad + (\bar{\bar{\mathbb{C}}}_{\text{NH}})_4 G^{IJ} \odot G^{KL} + \frac{2}{3} (I_1 (\bar{\bar{\mathcal{S}}}_{\text{NH}})_1 + II_1 (\bar{\bar{\mathcal{S}}}_{\text{NH}})_2) \bar{C}^{IJ} \odot \bar{C}^{KL} \\
&\quad - \frac{2}{I_1} (\bar{\bar{\mathcal{S}}}_{\text{NH}})_1 G^{IJ} G^{KL} - \frac{1}{II_1} \left( (\bar{\bar{\mathbb{C}}}_{\text{NH}})_4 + 2 (\bar{\bar{\mathcal{S}}}_{\text{NH}})_2 \right) C^{IJ} C^{KL} \tag{A.6}
\end{aligned}$$

$$\begin{aligned}
&= \frac{2}{I_1} (\bar{\bar{\mathcal{S}}}_{\text{NH}})_1 \left( G^{IJ} - \frac{1}{3} I_1 g^{IJ} \right) \left( G^{KL} - \frac{1}{3} I_1 g^{KL} \right) \\
&\quad + \frac{2}{3} I_1 (\bar{\bar{\mathcal{S}}}_{\text{NH}})_1 g^{IJ} \odot g^{KL} - \frac{2}{I_1} (\bar{\bar{\mathcal{S}}}_{\text{NH}})_1 G^{IJ} G^{KL}. \tag{A.7}
\end{aligned}$$

For the compressible shell model,

$$(S_{\text{NH}})_{\text{iso}}^{33} = (\bar{\bar{\mathcal{S}}}_{\text{NH}})_1 \left( 1 - \frac{1}{3C_{33}} I_1 \right) + (\bar{\bar{\mathcal{S}}}_{\text{NH}})_2 \left( C_{33} - \frac{1}{3C_{33}} II_1 \right) \tag{A.8}$$

$$= (\bar{\bar{\mathcal{S}}}_{\text{NH}})_1 \left( 1 - \frac{1}{3C_{33}} I_1 \right), \tag{A.9}$$

and

$$(\mathbb{C}_{\text{NH}})_{\text{iso}}^{\alpha\beta 33} = \left( (\bar{\bar{\mathbb{C}}}_{\text{NH}})_1 \left( 1 - \frac{1}{3C_{33}} I_1 \right) + (\bar{\bar{\mathbb{C}}}_{\text{NH}})_2 \left( C_{33} - \frac{1}{3C_{33}} II_1 \right) - \frac{2}{3C_{33}} (\bar{\bar{\mathcal{S}}}_{\text{NH}})_1 \right) G^{\alpha\beta}$$

$$\begin{aligned}
& + \left( (\bar{\bar{C}}_{\text{NH}})_2 \left( 1 - \frac{1}{3C_{33}} I_1 \right) + (\bar{\bar{C}}_{\text{NH}})_3 \left( C_{33} - \frac{1}{3C_{33}} II_1 \right) - \frac{1}{3C_{33}} (\bar{\bar{C}}_{\text{NH}})_4 - \frac{2}{3C_{33}} (\bar{\bar{S}}_{\text{NH}})_2 \right) C^{\alpha\beta} \\
& - \frac{1}{3} \left( I_1 (\bar{\bar{C}}_{\text{NH}})_1 \left( 1 - \frac{1}{3C_{33}} I_1 \right) + (\bar{\bar{C}}_{\text{NH}})_2 \left( C_{33} I_1 + II_1 - \frac{2}{3C_{33}} I_1 II_1 \right) \right. \\
& \quad \left. + II_1 (\bar{\bar{C}}_{\text{NH}})_3 \left( C_{33} - \frac{1}{3C_{33}} II_1 \right) + (\bar{\bar{C}}_{\text{NH}})_4 \left( C_{33} - \frac{1}{3C_{33}} II_1 \right) \right. \\
& \quad \left. + 2 (\bar{\bar{S}}_{\text{NH}})_1 \left( 1 - \frac{1}{3C_{33}} I_1 \right) + 2 (\bar{\bar{S}}_{\text{NH}})_2 \left( C_{33} - \frac{1}{3C_{33}} II_1 \right) \right) \bar{C}^{\alpha\beta},
\end{aligned} \tag{A.10}$$

$$= -\frac{2}{3C_{33}} (\bar{\bar{S}}_{\text{NH}})_1 G^{\alpha\beta} - \frac{2}{3} (\bar{\bar{S}}_{\text{NH}})_1 \left( 1 - \frac{1}{3C_{33}} I_1 \right) g^{\alpha\beta}, \tag{A.11}$$

$$\begin{aligned}
(\mathbb{C}_{\text{NH}})_{\text{iso}}^{3333} &= (\bar{\bar{C}}_{\text{NH}})_1 \left( 1 - \frac{1}{3C_{33}} I_1 \right)^2 + 2 (\bar{\bar{C}}_{\text{NH}})_2 \left( 1 - \frac{1}{3C_{33}} I_1 \right) \left( C_{33} - \frac{1}{3C_{33}} II_1 \right) \\
& \quad + (\bar{\bar{C}}_{\text{NH}})_3 \left( C_{33} - \frac{1}{3C_{33}} II_1 \right)^2 + \frac{1}{3} (\bar{\bar{C}}_{\text{NH}})_4 \left( 1 + \frac{1}{3C_{33}^2} II_1 \right) \\
& \quad + \frac{4}{3C_{33}} (\bar{\bar{S}}_{\text{NH}})_1 \left( \frac{2}{3C_{33}} I_1 - 1 \right) + \frac{4}{3C_{33}} (\bar{\bar{S}}_{\text{NH}})_2 \left( \frac{2}{3C_{33}} II_1 - C_{33} \right)
\end{aligned} \tag{A.12}$$

$$= \frac{4}{3C_{33}} (\bar{\bar{S}}_{\text{NH}})_1 \left( \frac{2}{3C_{33}} I_1 - 1 \right), \tag{A.13}$$

are given.

## A.2 The isotropic version of Kappa model

The Kappa model is originally proposed in [106], and it is for anisotropic material. The model is simplified for isotropic materials in [107]. Here, this simplified model is called the Kappa model. The isochoric part of the strain energy function for the model is written as:

$$(\varphi_{\text{iso}})_{\text{IK}} = c_{10}(\bar{I}_1 - 3) + D_1 \left( e^{D_2(\bar{I}_1 - 3)^2} - 1 \right) \quad (\text{A.14})$$

where  $c_{10}$  are  $D_1$  stress-like,  $D_2$  is a dimensionless material constant. With Eq. (2.183), the coefficients of  $\mathbf{S}$  for the Kappa model are

$$\left. \begin{aligned} (\bar{\bar{S}}_{\text{IK}})_1 &= J^{-2/3} (\bar{S}_{\text{IK}})_1 = 2J^{-2/3} \frac{\partial(\varphi_{\text{iso}})_{\text{IK}}}{\partial \bar{I}_1}, \\ &= 2J^{-2/3} \left( c_{10} + 2D_1 D_2 (\bar{I}_1 - 3) e^{D_2(\bar{I}_1 - 3)^2} \right), \\ (\bar{\bar{S}}_{\text{IK}})_2 &= 0. \end{aligned} \right\} \quad (\text{A.15})$$

The contravariant components of  $\mathbf{S}_{\text{iso}}$  for the Kappa model can be expressed with Eq. (2.202) and (A.15) as:

$$(S_{\text{IK}})_{\text{iso}}^{IJ} = (\bar{\bar{S}}_{\text{IK}})_1 \left( G^{IJ} - \frac{1}{3} I_1 \bar{C}^{IJ} \right) + (\bar{\bar{S}}_{\text{IK}})_2 \left( g_{KL} G^{IK} G^{JL} - \frac{1}{3} II_1 \bar{C}^{IJ} \right), \quad (\text{A.16})$$

$$= (\bar{\bar{S}}_{\text{IK}})_1 \left( G^{IJ} - \frac{1}{3} I_1 g^{IJ} \right). \quad (\text{A.17})$$

With Eq. (2.246), the coefficients of  $\mathbf{C}$  for the Kappa model are

$$\left. \begin{aligned} (\bar{\bar{C}}_{\text{IK}})_1 &= J^{-4/3} (\bar{C}_{\text{IK}}) = 8J^{-4/3} D_1 D_2 e^{D_2(\bar{I}_1 - 3)^2} \left( 1 + 2D_2 (\bar{I}_1 - 3)^2 \right), \\ (\bar{\bar{C}}_{\text{IK}})_2 &= (\bar{\bar{C}}_{\text{IK}})_3 = (\bar{\bar{C}}_{\text{IK}})_4 = 0. \end{aligned} \right\} \quad (\text{A.18})$$

The contravariant components of  $\mathbb{C}_{\text{iso}}$  for the Kappa model can be expressed with Eqs. (2.247)

and (A.18) as:

$$\begin{aligned}
(\mathbb{C}_{\text{IK}})_{\text{iso}}^{IJKL} &= \left( (\bar{\bar{\mathbb{C}}}_{\text{IK}})_1 + \frac{2}{I_1} (\bar{\bar{S}}_{\text{IK}})_1 \right) \left( G^{IJ} - \frac{1}{3} I_1 \bar{C}^{IJ} \right) \left( G^{KL} - \frac{1}{3} I_1 \bar{C}^{KL} \right) \\
&\quad + (\bar{\bar{\mathbb{C}}}_{\text{IK}})_2 \left( \left( G^{IJ} - \frac{1}{3} I_1 \bar{C}^{IJ} \right) \left( C^{KL} - \frac{1}{3} II_1 \bar{C}^{KL} \right) + \left( C^{IJ} - \frac{1}{3} II_1 \bar{C}^{IJ} \right) \left( G^{KL} - \frac{1}{3} I_1 \bar{C}^{KL} \right) \right) \\
&\quad + \left( (\bar{\bar{\mathbb{C}}}_{\text{IK}})_3 + \frac{1}{II_1} (\bar{\bar{\mathbb{C}}}_{\text{IK}})_4 + \frac{2}{II_1} (\bar{\bar{S}}_{\text{IK}})_2 \right) \left( C^{IJ} - \frac{1}{3} II_1 \bar{C}^{IJ} \right) \left( C^{KL} - \frac{1}{3} II_1 \bar{C}^{KL} \right) \\
&\quad + (\bar{\bar{\mathbb{C}}}_{\text{IK}})_4 G^{IJ} \odot G^{KL} + \frac{2}{3} (I_1 (\bar{\bar{S}}_{\text{IK}})_1 + II_1 (\bar{\bar{S}}_{\text{IK}})_2) \bar{C}^{IJ} \odot \bar{C}^{KL} \\
&\quad - \frac{2}{I_1} (\bar{\bar{S}}_{\text{IK}})_1 G^{IJ} G^{KL} - \frac{1}{II_1} \left( (\bar{\bar{\mathbb{C}}}_{\text{IK}})_4 + 2 (\bar{\bar{S}}_{\text{IK}})_2 \right) C^{IJ} C^{KL} \tag{A.19}
\end{aligned}$$

$$\begin{aligned}
&= \left( (\bar{\bar{\mathbb{C}}}_{\text{IK}})_1 + \frac{2}{I_1} (\bar{\bar{S}}_{\text{IK}})_1 \right) \left( G^{IJ} - \frac{1}{3} I_1 g^{IJ} \right) \left( G^{KL} - \frac{1}{3} I_1 g^{KL} \right) \\
&\quad + \frac{2}{3} I_1 (\bar{\bar{S}}_{\text{IK}})_1 g^{IJ} \odot g^{KL} - \frac{2}{I_1} (\bar{\bar{S}}_{\text{IK}})_1 G^{IJ} G^{KL}. \tag{A.20}
\end{aligned}$$

For the compressible shell model,

$$(\mathcal{S}_{\text{IK}})_{\text{iso}}^{33} = (\bar{\bar{S}}_{\text{IK}})_1 \left( 1 - \frac{1}{3C_{33}} I_1 \right) + (\bar{\bar{S}}_{\text{IK}})_2 \left( C_{33} - \frac{1}{3C_{33}} II_1 \right) \tag{A.21}$$

$$= (\bar{\bar{S}}_{\text{IK}})_1 \left( 1 - \frac{1}{3C_{33}} I_1 \right), \tag{A.22}$$

$$(\mathbb{C}_{\text{IK}})_{\text{iso}}^{\alpha\beta 33} = \left( (\bar{\bar{\mathbb{C}}}_{\text{IK}})_1 \left( 1 - \frac{1}{3C_{33}} I_1 \right) + (\bar{\bar{\mathbb{C}}}_{\text{IK}})_2 \left( C_{33} - \frac{1}{3C_{33}} II_1 \right) - \frac{2}{3C_{33}} (\bar{\bar{S}}_{\text{IK}})_1 \right) G^{\alpha\beta}$$



$$\begin{aligned}
& + \left( (\bar{\bar{C}}_{\text{IK}})_2 \left( 1 - \frac{1}{3C_{33}} I_1 \right) + (\bar{\bar{C}}_{\text{IK}})_3 \left( C_{33} - \frac{1}{3C_{33}} II_1 \right) - \frac{1}{3C_{33}} (\bar{\bar{C}}_{\text{IK}})_4 - \frac{2}{3C_{33}} (\bar{\bar{S}}_{\text{IK}})_2 \right) C^{\alpha\beta} \\
& - \frac{1}{3} \left( I_1 (\bar{\bar{C}}_{\text{IK}})_1 \left( 1 - \frac{1}{3C_{33}} I_1 \right) + (\bar{\bar{C}}_{\text{IK}})_2 \left( C_{33} I_1 + II_1 - \frac{2}{3C_{33}} I_1 II_1 \right) \right. \\
& \quad \left. + II_1 (\bar{\bar{C}}_{\text{IK}})_3 \left( C_{33} - \frac{1}{3C_{33}} II_1 \right) + (\bar{\bar{C}}_{\text{IK}})_4 \left( C_{33} - \frac{1}{3C_{33}} II_1 \right) \right. \\
& \quad \left. + 2 (\bar{\bar{S}}_{\text{IK}})_1 \left( 1 - \frac{1}{3C_{33}} I_1 \right) + 2 (\bar{\bar{S}}_{\text{IK}})_2 \left( C_{33} - \frac{1}{3C_{33}} II_1 \right) \right) \bar{C}^{\alpha\beta} \quad (\text{A.23})
\end{aligned}$$

$$\begin{aligned}
& = \left( (\bar{\bar{C}}_{\text{IK}})_1 \left( 1 - \frac{1}{3C_{33}} I_1 \right) - \frac{2}{3C_{33}} (\bar{\bar{S}}_{\text{IK}})_1 \right) G^{\alpha\beta} \\
& - \frac{1}{3} \left( I_1 (\bar{\bar{C}}_{\text{IK}})_1 \left( 1 - \frac{1}{3C_{33}} I_1 \right) + 2 (\bar{\bar{S}}_{\text{IK}})_1 \left( 1 - \frac{1}{3C_{33}} I_1 \right) \right) g^{\alpha\beta} \quad (\text{A.24})
\end{aligned}$$

$$\begin{aligned}
& = \left( (\bar{\bar{C}}_{\text{IK}})_1 \left( 1 - \frac{1}{3C_{33}} I_1 \right) - \frac{2}{3C_{33}} (\bar{\bar{S}}_{\text{IK}})_1 \right) G^{\alpha\beta} \\
& - \frac{1}{3} (I_1 (\bar{\bar{C}}_{\text{IK}})_1 + 2 (\bar{\bar{S}}_{\text{IK}})_1) \left( 1 - \frac{1}{3C_{33}} I_1 \right) g^{\alpha\beta}, \quad (\text{A.25})
\end{aligned}$$

and

$$\begin{aligned}
(\mathbb{C}_{\text{IK}})_{\text{iso}}^{3333} & = (\bar{\bar{C}}_{\text{IK}})_1 \left( 1 - \frac{1}{3C_{33}} I_1 \right)^2 + 2 (\bar{\bar{C}}_{\text{IK}})_2 \left( 1 - \frac{1}{3C_{33}} I_1 \right) \left( C_{33} - \frac{1}{3C_{33}} II_1 \right) \\
& + (\bar{\bar{C}}_{\text{IK}})_3 \left( C_{33} - \frac{1}{3C_{33}} II_1 \right)^2 + \frac{1}{3} (\bar{\bar{C}}_{\text{IK}})_4 \left( 1 + \frac{1}{3C_{33}^2} II_1 \right) \\
& + \frac{4}{3C_{33}} (\bar{\bar{S}}_{\text{IK}})_1 \left( \frac{2}{3C_{33}} I_1 - 1 \right) + \frac{4}{3C_{33}} (\bar{\bar{S}}_{\text{IK}})_2 \left( \frac{2}{3C_{33}} II_1 - C_{33} \right) \quad (\text{A.26})
\end{aligned}$$

$$= (\bar{\bar{C}}_{\text{IK}})_1 \left( 1 - \frac{1}{3C_{33}} I_1 \right)^2 + \frac{4}{3C_{33}} (\bar{\bar{S}}_{\text{IK}})_1 \left( \frac{2}{3C_{33}} I_1 - 1 \right), \quad (\text{A.27})$$

are given.

## Bibliography

- [1] H. Adachi, M. Ono, K. Sakamoto, H. Shimizu, and T. Miyata, *Textbook of cardiovascular surgery*. Chugai-Igakusha, 2016, ISBN 9784498039148, (in Japanese).
- [2] G. Holzapfel and T. Gasser, “A new constitutive framework for arterial wall mechanics and a comparative study of material models”, *Journal of Elasticity*, **61** (2000) 1–48.
- [3] Y. Fung, “Biomechanics: Circulation”, *Springer-Verlag*.
- [4] G. Holzapfel, G. Sommer, M. Auer, P. Regitnig, and R. Ogden, “Layer-specific 3D residual deformations of human aortas with non-atherosclerotic intimal thickening”, *Annals of Biomedical Engineering*, **35** (2007) 530–545.
- [5] D. Sokolis, G. Savva, S. Papadodima, and S. Kourkoulis, “Regional distribution of circumferential residual strains in the human aorta according to age and gender”, *Journal of the Mechanical Behaviour of Biomedical Materials*, **67** (2017) 87–100.
- [6] M.A. Scott, R.N. Simpson, J.A. Evans, S. Lipton, S.P.A. Bordas, T.J.R. Hughes, and T.W. Sederberg, “Isogeometric boundary element analysis using unstructured T-splines”, *Computer Methods in Applied Mechanics and Engineering*, **254** (2013) 197–221, doi:h10.1016/j.cma.2012.11.001.
- [7] A. Burton, “Relation of structure to function of the tissues of the wall of blood vessels”, *Physiological Reviews*, **34** (4) (1954) 619–642.
- [8] J. Humphrey, *Cardiovascular solid mechanics: cells, tissues, and organs*. Springer Science & Business Media, 2002, ISBN 978-1-4419-2897-9.

- [9] G. Holzapfel, “Determination of material models for arterial walls from uniaxial extension tests and histological structure”, *Journal of Theoretical Biology*, **238** (2006) 290–302.
- [10] W. Hoppmann and L. Wan, “Large deformation of elastic tubes”, *Journal of Biomechanics*, **3** (1970) 593–600.
- [11] E.S. Neto, D. Peric, and D. Owen, *Computational methods for plasticity: theory and applications*. John Wiley & Sons, 2011, ISBN 978-0-470-69452-7.
- [12] I. Mirsky, “Ventricular and arterial wall stresses based on large deformation analyses”, *Biophysical Journal*, **13** (1973) 1141–1159.
- [13] Y. Fung, K. Fronek, and P. Patitucci, “Pseudoelasticity of arteries and the choice of its mathematical expression”, *American Journal of Physiology*, **237** (1979) H620–H631.
- [14] Y. Fung, “On the foundations of biomechanics”, *Journal of Applied Mechanics*, **50** (1983) 1003–1009.
- [15] R. Vaishnav and J. Vossoughi, “Estimation of residual strains in aortic segments”, *Biomedical Engineering*, (1983) 330–333.
- [16] C. Chuong and Y. Fung, “Residual stress in arteries”, *Frontiers in Biomechanics*, **50** (1983) 1003–1009.
- [17] A. Rachev, “Theoretical study of the effect of stress-dependent remodeling on arterial geometry under hypertensive conditions”, *Journal of Biomechanics*, **30** (1997) 819–827.
- [18] A. Rachev and K. Hayashi, “Theoretical study of the effects of vascular smooth muscle contraction on strain and stress distributions in arteries”, *Annals of Biomechanical Engineering*, **27** (1999) 459–468.

- [19] A. Malek, S. Alper, and S. Izumo, “Hemodynamic shear stress and its role in atherosclerosis”, *JAMA*, **282** (1999) 2035–2042.
- [20] J. Paszkowiak and A. Dardik, “Arterial wall shear stress: Observations from the bench to the bedside”, *Vascular and Endovascular Surgery*, **37** (2003) 47–57.
- [21] H. Himburg, D. Grzybowski, A. Hazel, J. LaMack, X.-M. Li, and M. Friedman, “Spatial comparison between wall shear stress measures and porcine arterial endothelial permeability”, *American Journal of Physiology-Heart and Circulatory Physiology*, **286** (2004) 1916–1922.
- [22] R. Reneman, T. Arts, and A. Hoeks, “Wall shear stress - an important determinant of endothelial cell function and structure - in the arterial system in vivo”, *Journal of Vascular Research*, **43** (2006) 251–269.
- [23] L.-D. Jou, D. Lee, H. Morsi, and M. Mawad, “Wall shear stress on ruptured and unruptured intracranial aneurysms at the internal carotid artery”, *American Journal of Neuroradiology*, **29** (2008) 1761–1767.
- [24] T. Papaioannou and G. Stefanadis, “Vascular wall shear stress: basic principles and methods”, *Hellenic Journal of Cardiology*, **46** (2005) 9–15.
- [25] L. Speelman, E. Bosboom, G. Schurink, J. Buth, M. Breeuwer, M. Jacobs, and F. van de Vosse, “Initial stress and nonlinear material behavior in patient-specific AAA wall stress analysis”, *Journal of Biomechanics*, **42** (2009) 1713–1719.
- [26] V. Vavourakis, Y. Papaharilaou, and J. Ekaterinaris, “Coupled fluid-structure interaction hemodynamics in a zero-pressure state corrected arterial geometry”, *Journal of Biomechanics*, **44** (2011) 2453–2460.
- [27] K. Tatsuno, H. Shigematsu, H. Makuuchi, R. Yozu, and H. Adachi, *Textbook of cardiovascular surgery*. Chugai-Igakusha, 2011, ISBN 9784498039117.

- [28] C. Ochiai, *Visual Book of Cardiovascular Diseases*. Gakken, 2010, (in Japanese).
- [29] JCS Joint Working Group, “Guidelines for diagnosis and treatment of aortic aneurysm and aortic dissection (JCS 2011)”, *Circulation Journal*, **77** (2011) 789–828.
- [30] R. Araki, *Fundamentals of MRI*. Medical Science International, 2004, (in Japanese).
- [31] R. Torii, M. Oshima, T. Kobayashi, K. Takagi, and T.E. Tezduyar, “Computation of cardiovascular fluid–structure interactions with the DSD/SST method”, in *Proceedings of the 6th World Congress on Computational Mechanics (CD-ROM)*, Beijing, China, (2004).
- [32] R. Torii, M. Oshima, T. Kobayashi, K. Takagi, and T.E. Tezduyar, “Influence of wall elasticity on image-based blood flow simulations”, *Transactions of the Japan Society of Mechanical Engineers Series A*, **70** (2004) 1224–1231, in Japanese, doi:10.1299/kikaia.70.1224.
- [33] R. Torii, M. Oshima, T. Kobayashi, K. Takagi, and T.E. Tezduyar, “Computer modeling of cardiovascular fluid–structure interactions with the Deforming-Spatial-Domain/Stabilized Space–Time formulation”, *Computer Methods in Applied Mechanics and Engineering*, **195** (2006) 1885–1895, doi:10.1016/j.cma.2005.05.050.
- [34] R. Torii, M. Oshima, T. Kobayashi, K. Takagi, and T.E. Tezduyar, “Fluid–structure interaction modeling of aneurysmal conditions with high and normal blood pressures”, *Computational Mechanics*, **38** (2006) 482–490, doi:10.1007/s00466-006-0065-6.
- [35] Y. Bazilevs, V.M. Calo, Y. Zhang, and T.J.R. Hughes, “Isogeometric fluid–structure interaction analysis with applications to arterial blood flow”, *Computational Mechanics*, **38** (2006) 310–322.

- [36] Y. Bazilevs, V.M. Calo, T.E. Tezduyar, and T.J.R. Hughes, “ $\gamma$  discontinuity-capturing for advection-dominated processes with application to arterial drug delivery”, *International Journal for Numerical Methods in Fluids*, **54** (2007) 593–608, doi:10.1002/flid.1484.
- [37] Y. Bazilevs, V.M. Calo, T.J.R. Hughes, and Y. Zhang, “Isogeometric fluid–structure interaction: theory, algorithms, and computations”, *Computational Mechanics*, **43** (2008) 3–37.
- [38] J.G. Isaksen, Y. Bazilevs, T. Kvamsdal, Y. Zhang, J.H. Kaspersen, K. Waterloo, B. Romner, and T. Ingebrigtsen, “Determination of wall tension in cerebral artery aneurysms by numerical simulation”, *Stroke*, **39** (2008) 3172–3178.
- [39] Y. Bazilevs, J.R. Gohean, T.J.R. Hughes, R.D. Moser, and Y. Zhang, “Patient-specific isogeometric fluid–structure interaction analysis of thoracic aortic blood flow due to implantation of the Jarvik 2000 left ventricular assist device”, *Computer Methods in Applied Mechanics and Engineering*, **198** (2009) 3534–3550.
- [40] Y. Bazilevs, M.-C. Hsu, D. Benson, S. Sankaran, and A. Marsden, “Computational fluid–structure interaction: Methods and application to a total cavopulmonary connection”, *Computational Mechanics*, **45** (2009) 77–89.
- [41] Y. Bazilevs, M.-C. Hsu, Y. Zhang, W. Wang, X. Liang, T. Kvamsdal, R. Brekken, and J. Isaksen, “A fully-coupled fluid–structure interaction simulation of cerebral aneurysms”, *Computational Mechanics*, **46** (2010) 3–16.
- [42] K. Sugiyama, S. Ii, S. Takeuchi, S. Takagi, and Y. Matsumoto, “Full Eulerian simulations of biconcave neo-Hookean particles in a Poiseuille flow”, *Computational Mechanics*, **46** (2010) 147–157.
- [43] Y. Bazilevs, M.-C. Hsu, Y. Zhang, W. Wang, T. Kvamsdal, S. Hentschel, and J. Isaksen, “Computational fluid–structure interaction: Methods and applica-

- tion to cerebral aneurysms”, *Biomechanics and Modeling in Mechanobiology*, **9** (2010) 481–498.
- [44] Y. Bazilevs, J.C. del Alamo, and J.D. Humphrey, “From imaging to prediction: Emerging non-invasive methods in pediatric cardiology”, *Progress in Pediatric Cardiology*, **30** (2010) 81–89.
- [45] M.-C. Hsu and Y. Bazilevs, “Blood vessel tissue prestress modeling for vascular fluid–structure interaction simulations”, *Finite Elements in Analysis and Design*, **47** (2011) 593–599.
- [46] J.Y. Yao, G.R. Liu, D.A. Narmoneva, R.B. Hinton, and Z.-Q. Zhang, “Immersed smoothed finite element method for fluid–structure interaction simulation of aortic valves”, *Computational Mechanics*, **50** (2012) 789–804.
- [47] Y. Bazilevs, K. Takizawa, and T.E. Tezduyar, *Computational Fluid–Structure Interaction: Methods and Applications*. Wiley, February 2013, ISBN 978-0470978771.
- [48] Y. Bazilevs, K. Takizawa, and T.E. Tezduyar, “Challenges and directions in computational fluid–structure interaction”, *Mathematical Models and Methods in Applied Sciences*, **23** (2013) 215–221, doi:10.1142/S0218202513400010.
- [49] C.C. Long, A.L. Marsden, and Y. Bazilevs, “Fluid–structure interaction simulation of pulsatile ventricular assist devices”, *Computational Mechanics*, **52** (2013) 971–981, doi:10.1007/s00466-013-0858-3.
- [50] M. Esmaily-Moghadam, Y. Bazilevs, and A.L. Marsden, “A new preconditioning technique for implicitly coupled multidomain simulations with applications to hemodynamics”, *Computational Mechanics*, **52** (2013) 1141–1152, doi:10.1007/s00466-013-0868-1.
- [51] C.C. Long, M. Esmaily-Moghadam, A.L. Marsden, and Y. Bazilevs, “Computation



- of residence time in the simulation of pulsatile ventricular assist devices”, *Computational Mechanics*, **54** (2014) 911–919, doi:10.1007/s00466-013-0931-y.
- [52] J. Yao and G.R. Liu, “A matrix-form GSM–CFD solver for incompressible fluids and its application to hemodynamics”, *Computational Mechanics*, **54** (2014) 999–1012, doi:10.1007/s00466-014-0990-8.
- [53] C.C. Long, A.L. Marsden, and Y. Bazilevs, “Shape optimization of pulsatile ventricular assist devices using FSI to minimize thrombotic risk”, *Computational Mechanics*, **54** (2014) 921–932, doi:10.1007/s00466-013-0967-z.
- [54] M.-C. Hsu, D. Kamensky, Y. Bazilevs, M.S. Sacks, and T.J.R. Hughes, “Fluid–structure interaction analysis of bioprosthetic heart valves: significance of arterial wall deformation”, *Computational Mechanics*, **54** (2014) 1055–1071, doi:10.1007/s00466-014-1059-4.
- [55] M.-C. Hsu, D. Kamensky, F. Xu, J. Kiendl, C. Wang, M.C.H. Wu, J. Mineroff, A. Reali, Y. Bazilevs, and M.S. Sacks, “Dynamic and fluid–structure interaction simulations of bioprosthetic heart valves using parametric design with T-splines and Fung-type material models”, *Computational Mechanics*, **55** (2015) 1211–1225, doi:10.1007/s00466-015-1166-x.
- [56] D. Kamensky, M.-C. Hsu, D. Schillinger, J.A. Evans, A. Aggarwal, Y. Bazilevs, M.S. Sacks, and T.J.R. Hughes, “An immersogeometric variational framework for fluid–structure interaction: Application to bioprosthetic heart valves”, *Computer Methods in Applied Mechanics and Engineering*, **284** (2015) 1005–1053.
- [57] T.E. Tezduyar, S. Sathe, T. Cragin, B. Nanna, B.S. Conklin, J. Pausewang, and M. Schwaab, “Modeling of fluid–structure interactions with the space–time finite elements: Arterial fluid mechanics”, *International Journal for Numerical Methods in Fluids*, **54** (2007) 901–922, doi:10.1002/flid.1443.

- [58] T.E. Tezduyar, S. Sathe, M. Schwaab, and B.S. Conklin, “Arterial fluid mechanics modeling with the stabilized space–time fluid–structure interaction technique”, *International Journal for Numerical Methods in Fluids*, **57** (2008) 601–629, doi:10.1002/flid.1633.
- [59] T.E. Tezduyar, M. Schwaab, and S. Sathe, “Sequentially-Coupled Arterial Fluid–Structure Interaction (SCAFSI) technique”, *Computer Methods in Applied Mechanics and Engineering*, **198** (2009) 3524–3533, doi:10.1016/j.cma.2008.05.024.
- [60] K. Takizawa, J. Christopher, T.E. Tezduyar, and S. Sathe, “Space–time finite element computation of arterial fluid–structure interactions with patient-specific data”, *International Journal for Numerical Methods in Biomedical Engineering*, **26** (2010) 101–116, doi:10.1002/cnm.1241.
- [61] T.E. Tezduyar, K. Takizawa, C. Moorman, S. Wright, and J. Christopher, “Multiscale sequentially-coupled arterial FSI technique”, *Computational Mechanics*, **46** (2010) 17–29, doi:10.1007/s00466-009-0423-2.
- [62] K. Takizawa, C. Moorman, S. Wright, J. Christopher, and T.E. Tezduyar, “Wall shear stress calculations in space–time finite element computation of arterial fluid–structure interactions”, *Computational Mechanics*, **46** (2010) 31–41, doi:10.1007/s00466-009-0425-0.
- [63] K. Takizawa, C. Moorman, S. Wright, J. Purdue, T. McPhail, P.R. Chen, J. Warren, and T.E. Tezduyar, “Patient-specific arterial fluid–structure interaction modeling of cerebral aneurysms”, *International Journal for Numerical Methods in Fluids*, **65** (2011) 308–323, doi:10.1002/flid.2360.
- [64] T.E. Tezduyar, K. Takizawa, T. Brummer, and P.R. Chen, “Space–time fluid–structure interaction modeling of patient-specific cerebral aneurysms”, *International Journal for Numerical Methods in Biomedical Engineering*, **27** (2011) 1665–

1710, doi:10.1002/cnm.1433.

- [65] K. Takizawa, T.E. Tezduyar, A. Buscher, and S. Asada, “Space–time interface-tracking with topology change (ST-TC)”, *Computational Mechanics*, **54** (2014) 955–971, doi:10.1007/s00466-013-0935-7.
- [66] K. Takizawa, “Computational engineering analysis with the new-generation space–time methods”, *Computational Mechanics*, **54** (2014) 193–211, doi:10.1007/s00466-014-0999-z.
- [67] K. Takizawa, T.E. Tezduyar, A. Buscher, and S. Asada, “Space–time fluid mechanics computation of heart valve models”, *Computational Mechanics*, **54** (2014) 973–986, doi:10.1007/s00466-014-1046-9.
- [68] K. Takizawa, T.E. Tezduyar, T. Terahara, and T. Sasaki, “Heart valve flow computation with the Space–Time Slip Interface Topology Change (ST-SI-TC) method and Isogeometric Analysis (IGA)”, in P. Wriggers and T. Lenarz, editors, *Biomedical Technology: Modeling, Experiments and Simulation*, Lecture Notes in Applied and Computational Mechanics, 77–99, Springer, 2018, ISBN 978-3-319-59547-4, doi:10.1007/978-3-319-59548-1\_6.
- [69] K. Takizawa, T.E. Tezduyar, T. Terahara, and T. Sasaki, “Heart valve flow computation with the integrated Space–Time VMS, Slip Interface, Topology Change and Isogeometric Discretization methods”, *Computers & Fluids*, **158** (2017) 176–188, doi:10.1016/j.compfluid.2016.11.012.
- [70] K. Takizawa, T.E. Tezduyar, H. Uchikawa, T. Terahara, T. Sasaki, K. Shiozaki, A. Yoshida, K. Komiya, and G. Inoue, “Aorta flow analysis and heart valve flow and structure analysis”, in T.E. Tezduyar, editor, *Frontiers in Computational Fluid–Structure Interaction and Flow Simulation: Research from Lead Investigators under Forty – 2018*, Modeling and Simulation in Science, Engineering and Tech-

- nology, 29–89, Springer, 2018, ISBN 978-3-319-96468-3, doi:10.1007/978-3-319-96469-0\_2.
- [71] H. Suito, K. Takizawa, V.Q.H. Huynh, D. Sze, and T. Ueda, “FSI analysis of the blood flow and geometrical characteristics in the thoracic aorta”, *Computational Mechanics*, **54** (2014) 1035–1045, doi:10.1007/s00466-014-1017-1.
- [72] H. Suito, K. Takizawa, V.Q.H. Huynh, D. Sze, T. Ueda, and T.E. Tezduyar, “A geometrical-characteristics study in patient-specific FSI analysis of blood flow in the thoracic aorta”, in Y. Bazilevs and K. Takizawa, editors, *Advances in Computational Fluid–Structure Interaction and Flow Simulation: New Methods and Challenging Computations*, Modeling and Simulation in Science, Engineering and Technology, 379–386, Springer, 2016, ISBN 978-3-319-40825-5, doi:10.1007/978-3-319-40827-9\_29.
- [73] K. Takizawa, T.E. Tezduyar, H. Uchikawa, T. Terahara, T. Sasaki, and A. Yoshida, “Mesh refinement influence and cardiac-cycle flow periodicity in aorta flow analysis with isogeometric discretization”, *Computers & Fluids*, published online, DOI: 10.1016/j.compfluid.2018.05.025, May 2018, doi:10.1016/j.compfluid.2018.05.025.
- [74] K. Takizawa, R. Torii, H. Takagi, T.E. Tezduyar, and X.Y. Xu, “Coronary arterial dynamics computation with medical-image-based time-dependent anatomical models and element-based zero-stress state estimates”, *Computational Mechanics*, **54** (2014) 1047–1053, doi:10.1007/s00466-014-1049-6.
- [75] T.E. Tezduyar, T. Cragin, S. Sathe, and B. Nanna, “FSI computations in arterial fluid mechanics with estimated zero-pressure arterial geometry”, in E. Onate, J. Garcia, P. Bergan, and T. Kvamsdal, editors, *Marine 2007*, CIMNE, Barcelona, Spain, (2007).

- [76] K. Takizawa, Y. Bazilevs, and T.E. Tezduyar, “Space–time and ALE-VMS techniques for patient-specific cardiovascular fluid–structure interaction modeling”, *Archives of Computational Methods in Engineering*, **19** (2012) 171–225, doi:10.1007/s11831-012-9071-3.
- [77] M. Bischoff, E. Ramm, and J. Irslinger, “Models and finite elements for thin-walled structures”, *Encyclopedia of Computational Mechanics Second Edition*, (2017) 1–86.
- [78] G. Holzapfel and R. Ogden, “Constitutive modelling of arteries”, *Proceedings of the Royal Society A: Mathematical, Physical and Engineering Sciences*, **466** (2010) 1551–1597.
- [79] S. Kyriacou, A. Shah, and J. Humphrey, “Inverse finite element characterization of nonlinear hyperelastic membrane”, *Journal of Applied Mechanics-Transactions of the ASME*, **64** (1997) 257–262.
- [80] P. Seshaiyer, F. Hsu, A. Shah, S. Kyriacou, and J. Humphrey, “Multiaxial mechanical behavior of human saccular aneurysms”, *Computer Methods in Biomechanics and Biomedical Engineering*, **4** (2001) 281–289.
- [81] P. Seshaiyer and J. Humphrey, “A sub-domain inverse finite element characterization of hyperelastic membranes including soft tissues”, *Journal of Biomechanical Engineering-Transactions of the ASME*, **125** (2003) 363–371.
- [82] V. Fachinotti, A. Cardona, and P. Jetteur, “Finite element modelling of inverse design problems in large deformations anisotropic hyperelasticity”, *International Journal for Numerical Methods in Engineering*, **74** (2008) 894–910.
- [83] R. Wuchner and K.-U. Bletzinger, “Stress-adapted numerical form finding of prestressed surfaces by the updated reference strategy”, *International Journal for Numerical Methods in Engineering*, **64** (2005) 143–166.

- [84] F. de Vosse, J. Hart, C. Oijen, D. Bessems, T. Gunther, A. Segal, B. Wolters, and J. Stijnen, “Finite-element-based computational methods for cardiovascular fluid–structure interaction”, *Journal of Engineering Mathematics*, **47** (2003) 335–368.
- [85] J. Hart, G. Peters, P. Schreurs, and F. Baaijens, “A three-dimensional computational analysis of fluid–structure interaction in the aortic valve”, *Journal of Biomechanics*, **36** (2003) 103–112.
- [86] S. de Putter, B. Wolters, M. Rutten, M. Breeuwer, F. Gerritsen, and F. van de Vosse, “Patient-specific initial wall stress in abdominal aortic aneurysms with a backward incremental method”, *Journal of Biomechanics*, **40** (2007) 1081–1090.
- [87] M. Gee, C. Forster, and W. Wall, “A computational strategy for prestressing patient-specific biomechanical problems under finite deformation”, *International Journal for Numerical Methods in Biomedical Engineering*, **26** (2010) 52–72.
- [88] H. Weisbecker, D. Pierce, and G. Holzapfel, “A generalized prestressing algorithm for fine element simulations of preloaded geometries with application to the aorta”, *International Journal for Numerical Methods in Biomedical Engineering*, **30** (2014) 857–872.
- [89] K. Takizawa, H. Takagi, T.E. Tezduyar, and R. Torii, “Estimation of element-based zero-stress state for arterial FSI computations”, *Computational Mechanics*, **54** (2014) 895–910, doi:10.1007/s00466-013-0919-7.
- [90] G. Holzapfel, *Nonlinear solid mechanics: a continuum approach for engineering*. John Wiley & Sons, 2000, ISBN 978-0471-82304-9.
- [91] T. Belytschko, W. Liu, and B. Moran, *Nonlinear Finite Elements for Continua and Structures*. Wiley, 2000.
- [92] P. Flory, “Thermodynamic relations for high elastic materials”, *Transactions of the Faraday Society*, **57** (1961) 829–838.

- [93] E. Lee, “Elastic-plastic deformation at finite strain”, *Journal of Applied Mechanics*, **36** (1969) 1–6.
- [94] J.A. Cottrell, T.J.R. Hughes, and Y. Bazilevs, *Isogeometric Analysis. Toward Integration of CAD and FEA*. Wiley, 2009.
- [95] M. Cox, “The numerical evaluation of B-Splines”, *IMA Journal of Applied Mathematics*, **10** (1972) 134–149.
- [96] C. Boor, “On calculating with B-Splines”, *Journal of Approximation Theory*, **6** (1972) 50–62.
- [97] M.J. Borden, M.A. Scott, J.A. Evans, and T. Hughes, “Isogeometric finite element data structures based on Bézier extraction of NURBS”, *International Journal for Numerical Methods in Engineering*, **87** (2011) 15–47.
- [98] T. Sederberg, J. Zheng, A. Bakenov, and A. Nasri, “T-splines and T-NURCCs”, *ACM Transactions on Graphics (TOG)*, **22** (2003) 477–484.
- [99] K. Takizawa, T.E. Tezduyar, and T. Sasaki, “Estimation of element-based zero-stress state in arterial FSI computations with isogeometric wall discretization”, in P. Wriggers and T. Lenarz, editors, *Biomedical Technology: Modeling, Experiments and Simulation*, Lecture Notes in Applied and Computational Mechanics, 101–122, Springer, 2018, ISBN 978-3-319-59547-4, doi:10.1007/978-3-319-59548-1\_7.
- [100] K. Takizawa, T.E. Tezduyar, and T. Sasaki, “Aorta modeling with the element-based zero-stress state and isogeometric discretization”, *Computational Mechanics*, **59** (2017) 265–280, doi:10.1007/s00466-016-1344-5.
- [101] T. Sasaki, K. Takizawa, and T.E. Tezduyar, “Aorta zero-stress state modeling with T-spline discretization”, *Computational Mechanics*, published online, DOI: 10.1007/s00466-018-1651-0, November 2018, doi:10.1007/s00466-018-1651-0.

- [102] K. Takizawa, T.E. Tezduyar, and T. Sasaki, “Isogeometric hyperelastic shell analysis with out-of-plane deformation mapping”, *Computational Mechanics*, published online, DOI: 10.1007/s00466-018-1616-3, August 2018, doi:10.1007/s00466-018-1616-3.
- [103] T. Sasaki, K. Takizawa, and T.E. Tezduyar, “Medical-image-based aorta modeling with zero-stress-state estimation”, *Computational Mechanics*, to appear, 2019.
- [104] L. Treloar, “The elasticity of a network of long-chain molecules – I”, *Transactions of the Faraday Society*, **39** (1943) 36–41.
- [105] L. Treloar, “The elasticity of a network of long-chain molecules – II”, *Transactions of the Faraday Society*, **39** (1943) 36–41.
- [106] T. Gasser, R. Ogden, and G. Holzapfel, “Hyperelastic modelling of arterial layers with distributed collagen fibre orientations”, *Journal of the Royal Society Interface*, **3** (2006) 15–35.
- [107] J. Kiendl, M.-C. Hsu, M.C.H. Wu, and A. Reali, “Isogeometric kirchhoff-love shell formulations for general hyperelastic materials”, *Computer Methods in Applied Mechanics and Engineering*, **291** (2015) 280–303.



## 早稲田大学 博士（工学） 学位申請 研究業績書

(List of research achievements for application of doctorate (Dr. of Engineering), Waseda University)

氏名 Takafumi SASAKI

(As of February, 2019)

種 類 別 (By Type)	題名、 発表・発行掲載誌名、 発表・発行年月、 連名者（申請者含む） (theme, journal name, date & year of publication, name of authors inc. yourself)
Journal Articles (Peer-Reviewed)	<ul style="list-style-type: none"> <li>○ 1. <b>T. Sasaki</b>, K. Takizawa, and T.E. Tezduyar, “Aorta zero-stress state modeling with T-spline discretization”, <i>Computational Mechanics</i>, (<b>published online</b>).</li> <li>○ 2. <b>T. Sasaki</b>, K. Takizawa, and T.E. Tezduyar, “Medical-Image-Based Aorta Modeling with Zero-Stress-State Estimation”, <i>Computational Mechanics</i>, (<b>in printing</b>).</li> <li>3. K. Takizawa, T.E. Tezduyar, and <b>T. Sasaki</b>, “Isogeometric hyperelastic shell analysis with out-of-plane deformation mapping”, <i>Computational Mechanics</i>, (<b>published online</b>).</li> <li>4. K. Takizawa, T.E. Tezduyar, H. Uchikawa, T. Terahara, <b>T. Sasaki</b>, and A. Yoshida, “Mesh refinement influence and cardiac-cycle flow periodicity in aorta flow analysis with isogeometric discretization”, <i>Computers &amp; Fluids</i>, (<b>published online</b>).</li> <li>5. K. Takizawa, T.E. Tezduyar, T. Terahara, and <b>T. Sasaki</b>, “Heart valve flow computation with the integrated Space–Time VMS, Slip Interface, Topology Change and Isogeometric Discretization methods”, <i>Computers &amp; Fluids</i>, <b>158</b> (2017) 176–188.</li> <li>6. K. Takizawa, T.E. Tezduyar, and <b>T. Sasaki</b>, “Aorta modeling with the element-based zero-stress state and isogeometric discretization”, <i>Computational Mechanics</i>, <b>59</b> (2017) 265–280.</li> </ul>
Chapters in Books (Peer-Reviewed)	<ul style="list-style-type: none"> <li>1. K. Takizawa, T.E. Tezduyar, H. Uchikawa, T. Terahara, <b>T. Sasaki</b>, K. Shiozaki, A. Yoshida, K. Komiya, and G. Inoue, “Aorta flow analysis and heart valve flow and structure analysis”, in T.E. Tezduyar, editor, <i>Frontiers in Computational Fluid–Structure Interaction and Flow Simulation: Research from Lead Investigators under Forty – 2018, Modeling and Simulation in Science, Engineering and Technology</i>, 29–89, Springer, 2018.</li> <li>2. K. Takizawa, T.E. Tezduyar, T. Terahara, and <b>T. Sasaki</b>, “Heart valve flow computation with the Space–Time Slip Interface Topology Change (ST-SI-TC) method and Isogeometric Analysis (IGA)”, in P. Wriggers and T. Lenarz, editors, <i>Biomedical Technology: Modeling, Experiments and Simulation, Lecture Notes in Applied and Computational Mechanics</i>, 77–99, Springer, 2018.</li> <li>3. K. Takizawa, T.E. Tezduyar, and <b>T. Sasaki</b>, “Estimation of element-based zero-stress state in arterial FSI computations with isogeometric wall discretization”, in P. Wriggers and T. Lenarz, editors, <i>Biomedical Technology: Modeling, Experiments and Simulation, Lecture Notes in Applied and Computational Mechanics</i>, 101–122, Springer, 2018</li> </ul>
International Lectures	<ul style="list-style-type: none"> <li>1. <b>T. Sasaki</b>, K. Takizawa, and T.E. Tezduyar, “Arterial element-based zero-stress state estimation with T-spline representation”, in <i>Extended Abstracts of USACM Conference on Isogeometric Analysis and Meshfree Methods</i>, Pavia, Italy, 2017.</li> <li>2. T. Terahara, K. Takizawa, T.E. Tezduyar, and <b>T. Sasaki</b>, “Heart valve flow analysis with the integrated Space–Time VMS, Slip Interface, and Topology Change methods and isogeometric discretization”, in <i>Extended Abstracts of the 2017 Engineering Mechanics Institute Conference</i>, California, USA, 2017.</li> <li>3. <b>T. Sasaki</b>, K. Takizawa, and T.E. Tezduyar, “Estimation of arterial element-based zero-stress state with T-splines wall discretization”, in <i>Extended Abstracts of USACM Conference on Isogeometric Analysis and Meshfree Methods</i>, California, USA, 2016.</li> <li>4. <b>T. Sasaki</b>, K. Takizawa, H. Uchikawa, H. Takagi, T.E. Tezduyar, and K. Itatani, “Aorta FSI analysis with the element-based zero-stress state estimation and isogeometric discretization”, in <i>Extended Abstracts of the 12th World Congress on Computational Mechanics (WCCM XII) and the 6th Asia–Pacific Congress on Computational Mechanics (APCOM VI)</i>, Seoul, Korea, 2016.</li> <li>5. <b>T. Sasaki</b>, K. Takizawa, T.E. Tezduyar, H. Takagi, K. Itatani, S. Miyazaki, and K. Miyaji, “Arterial wall modeling with time-dependent surface extraction from medical images”, in <i>Extended Abstracts of International Conference on Biomedical Technology 2015</i>, Hannover, Germany, 2015.</li> </ul>

## 早稲田大学 博士（工学） 学位申請 研究業績書

(List of research achievements for application of doctorate (Dr. of Engineering), Waseda University)

種 類 別 By Type	題名、 発表・発行掲載誌名、 発表・発行年月、 連名者（申請者含む） (theme, journal name, date & year of publication, name of authors inc. yourself)
Domestic Lectures	<ol style="list-style-type: none"> <li>6. <b>T. Sasaki</b>, K. Takizawa, T.E. Tezduyar, H. Uchikawa, and K. Itatani, “Zero-stress state estimation in structural mechanics modeling of a human aorta with NURBS representation”, in <i>Proceedings of KSME–JSME Joint Symposium on Computational Mechanics &amp; CAE 2015</i>, Tokyo, Japan, 2015.</li> <li>7. <b>T. Sasaki</b>, K. Takizawa, T.E. Tezduyar, H. Uchikawa, and K. Itatani, “Zero-stress state estimation in structural mechanics modeling of a human aorta with NURBS representation”, in <i>Extended Abstracts of JST CREST–PRESTO Symposium 2015 — Mathematics for the 22nd Century</i>, Tokyo, Japan, 2015.</li> <li>8. <b>T. Sasaki</b>, H. Uchikawa, K. Takizawa, T.E. Tezduyar, K. Itatani, S. Miyazaki, and K. Miyaji, “Arterial wall modeling with time-dependent medical images”, in <i>Extended Abstracts of the 13th US National Congress on Computational Mechanics</i>, California, USA, 2015.</li> <li>9. <b>T. Sasaki</b>, K. Takizawa, T.E. Tezduyar, H. Takagi, K. Itatani, S. Miyazaki, and K. Miyaji, “Arterial dynamics computation with surface-extraction medical-image-based time-dependent anatomical models and element-based zero-stress estimates”, in <i>Extended Abstracts of the 18th International Conference on Finite Elements in Flow Problems</i>, Taipei, Taiwan, 2015.</li> <li>1. A. Yoshida, <b>T. Sasaki</b>, K. Takizawa, and T.E. Tezduyar, “Aorta surface re-parametrization based on principal curvatures”, in <i>Proceedings of JSME 31th Computational Mechanics Division Conference</i>, Tokushima, Japan, 2018.</li> <li>2. R. Kobayashi, T. Terahara, <b>T. Sasaki</b>, K. Takizawa, and T.E. Tezduyar, “A patient specific aortic valve analysis with resolved flow near the leaflet surfaces”, in <i>Extended Abstracts of Mechanical Engineering Congress 2017</i>, Osaka, Japan, 2018.</li> <li>3. G. Inoue, <b>T. Sasaki</b>, A. Yoshida, K. Takizawa, and T.E. Tezduyar, “Hyperelastic models for arterial mechanics with isogeometric discretization”, in <i>Proceedings of JSME 29th Conference on Frontiers in Bioengineering</i>, Chiba, Japan, 2018.</li> <li>4. G. Inoue, <b>T. Sasaki</b>, A. Yoshida, K. Takizawa, and T.E. Tezduyar, “Arterial isogeometric shell analysis with the lumen geometry extracted from medical images”, in <i>Extended Abstracts of Mechanical Engineering Congress 2018</i>, Osaka, Japan, 2018.</li> <li>5. <b>T. Sasaki</b>, H. Uchikawa, K. Komiya, K. Takizawa, and T.E. Tezduyar, “Effect for blood flow with arterial elasticity and arterial structure computation”, in <i>Extended Abstracts of Research Committee on Blood Flow and Cardiovascular System</i>, Chiba, Japan, 2018.</li> <li>6. K. Shiozaki, T. Terahara, <b>T. Sasaki</b>, K. Takizawa, and T.E. Tezduyar, “Effect of aortic valve shape on flow”, in <i>Proceedings of JSME 28th Conference on Frontiers in Bioengineering</i>, Tokushima, Japan, 2017.</li> <li>7. T. Terahara, <b>T. Sasaki</b>, K. Takizawa, and T.E. Tezduyar, “Heart valve computational flow analysis with resolved jet flow near leaflet surface”, in <i>Extended Abstracts of Research Committee on Blood Flow and Cardiovascular System</i>, Tokyo, Japan, 2017.</li> <li>8. T. Terahara, <b>T. Sasaki</b>, K. Shiozaki, K. Takizawa, and T.E. Tezduyar, “Aortic valve analysis based on high-fidelity computational fluid dynamics”, in <i>Proceedings of JSME 28th Conference on Frontiers in Bioengineering</i>, Tokushima, Japan, 2017.</li> <li>9. K. Shiozaki, T. Terahara, <b>T. Sasaki</b>, K. Takizawa, and T.E. Tezduyar, “Aortic valve and ST blood flow analysis”, in <i>Proceedings of JSME 30th Computational Mechanics Division Conference</i>, Osaka, Japan, 2017.</li> <li>10. A. Yoshida, K. Takizawa, <b>T. Sasaki</b>, and T.E. Tezduyar, “Arterial zero-stress estimation –extension to complex geometry–”, in <i>Proceedings of JSME 30th Computational Mechanics Division Conference</i>, Osaka, Japan, 2017.</li> <li>11. <b>T. Sasaki</b>, K. Takizawa, A. Yoshida, and T.E. Tezduyar, “Arterial zero-stress estimation –basic study–”, in <i>Proceedings of JSME 30th Computational Mechanics Division Conference</i>, Osaka, Japan, 2017.</li> <li>12. H. Uchikawa, T. Terahara, <b>T. Sasaki</b>, K. Takizawa, and T.E. Tezduyar, “Patient-specific aorta flow analysis with the space–time VMS method and isogeometric discretization”, in <i>Extended Abstracts of Mechanical Engineering Congress 2017</i>, Saitama, Japan, 2017.</li> </ol>

## 早稲田大学 博士（工学） 学位申請 研究業績書

(List of research achievements for application of doctorate (Dr. of Engineering), Waseda University)

種 類 別 By Type	題名、 発表・発行掲載誌名、 発表・発行年月、 連名者（申請者含む） (theme, journal name, date & year of publication, name of authors inc. yourself)
	<p>13. T. Terahara, K. Shiozaki, <b>T. Sasaki</b>, K. Takizawa, and T.E. Tezduyar, “Heart valve flow analysis with isogeometric discretization and resolved jet flow near leaflet surfaces”, in <i>Extended Abstracts of Mechanical Engineering Congress 2017</i>, Saitama, Japan, 2017.</p> <p>14. A. Yoshida, <b>T. Sasaki</b>, T. Terahara, K. Takizawa, and T.E. Tezduyar, “Estimation of zero-stress state in patient-specific aorta models with branches”, in <i>Proceedings of the 22nd Japan Society for Computational Engineering and Science Conference</i>, Saitama, Japan,</p> <p>15. K. Shiozaki, T. Terahara, <b>T. Sasaki</b>, K. Takizawa, and T.E. Tezduyar, “Space–time isogeometric analysis of aortic-valve fluid mechanics and flow validation near the leaflet surfaces”, in <i>Proceedings of the 22nd Japan Society for Computational Engineering and Science Conference</i>, Saitama, Japan, 2017.</p> <p>16. H. Uchikawa, T. Terahara, <b>T. Sasaki</b>, K. Takizawa, and T.E. Tezduyar, “Fluid and structure analysis of the human aorta — fluid mechanics analysis with space–time isogeometric discretization —”, in <i>Proceedings of the 22nd Japan Society for Computational Engineering and Science Conference</i>, Saitama, Japan, 2017.</p> <p>17. A. Yoshida, <b>T. Sasaki</b>, T. Terahara, K. Takizawa, and T.E. Tezduyar, “Estimation of zero-stress state in patient-specific aorta models with branches”, in <i>Proceedings of JSME 29th Bioengineering Conference</i>, Aichi, Japan, 2017.</p> <p>18. K. Shiozaki, T. Terahara, <b>T. Sasaki</b>, K. Takizawa, and T.E. Tezduyar, “Computational analysis and experimental validation of aortic valve fluid mechanics with experiment-based anatomical models”, in <i>Proceedings of JSME 29th Bioengineering Conference</i>, Aichi, Japan, 2017.</p> <p>19. K. Shiozaki, T. Terahara, <b>T. Sasaki</b>, K. Takizawa, and T.E. Tezduyar, “Computational analysis of aortic-valve fluid mechanics and experimental validation”, in <i>Proceedings of the 30th Symposium on Computational Fluid Dynamics</i>, Tokyo, Japan, 2016.</p> <p>20. H. Uchikawa, T. Terahara, <b>T. Sasaki</b>, K. Takizawa, and T.E. Tezduyar, “Vortex structure and periodicity studies on aorta and aortic valve flow analysis”, in <i>Proceedings of JSME 94th Fluids Engineering Conference</i>, Yamaguchi, Japan, 2016.</p> <p>21. <b>T. Sasaki</b>, K. Takizawa, T.E. Tezduyar, and K. Itatani, “Aortic zero-stress state estimation with isogeometric discretization”, in <i>Proceedings of JSME 29th Computational Mechanics Division Conference</i>, Aichi, Japan, 2016.</p> <p>22. <b>T. Sasaki</b>, K. Takizawa, T.E. Tezduyar, and K. Itatani, “Aorta modeling with zero-stress estimation, material-point tracking, and isogeometric discretization”, in <i>Proceedings of the 21st Japan Society for Computational Engineering and Science Conference</i>, Niigata, Japan, 2016.</p> <p>23. <b>T. Sasaki</b>, K. Takizawa, H. Uchikawa, T.E. Tezduyar, and K. Itatani, “Zero-stress state estimation of aortic wall with NURBS representation”, in <i>Proceedings of JSME 28th Bioengineering Conference</i>, Tokyo, Japan, 2016.</p> <p>24. <b>T. Sasaki</b>, H. Uchikawa, K. Takizawa, T.E. Tezduyar, K. Itatani, S. Miyazaki, and K. Miyaji, “Arterial wall modeling with time-dependent medical images”, in <i>Extended Abstracts of Mechanical Engineering Congress 2015</i>, Hokkaido, Japan, 2015.</p> <p>25. <b>T. Sasaki</b>, H. Uchikawa, K. Takizawa, T.E. Tezduyar, K. Itatani, S. Miyazaki, and K. Miyaji, “Physically based mapping and arterial wall modeling”, in <i>Proceedings of the 20th Japan Society for Computational Engineering and Science Conference</i>, Ibaraki, Japan, 2015.</p> <p>26. <b>T. Sasaki</b>, K. Takizawa, K. Itatani, H. Takagi, T.E. Tezduyar, S. Miyazaki, and K. Miyaji, “Arterial wall modeling and medical image mapping based on element-based zero-stress state estimation method”, in <i>Proceedings of JSME 27th Bioengineering Conference</i>, Niigata, Japan, 2015.</p> <p>27. <b>T. Sasaki</b>, K. Takizawa, K. Itatani, H. Takagi, T.E. Tezduyar, S. Miyazaki, and K. Miyaji, “An aorta dynamics computation with the element-based zero-stress state estimation method”, in <i>Proceedings of JSME 25th Conference on Frontiers in Bioengineering</i>, Tottori, Japan, 2014.</p> <p>6 others.</p>